**UNIVERSITÀ**
**DEGLI STUDI**
**DI PADOVA**

Head Office: Università degli Studi di Padova

Department of Geosciences

_____

Ph.D. COURSE IN: Geosciences
35th SERIES

**EXTRATERRESTRIAL DIAMONDS IN UREILITES**

Thesis written with the financial contribution of Fondazione Cassa di Risparmio di Padova e Rovigo

**Coordinator:** Prof. Claudia Agnini
**Supervisor**:  Prof. Fabrizio Nestola
**Co-Supervisor**: Prof. Frank E. Brenker

**Ph.D. student**: Oliver Christ

# Abstract

In this Phd thesis, carbon aggregates from ureilites have been extracted and analysed in a multimethodological approach to gain more insights in how ureilitic diamonds have formed. Ureilites represent the second largest group of achondrites and are known to contain significant amount of carbon, mainly in the form of graphite and diamond. The formation of these diamonds is a timely and strongly discussed topic. Over decades, three major hypotheses have been published: (i) the formation deep inside a planetary body, (ii) the direct transformation from graphite to diamond upon shock and (iii) the formation from a chemical vapour deposition (CVD). Generally, the direct transformation from graphite to diamond during a shock event, i.e., a major impact which destroyed the ureilite parent body, is the most accepted one. However, recent studies claimed to have found presumed large diamonds in a ureilite which were interpreted to have formed deep inside a planetary body which had a size in the range between Mercury and Mars and were the initiator for this work. Further large diamonds in ureilites were found and thoroughly characterised. The multimethodological approach included optical microscopy, scanning electron microscopy, micro-Raman spectroscopy, X-ray diffraction, field emission gun electron microprobe analyser, mass spectroscopy and first tests of micro-X-ray computed tomography. A few comparably very large ureilitic diamonds were found and characterised. Based on their crystallographic and isotopic features, it is evident that these microdiamonds originate from graphite which was present on the ureilite parent body and has been transformed to diamond upon high pressures and temperatures during a shock event. Hence, there is no necessity for a large ureilite parent body to produce microdiamonds.

# Sommario

In questo progetto, aggregati di carbonio provenienti da ureiliti sono stati estratti e analizzati attraverso un approccio multimetodologico al fine di comprendere la formazione dei diamanti ureilitici. Le ureiliti rappresentano il secondo gruppo più grande di achondriti e contengono significative quantità di carbonio, in particolare come grafite e diamante. La formazione di questi diamanti rappresenta uno degli aspetti più discussi. Nel corso degli ultimi decenni, sono state proposte e pubblicate tre principali ipotesi: (i) loro formazione allinterno di corpi planetari, (ii) la trasformazione diretta da grafite a diamante a seguito di eventi di shock, (iii) la formazione a seguito di deposizione chimica da vapore. In generale, la trasformazione diretta da grafite in diamante durante eventi di shock, ovvero un impatto che ha distrutto l'ureilite genitore, é ritenuta lipotesi più accreditata. Tuttavia, studi recenti sostengono di aver identificato diamanti in ureiliti la cui formazione è avvenuta allinterno di corpi planetari di dimensioni comprese tra quelle di Mercurio e Marte. Questi studi sono alla base del presente lavoro di tesi. Altri diamanti di dimensioni relevanti in ureiliti sono stati caratterizzati. L'approccio multimetodologico utilizzato nel presente lavoro di tesi comprende microscopia ottica, diffrazione a raggi X, spettroscopia Raman, FEG-SEM, spettrometria di massa e un primo test di micro-raggi-X tomografia computerizzata. Sulla base delle caratteristiche cristallografiche e isotopiche, é ipotizzabile che i microdiamanti studiati in questo lavoro di tesi si sono formati da grafite, la quale era presente nellureilite genitore e trasformata in diamante a seguito alle alte temperature e pressioni raggiunte durante un evento di shock. Di conseguenza, non sussiste la necessità di invocare un progenitore ureilitico di grandi dimensioni per la formazione di micro diamanti.

# Contents

# List of Figures

# List of Tables

## List of Abbreviations

**BSE** Backscatter Electron

**CAI** Calcium Aluminum Rich Inclusions

**CCAM** Carbonaceous Chondrite Anhydrous Mineral

**CRE** Cosmic Ray Exposure

**CT** Computed Tomography

**CVD** Chemical Vapor Deposition

**EDS** Energy Dispersive X-ray Spectroscopy

**EELS** Electron Energy-Loss Spectroscopy

**FEG-EPMA** Field Emission Gun Electron Probe Microanalyser

**FIB** Focused Ion Beam

**FWHM** Full Width Half Maximum

**HED** howarditeeucritediogenite

**LCP** Low-Ca Pyroxene

**LG-SIMS** Large-Geometry Secondary-Ion Mass Spectrometer

**MRS** Micro-Raman Spectroscopy

**NWA** Northwest Africa

**SE** Secondary Electron

**SEM** Scanning Electron Microscopy

**UDB** Ureilite Daughter Body

**UPB** Ureilite Parent Body

**WDS** Wavelength Dispersive X-ray Spectroscopy

**XRD** X-ray Diffraction

# 1 Introduction

The subject of this PhD thesis is the formation process which led to diamonds in ureilites. Therefore, the carbon polymorphs graphite and diamond from two meteorites which belong to the meteorite group of ureilites were studied. Since their discovery, meteorites have been used to study the nature and formation of other terrestrial bodies. Carbon polymorphs are relatively rare in meteorites, however, they can be found in different meteorite classes, mainly in the form of graphite and diamond. Ureilites represent a group of meteorites which is known for a significantly high carbon content and a high abundance of diamond. Therefore, some ureilites are almost impossible to cut with stone saws. As it will be shown in the following chapters, the formation process for ureilitic diamond is a highly discussed topic. Over the last 70 years three different hypothesis were introduced, however, the origin of these diamonds remains enigmatic which gave the starting impulse for this project. To draw a bigger picture, at first the formation of terrestrial planets over the steps of planetesimals and planetary embryos will be introduced, followed by meteorites, a description of the two carbon polymorphs graphite and diamond subsequently the combination of these topics with the state of the art regarding graphite and diamond in ureilites.

## 1.1 The Early Solar System and Planetary Formation

Beside astrophysical studies, meteorites, and especially chondrites, have long been used to understand the formation of planetary bodies in our Solar System. The early Solar System is characterised by the collapse of a molecular cloud which then formed a star, in the case of our Solar System the Sun or proto-Sun. Remaining material formed a disk which circulated around the newly formed star, generally called the protoplanetary disk or in the case of the Sun, the solar nebula (Morbidelli et al., 2012). Here, dust

grains undergo a sedimentation process and form a thin layer at the mid plane of the protoplanetary disk (Weidenschilling, 1980).

The next step which involves the formation of larger particles from dust grains is still not fully understood. However, different processes have been proposed where each one faces different difficulties to explain the process entirely. The first hypothesis consists of the simple process of dust grains sticking to each other forming progressively larger sized objects and is called the ordered-growth process (Morbidelli et al., 2012). The ordered-growth process however, faces the problem that centimetre sized objects are too small to perform gravitational attractions towards each other and too large to stick to each other by electrostatic forces (Morbidelli et al., 2012). Further, all objects in the protoplanetary disk undergo a gas drag which pulls them towards the star at relatively high velocities which, upon collision between two particles, would rather lead to a break up than to an accretion of material, i.e., the meter-size barrier problem (Morbidelli et al., 2012, and references therein).

The meter-size barrier problem can be avoided by the gravoturbulent model. Here, the total gravity of large populations of small particles leads to the formation of larger objects ranging up to 100 km in size (Cuzzi et al., 2008; Johansen et al., 2007). With objects of this size, the formation of planetesimals occurs extremely rapid depending on the availability of material, i.e., the solid/gas density ratio (Morbidelli et al., 2012, and references therein). With gas being constantly removed from the disk, this ratio increases over time which leads to different onsets of planetesimal formation throughout regions of the protoplanetary disk (Morbidelli et al., 2012, and references therein). Depending on the availability of short-lived radionuclides such as $^{26}$Al and $^{60}$Fe (Ghosh et al., 2006), by now formed planetesimals could undergo thermal heating and thus differentiation processes (Ghosh et al., 2006; Morbidelli et al., 2012). Most likely, the ureilite parent body (UPB) (see section 1.4.2) represented one of these planetesimals before it was disrupted.

After planetesimals were formed, a stage of planetary embryo formation follows which is characterised by runaway growth (Morbidelli et al., 2012). The underlying process of runaway growth is the gravitational attraction between two planetesimals and is called runaway growth because larger bodies grow faster than small ones (Greenberg et al., 1978). As soon as the large bodies accreted significant amounts of mass, the runaway growth stops and the system gets dominated by the perturbations of these bodies (Morbidelli et al., 2012). With the runaway growth stopped, the so called oligarchic growth (e.g., Chambers, 2006; Kokubo and Ida, 1998) starts. Here, the remaining small bodies stop accreting into larger bodies because they are subject to large velocities which will rather lead to breakups than accretion among each other. However, they take part in the further growth of the already formed planetary embryos. After the oligarchic growth, the early Solar System is populated by numerous planetary embryos which are not yet massive enough, too densely distributed, and formed too quickly to represent terrestrial bodies (Morbidelli et al., 2012). However, they are massive enough to undergo differentiation processes, i.e., the melting of rocky material and formation of a metallic core.

The final step from planetary embryos to terrestrial planets is again characterised by collisions and subsequent accretion of material to large bodies (Morbidelli et al., 2012, and references therein). As simulations have shown, collisions between embryos lead not only to accretion but also to the loss of material in the form of collisional fragments of which some might reaccrete into embryos or get lost in the form of dust (Morbidelli et al., 2012).

With the early stages of our Solar System being a rather violent period characterised by many collisions between differently sized celestial objects, material has also been ejected from these objects. Material ejected from its parent body then flew through the Solar System and is called meteoroids. Meteoroids then may impact on other planetary bodies including Earth where upon impact on its surface they will be called meteorites.

3

## 1.2 Meteorites

Meteorites are rocks with an extraterrestrial origin, e.g., other planetary bodies as Moon or Mars or asteroids from the asteroid belt, which landed on Earth's surface. Nowadays, different types of meteorites have been recognised which resulted in a detailed classification scheme (e.g., Weisberg et al., 2006). A first important distinction is the distinction between falls and finds. While falls are observed falls when a meteoroid crosses Earth's atmosphere and finally lands on Earth's surface as a meteorite, funds are simply found on Earth's surface without an observed fall. This distinction is important as any rock laying on Earth's surface can be affected by weathering processes, especially in wet/humid environments. As a consequence, dry places like hot deserts or Antarctica are favoured locations to find meteorite finds. However, also there meteorites can be affected by terrestrial weathering processes (Weisberg et al., 2006).

When a meteorite is found, it will be given a name which is usually based on the location where it was found, e.g., the eponymous ureilite Novo-Urei was found in the village Novo Urey in Russia. Meteorites found in deserts such as Sahara, are assigned the name North West Africa (NWA) and a number (Weisberg et al., 2006), e.g., NWA 6871 or NWA 3140, the two ureilites studied in the present work.

The next distinction is between chondrites and achondrites. Chondrites represent undifferentiated rocks. They are named after small spherical objects with sizes of up to 2 mm, so called chondrules, which can be found in their matrix. With chondrules representing one of the oldest solids in the Solar System, chondrites originate from rocky bodies which have not experienced differentiation processes. However, there are also chondrites which do not contain chondrules (Weisberg et al., 2006).

In contrast to chondrites, achondrites experienced differentiation processes. They are igneous rocks which have experienced melting processes and therefore do not contain chondrules anymore and originate from planetary bodies or their precursor. So far, some achondrites could be linked to Moon, Mars and the differentiated asteroid 4

Vesta (Weisberg et al., 2006). Using petrological characteristics (texture, mineralogical content, and compositions), whole-rock chemical compositions, and oxygen isotopic compositions, chondrites and achondrites can further be divided into classes and groups. Chondrites are further subdivided into the carbonaceous (C), ordinary (O), and enstatite (E) classes. Carbonaceous groups are CI, CM, CO, CV, CK, and CR, ordinary into H, L, and LL, and enstatite into EH and EL. However, there are also two groups which do not belong to any of the three classes: R and K chondrites (Weisberg et al., 2006). Achondrites are subdivided into iron meteorites (IC, IIAB, IIC, IID, IIE, IIIAB, IIIAB, IIIE, IVA, and IVB), pallasites (main-group pallasites, Eagle Station pallasites, and pyroxene pallasites), mesosiderites, angrites, aubrites, meteorites from 4 Vesta (HEDs, howardite–eucrite–diogenite), and meteorites from Mars (shergottites, nakhlites, chassignites, and orthopyroxenites). A special distinction are primitive achondrites, which exhibit features of planetary differentiation processes but contain also unprocessed material or features. Primitive achondrites consist of brachinites, ureilites, acapulcoites, lodranites, winonaites, IAB and IIICD meteorites (Weisberg et al., 2006). Detailed descriptions of each type of meteorites are beyond the scope of this thesis and can be found in Weisberg et al. (2006). Here, only ureilites will be described in greater detail in section 1.4.

As already mentioned, meteorites originate from specific parent bodies. The process which led to the detachment from their parent body is usually a violent collision of two celestial bodies. Hence, another important classification is the evaluation of the shock degree a specific meteorite has experienced. A first shock degree classification scheme for ordinary chondrites was published in 1991 (Stöffler and Keil, 1991). Later in 2018, a new classification scheme was published which also considers other planetary silicate rocks as well as sediments, including a classification scheme for ultramafic rocks where ureilites belong to (Stöffler et al., 2018). In general, shock effects are the product of hypervelocity impacts between asteroids/comets and planetary bodies such as Earth, Moon, Mars and 4 Vesta but also among asteroids (Stöffler et al., 2018). Depending on the velocity of

5

the impactor, impacts can be very violent and lead to the propagation of a shock wave throughout the target body which affects the rocks of the target. Peak shock pressures and temperatures differ depending on porosities, shock impedance and the impactor velocity (Stöffler et al., 2018). Shock effects in the target body depend also on the constituting minerals. Detailed descriptions of shock effects in different minerals can be found in Stöffler et al. (2018). Here, shock effects in ureilites will be presented as ureilites are the sample material of this study. The classification scheme differentiates between seven shock stages ranging from U-S1 to U-S7 whereof the U stands for ultramafic and considered minerals for diagnostic shock features are olivine, pyroxene, amphibole, and plagioclase (Stöffler et al., 2018):

The lowest shock stage is U-S1, shock pressures are below 4–5 GPa, post-shock temperatures between 20–50 °C and diagnostic shock effects include irregular fractures and sharp optical extinction of all minerals. With U-S2, shock pressure and post-shock temperatures reach up to ∼5–10 GPa and 50–100 °C. Minerals appear fractured and exhibit undulatory extinction. The shock stage U-S3 is characterised by a shock pressure of ∼15 GPa and post-shock temperatures in the range of 100–150 °C. Olivine, pyroxene and plagioclase show undulatory extinction, olivine in addition to that also planar fractures. Pyroxenes can display incipient mechanical twinning. Followed by U-S4, pressure and temperature reach ∼28–30 GPa and 250–300 °C, respectively. Olivine and pyroxene show weak mosaicism as well as planar features. Mechanical twinning of pyroxene becomes more abundant in respect to U-S3 and plagioclase occurs partially isotropic. Pressures of ∼50–55 GPa and post-shock temperatures of 650–850 °C are responsible for U-S5. Olivine displays strong mosaicism, planar fractures, and planar deformation features, pyroxene is mechanically twinned while plagioclase transforms to diaplectic glass. U-S6 is the second strongest shock degree a ultramafic meteorite can exhibit. It is characterised by high pressures and high post-shock temperatures of ∼60–70 GPa and 1500–1700 °C. Olivine affected by these high pressure and temperature conditions

show incipient melting and recrystallisation, while pyroxene shows incipient melting and melted plagioclase contains vesicles. In addition, U-S5 and U-S6 show accompanying disequilibrium shock effects in the form of local melt veins and pockets, and pervasive localised melt veins and pockets, respectively. The last and strongest shock degree is U-S7, where the whole rock is melted (Stöffler et al., 2018).

## 1.3 Carbon and its Polymorphs Graphite and Diamond

### 1.3.1 Carbon

The chemical element carbon can be found in the $14^{\text{th}}$ group and second period in the periodic table of elements. Carbon has the atom number ($Z$) 6, the symbol C and in its ground state an electron configuration of $1s^2 2s^2 2p^2$ with two valence electrons.

Due to different bonds of carbon–carbon atoms, a variety of different materials exist of which three are shown in Figure 1.1. These materials include the hexagonal, semi metallic, and soft ($sp^2$-bonded) graphite and the cubic, insulating and hardest natural material ($sp^3$-bonded) diamond (Pierson, 2012). The differences in bonding and crystallographic arrangement of the atoms in both minerals, makes them easily distinguishable, even on very small scales, e.g., carbon aggregates as investigated in this project in which both polymorphs occur alongside each other.

A mixture of both cubic and hexagonal features on the nanoscale is lonsdaleite, often also referred to as "hexagonal diamond". However, there is considerable doubt about whether or not lonsdaleite is a distinct mineral or not (e.g., Németh et al., 2014). Therefore, this study will follow the suggestion by Németh et al. (2014) to refer to lonsdaleite as "lonsdaleite" throughout this thesis.

Although carbon is the fourth most abundant element in the Solar System (Lodders, 2003), its abundance in meteorites is relatively low and only in ureilites concentrations reach values of up to 7 wt.% (Goodrich et al., 2015). Here, carbon occurs mainly in

the form of graphite, diamond, "lonsdaleite", cohenite (Goodrich, 1992), and organic compounds (Sabbah et al., 2010). A more detailed introduction of carbon in ureilites can be found in section 1.4.3.
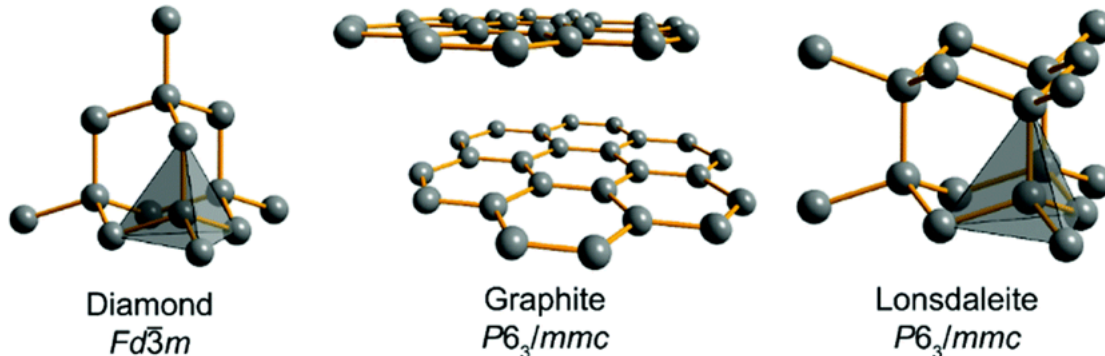


Figure 1.1: Crystal structures of diamond, graphite and "lonsdaleite", taken from Popov et al. (2019).

### 1.3.2 Graphite

Graphite is the hexagonal (rhombohedral) polymorph of carbon which is realised by $sp^2$ hybrid orbitals (Chung, 2002). The graphite structure is characterised by layers of covalent bound carbon atoms while the graphite layers are bound by weak van der Wall bonds (Chung, 2002). The layers can be stacked in two different orders: -ABAB- for hexagonal graphite, and -ABCABC- for rhombohedral graphite (Chung, 2002, and references therein). Hexagonal graphite has a hexagonal unit cell with $a \approx 2.46$ Å and $c \approx$ 6.71 Å, which consists of four carbon atoms and crystallises in the space group $P6_3/mmc$ (Chung, 2002, and references therein). A characteristic of the crystal structure for hexagonal graphite is a $d$-spacing of $\sim 3.34$ Å, which is the interplanar distance between two graphite layer planes (Chung, 2002).

Graphite can be easily identified by Raman spectroscopy where it shows a sharp band, called G-band, at $\sim 1582 \, \text{cm}^{-1}$ which is the $E_{2\text{g}}$ optical mode (Reich and Thomsen, 2004). Disordered graphite further exhibits the so called D-band at around $1350 \, \text{cm}^{-1}$ and a D' or G' band around $1620 \, \text{cm}^{-1}$ (Ferrari and Robertson, 2000; Reich and Thomsen,

2004). Graphite can further be easily identified by X-ray diffraction (XRD), where its most intense peaks are at *d*-spacings of 3.348 Å and 2.027 Å.

On Earth, graphite generally occurs in metamorphic rocks which had carbonaceous sedimentary rocks as precursor (Robinson Jr et al., 2017). However, also graphite with an extraterrestrial origin is known as graphite has been found in chondrites (e.g., Huss and Lewis, 1995), stony achondrites (e.g., Steele et al., 2012), and iron meteorites (e.g., Matsuda et al., 2005).

### 1.3.3 Diamond

Diamond is the $sp^3$-bonded polymorph of carbon, which is achieved by the formation of hybrid orbitals. Due to these hybrid orbitals which lead to four valence electrons, diamond shows very strong covalent bonds between carbon atoms which render diamond the hardest natural material (Pierson, 2012). It crystallises in the cubic space group $Fd3m$ with $a \approx 3.5668$ Å. Like graphite, diamond is easily identifiable by Raman spectroscopy and XRD. The Raman spectra of diamond shows only one band, the $T_{2\mathrm{g}}$ zone center mode at $\sim 1332$ cm$^{-1}$ (Knight and White, 1989) while in X-ray diffractograms, diamond shows peaks at the *d*-spacings of 2.059 Å, 1.261 Å, and 1.075 Å.

Diamond can be found on Earth in primary kimberlitic and lamprophyric magmatic deposits and in secondary deposits which are the product of weathering of primary deposits (Kjarsgaard et al., 2022). Despite diamond being an uncommon rock-forming mineral as it is always a xenocryst in the host rock, diamond can be found in a variety of mines and alluvial deposits around the world (Kjarsgaard et al., 2022). Diamond is the only mineral that crystallises throughout the entire Earth's mantle (Maeda et al., 2017) and therefore plays a major role in understanding Earth's interior as during its crystallisation, diamond often traps minerals and therefore represents the only mineral which provides a window into regions of the Earth's mantle of which it is still impossible to obtain direct sample material. In addition to Earth, diamond has also been reported

in meteorites such as iron meteorites (e.g., Foote, 1891; Nininger, 1939), chondrites (e.g., Huss and Lewis, 1995), and achondrites (e.g., Kunz, 1888). Similar to terrestrial diamonds, extraterrestrial diamonds were studied to obtain insights into the formation of the specific meteorite parent bodies (e.g., Fukunaga et al., 1987; Lipschutz, 1964; Lipschutz and Anders, 1961; Miyahara et al., 2015; Nabiei et al., 2018; Urey, 1956).

### 1.3.4 Lonsdaleite

The first report of "lonsdaleite" goes back to 1967 when Hanneman et al. (1967) and Frondel and Marvin (1967) found it in the Canyon Diablo iron meteorite. Later, "lonsdaleite" has also been found in ureilites (Le Guillou et al., 2010), terrestrial sediments (Israde-Alcántara et al., 2012; Khaliullin et al., 2011; Kvasnytsya et al., 2013) and shock wave experiments (Erskine and Nellis, 1992, 1991). It has therefore been interpreted to be an indicator for shock events such as asteroidal collisions and meteorite impacts on Earth and has been treated as a discrete mineral. Németh et al. (2014) proposed that "lonsdaleite" is moreover faulted and twinned cubic diamond instead of hexagonal diamond. Based on this assumption, more studies were conducted which came to the same conclusion that "lonsdaleite" is not a physical mixture of hexagonal and cubic diamond, but a stacking disordered diamond (Salzmann et al., 2015) and that in diamond with "lonsdaleite" features, multiple stacking faults occur along twin planes in cubic diamond which appear as a hexagonal symmetry (Murri et al., 2019). Despite the controversy of the exact definition of "lonsdaleite" being a discrete mineral or not (Murri et al., 2019; Németh et al., 2014; Salzmann et al., 2015), it is used as a shock indicator for diamond and can be seen as a product of the direct transformation of graphite to diamond upon shock. This stacking disordered and/or nano-twinned diamond can easily be detected as a shoulder towards lower $2\theta$ in the diffractograms of diamond.

**1.3.5 The Direct Transformation of Graphite to Diamond**

Due to extraordinary properties of diamond (e.g., hardness, electrical properties, thermal conductivity etc.), the direct transformation of graphite to diamond is of major interest for both academia and industry as diamond has a variety of applications which led to a high demand of synthesised diamond. However, as diamond is the high pressure polymorph of carbon, the synthesis requires high pressure and high temperature conditions. The first successful experiment to synthesise diamond was performed by Bundy et al. (1955). In these experiments, cubic diamond is the favoured form of diamond, but it is often accompanied by "lonsdaleite", which therefore has been described as an intermediate phase between graphite and diamond (Britun et al., 2004; Xie et al., 2017). Following this, experiments (Irifune et al., 2004; Wheeler and Lewis, 1975) have since then shown, that graphite which undergoes high temperatures and high pressures forms diamond including "lonsdaleite" (Irifune et al., 2004; Khaliullin et al., 2011; Wheeler and Lewis, 1975). However, there are also studies which report that the graphite-to-diamond transition occurs without any intermediate phase (Garvie et al., 2014). The transformation of graphite to diamond has recently been summarised and further investigated by Zhu et al. (2020b). In the literature, a three possible mechanism have been proposed which are shown in Figure 1.2 including puckering, buckling and lateral displacement (Britun and Kurdyumov, 2000; Dong et al., 2013; Gruber and Grüneis, 2018; Kurdyumov et al., 1996; Zhou et al., 2010). During the puckering mechanism, graphite (001) planes collapse under compression and form puckered graphite basal planes which subsequently transform from $sp^2$ to $sp^3$ forming cubic diamond (111) or "hexagonal diamond" (001) layers (Fahy et al., 1987, 1986; Tateyama et al., 1996). The buckling mechanism also involves the graphite (001) plane which in comparison the puckering mechanism transforms to the "hexagonal diamond" (100) boat architecture before it transitions to "hexagonal diamond" (Xie et al., 2017). Understanding this transition was and is of major interest in order to produce diamond in an efficient way. Recently, the graphite

11

to diamond transition using high temperatures and high pressures has been modelled by Zhu et al. (2020b) who described the transition in detail.
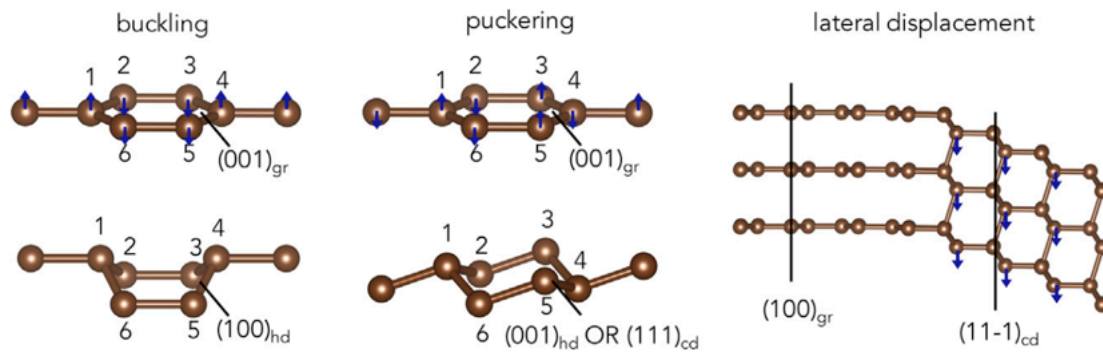


Figure 1.2: Schematic visualisation of the three different mechanisms which lead to the transition of graphite to diamond. Taken from Zhu et al. (2020b) with permission from Elsevier.

## 1.4 Ureilites

### 1.4.1 Overview

Ureilites are coarse-grained ultramafic rocks (Goodrich, 1992). Not only do ureilites represent the second largest group of achondrites after the HED group (2700 vs. 649 samples at the time of writing, see meteoritical bulletin ), they also represent the only sample group originating from the mantle of a differentiated body (Rai et al., 2020). Ureilites show several characteristics which distinguish them from other achondrites which will be summarised in this section.

Based on the petrographic characteristics, ureilites can be divided into main group (about 95%) and polymict (about 5%) ureilites (Goodrich et al., 2022).

Main group ureilites can further be subdivided into low-Ca pyroxene ureilites consisting of either olivine and pigeonite or olivine and orthopyroxene and into ureilites which contain augite (Goodrich et al., 2004). Main group ureilites are usually equilibrated rocks which can be seen in their textures including slightly rounded grain boundaries.

Further, grains usually meet in triple junctions. Within one sample, Fo contents are homogenous, however, among samples a continuous range can be observed between $Fo_{75}$ and $Fo_{95}$. These Fo contents are related to olivine cores as another typical feature of ureilites are so called *reduction rims* of olivine grains in which the Fo differs from the core composition (Goodrich et al., 2022). Sizes of these reduction rims range between 10–100 μm for olivine, for pigeonite these rims are smaller (Goodrich, 1992). Often, reduction rims contain abundant low-Ni iron metal inclusions (Goodrich, 1992). The occurring pyroxenes are related to these Fo contents: ureilites with $Fo_{75-85}$ contain almost solely pigeonite, ureilites with $Fo_{86-95}$ may contain orthopyroxene (Goodrich et al., 2022).

As the name suggests, augite-bearing main group ureilites contain augite (up to 40 vol.%) that occurs together with orthopyroxene and/or pigeonite and shows compositions of $Wo_{33-37}$ (Goodrich et al., 2022). Olivine compositions are often higher in Fo with $Fo_{86-88}$ (Goodrich et al., 2022).

Polymict ureilites contain main-group ureilitic material as well as small clasts which can be, based on oxygen and chromium isotopes, ureilitic-feldspathic or non-ureilitic xenoliths (Goodrich et al., 2022, and references therein). These ureilites are thought to be fragmental and regolith breccias (Goodrich et al., 2022).

Another distinctive feature of ureilites is the significant amount of carbon which can reach up to 7 wt.% in specific samples (Goodrich et al., 2015). Ureilitic carbon usually occurs interstitial along the grain boundaries of silicates in the form of graphite and diamond (Goodrich, 1992). Of these two polymorphs, graphite is the dominant phase. Graphite occurs mainly very fine-grained, but also mm-sized euhedral (based to their morphology) graphite crystals have been reported in unshocked/low-shocked ureilites (Berkley and Jones, 1982; Treiman and Berkley, 1992). Ureilites display a wide range of shock degrees ranging from very low/unshocked (U-S1) to very high (U-S6). A detailed classification scheme for shock degrees of meteorites can be found in Stöffler and Keil

(1991) and Stöffler et al. (2018), whereof Stöffler et al. (2018) contains classification schemes for different types of rocks including ultramafic rocks to which ureilites belong. Diamond only occurs in shocked ureilites, low shocked ureilites are generally devoid of diamond (Goodrich, 1992). In shocked ureilites, diamond can occur in nanometric and micrometric grainsizes, however, precise grainsize determinations for micrometric diamonds is rather difficult as it always occurs together with nanometric diamond and graphite in carbon aggregates (e.g., Barbaro et al., 2021, 2022; Christ et al., 2022; Nakamuta and Aoki, 2000; Nestola et al., 2020). The origin of these diamonds is still a debated topic among the scientific community and is summarised in section 1.4.3.

In contrast to other achondrites, i.e., samples from Mars or Moon, oxygen isotopes in ureilites do not plot on a mass-dependent fractionation line. Moreover, ureilitic oxygen isotopes plot along the carbonaceous chondrite anhydrous mineral (CCAM) line which lies between CAI, dark inclusions, and matrix from carbonaceous chondrites (Clayton and Mayeda, 1988). Further, ureilites show a correlation of the samples specific Mg-# and its $^{16}O$ enrichment (Clayton et al., 1991). The fact, that ureilites do not show a mass-dependent fractionation in terms of oxygen isotopes is rather surprising as this is usually expected for processed planetary material. Hence, ureilites display both features of processed (mineralogy, i.e., the absence of chondrules) and unprocessed material (e.g., O-isotopes).

The age of ureilites has long been investigated by a variety of authors. Ureilites have been assumed to be of very old ages based on very low $^{40}Ar/^{36}Ar$ and $^{129}Xe/^{132}Xe$ ratios (Goodrich, 1992). In the past, $^{87}Rb$-$^{86}Sr$ and $^{147}Sm$-$^{144}Nd$ data has been used to determine the age of ureilites. According to Goodrich et al. (1991), interpretation of Rb-Sr data is difficult and may either reflect a redistribution of Rb and Sr during shock or terrestrial contamination of Rb (Goodrich et al., 1991). However, Rb-Rr ages have been published and showed a model age of 4.55 Ga and a 4.01(6) Ga internal isochron for the META 78008 ureilite (Takahashi and Masuda, 1990). In terms of Sr-Nd data,

ureilites show three groups: (i) ureilites which show a whole-rock age which falls onto the 4.55 Ga chondritic isochron; (ii) ureilites which show a 4.23 Ga isochron; and (iii) ureilites which show a 3.74 Ga isochron (Goodrich, 1992). More recently, further dating systems have been applied to ureilites including $^{53}$Mn-$^{53}$Cr (Goodrich et al., 2021; Qin et al., 2010; van Kooten et al., 2017; Yamakawa et al., 2010; Zhu et al., 2020a), $^{26}$Al-$^{26}$Mg (Baker et al., 2012; Bischoff et al., 2014; Goodrich et al., 2021; Kita et al., 2003) and U-Pb (Amelin et al., 2015) which led to an average age of $4.564 \pm 0.002$ Ga for the UPB. Hence, ureilites originate from the very first stage of our Solar System.

### 1.4.2 The Ureilite Parent Body

The origin of ureilites is the so called ureilite parent body, a planetesimal from which all ureilites originate from (Goodrich et al., 2004, 2015; Scott et al., 1993). This planetesimal has already experienced differentiation processes as ureilites show processed features but was destroyed by one or more violent impact events before it could homogenise its isotopic contents and accrete into a terrestrial planet. These impact events led to the formation of smaller ureilite daughter bodies (UDB) from which some ureilites originate from (Rai et al., 2020).

A model which describes the evolution of the UPB has recently been published by Rai et al. (2020), which includes previous hypotheses (Bischoff et al., 2014; Goodrich et al., 2015; Herrin et al., 2010; Sanders et al., 2017; Warren, 2012). In this model, the UPB accreted in a region of the solar nebula with a high abundance of MgO- and FeO-rich chondrules which display low $\Delta^{17}$O and high $\Delta^{17}$O values, respectively. In the first stage, this material accreted which explains the different oxygen isotopic values for ureilites. The beginning of the accretion of the UPB was characterised by a higher availability of MgO-rich material which led to a compositional gradient and hence a compositionally zoned single UPB (Rai et al., 2020). The new formed planetesimal contained the radioactive isotope $^{26}$Al which upon decay heats planetesimals (e.g., Hevey

and Sanders, 2006; Sahijpal et al., 1995). However, in the case of ureilites, the amount of $^{26}$Al was not sufficient to completely melt the UPB (Budde et al., 2015) but the temperature increase still led to the formation of an Fe sulfide melt and subsequently to the formation of a core and by this to the removal of siderophile and chalcophile elements as well as heavy Fe isotope compositions (Rai et al., 2020, and references therein). Another consequence of the heating of the UPB was partial melting which led to silicate melts by fractional melting (Rai et al., 2020). However, the partial melting did not evolve into a complete melting of the UPB. $^{26}$Al was removed and led to a cooling of the planetesimal which then was stopped by a major impact (Herrin et al., 2010; Rai et al., 2020; Warren and Kallemeyn, 1989). Olivine and pyroxene were still hot and reacted with present carbon which lead to for ureilites characteristic reduction rims (Rai et al., 2020). Through reaccretion of ejected material from the UPB, UDBs were formed (Rai et al., 2020), e.g., the asteroid TC$_3$ from which Almahata Sitta originates (Herrin et al., 2010). Hence, ureilites in our collection nowadays may mostly originate from UDBs instead of the original UPB from which they found their way throughout the Solar System and finally ending upon Earth's surface.

The flight duration of a meteoroid from its parent body to Earth's surface can be measured and is given by its cosmic ray exposure (CRE) age. In particular, CRE ages describe the time a fragment has been exposed to cosmic rays and therefore its time of flight through the Solar System until it hit Earth's surface. For ureilites, CRE ages have been determined for a variety of different samples (Leya and Stephenson, 2019). In regard of ureilites, it is the time a specific ureilite fragment flew through the Solar System after it was extracted from the UPB/UDB during a shock event. Leya and Stephenson (2019) measured the isotopic concentrations of He, Ne and Ar for 10 ureilites and added literature data to create a set of ureilitic CRE ages. The authors report a range of CRE ages from $0\,\mathrm{Ma}$ to $\sim 40\,\mathrm{Ma}$ with a peak at $30\,\mathrm{Ma}$ as well as a decrease of ureilites with increasing CRE ages.

The size of the UPB is still an open question and possible reported diameters range from at least $150\,\text{km}$ (Rai et al., 2020) up to $6779\,\text{km}$ (Nabiei et al., 2018). However, it is certain that the UPB must have had a significant size to enable partial melting and the onset of a core formation as seen in ureilites (Barrat et al., 2015; Warren et al., 2006).

A few studies regarding the size of the UPB were based on ureilitic diamond and inclusions therein (e.g., Miyahara et al., 2015; Nabiei et al., 2018). Miyahara et al. (2015) found a unique large diamond in MS-170 and proposed a size of at least $1000\,\text{km}$ which would lead to interior pressures of more than $2\,\text{GPa}$, according to the authors a pressure sufficient for diamond nucleation and growth. Nabiei et al. (2018) analysed diamonds from the same ureilite and reported inclusions which would require pressure of more than $20\,\text{GPa}$, which would require a planetary body of at least the size of Mercury ($d \approx 4698\,\text{km}$). However, there is considerable doubt about these interpretations: Nestola et al. (2020) discussed that with the help of Fe as a catalyst, large diamonds can in fact be produced by the direct transformation of graphite to diamond during a shock event. Moreover, these authors delivered the first clear evidence for the existence of large diamonds by single crystal XRD (Nestola et al., 2020), whereas the interpretation of Miyahara et al. (2015) was based on the same crystallographic orientation of smaller adjacent diamond fragments. This shows that size estimations based on ureilitic diamonds are not straightforward.

### 1.4.3 Carbon in Ureilites

Diamonds in ureilites are known for more than one century (Kunz, 1888) and have been ever since a characteristic feature of ureilites. The origin of these diamonds, however, is still an open question. As a precursor for ureilitic carbon, carbonaceous chondrites were proposed, in particular CV-chondrite-like material (Rubin, 1988). Not only would a CV-chondrite-like precursor explain the heterogeneity of ureilitic isotopic composition, it would also be consistent with the evolution of the UPB which includes several im-

pact events which led to impact melting (Rubin, 1988). Having a possible source for carbonaceous material in ureilites, one question remains: how did ureilitic diamonds form?

Over decades, three hypothesis have been established: (i) the formation deep inside a planetary body, analogue to terrestrial diamonds (Urey, 1956), (ii) the direct formation from graphite during a shock event (Lipschutz, 1964), (iii) the formation by crystal vapor deposition (CVD) (Fukunaga et al., 1987).

The hypothesis of the formation inside a planetary body is simply based on the fact that diamond formation requires sufficiently high pressures which can be found inside planetary bodies of at least the size of the Moon (Urey, 1956). Although widely rejected, this hypothesis was again favoured by Miyahara et al. (2015) and Nabiei et al. (2018). Miyahara et al. (2015) found sub-euhedral diamond grains and diamond grain assemblages of up to 100 µm with similar crystallographic orientation which were interpreted to be a former large diamond grain. Based on the low shock degree (S3) of Almahata Sitta (Bischoff et al., 2010), the absence of other high-pressure minerals such as polymorphs of olivine and/or olivine (see Tschauner, 2019) and the absence of lamellar texture and topotactic relations as would be expected from static high-pressure experiments (Erskine and Nellis, 1991; Le Guillou et al., 2007; Sumiya et al., 2004), the authors rule the formation from graphite to diamond upon shock out (Miyahara et al., 2015). Moreover, they propose that based on sector zoning of nitrogen in the diamond from MS-170, the diamond could have formed under static conditions as sector zoning of nitrogen is known from terrestrial diamond (Bulanova, 1995; Kaminsky and Khachatryan, 2004). As this would involve a large planetary body with a diameter of 1000 km to account for pressures high enough (2 GPa to trigger diamond nucelation), the authors also suggest an alternative formation scenario as at the time of writing their publication the estimated radius of the UPB was at least 250 km (Goodrich et al., 2004).

The alternative formation scenario is the formation from a CVD process (Fukunaga

et al., 1987) and a subsequent accretion to the UPB (Miyahara et al., 2015). Following the discovery of this "large" ureilitic diamond in the Almahata Sitta fragment MS-170, Nabiei et al. (2018) analysed the same fragment by TEM and EELS. These authors found iron-sulfur inclusions in diamond which would require pressure above $20\,\text{GPa}$ and could therefore only be formed at the core-mantle boundary of a UPB with a size between Mercury ($r \approx 2439\,\text{km}$) and Mars ($r \approx 3389\,\text{km}$) (Nabiei et al., 2018). However, the "large" diamond from Miyahara et al. (2015) has recently been questioned by Nestola et al. (2020) and therefore also the large planetary body from Nabiei et al. (2018). The second hypothesis is based on noble gases trapped in diamond (Fukunaga et al., 1987; Göbel et al., 1978). These authors showed that there is a significant variation in noble gas concentrations between graphite and diamond: while graphite is noble gas free, diamond is the dominant noble gas carrying carbon phase (Fukunaga et al., 1987; Göbel et al., 1978). It was concluded that the origin of ureilitic diamond is the solar nebula where CVD processes took place rather than a shock event because noble gas carrying diamond could not have been formed from noble gas free graphite (Fukunaga et al., 1987; Le Guillou et al., 2010). However, this interpretation has been questioned by Nakamuta et al. (2016) because shock experiments have shown that noble gases can be trapped in shock-produced diamond while the graphite precursor remains almost noble gas free and moreover that noble gases from the pore spaces of the starting material will be incorporated into diamond (Matsuda et al., 1995). Another argument for the formation by CVD was delivered by Miyahara et al. (2015) (see preceding paragraph) and Nagashima et al. (2012), who analysed ureilitic carbon with Raman spectroscopy and reported a peak shift towards higher accompanied by large full width half maximus (FWHM) for the diamond band. The authors state that a large FWHM of the diamond band is not indicative for a CVD origin, however, the peak shift towards higher wavenumbers could be. They conclude, that all carbon material in ureilites originate from the primitive solar nebula (Nagashima et al., 2012).

The third hypothesis consists of the direct formation from graphite during a shock event in which high pressure and temperature regimes were reached and was first postulated by Lipschutz (1964). Three years earlier, the successful shock-induced synthesis of diamond from graphite during explosive experiments laid the foundation for this hypothesis. In addition to that, the conversion of graphite to diamond on a crystallographic level was already understood to be of non-complex nature (Lipschutz, 1964). Nakamuta and Aoki (2000) delivered a further indicator for this formation process with the report of compressed graphite in ureilites. The authors report, that the 002 reflection of graphite tails towards higher $2\theta$ values if it coexists with diamond in the same sample. The asymmetry of the peak arises due to smaller $d$-spacings compared to normal/uncompressed graphite (Nakamuta and Aoki, 2000). As shown by laboratory experiments, compressed graphite can be seen as an intermediate product of the direct graphite to diamond transformation when high pressure and temperature regimes are reached (Endo et al., 1994). Another mineralogical indicator for this formation scenario is stacking disordered diamond, often referred to as "lonsdaleite". First described from the iron meteorite Canyon Diablo, it has then become a widely accepted shock indicator (Frondel and Marvin, 1967; Hanneman et al., 1967; Israde-Alcántara et al., 2012; Kvasnytsya et al., 2013; Le Guillou et al., 2010).

Generally, the shock-induced direct transformation of graphite to diamond is the most accepted one as many publications show (e.g., Barbaro et al., 2021, 2022; Christ et al., 2022; Hezel et al., 2008; Lipschutz, 1964; Nakamuta and Aoki, 2000; Nakamuta and Toh, 2013; Nakamuta et al., 2016; Nestola et al., 2020) and since the evolution of the UPB is characterised by at least one major impact event. However, recent studies have questioned this process to be the only responsible formation scenario for ureilitic diamond, and especially for large diamonds (Miyahara et al., 2015; Nabiei et al., 2018).

The literature shows that the origin of diamond in ureilites is a strongly discussed topic. It is noteworthy that there are also studies who cannot ascribe any formation

scenario to diamonds found in ureilites (e.g., Ross et al., 2011).

**Carbon Isotopes of Ureilitic Graphite and Diamond**

Carbon from ureilites has also been investigated in regard of its isotopic composition. The method which has been applied in most studies is the (stepped) combustion method in which graphite and diamond were heated up until their specific combustion temperature (Barrat et al., 2017; Downes et al., 2015; Grady et al., 1985; Grady and Pillinger, 1986; Hudon et al., 2004; Russell et al., 1993; Smith et al., 2001). A problem with this method however is that both combustion temperatures overlap (diamond combusts at 600 °C–1000 °C, graphite at 600 °C–800 °C) which makes an ascription of $\delta^{13}$C values to either graphite or diamond difficult (Grady et al., 1985).

The first isotopic study of carbon in ureilites was done by Vdovykin (1970), who analysed carbon in the ureilites Novo Urei and Goalpara. Goalpara showed a total carbon isotopic composition of $\delta^{13}$C $= -8.4$‰ while the $\delta^{13}$C for Novo Urei was $-7.1$‰. Of the latter also intergrowths of diamond and graphite and a pure diamond fraction have been analysed yielding to $\delta^{13}$C values of $-6.3$‰ and $-5.7$‰ (Vdovykin, 1970).

Later, Grady et al. (1985) used the stepped combustion method on carbon from fourteen different ureilites. The samples were 200 µg chips which were crushed into a fine powder and then heated from room temperature to up to 1200 °C. During the experiment, ureilites showed a release of carbon with $\delta^{13}$C values between $-25$‰ to $-30$‰ at low temperatures (200 °C–500 °C), which is ascribed to terrestrial organic contamination (Grady et al., 1985). The authors found that $\delta^{13}$C values released between 500 °C–1000 °C are constant within a sample but vary between samples and form two groups: one group at $-8$‰ to $-11$‰ and a second one from $-1$‰ to $-3$‰ (Grady et al., 1985).

The method was used by Grady and Pillinger (1986) on carbon from the ALHA 82130 ureilite. Here, graphite was the dominant carbon carrier and showed a $\delta^{13}$C value of

$-9.8\,‰$ (Grady and Pillinger, 1986).

Russell et al. (1993) also applied the stepped combustion method on 5 different ureilites which were crushed and treated with acids to eliminate silicates and metal. Two samples have further been treated with oxidising acids to produce a "diamond rich residue". Mean $\delta^{13}C$ values for the five whole rock samples range between $-1.1\,‰$ to $4.8\,‰$, while the two diamond rich residues show mean $\delta^{13}C$ values of $-1.8\,‰$ and $-5.0\,‰$, respectively (Russell et al., 1993).

Stepped combustion on ureilitic carbon was again applied by Smith et al. (2001) who report $\delta^{13}C$ values of $-1.3\,‰$ and $-9.2\,‰$ for five different ureilites.

Hudon et al. (2004) also used the stepped combustion method and found a negative correlation between the Mg-# and $\delta^{13}C$ as well as a correlation between the carbon content and the $\delta^{13}C$ values: the lower the carbon content, the heavier the $\delta^{13}C$ values.

In 2015, five samples of the Almahata Sitta ureilite were analysed by Downes et al. (2015) again using stepped combustion method. The authors report a $\delta^{13}C$ values ranging from $-5.4\,‰$ to $0.1\,‰$. In contrast to Grady et al. (1985) and Hudon et al. (2004), Downes et al. (2015) reported no correlation to olivine core compositions as well as no correlation between $\delta^{13}C$ and the shock degree of a specific ureilite sample (Downes et al., 2015).

A different approach than the stepped combustion method was published by Miyahara et al. (2015) who analysed another sample from the Almahata Sitta ureilite. Here, "large" diamond grains were identified of which focused ion beam (FIB) cuts were produced and analysed in regard of their carbon isotopic composition. Diamond yield to $\delta^{13}C$ values of $-4.1\,‰$, whereas fine-grained graphite which was located between diamond grains showed $\delta^{13}C$ values of $-5.7\,‰$ (Miyahara et al., 2015). The same $\delta^{13}C$ value is also reported for another large diamond grain which is surrounded by graphite (Miyahara et al., 2015).

In 2017, Barrat et al. (2017) analysed 32 ureilites by using the combustion method.

$\delta^{13}$C values range between $-8.48\,\text{‰}$ to $0.11\,\text{‰}$, which is in good agreement with previous studies. The data of this study shows a correlation between the Fe/Mg ratios of olivine core compositions and the carbon isotopic content: a negative hyperbolae for $\delta^{13}$C against olivine core compositions. The authors discuss that ureilitic mantle records two different C-rich reservoirs, which were not perfectly mixed during the evolution of the UPB Barrat et al. (2017). Further, the authors derive a size for the UPB which must have been larger than $690\,\text{km}$, which would be in agreement with Warren (2012).

A comprehensive study of graphite in ureilites, enstatite chondrites and ordinary chondrites was published by Storz et al. (2021). The authors investigated 19 ureilites using in-situ methods to analyse graphite regarding its carbon isotopic composition and report $\delta^{13}$C values from $-9.22\,\text{‰}$ to $10.36\,\text{‰}$ and a relationship between the ureilites grain size and the carbon isotopic content: coarse-grained ureilites have lighter carbon isotopic composition (mean $\delta^{13}$C $= -5.29\,\text{‰}$) than fine-grained ureilites (mean $\delta^{13}$C $= 1.94\,\text{‰}$) (Storz et al., 2021). Furthermore, in coarse-grained ureilites the isotopic composition falls into a well defined range, while fine-grained ureilites show large heterogeneities (Storz et al., 2021). The authors suggest, that the difference between coarse-grained and fine-grained ureilites can be explained by fine-grained ureilites being the product of impact smelting of former coarse-grained ureilites (Horstmann et al., 2014; Warren and Rubin, 2010). This means, that during the impact a CO gas was produced which was then lost to space whereby preferably $^{12}$C was lost (Storz et al., 2021).

In summary, the most common used method to measure carbon isotopic compositions from graphite and diamond is the (stepped) combustion method (Barrat et al., 2017; Downes et al., 2015; Grady et al., 1985; Grady and Pillinger, 1986; Hudon et al., 2004; Russell et al., 1993; Smith et al., 2001) and only in two studies ureilitic diamond (Miyahara et al., 2015; Russell et al., 1993) were analysed without any graphite possibly influencing the measurement. Hence, there is a necessity for a preferably non-destructive method to analyse the carbon isotopic composition of ureilitic diamond.

The histogram in Figure 1.3 summarises all $\delta^{13}C$ values and highlights those of ureilitic diamond. From the histogram the two groups of $\delta^{13}C$ values at $\sim\!-2\,\permil$ and $\sim\!-8\,\permil$ are clearly visible with ureilitic diamonds plotting between these groups.


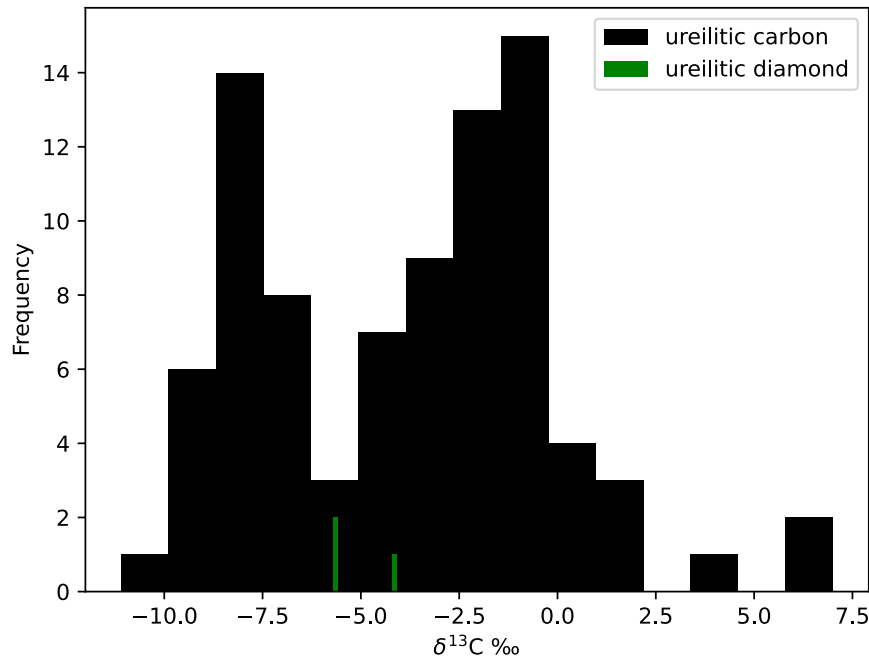
Figure 1.3: Histogram summarising all ureilitic $\delta^{13}C$ values (black and green) from literature (Barrat et al., 2017; Downes et al., 2015; Grady et al., 1985; Grady and Pillinger, 1986; Hudon et al., 2004; Miyahara et al., 2015; Russell et al., 1993; Smith et al., 2001; Storz et al., 2021). The histogram clearly shows the two groups of $\delta^{13}C$ at $\sim\!-8\,\permil$ and $\sim\!-2\,\permil$. Ureilitic carbon (black) includes data which was acquired using the combustion method which makes a differentiation between graphite and diamond difficult, hence the summary as ureilitic carbon. Bins were set to 15.

## 1.4.4 Geothermometry on Ureilites

Ureilites have also been investigated with geothermometric methods to constrain the thermic history of the UPB. Different methods based on different mineral assemblages have been used and will be summarised in this section.

Due to the very limited mineralogical components of ureilites, i.e., olivine and pigeonite, the application of common geothermometers as the two-pyroxene or olivine-

chromite thermometer is very limited (Collinet and Grove, 2020). However, on a few samples augite-orthopyroxene or pigeonite-orthopyroxene thermometers have been applied and yielded temperatures between 1200 °C–1270 °C (Chikami et al., 1997; Sinha et al., 1997; Takeda, 1989; Takeda et al., 1989; Weber et al., 2003). Temperatures from olivine-chromite thermometry yielded lower temperatures of 1040 °C–1060 °C (Goodrich et al., 2014). The applicability limitation of these thermometers to a limited set of samples led to the development of a geothermometer based on the partitioning of Cr between olivine and low-calcium pyroxene (LCP) with the aim to establish a geothermometer which is applicable to all ureilites [...] as long as they contain olivine and at least one LCP (Collinet and Grove, 2020). The so called $D_{Cr}^{oliv-LCP}$ was used on a variety of ureilites and yielded a temperature range of 1054 °C–1276 °C which is in perfect agreement to previous methods, but easier to apply (Collinet and Grove, 2020).

Another geothermometer is the graphite-based geothermometer by Cody et al. (2008). Originally developed for chondrites, it uses the FWHM of the graphite G-band and represents a temperature which was present on the chondritic parent body. Later, this geothermometer has also been applied to graphite in ureilites (Barbaro et al., 2020, 2021, 2022; Ross et al., 2011). The temperatures of this geothermometer span a wide range of 990 °C–1314 °C (Barbaro et al., 2020, 2021, 2022; Ross et al., 2011), however, this geothermometer has a relatively large error of ±120 °C (Cody et al., 2008). While the silicate based geothermometers refer to equilibrium temperatures, the meaning of the graphite-based geothermometer was only recently ascribed to the temperature which was reached during the shock event which destroyed the UPB (Barbaro et al., 2020). However, both techniques have not yet been applied to the same sample and it is not clearly understood if there is a correlation between the shock degree of a ureilite and the temperature recorded by graphite.

## 1.5 References

Y. Amelin, P. Koefoed, A. Bischoff, G. Budde, G. Brennecka, and T. Kleine. Pb isotopic age of ALM-A—A feldspar-rich volcanic rock from the crust of the ureilite parent body. In *78th Annual Meeting of the Meteoritical Society*, 2015

J. A. Baker, M. Schiller, and M. Bizzarro. $^{26}$Al–$^{26}$Mg deficit dating ultramafic meteorites and silicate planetesimal differentiation in the early Solar System? *Geochimica et Cosmochimica Acta*, 77:415–431, 2012.
doi.org/10.1016/j.gca.2011.10.030

A. Barbaro, M. C. Domeneghetti, C. A. Goodrich, M. Meneghetti, L. Litti, A. M. Fioretti, P. Jenniskens, M. H. Shaddad, and F. Nestola. Graphite-based geothermometry on almahata sitta ureilitic meteorites. *Minerals*, 10(11):1005, 2020.
doi.org/10.3390/min10111005

A. Barbaro, M. C. Domeneghetti, K. D. Litasov, L. Ferrière, L. Pittarello, O. Christ, S. Lorenzon, M. Alvaro, and F. Nestola. Origin of micrometer-sized impact diamonds in ureilites by catalytic growth involving Fe-Ni-silicide: The example of Kenna meteorite. *Geochimica et Cosmochimica Acta*, 309:286–298, 2021.
doi.org/10.1016/j.gca.2021.06.022

A. Barbaro, F. Nestola, L. Pittarello, L. Ferrière, M. Murri, K. D. Litasov, O. Christ, M. Alvaro, and M. C. Domeneghetti. Characterization of carbon phases in Yamato 74123 ureilite to constrain the meteorite shock history. *American Mineralogist: Journal of Earth and Planetary Materials*, 107(3):377–384, 2022.
doi.org/10.1016/j.gca.2021.06.022

J.-A. Barrat, O. Rouxel, K. Wang, F. Moynier, A. Yamaguchi, A. Bischoff, and J. Langlade. Early stages of core segregation recorded by Fe isotopes in an asteroidal mantle. *Earth and Planetary Science Letters*, 419:93–100, 2015.
doi.org/10.1016/j.epsl.2015.03.026

J.-A. Barrat, P. Sansjofre, A. Yamaguchi, R. C. Greenwood, and P. Gillet. Carbon isotopic variation in ureilites: Evidence for an early, volatile-rich Inner Solar System. *Earth and Planetary Science Letters*, 478:143–149, 2017.
doi.org/10.1016/j.epsl.2017.08.039

J. L. Berkley and J. H. Jones. Primary igneous carbon in ureilites: Petrological implications. *Journal of Geophysical Research: Solid Earth*, 87(S01):A353–A364, 1982.
doi.org/10.1029/JB087iS01p0A353

A. Bischoff, M. Horstmann, A. Pack, M. Laubenstein, and S. Haberer. Asteroid 2008 TC$_3$—Almahata Sitta: A spectacular breccia containing many different ureilitic and chondritic lithologies. *Meteoritics & Planetary Science*, 45(10-11):1638–1656, 2010.
doi.org/10.1111/j.1945-5100.2010.01108.x

A. Bischoff, M. Horstmann, J.-A. Barrat, M. Chaussidon, A. Pack, D. Herwartz, D. Ward, C. Vollmer, and S. Decker. Trachyandesitic volcanism in the early Solar System. *Proceedings of the National Academy of Sciences*, 111(35):12689–12692, 2014.
  doi.org/10.1073/pnas.1404799111

V. Britun and A. Kurdyumov. Mechanisms of martensitic transformations in boron nitride and conditions of their development. *International Journal of High Pressure Research*, 17(2):101–111, 2000.
  doi.org/10.1080/08957950008200933

V. F. Britun, A. V. Kurdyumov, and I. A. Petrusha. Diffusionless nucleation of lonsdaleite and diamond in hexagonal graphite under static compression. *Powder Metallurgy and Metal Ceramics*, 43(1):87–93, 2004.
  doi.org/10.1023/B:PMMC.0000028276.63784.8e

G. Budde, T. S. Kruijer, M. Fischer-Gödde, A. J. Irving, and T. Kleine. Planetesimal differentiation revealed by the Hf–W systematics of ureilites. *Earth and Planetary Science Letters*, 430:316–325, 2015.
  doi.org/10.1016/j.epsl.2015.08.034

G. Bulanova. The formation of diamond. *Journal of Geochemical Exploration*, 53(1-3): 1–23, 1995.
  doi.org/10.1016/0375-6742(94)00016-5

F. Bundy, H. T. Hall, H. Strong, et al. Man-made diamonds. *Nature*, 176(4471):51–55, 1955.
  doi.org/10.1038/176051a0

J. Chambers. A semi-analytic model for oligarchic growth. *Icarus*, 180(2):496–513, 2006.
  doi.org/10.1016/j.icarus.2005.10.017

J. Chikami, T. Mikouchi, H. Takeda, and M. Miyamoto. Mineralogy and cooling history of the calcium-aluminum-chromium enriched ureilite, Lewis Cliff 88774. *Meteoritics & Planetary Science*, 32(3):343–348, 1997.
  doi.org/10.1111/j.1945-5100.1997.tb01277.x

O. Christ, A. Barbaro, F. E. Brenker, P. Nimis, D. Novella, M. C. Domeneghetti, and F. Nestola. Shock degree and graphite geothermometry in ureilites NWA 6871 and NWA 3140. *Meteoritics & Planetary Science*, 57(10):1861–1878, 2022.
  doi.org/10.1111/maps.13907

D. Chung. Review graphite. *Journal of Materials science*, 37(8):1475–1489, 2002.
  doi.org/10.1023/A:1014915307738

R. N. Clayton and T. K. Mayeda. Formation of ureilites by nebular processes. *Geochimica et Cosmochimica Acta*, 52(5):1313–1318, 1988.
  doi.org/10.1016/0016-7037(88)90286-4

27

R. N. Clayton, T. K. Mayeda, J. Goswami, and E. J. Olsen. Oxygen isotope studies of ordinary chondrites. *Geochimica et Cosmochimica Acta*, 55(8):2317–2337, 1991.
doi.org/10.1016/0016-7037(91)90107-G

G. Cody, H. Yabuta, A. Kilcoyne, T. Araki, H. Ade, P. Dera, M. Fogel, B. Militzer, B. Mysen, et al. Organic thermometry for chondritic parent bodies. *Earth and Planetary Science Letters*, 272(1-2):446–455, 2008.
doi.org/10.1016/j.epsl.2008.05.008

M. Collinet and T. L. Grove. Incremental melting in the ureilite parent body: Initial composition, melting temperatures, and melt compositions. *Meteoritics & Planetary Science*, 55(4):832–856, 2020.
doi.org/10.1111/maps.13471

J. N. Cuzzi, R. C. Hogan, and K. Shariff. Toward planetesimals: Dense chondrule clumps in the protoplanetary nebula. *The Astrophysical Journal*, 687(2):1432, 2008.
doi.org/10.1086/591239

X. Dong, X.-F. Zhou, G.-R. Qian, Z. Zhao, Y. Tian, and H.-T. Wang. An ab initio study on the transition paths from graphite to diamond under pressure. *Journal of Physics: Condensed Matter*, 25(14):145402, 2013.
doi.org/10.1088/0953-8984/25/14/145402

H. Downes, F. Abernethy, C. Smith, A. Ross, A. Verchovsky, M. Grady, P. Jenniskens, and M. Shaddad. Isotopic composition of carbon and nitrogen in ureilitic fragments of the Almahata Sitta meteorite. *Meteoritics & Planetary Science*, 50(2):255–272, 2015.
doi.org/10.1111/maps.12413

S. Endo, N. Idani, R. Oshima, K. J. Takano, and M. Wakatsuki. X-ray diffraction and transmission-electron microscopy of natural polycrystalline graphite recovered from high pressure. *Physical Review B*, 49(1):22, 1994.
doi.org/10.1103/PhysRevB.49.22

D. J. Erskine and W. J. Nellis. Shock-induced martensitic transformation of highly oriented graphite to diamond. *Journal of Applied Physics*, 71(10):4882–4886, 1992.
doi.org/10.1063/1.350633

D. Erskine and W. Nellis. Shock-induced martensitic phase transformation of oriented graphite to diamond. *Nature*, 349(6307):317–319, 1991.
doi.org/10.1038/349317a0

S. Fahy, S. G. Louie, and M. L. Cohen. Theoretical total-energy study of the transformation of graphite into hexagonal diamond. *Physical Review B*, 35(14):7623, 1987.
doi.org/10.1103/PhysRevB.35.7623

S. Fahy, S. G. Louie, and M. L. Cohen. Pseudopotential total-energy study of the transition from rhombohedral graphite to diamond. *Physical Review B*, 34(2):1191,

1986.
- doi.org/10.1103/PhysRevB.34.1191

A. C. Ferrari and J. Robertson. Interpretation of Raman spectra of disordered and amorphous carbon. *Physical Review B*, 61(20):14095, 2000.
- doi.org/10.1103/PhysRevB.61.14095

A. E. Foote. ART. XLIV.–A New Locality for Meteoric Iron with a Preliminary Notice of the Discovery of Diamonds in the Iron. *American Journal of Science (1880-1910)*, 42(251):413, 1891

C. Frondel and U. B. Marvin. Lonsdaleite, a hexagonal polymorph of diamond. *Nature*, 214(5088):587–589, 1967.
- doi.org/10.1038/214587a0

K. Fukunaga, J.-i. Matsuda, K. Nagao, M. Miyamoto, and K. Ito. Noble-gas enrichment in vapour-growth diamonds and the origin of diamonds in ureilites. *Nature*, 328(6126): 141–143, 1987.
- doi.org/10.1038/328141a0

L. A. Garvie, P. Németh, and P. R. Buseck. Transformation of graphite to diamond via a topotactic mechanism. *American Mineralogist*, 99(2-3):531–538, 2014.
- doi.org/10.2138/am.2014.4658

A. Ghosh, S. Weidenschilling, H. McSween Jr, and A. Rubin. Asteroidal heating and thermal stratification of the asteroid belt. *Meteorites and the early solar system II*, pages 555–566, 2006

R. Göbel, U. Ott, and F. Begemann. On trapped noble gases in ureilites. *Journal of Geophysical Research: Solid Earth*, 83(B2):855–867, 1978.
- doi.org/10.1029/JB083iB02p00855

C. A. Goodrich, M. E. Sanborn, Q.-Z. Yin, I. Kohl, D. Frank, R. T. Daly, K. J. Walsh, M. E. Zolensky, E. R. Young, P. Jenniskens, et al. Chromium isotopic evidence for mixing of NC and CC reservoirs in polymict ureilites: implications for dynamical models of the early solar system. *The planetary science journal*, 2(1):13, 2021.
- doi.org/10.3847/PSJ/abd258

C. A. Goodrich, M. Collinet, A. Treiman, T. C. Prissel, M. Patzek, S. Ebert, M. J. Jercinovic, A. Bischoff, A. Pack, J.-A. Barrat, et al. The first main group ureilite with primary plagioclase: A missing link in the differentiation of the ureilite parent body. *Meteoritics & Planetary Science*, 57(8):1589–1616, 2022.
- doi.org/10.1111/maps.13889

C. A. Goodrich. Ureilites: A critical review. *Meteoritics*, 27(4):327–352, 1992.
- doi.org/10.1111/j.1945-5100.1992.tb00215.x

C. A. Goodrich, P. J. Patchett, G. W. Lugmair, and M. J. Drake. Sm-Nd and Rb-Sr isotopic systematics of ureilites. *Geochimica et Cosmochimica Acta*, 55(3):829–848, 1991.
  doi.org/10.1016/0016-7037(91)90345-6

C. A. Goodrich, E. R. Scott, and A. M. Fioretti. Ureilitic breccias: clues to the petrologic structure and impact disruption of the ureilite parent asteroid. *Geochemistry*, 64(4): 283–327, 2004.
  doi.org/10.1016/j.chemer.2004.08.001

C. A. Goodrich, G. E. Harlow, J. A. Van Orman, S. R. Sutton, M. J. Jercinovic, and T. Mikouchi. Petrology of chromite in ureilites: Deconvolution of primary oxidation states and secondary reduction processes. *Geochimica et Cosmochimica Acta*, 135: 126–169, 2014.
  doi.org/10.1016/j.gca.2014.02.028

C. A. Goodrich, W. K. Hartmann, D. P. O'Brien, S. J. Weidenschilling, L. Wilson, P. Michel, and M. Jutzi. Origin and history of ureilitic material in the solar system: The view from asteroid 2008 $TC_3$ and the Almahata Sitta meteorite. *Meteoritics & Planetary Science*, 50(4):782–809, 2015.
  doi.org/10.1111/maps.12401

M. Grady, I. Wright, P. Swart, and C. Pillinger. The carbon and nitrogen isotopic composition of ureilites: Implications for their genesis. *Geochimica et Cosmochimica Acta*, 49(4):903–915, 1985.
  doi.org/10.1016/0016-7037(85)90306-0

M. M. Grady and C. Pillinger. The ALHA 82130 ureilite: Its light element stable isotope composition and relationship to other ureilites. In *49th Annual Meeting of the Meteoritical Society*, volume 600, page 196, 1986

R. Greenberg, J. F. Wacker, W. K. Hartmann, and C. R. Chapman. Planetesimals to planets: Numerical simulation of collisional evolution. *Icarus*, 35(1):1–26, 1978.
  doi.org/10.1016/0019-1035(78)90057-X

T. Gruber and A. Grüneis. Ab initio calculations of carbon and boron nitride allotropes and their structural phase transitions using periodic coupled cluster theory. *Physical Review B*, 98(13):134108, 2018.
  doi.org/10.1103/PhysRevB.98.134108

R. Hanneman, H. Strong, and F. Bundy. Hexagonal diamonds in meteorites: Implications. *Science*, 155(3765):995–997, 1967.
  doi.org/10.1126/science.155.3765.995

J. S. Herrin, M. E. Zolensky, M. Ito, L. Le, D. W. Mittlefehldt, P. Jenniskens, A. J. Ross, and M. H. Shaddad. Thermal and fragmentation history of ureilitic asteroids: Insights from the Almahata Sitta fall. *Meteoritics & Planetary Science*, 45(10-11):

1789–1803, 2010.
   doi.org/10.1111/j.1945-5100.2010.01136.x

P. J. Hevey and I. S. Sanders. A model for planetesimal meltdown by [26]Al and its implications for meteorite parent bodies. *Meteoritics & Planetary Science*, 41(1):95–106, 2006.
   doi.org/10.1111/j.1945-5100.2006.tb00195.x

D. C. Hezel, L. Dubrovinsky, L. Nasdala, J. Cauzid, A. Simionovici, M. Gellissen, and T. SCHÖNBECK. In situ micro-Raman and X-ray diffraction study of diamonds and petrology of the new ureilite UAE 001 from the United Arab Emirates. *Meteoritics & Planetary Science*, 43(7):1127–1136, 2008.
   doi.org/10.1111/j.1945-5100.2008.tb01117.x

M. Horstmann, M. Humayun, M. Fischer-Gödde, A. Bischoff, and M. Weyrauch. Si-bearing metal and niningerite in Almahata Sitta fine-grained ureilites and insights into the diversity of metal on the ureilite parent body. *Meteoritics & Planetary Science*, 49(10):1948–1977, 2014.
   doi.org/10.1111/maps.12370

P. Hudon, C. Romanek, L. Paddock, and D. Mittlefehldt. Evolution of the ureilite parent body. In *35th Lunar and Planetary Science Conference*, page 2075, 2004

G. R. Huss and R. S. Lewis. Presolar diamond, SiC, and graphite in primitive chondrites: Abundances as a function of meteorite class and petrologic type. *Geochimica et Cosmochimica Acta*, 59(1):115–160, 1995.
   doi.org/10.1016/0016-7037(94)00376-W

T. Irifune, A. Kurio, S. Sakamoto, T. Inoue, H. Sumiya, and K.-i. Funakoshi. Formation of pure polycrystalline diamond by direct conversion of graphite at high pressure and high temperature. *Physics of the Earth and Planetary Interiors*, 143:593–600, 2004.
   doi.org/10.1016/j.pepi.2003.06.004

I. Israde-Alcántara, J. L. Bischoff, G. Domínguez-Vázquez, H.-C. Li, P. S. DeCarli, T. E. Bunch, J. H. Wittke, J. C. Weaver, R. B. Firestone, A. West, et al. Evidence from central Mexico supporting the Younger Dryas extraterrestrial impact hypothesis. *Proceedings of the National Academy of Sciences*, 109(13):E738–E747, 2012.
   doi.org/10.1073/pnas.1110614109

A. Johansen, J. S. Oishi, M.-M. M. Low, H. Klahr, T. Henning, and A. Youdin. Rapid planetesimal formation in turbulent circumstellar disks. *Nature*, 448(7157):1022–1025, 2007.
   doi.org/10.1038/nature06086

F. V. Kaminsky and G. K. Khachatryan. The relationship between the distribution of nitrogen impurity centres in diamond crystals and their internal structure and mechanism of growth. *Lithos*, 77(1-4):255–271, 2004.
   doi.org/10.1016/j.lithos.2004.04.035

R. Z. Khaliullin, H. Eshet, T. D. Kühne, J. Behler, and M. Parrinello. Nucleation mechanism for the direct graphite-to-diamond phase transition. *Nature Materials*, 10 (9):693–697, 2011.
doi.org/10.1038/nmat3078

N. Kita, Y. Ikeda, H. Shimoda, Y. Morishita, and S. Togashi. Timing of basaltic volcanism in ureilite parent body inferred from the 26al ages of plagioclase-bearing clasts in dag-319 polymict ureilite. In *34th Lunar and Planetary Science Conference*, page 1557, 2003

B. A. Kjarsgaard, M. de Wit, L. M. Heaman, D. G. Pearson, J. Stiefenhofer, N. Januszczak, and S. B. Shirey. A review of the geology of global diamond mines and deposits. *Reviews in Mineralogy and Geochemistry*, 88(1):1–117, 2022.
doi.org/10.2138/rmg.2022.88.01

D. S. Knight and W. B. White. Characterization of diamond films by Raman spectroscopy. *Journal of Materials Research*, 4(2):385–393, 1989.
doi.org/10.1557/JMR.1989.0385

E. Kokubo and S. Ida. Oligarchic growth of protoplanets. *Icarus*, 131(1):171–178, 1998.
doi.org/10.1006/icar.1997.5840

G. F. Kunz. Diamonds in meteorites. *Science*, 11(266):118–119, 1888.
doi.org/10.1126/science.ns-11.266.118.b

A. Kurdyumov, V. Britun, and I. Petrusha. Structural mechanisms of rhombohedral BN transformations into diamond-like phases. *Diamond and related materials*, 5(11): 1229–1235, 1996.
doi.org/10.1016/0925-9635(96)00515-8

V. Kvasnytsya, R. Wirth, L. Dobrzhinetskaya, J. Matzel, B. Jacobsen, I. Hutcheon, R. Tappero, and M. Kovalyukh. New evidence of meteoritic origin of the Tunguska cosmic body. *Planetary and Space Science*, 84:131–140, 2013.
doi.org/10.1016/j.pss.2013.05.003

C. Le Guillou, F. Brunet, T. Irifune, H. Ohfuji, and J.-N. Rouzaud. Nanodiamond nucleation below 2273 K at 15 GPa from carbons with different structural organizations. *Carbon*, 45(3):636–648, 2007.
doi.org/10.1016/j.carbon.2006.10.005

C. Le Guillou, J. Rouzaud, L. Remusat, A. Jambon, and M. Bourot-Denise. Structures, origin and evolution of various carbon phases in the ureilite Northwest Africa 4742 compared with laboratory-shocked graphite. *Geochimica et Cosmochimica Acta*, 74 (14):4167–4185, 2010.
doi.org/10.1016/j.gca.2010.03.038

I. Leya and P. C. Stephenson. Cosmic ray exposure ages for ureilites—New data and a literature study. *Meteoritics & Planetary Science*, 54(7):1512–1532, 2019.
  doi.org/10.1111/maps.13288

M. E. Lipschutz. Origin of diamonds in the ureilites. *Science*, 143(3613):1431–1434, 1964.
  doi.org/10.1126/science.143.3613.1431.b

M. E. Lipschutz and E. Anders. The record in the meteorites—IV: origin of diamonds in iron meteorites. *Geochimica et Cosmochimica Acta*, 24(1-2):83–105, 1961.
  doi.org/10.1016/0016-7037(61)90009-6

K. Lodders. Solar system abundances and condensation temperatures of the elements. *The Astrophysical Journal*, 591(2):1220, 2003.
  doi.org/10.1086/375492

F. Maeda, E. Ohtani, S. Kamada, T. Sakamaki, N. Hirao, and Y. Ohishi. Diamond formation in the deep lower mantle: a high-pressure reaction of $MgCO_3$ and $SiO_2$. *Scientific Reports*, 7(1):1–7, 2017.
  doi.org/10.1038/srep40602

J.-I. Matsuda, A. Kusumi, H. Yajima, and Y. Syono. Noble gas studies in diamonds synthesized by shock loading in the laboratory and their implications on the origin of diamonds in ureilites. *Geochimica et Cosmochimica Acta*, 59(23):4939–4949, 1995.
  doi.org/10.1016/0016-7037(95)00333-9

J.-i. Matsuda, M. Namba, T. Maruoka, T. Matsumoto, and G. Kurat. Primordial noble gases in a graphite-metal inclusion from the Canyon Diablo IAB iron meteorite and their implications. *Meteoritics & Planetary Science*, 40(3):431–443, 2005.
  doi.org/10.1111/j.1945-5100.2005.tb00392.x

M. Miyahara, E. Ohtani, A. El Goresy, Y. Lin, L. Feng, J.-C. Zhang, P. Gillet, T. Nagase, J. Muto, and M. Nishijima. Unique large diamonds in a ureilite from Almahata Sitta 2008 $TC_3$ asteroid. *Geochimica et Cosmochimica Acta*, 163:14–26, 2015.
  doi.org/10.1016/j.gca.2015.04.035

A. Morbidelli, J. I. Lunine, D. P. Obrien, S. N. Raymond, and K. J. Walsh. Building terrestrial planets. *Annual Reviews of Earth and Planetary Sciences*, 40(1):251–275, 2012.
  doi.org/10.48550/arXiv.1208.4694

M. Murri, R. L. Smith, K. McColl, M. Hart, M. Alvaro, A. P. Jones, P. Németh, C. G. Salzmann, F. Corà, M. C. Domeneghetti, et al. Quantifying hexagonal stacking in diamond. *Scientific Reports*, 9(1):1–8, 2019.
  doi.org/10.1038/s41598-019-46556-3

F. Nabiei, J. Badro, T. Dennenwaldt, E. Oveisi, M. Cantoni, C. Hébert, A. El Goresy, J.-A. Barrat, and P. Gillet. A large planetary body inferred from diamond inclusions in a ureilite meteorite. *Nature Communications*, 9(1):1–6, 2018.
  doi.org/10.1038/s41467-018-03808-6

K. Nagashima, M. Nara, and J.-i. Matsuda. Raman spectroscopic study of diamond and graphite in ureilites and the origin of diamonds. *Meteoritics & Planetary Science*, 47 (11):1728–1737, 2012.
  doi.org/10.1111/maps.12007

Y. Nakamuta and Y. Aoki. Mineralogical evidence for the origin of diamond in ureilites. *Meteoritics & Planetary Science*, 35(3):487–493, 2000.
  doi.org/10.1111/j.1945-5100.2000.tb01430.x

Y. Nakamuta and S. Toh. Transformation of graphite to lonsdaleite and diamond in the Goalpara ureilite directly observed by TEM. *American Mineralogist*, 98(4):574–581, 2013.
  doi.org/10.2138/am.2013.4341

Y. Nakamuta, F. Kitajima, and K. Shimada. In situ observation, X–ray diffraction and Raman analyses of carbon minerals in ureilites: Origin and formation mechanisms of diamond in ureilites. *Journal of Mineralogical and Petrological Sciences*, 111(4): 252–269, 2016.
  doi.org/10.2465/jmps.150906

P. Németh, L. A. Garvie, T. Aoki, N. Dubrovinskaia, L. Dubrovinsky, and P. R. Buseck. Lonsdaleite is faulted and twinned cubic diamond and does not exist as a discrete material. *Nature Communications*, 5(1):1–5, 2014.
  doi.org/10.1038/ncomms6447

F. Nestola, C. A. Goodrich, M. Morana, A. Barbaro, R. S. Jakubek, O. Christ, F. E. Brenker, M. C. Domeneghetti, M. C. Dalconi, M. Alvaro, et al. Impact shock origin of diamonds in ureilite meteorites. *Proceedings of the National Academy of Sciences*, 117(41):25310–25318, 2020.
  doi.org/10.1073/pnas.1919067117

H. Nininger. Diamonds in Canyon Diablo, Arizona, meteorites. *Contributions of the Society for Research on Meteorites*, 2(5):142–145, 1939.
  doi.org/10.1111/j.1945-5100.1939.tb00239.x

H. O. Pierson. *Handbook of carbon, graphite, diamonds and fullerenes: processing, properties and applications.* William Andrew, 2012

I. V. Popov, A. L. Görne, A. L. Tchougréeff, and R. Dronskowski. Relative stability of diamond and graphite as seen through bonds and hybridizations. *Physical Chemistry Chemical Physics*, 21(21):10961–10969, 2019.
  doi.org/10.1039/C8CP07592A

L. Qin, D. Rumble, C. M. O. Alexander, R. W. Carlson, P. Jenniskens, and M. H. Shaddad. The chromium isotopic composition of Almahata Sitta. *Meteoritics & Planetary Science*, 45(10-11):1771–1777, 2010.
  doi.org/10.1111/j.1945-5100.2010.01109.x

N. Rai, H. Downes, and C. Smith. Ureilite meteorites provide a new model of early planetesimal formation and destruction. *Geochemical Perspectives Letters*, 14:20–25, 2020.
  doi.org/10.7185/geochemlet.2018

S. Reich and C. Thomsen. Raman spectroscopy of graphite. *Philosophical Transactions of the Royal Society of London. Series A: Mathematical, Physical and Engineering Sciences*, 362(1824):2271–2288, 2004.
  doi.org/10.1098/rsta.2004.1454

G. R. Robinson Jr, J. M. Hammarstrom, and D. W. Olson. Graphite. Technical report, US Geological Survey, 2017

A. J. Ross, A. Steele, M. D. Fries, L. Kater, H. Downes, A. P. Jones, C. L. Smith, P. M. Jenniskens, M. E. Zolensky, and M. H. Shaddad. MicroRaman spectroscopy of diamond and graphite in Almahata Sitta and comparison with other ureilites. *Meteoritics & Planetary Science*, 46(3):364–378, 2011.
  doi.org/10.1111/j.1945-5100.2010.01157.x

A. E. Rubin. Formation of ureilites by impact-melting of carbonaceous chondritic material. *Meteoritics*, 23(4):333–337, 1988.
  doi.org/10.1111/j.1945-5100.1988.tb00918.x

S. Russell, J. Arden, I. Franchi, and C. Pillinger. A carbon and nitrogen isotope study of carbonaceous vein material in ureilite meteorites. In *24th Lunar and Planetary Science Conference*, 1993

H. Sabbah, A. L. Morrow, P. Jenniskens, M. H. Shaddad, and R. N. Zare. Polycyclic aromatic hydrocarbons in asteroid 2008 $TC_3$: Dispersion of organic compounds inside asteroids. *Meteoritics & Planetary Science*, 45(10-11):1710–1717, 2010.
  doi.org/10.1111/j.1945-5100.2010.01103.x

S. Sahijpal, M. Ivanova, L. Kashkarov, N. Korotkova, L. Migdisova, M. Nazarov, and J. Goswami. $^{26}$Al as a heat source for early melting of planetesimals: Results from isotopic studies of meteorites. *Proceedings of the Indian Academy of Sciences-Earth and Planetary Sciences*, 104(4):555–567, 1995.
  doi.org/10.1007/BF02839296

C. G. Salzmann, B. J. Murray, and J. J. Shephard. Extent of stacking disorder in diamond. *Diamond and Related Materials*, 59:69–72, 2015.
  doi.org/10.1016/j.diamond.2015.09.007

I. Sanders, E. Scott, and J. Delaney. Origin of mass-independent oxygen isotope varia-
tion among ureilites: Clues from chondrites and primitive achondrites. *Meteoritics &
Planetary Science*, 52(4):690–708, 2017.
  doi.org/10.1111/maps.12820

E. R. Scott, G. J. Taylor, and K. Keil. Origin of ureilite meteorites and implications for
planetary accretion. *Geophysical Research Letters*, 20(6):415–418, 1993.
  doi.org/10.1029/93GL00474

S. K. Sinha, R. O. Sack, and M. E. Lipschutz. Ureilite meteorites: Equilibration temper-
atures and smelting reactions. *Geochimica et Cosmochimica Acta*, 61(19):4235–4242,
1997.
  doi.org/10.1016/S0016-7037(97)00254-8

C. Smith, I. Franchi, I. Wright, M. Grady, and C. Pillinger. New data on carbon isotopic
compositions of some ureilites. In *32nd Lunar and Planetary Science Conference*, 2001

A. Steele, F. M. McCubbin, M. D. Fries, D. Golden, D. W. Ming, and L. G. Benning.
Graphite in the martian meteorite Allan Hills 84001. *American Mineralogist*, 97(7):
1256–1259, 2012.
  doi.org/10.2138/am.2012.4148

D. Stöffler and K. Keil. Shock metamorphism of ordinary chondrites. *Geochimica et
Cosmochimica Acta*, 55(12):3845–3867, 1991.
  doi.org/10.1016/0016-7037(91)90078-J

D. Stöffler, C. Hamann, and K. Metzler. Shock metamorphism of planetary silicate
rocks and sediments: Proposal for an updated classification system. *Meteoritics &
Planetary Science*, 53(1):5–49, 2018.
  doi.org/10.1111/maps.12912

J. Storz, T. Ludwig, A. Bischoff, W. H. Schwarz, and M. Trieloff. Graphite in ure-
ilites, enstatite chondrites, and unique clasts in ordinary chondrites–Insights from the
carbon-isotope composition. *Geochimica et Cosmochimica Acta*, 307:86–104, 2021.
  doi.org/10.1016/j.gca.2021.05.028

H. Sumiya, T. Irifune, A. Kurio, S. Sakamoto, and T. Inoue. Microstructure features of
polycrystalline diamond synthesized directly from graphite under static high pressure.
*Journal of Materials Science*, 39(2):445–450, 2004.
  doi.org/10.1023/B:JMSC.0000011496.15996.44

K. Takahashi and A. Masuda. The Rb-Sr and Sm-Nd dating and REE measurements
of ureilites. *Meteoritics*, 25:413, 1990

H. Takeda. Mineralogy of coexisting pyroxenes in magnesian ureilites and their formation
conditions. *Earth and Planetary Science Letters*, 93(2):181–194, 1989.
  doi.org/10.1016/0012-821X(89)90067-8

H. Takeda, H. Mori, and H. Ogata. Mineralogy of augite-bearing ureilites and the origin of their chemical trends. *Meteoritics*, 24(2):73–81, 1989.
  doi.org/10.1111/j.1945-5100.1989.tb00947.x

Y. Tateyama, T. Ogitsu, K. Kusakabe, and S. Tsuneyuki. Constant-pressure first-principles studies on the transition states of the graphite-diamond transformation. *Physical Review B*, 54(21):14994, 1996.
  doi.org/10.1103/PhysRevB.54.14994

A. Treiman and J. Berkley. A new ureilite: Preliminary data on nuevo mercurio (b). In *23rd Lunar and Planetary Science Conference*, 1992

O. Tschauner. High-pressure minerals. *American Mineralogist*, 104(12):1701–1731, 2019.
  doi.org/10.2138/am-2019-6594

H. C. Urey. Diamonds, Meteorites, and the Origin of the Solar System. *The Astrophysical Journal*, 124:623, 1956

E. M. van Kooten, M. Schiller, and M. Bizzarro. Magnesium and chromium isotope evidence for initial melting by radioactive decay of $^{26}$Al and late stage impact-melting of the ureilite parent body. *Geochimica et Cosmochimica Acta*, 208:1–23, 2017.
  doi.org/10.1016/j.gca.2017.03.033

G. Vdovykin. Ureilites. *Space Science Reviews*, 10(4):483–510, 1970

P. H. Warren. Parent body depth–pressure–temperature relationships and the style of the ureilite anatexis. *Meteoritics & Planetary Science*, 47(2):209–227, 2012.
  doi.org/10.1111/j.1945-5100.2011.01320.x

P. H. Warren and G. W. Kallemeyn. Geochemistry of polymict ureilite EET83309, and a partially-disruptive impact model for ureilite origin. *Meteoritics*, 24(4):233–246, 1989.
  doi.org/10.1111/j.1945-5100.1989.tb00698.x

P. H. Warren and A. E. Rubin. Pyroxene-selective impact smelting in ureilites. *Geochimica et Cosmochimica Acta*, 74(17):5109–5133, 2010.
  doi.org/10.1016/j.gca.2010.05.026

P. H. Warren, F. Ulff-Møller, H. Huber, and G. W. Kallemeyn. Siderophile geochemistry of ureilites: a record of early stages of planetesimal core formation. *Geochimica et Cosmochimica Acta*, 70(8):2104–2126, 2006.
  doi.org/10.1016/j.gca.2005.12.026

I. Weber, A. Bischoff, and D. Weber. TEM investigations on the monomict ureilites Jalanash and Hammadah al Hamra 064. *Meteoritics & Planetary Science*, 38(1):145–156, 2003.
  doi.org/10.1111/j.1945-5100.2003.tb01051.x

S. Weidenschilling. Dust to planetesimals: Settling and coagulation in the solar nebula. *Icarus*, 44(1):172–189, 1980.
  doi.org/10.1016/0019-1035(80)90064-0

M. K. Weisberg, T. J. McCoy, A. N. Krot, et al. Systematics and evaluation of meteorite classification. *Meteorites and the early solar system II*, 19:19–52, 2006

E. Wheeler and D. Lewis. The structure of a shock-quenched diamond. *Materials Research Bulletin*, 10(7):687–693, 1975.
  doi.org/10.1016/0025-5408(75)90052-5

Y.-P. Xie, X.-J. Zhang, and Z.-P. Liu. Graphite to diamond: origin for kinetics selectivity. *Journal of the American Chemical Society*, 139(7):2545–2548, 2017.
  doi.org/10.1021/jacs.6b11193

A. Yamakawa, K. Yamashita, A. Makishima, and E. Nakamura. Chromium isotope systematics of achondrites: Chronology and isotopic heterogeneity of the inner solar system bodies. *The Astrophysical Journal*, 720(1):150, 2010.
  dx. doi.org/10.1088/0004-637X/720/1/150

X.-F. Zhou, G.-R. Qian, X. Dong, L. Zhang, Y. Tian, H.-T. Wang, et al. Ab initio study of the formation of transparent carbon under pressure. *Physical Review B*, 82(13): 134126, 2010.
  doi.org/10.1103/PhysRevB.82.134126

K. Zhu, F. Moynier, M. Schiller, D. Wielandt, K. K. Larsen, E. M. van Kooten, J.-A. Barrat, and M. Bizzarro. Chromium isotopic constraints on the origin of the ureilite parent body. *The Astrophysical Journal*, 888(2):126, 2020a.
  doi.org/10.3847/1538-4357/ab5af7

S.-c. Zhu, X.-z. Yan, J. Liu, A. R. Oganov, and Q. Zhu. A revisited mechanism of the graphite-to-diamond transition at high temperature. *Matter*, 3(3):864–878, 2020b.
  doi.org/10.1016/j.matt.2020.05.013

# 2 Materials and Methods

## 2.1 Material

The samples analysed in this project are the two ureilites NWA 6871 and NWA 3140 which are shown in Figure 2.1. Both samples were investigated using a multi methodological approach including optical microscopy, scanning electron microscopy, X-ray diffraction, Raman spectroscopy, mass spectrometry, and micro-X-ray computed tomography.



Figure 2.1: The samples NWA 3140 (top two fragments) and NWA 6871 (lower fragment and thin section). Edge length of the grey cube = 1 cm.

NWA 6871 is a 199 g heavy fund from 2011 in Morocco. The meteorite is described as highly shocked, extremely hard and almost impossible to cut (Ruzicka et al., 2014), probable due to the presence of abundant diamonds, which makes it a perfect sample for this project. The sample was provided by Anthony Love, Appalachian State University and consists of two fragments, one is a $\sim 2\,\text{cm} \times 2\,\text{cm} \times 0.1\,\text{cm}$ thick section from which

carbon aggregates were extracted. The second fragment is smaller, $\sim 0.9\,\mathrm{cm} \times 0.8\,\mathrm{cm} \times 0.1\,\mathrm{cm}$, and was used to produce a thin section. NWA 3140 was also fund in Morocco in 2004 and weighs 750 g. Similar to NWA 6871, NWA 3140 is also described as hard to cut, again probably due to the presence of diamond (Ruzicka et al., 2014). An irregular fragment of NWA 3140 was provided from the collection of Prof. Frank E. Brenker, Goethe University Frankfurt am Main. The fragment was cut into two halves, one half was used to extract carbon aggregates, the other one to produce a thin section.

From both samples thin sections were produced using SiC paper to avoid contamination with diamond. Thin sections were analysed by optical microscopy to describe both ureilites petrologically and to determine the shock stage of both ureilites according to the shock classification scheme by Stöffler et al. (2018).

## 2.2 Methods

### 2.2.1 Electromagnetic Radiation

Since optical microscopy, Raman spectroscopy, X-ray diffraction, and X-ray computed tomography use electromagnetic radiation, a short introduction about electromagnetic radiation will precede the used methods. Electromagnetic radiation is characterised by both an electric and magnetic field which are perpendicular to each other (Larkin, 2017). The propagation of both fields can be described by a continuous sinusodial wave-like motion (Larkin, 2017). Parameters to describe these waves are the wavelength $\lambda$, the frequency $\nu$, and wavenumbers $\bar{\nu}$. These three parameters are related to each other by:

$$\bar{\nu} = \frac{\nu}{(c/n)} = \frac{1}{\lambda} \tag{2.1}$$

Here, $c =$ speed of light $(299\,792\,458\,\mathrm{m\,s^{-1}})$ and $n =$ refractive index. Another description of radiation stems from quantum theory where radiation is described as photons

which are emitted from a source. Photons are discrete units which own a frequency $\nu$ and a photon energy $E_\text{p}$:

$$E_\text{p} = h\nu \tag{2.2}$$

Here, $h = $ Planck's constant ($6.626\,070\,15 \times 10^{-34}\,\text{J\,s}$). Combining this quantum theoretical and the classical description of radiation is the basis of the wave-particle duality.

### 2.2.2 Optical Microscopy

Optical microscopy was done using a petrographic microscope which consists of a light source, a first polarisation filter, a rotatable sample stage, a second polarisation filter also called analysator. The light from the light source initially oscillates in all directions, upon passing the polarisation filter the light waves only oscillate in one direction, e.g., N-S, all other directions will be blocked. The now polarised light passes through the thin section on the sample stage and hits the users eyes. The sample can now be seen in the so called *brightfield mode.* The second polarisation filter is arranged in 90° in respective to the first filter and therefore only allows the passing of light oscillating in E-W direction. The initial N-S polarised light is now blocked and samples are viewed in the *darkfield mode.* The user can now observe the so called interference colours of the specific minerals which can be used for their identification.

### 2.2.3 Scanning Electron Microscopy

When the resolution of an optical microscope is not sufficient anymore, e.g., in the case of very small samples, electron microscopes can be used. By using electrons instead of optical light, higher resolutions and magnifications can be reached which enable to observe samples on the nanoscale.

A scanning electron microscope uses an electron gun to produce free electrons which will then be directed towards the sample by applying a negative potential. The electron

gun consists of a cathode (depending on the instrument e.g., a tungsten filament or an LaB$_6$ crystal) which is heated electrically so the electrons can overcome the potential barrier of the cathode material. On their way towards the sample the electrons are focused by electron lenses. The electrons fly towards the column and subsequently interact with the sample. Here, depending on the specific question about the sample different signals can be measured by different detectors. The signals include backscattered electrons, secondary electrons, continuous X-rays, characteristic X-rays, Auger electrons, and cathodoluminescence (Reed, 2005). In this work, only backscattered electrons (BSE), secondary electrons (SE) and characteristic X-rays were used and will therefore be described.

BSEs and SEs are used for imaging and are produced when electrons of the incident electron beam hit the sample (Reed, 2005). SEs are electrons which were originally part of the sample forming atoms whereof they were ejected from. In comparison to backscattered electrons, secondary electrons have a much lower energy in the range of a few eV versus 5–30 keV of BSEs. A consequence of these low energies is that secondary electrons originate only from the very first few nanometers of the sample, which is why SEs are usually used to obtain detailed (high resolution) topographic images of the sample. BSEs originate from deeper regions than secondary electrons, their energy is higher (close to $E_0$, the energy of the incident beam) and the fraction of scattered electrons depends on the atomic number $Z$: the higher $Z$, the higher the backscattering coefficient ($\eta$) (Reed, 2005). BSE images are commonly used to produce compositional contrast images of the sample, i.e., the produced image shows the distribution of average $Z$s throughout the sample: the heavier the atoms from the analysed area, the brighter the color on the material contrast image.

Characteristic X-rays are emitted from the sample atom when the initial electron beam removes an electron of the atom, i.e., the atom becomes ionised. The hereby produced electron vacancy is then filled by another electron of an outer laying shell falling down to

the vacant shell. The energy difference between the electron from the outer shell and the electron which was removed is then emitted in form of an X-ray photon (Reed, 2005). In this work, characteristic X-rays were detected in two ways: energy-dispersive X-ray spectroscopy (EDS) and wavelength-dispersive X-ray spectroscopy (WDS). For EDS, X-rays of all energies are detected by the detector. For WDS, X-rays of different wavelength are detected for which the detector has to be specifically set up. The advantage of the later is, that there are no overlaps between the wavelengths while overlaps may occur when using EDS because energies from different shells of different atoms may have the same energy. The overlap problems for EDS is definitively mitigated by modern EDS equipped with silicon drift which show a much stronger spectral resolution. The disadvantage of WDS is a lower intensity in regard to EDS and therefore a longer measurement (Reed, 2005).

SEM was conducted to localise and identify carbon aggregates but also to characterise the containing minerals qualitatively by energy EDS. For this step, an FEI Quanta 200 instrument was used in collaborated with the CEASC (Centro di Analisi e Servizi per la Certificazione, University of Padua). Measurement conditions were 20 keV at a working distance of 12.60 mm. This instrument is able to work in a low-vacuum mode which enables analyses of the samples without carbon coating them which subsequently enables the localisation of carbon phases. If the samples would have been carbon coated, EDS spectra would have shown a carbon signal even for carbon free silicates. In BSE image mode, carbon aggregates are easy to localise as they appear very dark due to the low atomic number of carbon. EDS spectra were taken to confirm the presence of carbon. Further, a Tescan Solaris instrument at the department of Geoscience, University of Padua, was used which operates with a field emission gun at 15 keV. A WDS detector was used for quantitative chemical analyses to characterise metal phases accompanying the carbon aggregates which were identified in the first step. Each measurement point was collected for 20 s. Subsequently, carbon aggregates were extracted manually from

the fragments using a needle and a sharp knife, glued on top of glass fibres (Figure 2.2), and characterised by XRD and MRS.
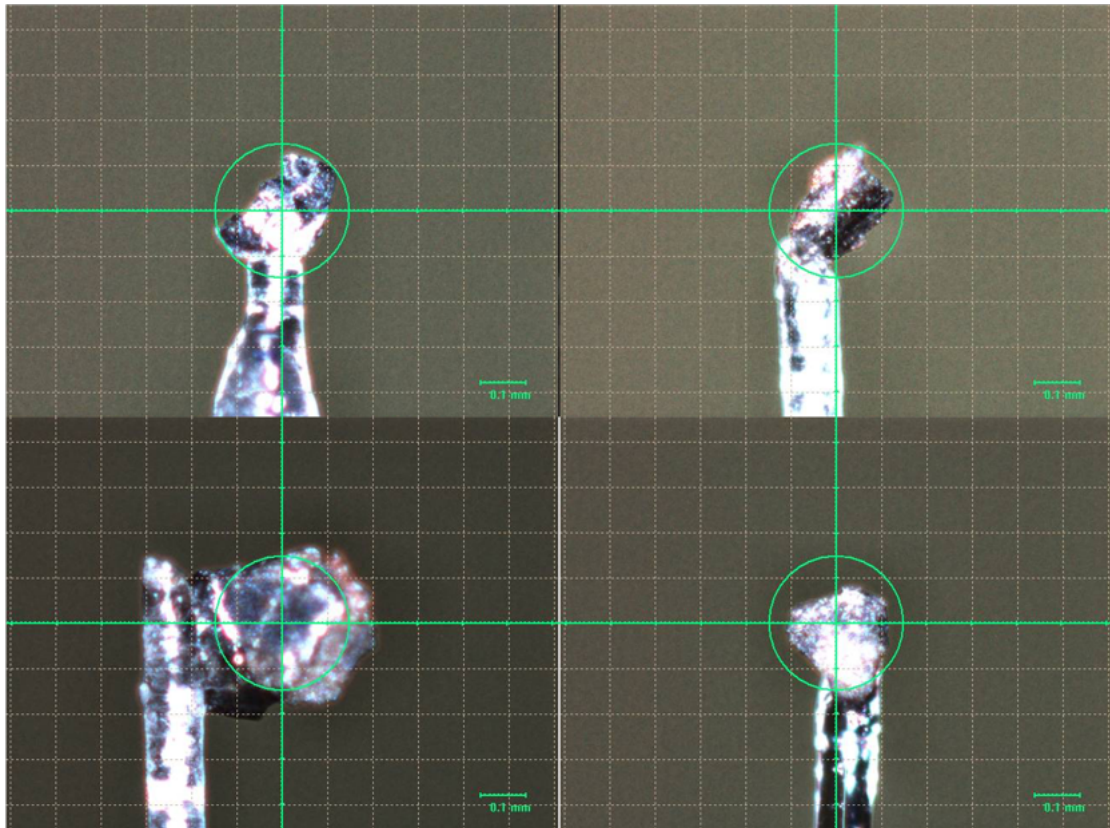


Figure 2.2: Four carbon bearing aggregates from NWA 6871 glued on top of glass fibres. Images were taken with the camera of the XRD instrument.

### 2.2.4 Field Emission Gun Electron Probe Microanalysis

Electron Probe Microanalysis works similar as an SEM but is mainly used for quantitativ chemical measurements. Imaging in both BSE and SE modes is possible. Quantitativ chemical WDS are achieved by comparing the measured concentration to a standard of known concentration which results in very low relative errors ($<1\%$) of the measured sample concentrations. Here, a field emission gun electron probe microanalysis was used to precisely measure the $Cr_2O_3$ contents of olivine and pyroxene, which was then used for a geothermometer published by Collinet and Grove (2020). The geothermometer can

be seen in equation (2.3) which shows that it is based on the Cr partitioning between olivine and low-Ca pyroxene in ureilites.

$$T(°\text{C}) = 913.9 + 465.6 * D_{Cr}^{oliv-LCP} \qquad (2.3)$$

Here, $D_{Cr}^{oliv-LCP}$ is the partition coefficient between olivine and low-Ca pyroxene. Both samples were carbon coated and analysed at the Department of Geosciences, Goethe-University, Frankfurt am Main, Germany where a JEOL JXA-8530F Plus Hyperprobe FEG-EPMA was used. For comparison, the same elements were collected as in Collinet and Grove (2020), i.e., Ca, Si, Mg, Fe, Al, Cr, Mn and K. The corresponding standards which were used for calibration (precision <1 rel.%) were: $CaSiO_3$, $Mg_2SiO_4$, $Fe_2O_3$, $Al_2O_3$, Astimex chromite, Astimex rhodonite, $KTiOPO_4$.

### 2.2.5 Single Crystal X-ray Diffraction

Single crystal X-ray diffraction uses X-rays to determine the crystal structure of a sample. X-rays are electromagnetic radiation with energies and wavelength between 100–10 eV and $10$–$10^{-3}$ nm, respectively (Waseda et al., 2011). To produce X-rays, an electron gun is used. A high voltage is applied between two electrodes which will produce an electron beam from the cathode towards an anode. In the anode material, the electrons are stopped which results in a loss of kinetic energy and subsequently the production of X-rays (Waseda et al., 2011). The produced X-rays then get directed towards the sample in form of an X-ray beam. The investigated samples in this work are minerals and therefore crystals. In crystals, atoms are arranged in a periodic pattern, the so called crystal structure. If the incident X-ray beam hits the atoms in the crystal structure it comes to diffraction if the Bragg Equation 2.4 is fulfilled:

$$n\lambda = 2d\sin\theta \qquad (2.4)$$

Here, $n$ = diffraction order, $\lambda$ = wavelength of the incident X-ray beam, $d$ = inter-planar spacing, and $\theta$ = Bragg angle (Waseda et al., 2011). The diffracted X-rays will then be detected by detector from which the diffraction image gets detected. By using the diffraction data, the crystal structure of the sample can be determined and minerals identified.

For XRD, the Rigaku Oxford Diffraction SuperNova single-crystal diffractometer of the Department of Geosciences, University of Padua was used. This instrument works with a MoK$\alpha$ X-ray microsource that produces an X-ray beam with a diameter of $0.120\,\mathrm{mm}$ with a wavelength of $0.710\,73\,\text{Å}$. The distance between the sample and the detector was set to $68\,\mathrm{mm}$. Carbon aggregates mounted on glass fibres were centred and a measurement program was set up in which the sample rotates for 360° in 1° steps around the $\phi$-axis. Each 1° step, a measurement was conducted for $100\,\mathrm{s}$. Diffractograms were processed and analysed using CrysAlisPro and Panalytical HighScore Plus in regard of peak positions, $d$-spacings and full width half maximums to identify minerals and to determine crystallite sizes ($L$) of nanomaterial using the Scherrer Equation 2.5 (Scherrer, 1912):

$$L = \frac{K * \lambda}{\beta * \cos\theta} \tag{2.5}$$

Here, $K$ = shape factor, $\lambda$ = wavelength, $\beta$ = full width half maximum of the peak, $\theta$ = Bragg angle.

### 2.2.6 Raman Spectroscopy

Raman spectroscopy is a vibrational spectroscopy technique (Larkin, 2017). Nowadays, Raman spectroscopy is widely used in geosciences (and other disciplines) because it is (mostly) nondestructive, delivers a fingerprint of the investigated sample and sample preparation is comparably simple (Dubessy et al., 2012; Larkin, 2017). When light interacts with matter, it may get scattered elastically and inelastically. These processes

are called *Raman scattering* and *Rayleigh scattering* and are characterised by a change of energy or the conservation of energy (Raman and Krishnan, 1928; Rayleigh, 1899). The loss or gain in energy occurs because of a variety of elementary excitations. In an ordered crystal structure, these excitations are phonons (lattice vibrations), in a molecule internal vibration modes (vibrons) (Dubessy et al., 2012).The sample gets irradiated by a laser beam with an initial frequency $\nu_0$ in the ultraviolet–visible region (Dubessy et al., 2012). During the scattering effect, two types of scattered light are produced, i.e., Rayleigh-scattering with $\nu = \nu_0$ and Raman-scattering with frequencies of $\nu_0 \pm \nu_{\mathrm{m}}$. Here, $\nu_{\mathrm{m}}$ corresponds to the vibrational frequency, which is the measured parameter in Raman spectroscopy. Depending on if $\nu_0 - \nu_{\mathrm{m}}$ or $\nu_0 + \nu_{\mathrm{m}}$, the lines are called *Stokes* or *Anti-Stokes* lines (Dubessy et al., 2012).

A sample at room temperature is usually in the lowest-energy vibrational level, the $m$ state. If the sample gets irradiated by the laser, the light gets scattered. Most of the light gets Rayleigh scattered, i.e., no energy change takes place. Only a small proportion of the light ($\sim 10^{-5}$–$10^{-8}$ of the incident beam) will get Raman-scattered. Raman-scattering will again lead to two different kind of scattering processes: Stokes and Anti-Stokes scattering. In the case of Stoke scattering, energy of the laser beam will be absorbed by the phonons and the irradiated part of the sample transfers to a virtual state ($n$) with higher energy depending on the frequency $\nu_0$ of the laser. Some phonones however exhibit Anti-Stokes scattering. This happens when the sample has already been in an excited state $n$ and falls back to the ground state $m$. As both Stokes and anti-Stokes scattering will give the same information and $m$ states are more frequent than $n$ states, it is common to measure only Stokes scattering (Dubessy et al., 2012). The intensity $I_{\mathrm{R}}$ of the Raman scattered light can be expressed by the following Equation 2.6:

$$I_{\mathrm{R}} \propto \nu^4 I_0 N \left( \frac{\partial a}{\partial Q} \right)^2 \tag{2.6}$$

Here, $I_0$ = laser intensity, $N$ = number of atoms which scatter the light, $\nu$ = laser

47

frequency, $\alpha$ = polarisability of the sample, and $Q$ = vibrational amplitude (Larkin, 2017). Equation (2.6) shows that the intensity depends on several parameters: the concentration, the wavelength (the larger the wavelength/frequency $\lambda/\nu$, the higher the intensity $I_R$, and the polarisability. This means, if a sample does not exhibit a change in polarisability, it will not be Raman active (Larkin, 2017). In the spectra of a Raman spectroscopy measurement vibrational bands can be seen. These bands can be described by the parameters frequency, intensity, and band shape (Larkin, 2017). By providing a fingerprint of a sample, Raman spectroscopy is a powerful analytical method to distinguish polymorphs, see Figure 2.3 where the "fingerprints" of both carbon polymorphs graphite and diamond are shown.
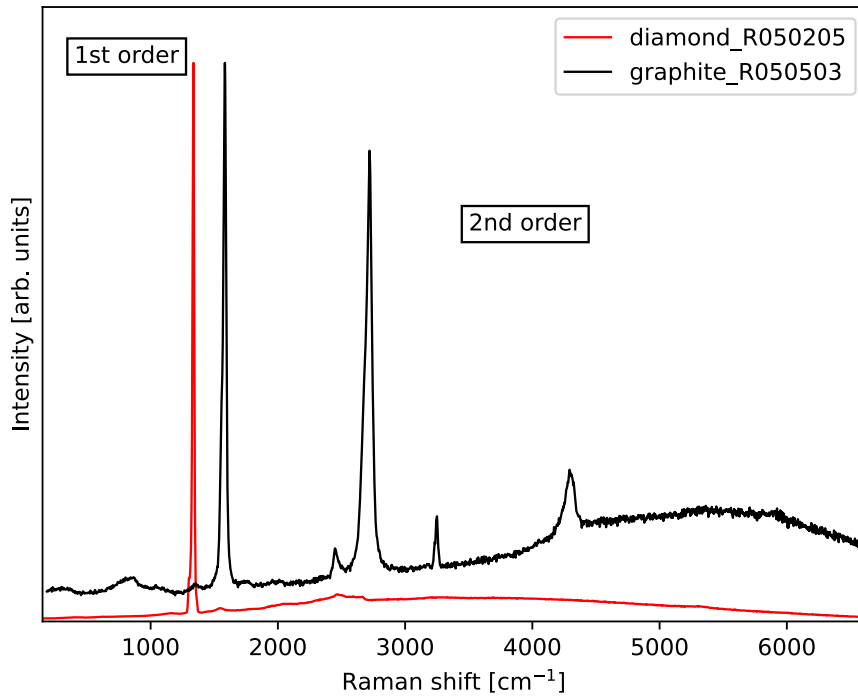


Figure 2.3: Comparison of the Raman spectra of graphite (black) and diamond (red) showing the graphites G-band at $\sim 1580 \, \mathrm{cm^{-1}}$ and the diamond band at $\sim 1332 \, \mathrm{cm^{-1}}$. Data was taken from the RRUFF database (Lafuente et al., 2015).

Carbon aggregates were analysed by micro Raman spectroscopy (MRS) both in situ

in the fragments and on top of the glass fibers. For MRS, the WITec alpha 300 R instrument of the Department of Geosciences, University of Padua was used which operates with a green laser at a wavelength of 532 nm. Depending on the investigated mineral, the laser power was set to 1 mW  3 mW for graphite and 10 mW for diamond and silicates. Calibration of the instrument was done using the 520 cm$^{-1}$ band of a Si-disk. The collected spectra were background corrected using Thermo-Scientific OMNIC$^{TM}$ for Dispersive Raman Software with which band positions and full width half maximums ($\Gamma_G$) were determined. The $\Gamma_G$ values of the graphite G-band were used to calculate the temperature recorded by graphite using a geothermometer, see Equation 2.7 which was published by Cody et al. (2008):

$$T_{max}(°C) = 1594.4 - 20.4 * \Gamma_G - 5.8 * 10^{-2} * \Gamma_G^2 \tag{2.7}$$

The authors also published an equation which uses the FWHM of the graphite D-band ($\Gamma_D$). However, for two reasons this equation was not used. First, previous studies which applied the geothermometer only used the ($\Gamma_G$) value (Barbaro et al., 2020, 2021, 2022; Ross et al., 2011). Hence, for a comparison of different ureilites the $\Gamma_G$ is more important. Second, although the D-band is more sensitive towards geothermometric calculations (see Cody et al. (2008)), the D-band can be heavily and moreover randomly affected by polishing procedures (Lasithiotakis et al., 2020) which makes it less reliable for polished meteorites.

### 2.2.7 Mass Spectrometry

Mass spectrometry is used to determine the ions of which a sample consists. Simplified, every mass spectrometer consists of three components: the ion source, a mass analyser, and the detector (Gross, 2017). In a mass spectrometer, atoms from the sample get unbound and ionised in order to be detected. This means, mass spectrometry is a destructive analytical method. However, the needed sample size is in the range of a

few microgamms or even lower, i.e., mass spectrometry is in fact almost non destructive (Gross, 2017). In order to detect the ions, and especially isotopes of the same atom, the ions will be separated on the base of their mass-to-charge ratio ($m/z$) in the mass analyser before they hit the detector. The ionisation of the sample can be achieved via different methods including thermal processes, electric fields or impacting energetic electrons, ions or photons (Gross, 2017). To avoid contamination, the whole process has to occur under high vacuum conditions, otherwise ions originating from air would be detected along the sample ions. When detecting ions, isotopes have to be considered. Isotopes are atoms with the same atomic number but a different number in neutrons, e.g., $^{12}_{6}$C, and $^{13}_{6}$C, and $^{14}_{6}$C. Due to their different isotopic masses they can easily be distinguished by a mass spectrometer. Isotopes are often measured as isotope ratios, e.g., $^{13}$C/$^{12}$C. Isotope ratios however can be very small. To express these small variations, the so called delta notation (Equation 2.8) has been established:

$$\delta^{13}\text{C}(\text{\textperthousand}) = \left( \frac{\left(\frac{^{13}\text{C}}{^{12}\text{C}}\right)_{sample}}{\left(\frac{^{13}\text{C}}{^{12}\text{C}}\right)_{standard}} - 1 \right) * 10^3 \tag{2.8}$$

Multiple carbon aggregates were extracted from both ureilites. In NWA 6871, three large ($>100\,\mu$m) carbon grains were found of which one represents the largest ureilitic diamond found so far ($450\,\mu$m). By collaborating with the Department of Chemistry, University of Padua, these three grains were cleaned from graphite to measure the carbon isotopic composition of diamond. The samples were put into a solution of $18\,$ml of HNO$_3$ 65% and H$_2$SO$_4$ 96% inside a $150\,$ml PTFE cup, placed in a Berghof stainless steel Acid-Digestion Bomb (filling ration of 12%). The sealed bomb was heated to $250\,°$C and kept at this temperature for $48\,$h. After recovering the samples at room temperature, they were cleaned several times with deionised water and separated by centrifugation. The samples were then again analysed by XRD and MRS to ensure that the cleaning process was successful. Due to their size, the grains were sent to Université de Lorraine, CNRS,

Centre de Recherches Pétrographiques et Géochimiques (CRPG) in Nancy, France, LG-SIMS analysis. Here, carbon isotopes were measured using a CAMECA 1280 High-resolution Large-Geometry Secondary-Ion Mass Spectrometer. The used standard was Vienna PeeDee Belemnite (VPDB), thus carbon isotopic data was reported using the $\delta^{13}C_{VPDB}$ notation.

## 2.2.8 Micro-X-ray Computed Tomography

X-ray computed tomography is a non-destructive method to obtain information about the internal structure of a sample and is used in a variety of fields (Withers et al., 2021). Generally, a computed tomography (CT) instrument consists of an X-ray source, a rotatable sample holder and a detector (Withers et al., 2021). The sample will be exposed to X-ray radiation while being rotated in order to obtain a variety of two-dimensional images, so called radiographs (Withers et al., 2021). By applying computer reconstruction algorithms, the radiographs will be stacked to create a digital three-dimensional reconstruction of the investigated sample. The underlying principle which leads to a visualisation of the inner structure is the penetration power of X-rays, which leads to a contrast image, i.e., attenuation contrast or phase contrast (Withers et al., 2021). Depending on the chosen contrast method, different interaction processes are being used: the X-ray wave passes through the sample where it experiences a change in intensity and a phase shift which are both related to the refractive index $n$:

$$n = 1 - \delta + i\beta \tag{2.9}$$

Here, $\beta$ = imaginary part controlling the absorption, used for the absorption contrast, $\delta$ the phase shift, used to obtain the phase contrast (Withers et al., 2021). To investigate the internal structure of the sample, specific softwares, e.g., FIJI (Schindelin et al., 2012) can be used. Depending on the question, the three-dimensional reconstruction of the sample can then be sliced, specific areas be made transparent or coloured (Withers et al.,

2021). CT scans can be performed on very small samples ranging down to nanoCT with voxel sizes of ∼10 nm. Voxels are, in contrast to two-dimensional pixels, three-dimensional cubic volumes creating the three-dimensional images (Withers et al., 2021). In the case of small ureilitic diamonds, the question was wether micro-CT was sufficient to obtain enough informations of the internal structure of these diamonds or if nano-CT would be the better choice. Therefore, micro-X-ray CT was performed at the Elettra Synchrotron in Trieste, Italy. One of the large diamond grains was used for a first test to see if the resolution of the in-house CT device would be sufficient to obtain good CT images. With the aim to look for small inclusions in these diamonds, the experiments were conducted, unfortunately, without success due to the very small grain size. However, one of the synchrotrons beam lines was free at that time. We used the beamline which was already set up for a different experiment with a different aim. Hence, the measurement conditions were not optimised for the small diamond sample. However, the measurement showed that microX-ray CT is suitable to obtain good images of the interior of a sample as shown in chapter 5.

## 2.3 References

A. Barbaro, M. C. Domeneghetti, C. A. Goodrich, M. Meneghetti, L. Litti, A. M. Fioretti, P. Jenniskens, M. H. Shaddad, and F. Nestola. Graphite-based geothermometry on almahata sitta ureilitic meteorites. *Minerals*, 10(11):1005, 2020.
doi.org/10.3390/min10111005

A. Barbaro, M. C. Domeneghetti, K. D. Litasov, L. Ferrière, L. Pittarello, O. Christ, S. Lorenzon, M. Alvaro, and F. Nestola. Origin of micrometer-sized impact diamonds in ureilites by catalytic growth involving Fe-Ni-silicide: The example of Kenna meteorite. *Geochimica et Cosmochimica Acta*, 309:286–298, 2021.
doi.org/10.1016/j.gca.2021.06.022

A. Barbaro, F. Nestola, L. Pittarello, L. Ferrière, M. Murri, K. D. Litasov, O. Christ, M. Alvaro, and M. C. Domeneghetti. Characterization of carbon phases in Yamato 74123 ureilite to constrain the meteorite shock history. *American Mineralogist: Journal of Earth and Planetary Materials*, 107(3):377–384, 2022.
doi.org/10.1016/j.gca.2021.06.022

G. Cody, H. Yabuta, A. Kilcoyne, T. Araki, H. Ade, P. Dera, M. Fogel, B. Militzer, B.

Mysen, et al. Organic thermometry for chondritic parent bodies. *Earth and Planetary Science Letters*, 272(1-2):446–455, 2008.
  doi.org/10.1016/j.epsl.2008.05.008

M. Collinet and T. L. Grove. Incremental melting in the ureilite parent body: Initial composition, melting temperatures, and melt compositions. *Meteoritics & Planetary Science*, 55(4):832–856, 2020.
  doi.org/10.1111/maps.13471

J. Dubessy, M.-C. Caumon, and F. Rull. *Raman spectroscopy applied to earth sciences and cultural heritage*, volume 12. The Mineralogical Society of Great Britain and Ireland, 2012

J. H. Gross. *Mass spectrometry: a textbook.* Springer Science & Business Media, 2017

B. Lafuente, R. T. Downs, H. Yang, and N. Stone. 1. the power of databases: The rruff project. In *Highlights in mineralogical crystallography*, pages 1–30. De Gruyter (O), 2015.
  doi.org/10.1515/9783110417104-003

P. Larkin. *Infrared and Raman spectroscopy: principles and spectral interpretation.* Elsevier, 2017

M. Lasithiotakis, J. T. Marrow, and B. J. Marsden. Evaluation of damage induced in graphite due to sample preparation by standard non-destructive techniques. *Materials Physics and Mechanics*, 44(3), 2020.
  doi.org/10.18720/MPM.4432020_1

C. V. Raman and K. S. Krishnan. A new type of secondary radiation. *Nature*, 121 (3048):501–502, 1928.
  doi.org/10.1038/121501c0

L. Rayleigh. XXXIV. On the transmission of light through an atmosphere containing small particles in suspension, and on the origin of the blue of the sky. *The London, Edinburgh, and Dublin Philosophical Magazine and Journal of Science*, 47(287):375–384, 1899.
  doi.org/10.1080/14786449908621276

S. J. B. Reed. *Electron microprobe analysis and scanning electron microscopy in geology.* Cambridge university press, 2005

A. J. Ross, A. Steele, M. D. Fries, L. Kater, H. Downes, A. P. Jones, C. L. Smith, P. M. Jenniskens, M. E. Zolensky, and M. H. Shaddad. MicroRaman spectroscopy of diamond and graphite in Almahata Sitta and comparison with other ureilites. *Meteoritics & Planetary Science*, 46(3):364–378, 2011.
  doi.org/10.1111/j.1945-5100.2010.01157.x

A. Ruzicka, J. N. Grossman, and L. Garvie. The Meteoritical Bulletin, No. 100, 2014 June, 2014

P. Scherrer. Bestimmung der inneren Struktur und der Größe von Kolloidteilchen mittels Röntgenstrahlen. In *Kolloidchemie Ein Lehrbuch*, pages 387–409. Springer, 1912.
 doi.org/10.1007/978-3-662-33915-2_7

J. Schindelin, I. Arganda-Carreras, E. Frise, V. Kaynig, M. Longair, T. Pietzsch, S. Preibisch, C. Rueden, S. Saalfeld, B. Schmid, et al. Fiji: an open-source platform for biological-image analysis. *Nature Methods*, 9(7):676–682, 2012.
 doi.org/10.1038/nmeth.2019

D. Stöffler, C. Hamann, and K. Metzler. Shock metamorphism of planetary silicate rocks and sediments: Proposal for an updated classification system. *Meteoritics & Planetary Science*, 53(1):5–49, 2018.
 doi.org/10.1111/maps.12912

Y. Waseda, E. Matsubara, and K. Shinoda. *X-ray diffraction crystallography: introduction, examples and solved problems.* Springer Science & Business Media, 2011

P. J. Withers, C. Bouman, S. Carmignato, V. Cnudde, D. Grimaldi, C. K. Hagen, E. Maire, M. Manley, A. Du Plessis, and S. R. Stock. X-ray computed tomography. *Nature Reviews Methods Primers*, 1(1):1–21, 2021.
 doi.org/10.1038/s43586-021-00015-4

# 3 Shock Degree and Graphite Geothermometry in Ureilites NWA 6871 and NWA 3140

This manuscript has been accepted in Meteoritics & Planetary Science. OC and FN designed the study. OC, AB, and FN developed the methods. OC, AB and FN collected the data. DN helped with analysis, PN helped with the interpretation of geothermometric data. All the authors discussed the data and agree on their interpretation. OC, AB, FB, MCD, and FN wrote the manuscript. All the co-authors contributed to the final polishing of the manuscript. The original pdf file can be found in the Appendix A or online 🔗.

Oliver CHRIST[1][*], Anna BARBARO[1], Frank E. BRENKER[2], Paolo NIMIS[1], Davide NOVELLA[1], M. Chiara DOMENEGHETTI[3], and Fabrizio NESTOLA[1,2]

[1]Department of Geosciences, University of Padova, Via Gradenigo 6, 35131 Padova, Italy

[2]Geoscience Institute, Goethe-University Frankfurt, Altenhöferallee 1, 60438 Frankfurt, Germany

[3]Department of Earth and Environmental Sciences, University of Pavia, Via A. Ferrata 1, I-27100 Pavia, Italy

[*]Corresponding author. E-mail: oliver.christ@phd.unipd.it

**Abstract** Carbon aggregates from two differently shocked ureilites were analyzed to gain insight into the shock transformation of graphite to diamond in ureilites, which happened when the ureilite parent body (UPB) was most likely destroyed by massive impact events. We present data for carbon aggregates from the highly shocked (U-S6) Northwest

Africa (NWA) 6871 and the medium shocked (U-S3) NWA 3140. Both samples contain abundant carbon aggregates which were analyzed by X-ray diffraction and micro-Raman spectroscopy revealing the presence of close associations of (compressed) nanographite, micro- and nanodiamond, as well as Fe-rich phases. Graphite and diamond in NWA 6871 show shock indicators that are absent in NWA 3140. Based on Raman geothermometry on graphite, we calculated mean temperatures of $1368 \pm 120\,°C$ and $1370 \pm 120\,°C$ for NWA 3140 and NWA 6871, respectively. For comparison, a geothermometer based on the partitioning of Cr between olivine and low-Ca pyroxene was applied on NWA 3140, which yielded a temperature of only $1215 \pm 16\,°C$. The graphite-based temperatures are the highest reported for graphite in ureilites so far and exceed calculated magmatic temperatures for ureilites from silicate- and chromite-based geothermometers. Graphite temperatures fall into the temperature field of catalytic diamond synthesis, which supports the hypothesis of direct transformation from graphite to diamond upon shock. Although the temperatures estimated seem to be independent of the shock degree, they can be ascribed to the shock event that destroyed the UPB.

## 3.1 Introduction

Ureilites are coarse-grained ultramafic meteorites (Goodrich, 1992). They are the second largest group of achondrites after the howardite–eucrite–diogenite meteorites and have unique properties compared to other achondrites. In particular, ureilites can contain significant amounts of carbon and show features of both planetary differentiation and undifferentiated material as well as very old ages of up to $\sim$4566.7 $\pm$ 1.5 Ma (Zhu et al., 2020). Therefore, ureilites originate from the early stages of our solar system, a period characterized by violent collisions among planetesimals, planetary embryos, and protoplanets (Morbidelli et al., 2012). Ureilites represent mantle material of a partially differentiated parent body (Mittlefehldt et al., 2018), the ureilite parent body (UPB).

The UPB was destroyed by one or more large collisions and/or impact events, which led to the formation of ureilite daughter bodies (UDB) and eventually to the distribution of ureilitic material throughout the solar system (Downes et al., 2008; Goodrich et al., 2004; Herrin et al., 2010; Rai et al., 2020). Consequences of these shock events are preserved in ureilitic silicates, that is, olivine and pyroxene, and are used to characterize different degrees of shock ranging from very low U-S1 to high U-S6, where the U stands for ultramafic (Stöffler et al., 2018). The original shock classification based on olivine and plagioclase in chondrites was adapted for ureilites by Nakamuta et al. (2016). Stöffler et al. (2018) updated the original shock classification from Stöffler and Keil (1991) to consider also shock effects in different groups of rocks, including ultramafic rocks, to which ureilites belong.

Ureilites mainly consist of olivine and pyroxene with minor accessory phases of carbon (up to 8 wt.%), metal, and sulfides. Carbon may occur as graphite and diamond, cohenite (Goodrich et al., 2020, 2015), or organic compounds (Sabbah et al., 2010). Unshocked ureilites usually contain solely graphite (Nakamuta and Aoki, 2000; Wacker, 1986), which was interpreted to represent the primary form of carbon in ureilites (Berkley and Jones, 1982; Treiman and Berkley, 1994). Shocked samples, however, contain close associations of graphite and diamond (e.g., Nestola et al. (2020) and references therein). They often show blade-shaped structures in their longest dimension (see fig. 1a in Nestola et al. (2020)), which resemble the shape of millimeter-sized graphite in low-shocked ureilites. Carbon associations in shocked ureilites are polycrystalline and consist of graphite, diamond, and stacking-disordered diamond (Murri et al., 2019; Németh et al., 2014, 2020a,b; Nestola et al., 2020; Salzmann et al., 2015). Despite being known for over a century (Kunz, 1888), the origin of these diamonds remains a strongly debated topic. There are three different major hypotheses: (i) formation under high pressure conditions inside a large planetary body (e.g., Desch et al., 2019; Miyahara et al., 2015; Nabiei et al., 2018; Urey, 1956), (ii) formation from graphite during shock (e.g., (Lipschutz, 1964; Nestola

et al., 2020)), and (iii) formation by chemical vapor deposition (Fukunaga et al., 1987; Matsuda et al., 1995). Of these, formation by shock is the most accepted hypothesis, but recent studies by (Miyahara et al., 2015) and (Nabiei et al., 2018) claim that large diamonds were formed under high pressures in a large planetary body with a size between Mercury ($r \approx 2439 \, \text{km}$) and Mars ($r \approx 3389 \, \text{km}$). In a comprehensive study of three different ureilites, Northwest Africa (NWA) 7983 and Almahata Sitta (AhS 209b and AhS 72), by scanning electron microscopy (SEM), micro X-ray diffraction (XRD), transmission electron microscopy (TEM), and micro-Raman spectroscopy (MRS), Nestola et al. (2020) provided the first clear evidence for the coexistence of large (up to $100 \, \text{µm}$) single-crystal diamonds, polycrystalline nanodiamonds, and nanographite in close associations in the carbon matrix of ureilites and concluded that these diamonds were formed by shock. Further proof for this kind of carbon associations and the formation of micro-sized diamonds during a shock event was given by Barbaro et al. (2021, 2022) for the Kenna and Yamato 74123 ureilites.

Following Gillet and Goresy (2013), the time scale of shock events depends on the type of impactor (e.g., its size, density, speed, and angle of impact) and ranges from a few hundred milliseconds to a few seconds. Despite the short duration, high pressure and temperature regimes can be reached during a shock event (Gillet and Goresy, 2013). These extreme conditions affect the impacted planetary body in terms of melting and ejection of material and can lead to the formation of high-pressure and high-temperature minerals, which includes the formation of diamond from graphite. The transition from graphite to diamond is well understood and occurs when the $sp^2$ carbon bonds of graphite are unbound to form $sp^3$ carbon bonds of diamond. However, the required energy for this direct transition is high, as shown by Irifune et al. (2003), who produced diamond directly from graphite at pressures ranging from 12 to $25 \, \text{GPa}$ and temperatures above $2000\,°\text{C}$. To lower the energy barrier, metals (usually Fe, Co, Ni but also Pt, Rh, Ru, Pa, Ir, Os, Mn, Cr, Cu, Ti, and Zr) are added as a catalyst (Bovenkerk et al., 1959;

Bundy et al., 1955). These metals have a eutectic or peritectic relationship with C and react easily with C, which leads to a breakup of the $sp^2$ carbon bonds of graphite and subsequentially to diamond nucleation (Dobrzhinetskaya, 2012). This catalyzed reaction starts at $P = 5\,\text{GPa}$ and $T = 1400\text{--}1600\,^\circ\text{C}$ with a reaction time ranging between 5 and 20 min (e.g., Bovenkerk et al., 1959; Bundy et al., 1955). A graphical summary of different forms of diamond syntheses from graphite was published by Dobrzhinetskaya (2012). Based on these experimental findings, it is reasonable to assume that Fe-Ni-C melts, formed when the UPB was destroyed, could have acted as a catalyst for the graphite to diamond transition (Nestola et al., 2020).

Geothermometry based on the composition of coexisting silicates has been applied to ureilites. However, since most ureilites contain only olivine and pigeonite, geothermometry on ureilites was limited to specific samples containing further phases like augite or chromite. The two-pyroxene thermometer yielded temperatures of 1070–1280 °C (Chikami et al., 1997; Sinha et al., 1997; Takeda, 1989; Takeda et al., 1989; Weber et al., 2003), the olivine–pigeonite–melt thermometer a range of 1240–1300 °C (Herrin et al., 2010; Singletary and Grove, 2003), and the olivine–chromite thermometer a range of 1040–1060 °C (Goodrich et al., 2014). Application of these geothermometers relies on the availability of the required minerals and is therefore limited. Recently, a new geothermometer was introduced by Collinet and Grove (2020), based on partitioning of Cr between olivine and low-Ca pyroxene and is applicable to all ureilites as long as they contain at least one low-Ca pyroxene. In addition to these geothermometers, a graphite-based geothermometer established for carbonaceous chondrites by Cody et al. (2008) was applied to ureilitic graphite by Ross et al. (2011) and Barbaro et al. (2020, 2021, 2022) which yielded temperatures of 990 ± 120 °C and 1242 ± 120 °C to 1314 ± 120 °C, respectively.

The main aim of this work is to further characterize the impact event that destroyed the UPB/UDB and to understand whether the presence of micrometer-sized diamond is

a unique feature of NWA 7983, Kenna, and Yamato 74123 or a general feature of every shocked ureilite. Therefore, the ureilites NWA 6871 and NWA 3140 were analyzed using the same multimethodological approach that was applied to NWA 7983, Kenna, and Yamato 74123, combining SEM, XRD, MRS including graphite-based geothermometry and field emission gun electron probe microanalyzer (FEG-EPMA). We will show that applying the graphite-based geothermometer and comparing it to the Cr-based geothermometer helps us to better understand the meaning of the former.

## 3.2 Samples and Preparation

Sample NWA 6871 was provided by Anthony Love, Appalachian State University, while NWA 3140 is from the collection of Frank Brenker, Goethe-University, Frankfurt am Main.

NWA 6871 is a find from 2011 in Morocco and was described as very hard to cut due to a very high abundance of diamond (Ruzicka et al., 2014). NWA 6871 is a unique ureilite because the complete recrystallization of silicates implies that it must have experienced a high shock level (Ruzicka et al., 2014). This is in agreement with Bunch et al. (2012), who reported a shock degree of S6 (Stöffler and Keil, 1991). We examined two fragments of NWA 6871. The first fragment is an $\tilde{2}$ cm $\times$ 2 cm $\times$ 0.1 cm thick section. Six carbon-bearing aggregates were extracted from this fragment: NWA6871_1, NWA6871_2, NWA6871_3, NWA6871_4, NWA6871_5, and NWA6871_6.

The second fragment of NWA 6871 is 0.9 cm $\times$ 0.8 cm $\times$ 0.1 cm. We used this smaller fragment to produce a thin section for petrographic description by optical microscopy and FEG-EPMA analyses. Probably due to the high abundance of (micro)diamonds, polishing was difficult. To avoid contamination with diamonds from the abrasive, the fragment was polished using SiC paper.

NWA 3140 was found in Morocco in 2004. We examined only a small irregularly shaped fragment, from which it was impossible to directly extract carbon aggregates.

Therefore, we cut the sample into two pieces, put one half into epoxy, and polished it to obtain a plane surface. The cutting process was done using a water-cooled diamond saw and was very difficult, presumably due to the presence of diamond. Polishing was done with SiC paper. The obtained surface covers an area of $\sim 20\,\text{mm}^2$ from which we extracted two carbon-bearing aggregates: NWA 3140_1 and NWA 3140_2. To prevent sampling diamonds from the diamond saw, we avoided material from the surface. Therefore, we scratched away the uppermost layer and extracted the underlying material. In comparison to NWA 6871, the extraction was more difficult, and the extracted aggregates were very small. Eventually, we produced a thin section of the half, which was already in epoxy, again using SiC paper to avoid contamination.

## 3.3 Methods

### 3.3.1 Scanning Electron Microscopy

SEM was done in two steps. The first analyses were conducted at the CEASC (Centro di Analisi e Servizi per la Certificazione, University of Padua), with an FEI Quanta 200 instrument operating at 20 keV with a working distance of 12.60 mm under low-vacuum conditions. These conditions allow us to analyze the sample without carbon coating, which otherwise would have prevented the identification of carbon aggregates by energy-dispersive X-ray spectroscopy (EDS). Backscattered electron (BSE) images were taken to characterize the overall appearance of carbon aggregates.

The second step of SEM was done at the Department of Geosciences, University of Padua, using a Tescan Solaris instrument operating at 15 keV with a working distance of 5 mm. For this step, the thin sections were carbon coated. EDS point measurements were conducted for 20 s to qualitatively analyze metal phases accompanying the previously identified carbon aggregates.

### 3.3.2 X-Ray Diffraction

XRD analyses were carried out at the Department of Geosciences, University of Padua, using a Rigaku Oxford Diffraction SuperNova single-crystal diffractometer equipped with a 200 K Dectris detector operating with a microsource MoK$\alpha$ X-ray radiation at a wavelength of 0.710 73 Å (X-ray beam diameter was 0.120 mm; the sample-to-detector distance was 68 mm). Samples were glued on top of glass fibers and measured in the range of 1–360° with a step size of 1° around the $\phi$-axis. Each measurement had an acquisition time of 100 s per frame. The data were processed using the CrysAlisPro 40_64.67a and Panalytical HighScore Plus Software packages. The crystallite sizes ($L$) on powder material were calculated using the Scherrer Equation 3.1 (Scherrer, 1912):

$$L = \frac{K \times \lambda}{\beta \times \cos\theta} \tag{3.1}$$

where $K$ is the shape factor, $\lambda$ is the wavelength, $\beta$ is the integral breadth of the peak, and $\theta$ is the Bragg angle.

### 3.3.3 Micro-Raman spectroscopy

MRS was performed using a WITec alpha300 R spectrometer (wavelength = 532 nm) at the Department of Geosciences, University of Padua. The instrument was calibrated with an Si-disk. Each measurement was accumulated four times with an integration time of 30 s and varying laser powers depending on the investigated grain. Graphite was measured with 1–3 mW, to avoid damaging graphite grains. The data was processed using the Thermo-Scientific OMNIC$^{\mathrm{TM}}$ for Dispersive Raman Software adopting Gaussian + Laurentzian curves to obtain the best fit.

In addition to phase identification, we used the graphite geothermometer (Equation 3.2), established by Cody et al. (2008) and modified by Ross et al. (2011):

$$T_{max}(°C) = 1594.4 - 20.4\Gamma_G - 5.8 \times 10^{-2}\Gamma_G^{-2} \tag{3.2}$$

The equation is used to calculate the temperature recorded by graphite. Here, $\Gamma_G$ is the full width half maximum (FWHM) of the graphite G-band. The original data from which Equation 3.2 originates can be seen in Cody et al. (2008), who report a relatively high error $2\sigma$ of $\pm 120\,°C$ for $T_{\max}$ due to the scatter in the original plot. However, data for 25 different chondrites show a relationship between the petrological type and $T_{\max}$: the higher the petrological type, the higher the $T_{\max}$. Hence, Raman-based geothermometry can be used to classify samples in terms of whether they have experienced low, medium, or high temperatures (Cody et al., 2008).

### 3.3.4 Field Emission Gun Electron Probe Microanalysis

FEG-EPMA analyses were performed at the Department of Geosciences, Goethe-University Frankfurt am Main, Germany using a JEOL JXA-8530F Plus Hyperprobe instrument. Measurement conditions were set to an acceleration voltage of $15\,kV$ and a probe current of $20\,nA$. Wavelength-dispersive X-ray spectroscopy (WDS) point analyses of silicates were measured in spot mode ($<100\,nm$) and collected using a counting time of 20 or $30\,s$ on the peak and half that time on the upper and lower background, respectively. Both thin sections were carbon coated. For calibration, the following standards were used: Ca, Si (CaSiO ), $Mg_3$ ($Mg_2SiO_4$), Fe ($Fe_2O_3$), Al ($Al_2O_3$), Cr (Astimex chromite), Mn (Astimex rhodonite), K ($KTiOPO_4$). Elements were calibrated to a $<1$ rel.% precision. EPMA data were used to apply the Cr-based geothermometer of Collinet and Grove (2020), which gives the temperature of equilibration for a specific ureilite according to the equation:

$$T(°C) = 913.9 + 465.6 \times D_{Cr}^{oliv\text{-}LCP} \tag{3.3}$$

where $D_{Cr}^{oliv\text{-}LCP} = Cr_2O_3^{oliv}/Cr_2O_3^{LCP}$ is the partition coefficient of Cr between olivine (oliv) and low-calcium pyroxene (LCP: orthopyroxene or pigeonite).

## 3.4 Results

### 3.4.1 Optical Microscopy

Optical microscopy observations show that NWA 6871 consists of olivine aggregates with subhedral forms of former large olivine crystals and sizes in a range between $\sim$0.3 and $\sim$2 mm in their longest dimensions (bright grains in Fig. 1a). These olivine aggregates are fractured and contain small olivine grains with an average grain size of $\sim$20 μm, which meet in triple junction points (Fig. 1b and 1c). The space between the aggregates is filled with opaque material that contains carbon aggregates, metallic phases, and sulfides. In some areas, veins crosscutting multiple aggregates can be observed. Based on the textural observations, NWA 6871 can be classified as highly shocked with a shock degree of U-S6, which corresponds to a pressure of $\sim$60 to 70 GPa (Stöffler et al., 2018). It was not possible to identify pyroxene grains by optical microscopy. However, both MRS and WDS revealed the presence of $\sim$20 μm sized pyroxene grains.

In contrast to NWA 6871, NWA 3140 contains olivine and pyroxene grains up to 1 mm in their longest dimension (Fig. 2a). From the absence of recrystallization features, it is evident that NWA 3140 experienced a lower shock degree than NWA 6871. All olivine and pyroxene grains are fractured (Fig. 2b and 2c). As reported in Fig. 2b, olivine grains show planar fractures, typical for low–medium shock deformation (Stöffler et al., 2018). No mosaicism can be observed, but some olivine grains exhibit a sawtooth texture on their edges. In addition, pyroxene displays twinning (see black arrows). Olivine and pyroxene grains are set into an opaque matrix that consists of carbon aggregates and very fine material (including metal phases and sulfides). Based on the described features, NWA 3140 can be classified as medium shocked with a shock degree of U-S3, which

corresponds to peak pressures of ∼15 to 20 GPa (Stöffler et al., 2018).
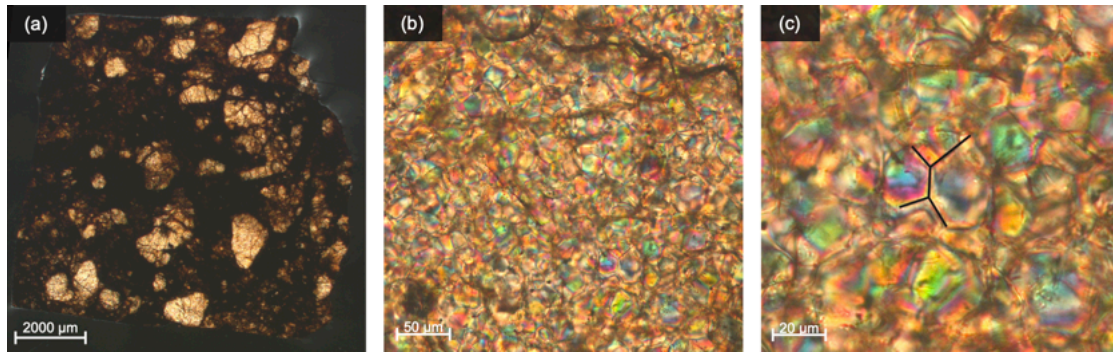


Figure 3.1: NWA 6871 in cross polarized light. a) Overview of the sample. b) Close-up of a large bright grain from (a). c) Triple junction points between olivine grains indicated by black lines.

### 3.4.2 Scanning Electron Microscopy

Figures 3 and 4 show BSE images of NWA 6871 and NWA 3140, in which silicate phases (light gray), carbon phases (dark gray), and metal-bearing phases (white) can be seen. BSE images of the uncoated NWA 6871 thick section show several dark gray-black areas indicative of carbon. These areas appear irregular or elongated (Fig. 3) and sometimes show blade-shaped structures (Fig. 3c) like those observed in NWA 7983 by Nestola et al. (2020). In NWA 6871, an internally layered aggregate up to 250 µm in length and 80 µm in width is present (Fig. 3c). EDS spectra collected on the brighter areas of the carbon aggregates revealed the presence of Fe, Ni, Si, and S, attributed to Fe,Ni-metal and Fe-sulfides, but also iron-oxides were identified. Additional elements are Mg, Si, and O from the adjacent silicate matrix material. Carbon aggregates are also present in the polished surface of NWA 3140 (Fig. 4a). However, the areas do not show any kind of blade-shaped structures and appear amoeboid (Fig. 4b and 4c).

EDS measurements (Fig. 5) directly on metal phases accompanying carbon aggregates in NWA 3140 revealed the presence of Fe, Ni, and Si. These elements could be ascribed to kamacite, Si-bearing kamacite, and pure taenite. Many grains also showed

the presence of oxygen, probably due to terrestrial weathering. In NWA 6871, kamacite, Si-bearing kamacite, troilite, and oxidized metal grains can be found in and around carbon aggregates. Minor elements which occur with Fe and Ni are Cr and P.

### 3.4.3 X-Ray Diffraction

*NWA 6871:* As reported in Fig. 6, the XRD analysis revealed the presence of diamond (*d*-spacing of 2.06, 1.26, and 1.07 Å), graphite (*d*-spacing of 3.35 Å), and Fe-metal and Ni-rich Fe-metal (*d*-spacing of 1.78, 1.43, and 1.17 Å). Additional phases are troilite (*d*-spacing of 1.74 Å), goethite (*d*-spacing of 4.17 Å), magnetite (*d*-spacing of 2.53 Å), and olivine with multiple diffraction spots (e.g., *d*-spacing of 2.46 Å in Fig. 6d). For carbon phases, the reconstructed diffraction images (Fig. 6) show rings for both graphite and diamond, indicating polycrystalline material. Figure 6e also shows single crystal diffraction spots of diamond at *d*-spacing of 1.26 Å. The diffractograms (Fig. 6b and 6f) further reveal a shoulder on the highest peak of diamond at *d*-spacing of 2.06 Å towards higher *d*-spacings (about 2.15–2.18 Å), ascribed to ascribed to stacking disordered diamond and is a shock indicator (Murri et al., 2019; Németh et al., 2014, 2020a,b).

After a careful line profile analysis for the powdery graphite and diamond, the crystallite sizes were estimated with Equation 3.1, which yielded sizes of 5–7 nm and 5–9 nm for diamond and graphite, respectively (Table 3.1). For this calculation, we only used the *d*-spacing at 1.26 and 1.07 Å for diamond and 3.34 Å for graphite (Fig. 6). Graphite, in some spectra, shows 002-diffraction peaks at *d*-spacings of 3.34 Å with a strong asymmetry and the peak center appear to be shifted toward higher 2θ and therefore lower *d*-spacings (e.g., Fig. 6f), indicative of compressed graphite, which is a further shock indicator (Nakamuta and Aoki, 2000).

66
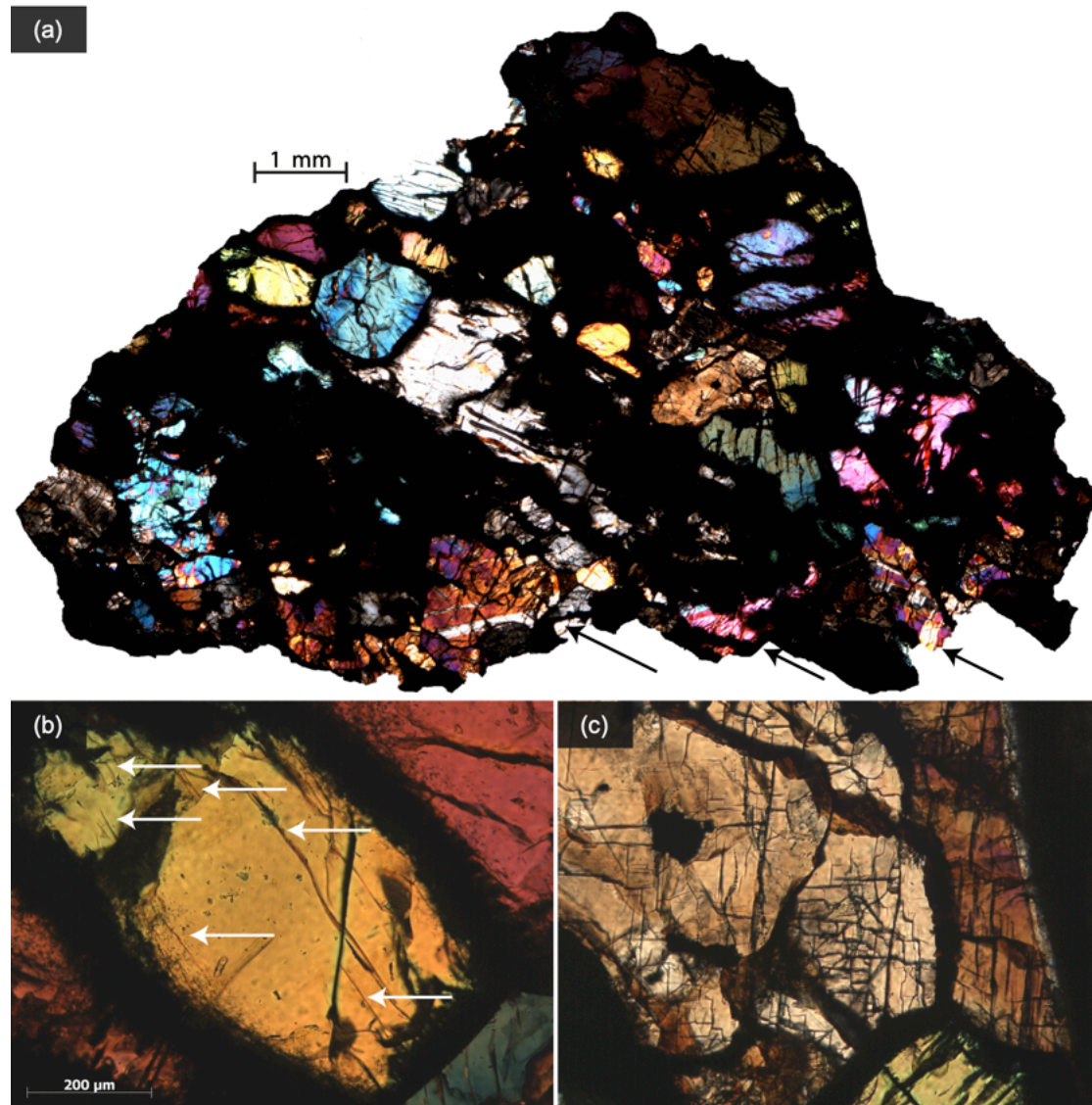
Figure 3.2: a) Thin section of NWA 3140 under cross polarized light. b) Close-up of a fractured olivine grain showing planar fractures in the NWSE direction, white arrows. c) Close-up of a fractured pyroxene grain showing ~90° cleavage structure on the basal section. Mineral identification based on the interference colors was difficult on this sample because of difficulties in the polishing process due to the presence of diamond which led to differences in thickness.

*NWA 3140:* As reported in Fig. 7, XRD on carbon aggregates from NWA 3140 shows diamond (*d*-spacing of 2.06, 1.26, and 1.07 Å), graphite (*d*-spacing of 3.35 Å), Fe-metal and Fe,Ni-metal (*d*-spacing of 1.78, 1.43, and 1.17 Å). In Fig. 7d, peaks for

olivine can be seen that most likely originate from the matrix material ($d$-spacing of 2.98, 2.76, 2.51, 2.26, 1.74, 1.60, 1.47, and 1.34 Å. In contrast to NWA 6871, no graphite peak asymmetries or diamond peak shoulders can be seen. The diffraction images and powder diffraction patterns of NWA 3140 are shown in Fig. 7a–d. Carbon-bearing aggregates from NWA 3140 show diffraction rings for graphite and diamond from which the crystallite sizes were calculated using Equation 3.1. Graphite is about 7–9 nm in size, while diamond crystallites measure 4–10 nm (Table 3.1). However, NWA 3140 also shows diffraction spots for diamond at $d$-spacing of 2.06 Å, which indicate single-crystal material closely associated with the polycrystalline one in the same aggregate. Hence, XRD results on NWA 6871 and NWA 3140 showed the coexistence of nanodiamond, microdiamond, and nanographite. In addition, in NWA 6871, compressed graphite and stacking disordered diamond can be observed.
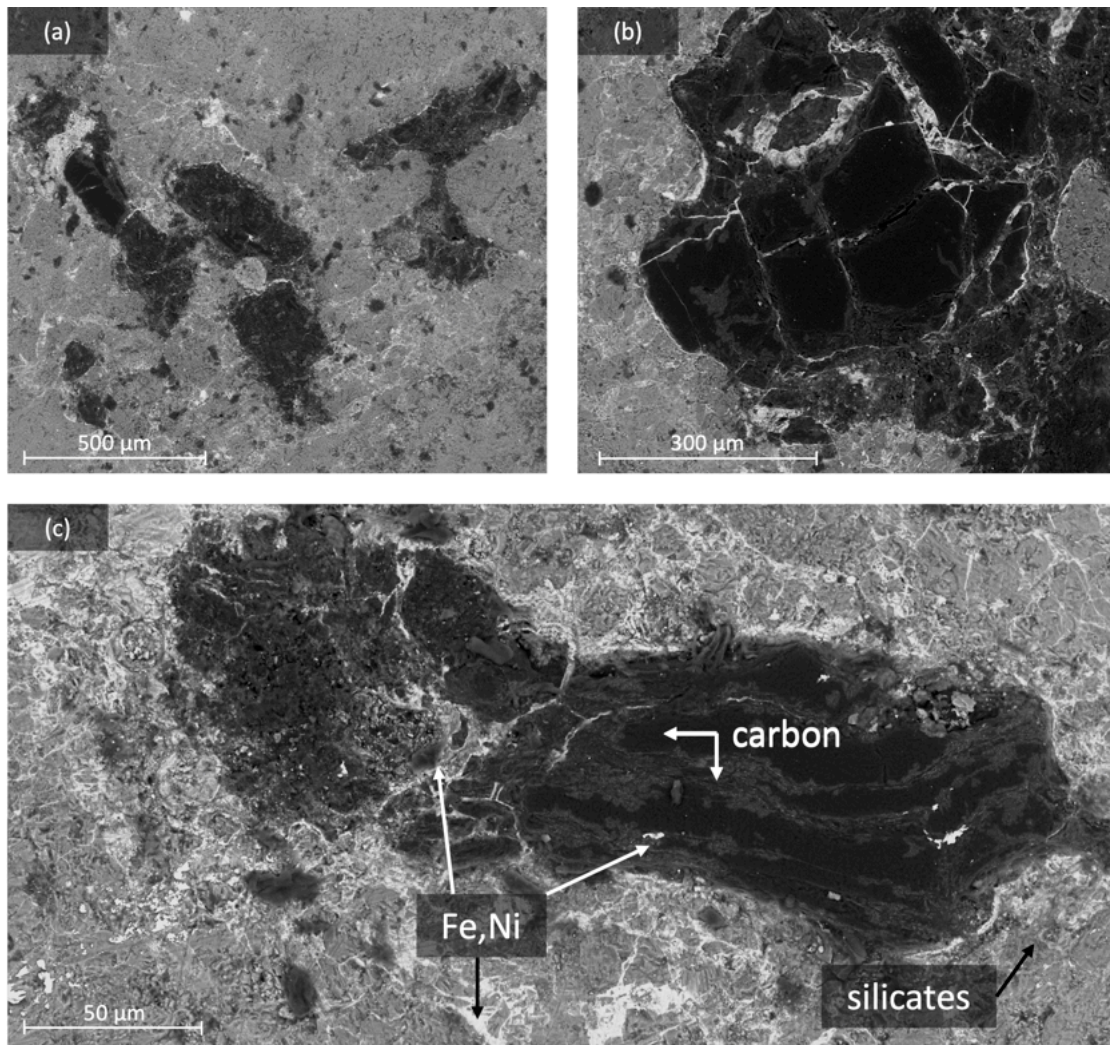
Figure 3.3: BSE images of NWA 6871 carbon aggregates (black and dark gray) in a silicate matrix (light gray) and interstitial Fe-Ni alloys (white). In (a), several carbon aggregates in the ureilite silicate matrix are shown. In (b), a close-up image of a carbon aggregate crossed by Fe-Ni veins is reported. In (c), the blade-like structure on the right side of the carbon aggregate is shown, while the left side appears fractured. Fe-bearing veins and blebs can be seen inside the aggregate.
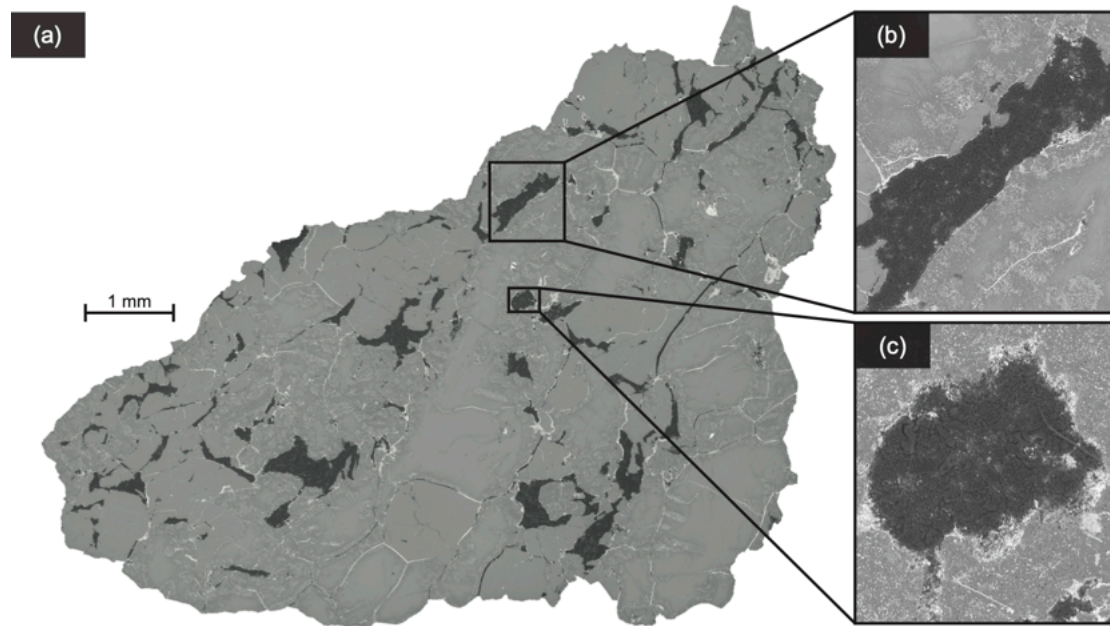
Figure 3.4: a) BSE image of NWA 3140 with close-ups of two carbon aggregates showing amoeboid structure in (b) and (c). Although some aggregates are elongated as shown in (b), no blade-like structure can be observed. A notable feature of this sample are the various small Fe-bearing blebs in the rims of silicates, but also in some silicate cores.

### 3.4.4 Micro-Raman Spectroscopy

MRS on carbon aggregates, both within the bulk samples and on the extracted aggregates, shows first-order Raman bands at $\sim$1580 cm$^{-1}$ and $\sim$1352 cm$^{-1}$ and sometimes at $\sim$1620 cm$^{-1}$. These bands are the so-called G-band, D-band, and D0-band of graphite (Ferrari and Robertson, 2000). While the G-band originates from the zone center phonons with E$_{2g}$ symmetry, the D-band is a breathing mode with A$_{1g}$ symmetry, which is forbidden in perfectly ordered graphite and appears only in disordered graphite (Ferrari and Robertson, 2000). Generally, two different types of graphite spectra are observable (see Fig. 8a and 8b). In Fig. 8a, type 1 spectra show a sharp G-band. In addition, a small D-band and often a D'-band as a shoulder of the G-band can be seen. In contrast to type 1 spectra, type 2 (Fig. 8b) spectra show a very high D-band, which seems to affect also the $\Gamma_G$ of the G-band. However, type 2 spectra are very rare in

comparison to type 1 spectra.

Temperature calculations using Equation 3.2 on graphite from NWA 6871 and NWA 3140 were carried out using the data reported in Table 3.2. To compare our temperatures to the temperatures of Ross et al. (2011) and Barbaro et al. (2020, 2021, 2022), the G-band $\Gamma_G$ values were corrected for the instrumental peak broadening using the same approach as Barbaro et al. (2020), where a lithospheric diamond of high gem quality was used. Ross et al. (2011) report an FWHM of $3\,\mathrm{cm}^{-1}$ for a kimberlitic diamond, while Barbaro and coauthors reported an FWHM of $6\,\mathrm{cm}^{-1}$ (Barbaro et al., 2020) and $5\,\mathrm{cm}^{-1}$ (Barbaro et al., 2021, 2022) for lithospheric diamonds. In this work, we used a set of six different lithospheric diamonds from Canada to obtain the correction factor for our instrument. On each diamond, five measurement points were measured five times for 1 s using a magnification of $50\times$.

Our lithospheric diamonds showed an FWHM of $6.56 \pm 0.29\,\mathrm{cm}^{-1}$. Divided by the FWHM of Ross et al. (2011), this led to a correction factor of $2.19 \pm 0.24\,\mathrm{cm}^{-1}$. The FWHM of our graphite were divided by this correction factor, which resulted in average temperatures of $1370 \pm 39\,^{\circ}\mathrm{C}$ ($120\,^{\circ}\mathrm{C}$) for NWA 6871 and $1368 \pm 33\,^{\circ}\mathrm{C}$ ($120\,^{\circ}\mathrm{C}$) for NWA 3140. Here, $\pm 39\,^{\circ}\mathrm{C}$ and $\pm 33\,^{\circ}\mathrm{C}$ are the standard deviations of our data, while the error of $120\,^{\circ}\mathrm{C}$ is the maximum temperature uncertainty published by (Cody et al., 2008). Of course, the correction factor influences the temperature and the correction factor used in our calculations is slightly higher than the one of Barbaro et al. (2020, 2021, 2022). However, error calculations using Equation 3.4 with our correction factor $c = 2.19 \pm 0.09\,\mathrm{cm}^{-1}$ and the $\Gamma_G = 23.4 \pm 4\,\mathrm{cm}^{-1}$ ($\Delta\Gamma_G$ of $\pm 4\,\mathrm{cm}^{-1}$ is the standard deviation of the $\Gamma_G$ values) led to an error of $\pm 47\,^{\circ}\mathrm{C}$ for $T_{\max}$, which is lower than the cited error of $\pm 120\,^{\circ}\mathrm{C}$ by Cody et al. (2008).

$$\Delta T_{max} = \sqrt{\left(\frac{\partial}{\partial c} * T_{max}\right)^2 \times \Delta c^2 + \left(\frac{\partial}{\partial \Gamma_G} * T_{max}\right)^2 \times \Delta\Gamma_G^2} \qquad (3.4)$$

Type 2 graphite spectra were excluded from the calculations because the high D-band

seems to affect the G-band FWHM. This effect on the FWHM could be due to polishing effects, which can lead to an unpredictable increase of the D-band (Lasithiotakis et al., 2020).
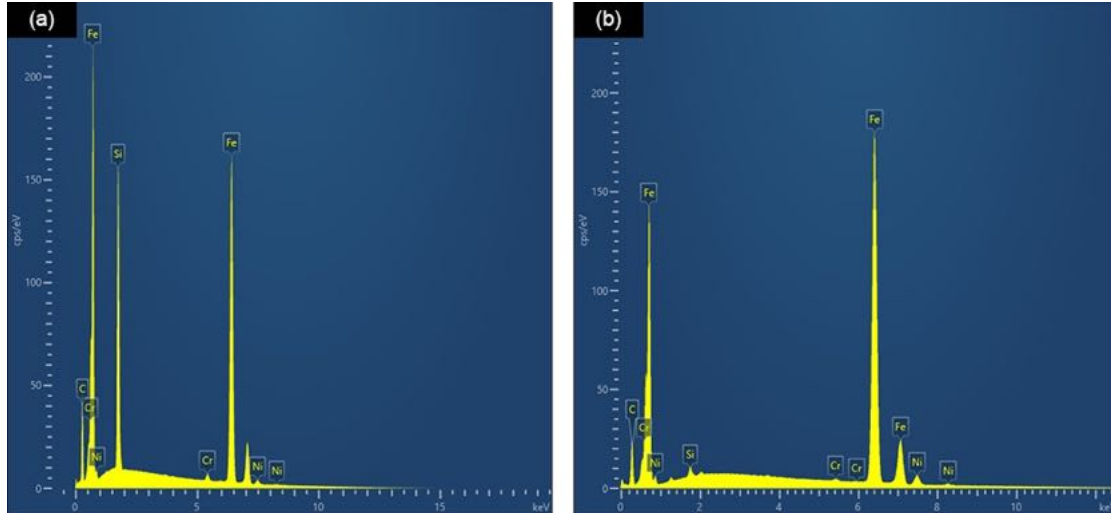


Figure 3.5: Examples of EDS spectra of metal-bearing phases accompanying carbon aggregates of NWA 6871 (a) and NWA 3140 (b). Both spectra show possibly Si-bearing kamacite with minor Cr contents. In NWA 6871, many similar EDS spectra were observed with Si-contents of up to ∼14 wt.%.

### 3.4.5 Field Emission Gun Electron Probe Microanalysis

WDS was performed on the cores of silicate grains to identify olivine and low-Ca pyroxene and to measure $Cr_2O_3$ contents for the Cr-based geothermometer by Collinet and Grove (2020).

In NWA 3140, olivine grains show mean composition $Fo_{80.5}$, while low-Ca pyroxenes have a mean composition $En_{77}Wo_{6.2}$ (Table 3.3). The homogeneity of silicates in NWA 3140 shows that the sample experienced equilibrium and enabled the application of the Cr-based gothermometer, which led to a mean temperature of ∼1215 ± 16 °C. Here, the error was calculated using $D_{Cr}^{olv\text{-}LCP}$ from combining the lowest to lowest, highest to highest, lowest to highest, and highest to lowest Cr contents in olivine and pyroxene, respectively, and eventually by calculating a standard deviation of these temperatures.

NWA 6871 contains olivine with mean composition $Fo_{85.5}$. Low-Ca pyroxenes show a composition $En_{88.2}Wo_{1.2}$, but also three grains with higher Wo contents of $Wo_{30.1}$, $Wo_{27.3}$, and $Wo_{8.4}$ have been identified. The comparably high standard deviation of the $Cr_2O_3$ content in pyroxenes in NWA 6871 makes the geothermometer inapplicable to this sample, because the sample evidently did not reach equilibrium. Hence, no temperature was calculated for silicates in NWA 6871.

Figure 3.6: Reconstructed diffraction images (a,c,e) of three carbon aggregates of NWA 6871 with their corresponding diffractograms (b,d,f). ac) Powder rings for diamond and graphite. In addition to powder rings in (e), diffraction spots can be seen; in detail, see the arrow indicating the *d*-spacing of 1.26 Å for diamond. To provide better readability, not all peaks have been marked. Mineral abbreviations: Dia = diamond, Goe = goethite, Gra = graphite, Mag = magnetite, Ol = olivine, Tro = troilite.

Table 3.1: 2θ and *d*-spacing of diamond and graphite from carbon-bearing aggregates of NWA 6871 and NWA 3140, which were used to calculate the crystallite sizes using the Scherrer Equation 3.1.

| Sample | Diamond | | | Graphite | | |
|---|---|---|---|---|---|---|
| | 2θ (°) | *d*-spacing (Å) | *L* (nm) | 2θ (°) | *d*-spacing (Å) | *L* (nm) |
| NWA 6871_1 | n.d. | n.d. | n.d. | 12.11 | 3.36 | 9 |
| NWA 6871_2 | 32.62 | 1.27 | 6 | 12.19 | 3.34 | 7 |
| | 38.46 | 1.07 | 6 | n.d. | n.d. | n.d. |
| NWA 6871_3 | 32.66 | 1.27 | 7 | 12.12 | 3.35 | 9 |
| | 38.52 | 1.97 | 6 | n.d. | n.d. | n.d. |
| NWA 6871_4 | 32.65 | 1.27 | 6 | 12.1 | 3.35 | 7 |
| | 38.47 | 1.97 | 5 | n.d. | n.d. | n.d. |
| NWA 6871_5 | 32.95 | 1.27 | 5 | n.d. | n.d. | n.d. |
| | 38.77 | 1.07 | 7 | n.d. | n.d. | n.d. |
| NWA 6871_6 | 32.69 | 1.27 | 5 | 12.2 | 3.34 | 5 |
| | 38.49 | 1.07 | 5 | n.d. | n.d. | n.d. |
| NWA 3140_1 | 32.61 | 1.27 | 7 | 12.11 | 3.34 | 5 |
| | 38.44 | 1.07 | 4 | n.d. | n.d. | n.d. |
| NWA 3140_2 | 32.61 | 1.26 | 10 | 12.14 | 3.34 | 9 |
| | 38.6 | 1.07 | 4 | n.d. | n.d. | n.d. |

n.d. = not detected.
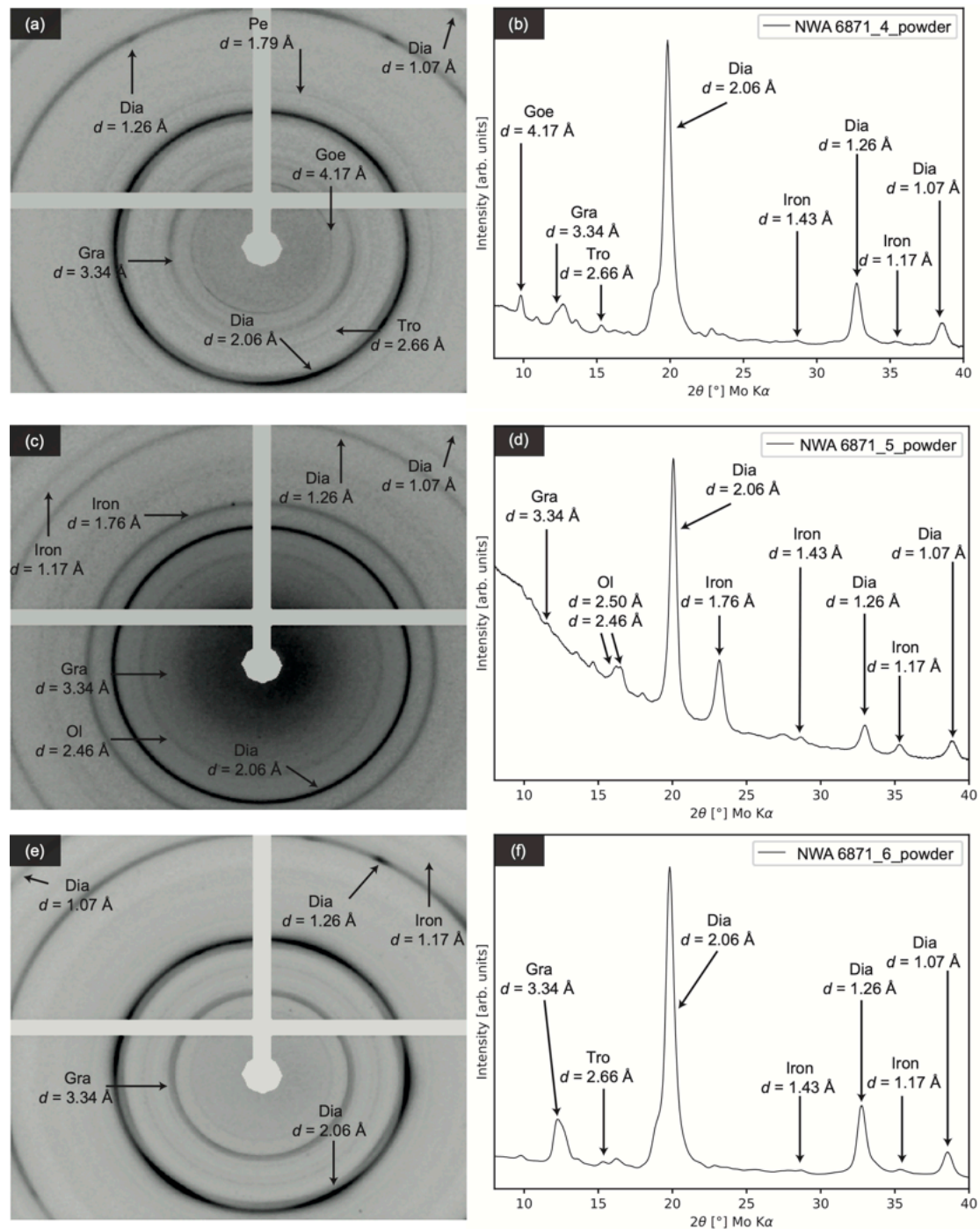
Figure 3.7: Reconstructed diffraction images (a,c) of the three carbon aggregates NWA 3140 with their corresponding diffractograms (b,d). a) Diffraction spots can be seen; in detail, see the arrow indicating the $d$-spacing of 2.06 Å for diamond in (c). To provide better readability, not all peaks have been marked. Mineral abbreviations: Dia = diamond, Gra = graphite.

Table 3.2: Data obtained by Raman spectroscopy on carbon aggregates from NWA 6871 and NWA 3140 which were used to calculate the $T_{\max}$ by using Equation 3.2. All data are given in cm$^{-1}$. The reported errors are the standard deviations of the respective sample.

| G-band center | G-band FWHM ($\Gamma_G$) | G-band FWHM $\Gamma_G$) corrected | D-band center | D-band FWHM | D'-band center | D'-band FWHM | $T_{\max}$ (°C) |
|---|---|---|---|---|---|---|---|
| **NWA 6871** | | | | | | | |
| 1585 | 29 | 13.2 | 1350 | 43 | 1619 | 28 | 1314 |
| 1582 | 17 | 7.8 | 1353 | 40 | 1624 | 7 | 1432 |
| 1570 | 27 | 12.3 | n.d. | n.d. | 1607 | 24 | 1334 |
| 1579 | 24 | 11 | 1354 | 28 | 1616 | 21 | 1363 |
| 1582 | 26 | 11.9 | 1346 | 42 | 1615 | 22 | 1344 |
| 1584 | 26 | 11.9 | 1360 | 28 | 1619 | 20 | 1344 |
| 1584 | 25 | 11.4 | 1350 | 39 | 1621 | 9 | 1353 |
| 1583 | 24 | 11 | 1352 | 40 | 1621 | 16 | 1363 |
| 1582 | 18 | 8.2 | 1354 | 37 | 1623 | 8 | 1422 |
| 1581 | 17 | 7.8 | 1352 | 45 | n.d. | n.d. | 1432 |
| 1583 | 23 | 10.5 | 1349 | 51 | 1619 | 23 | 1373 |
| 1572 | 21 | 9.6 | 1341 | 47 | 1610 | 19 | 1393 |
| 1584 | 27 | 12.3 | 1350 | 41 | 1620 | 19 | 1334 |
| | | | | | | | 1370 ± 39 |
| **NWA 3140** | | | | | | | |
| 1583 | 22 | 10 | 1351 | 38 | 1621 | 18 | 1383 |
| 1584 | 21 | 9.6 | 1344 | 41 | n.d. | n.d. | 1393 |
| 1582 | 25 | 11.4 | 1351 | 41 | n.d. | n.d. | 1353 |
| 1582 | 25 | 11.4 | 1353 | 60 | 1624 | 14 | 1353 |
| 1579 | 27 | 12.3 | 1344 | 69 | 1616 | 21 | 1334 |
| 1581 | 22 | 10 | 1349 | 42 | 1620 | 16 | 1383 |
| 1584 | 25 | 11.4 | 1352 | 41 | 1622 | 13 | 1353 |
| 1580 | 23 | 10.5 | 1348 | 39 | 1618 | 16 | 1373 |
| 1574 | 25 | 11.4 | 1347 | 38 | 1613 | 12 | 1353 |
| 1571 | 23 | 10.5 | n.d. | n.d. | n.d. | n.d. | 1373 |
| 1581 | 25 | 11.4 | 1349 | 42 | 1619 | 14 | 1353 |
| 1571 | 23 | 10.5 | 1337 | 48 | n.d. | n.d. | 1373 |
| 1581 | 17 | 7.8 | 1350 | 36 | n.d. | n.d. | 1432 |
| 1574 | 23 | 10.5 | 1346 | 39 | n.d. | n.d. | 1373 |
| 1581 | 19 | 8.7 | 1352 | 36 | 1623 | 7 | 1413 |
| 1582 | 32 | 14.6 | 1347 | 47 | n.d. | n.d. | 1283 |
| | | | | | | | 1368 ± 33 |

n.d. = not detected.

Table 3.3: Mean compositions for olivine and low-Ca pyroxene grains in NWA 6871 and NWA 3140. The temperature was calculated using Equation 3.3.

| Sample | NWA 6871 | | NWA 3140 | |
|---|---|---|---|---|
| Mineral | olivine | low-Ca pyroxene | olivine | low-Ca pyroxene |
| $SiO_2$ | 39.94 | 57.45 | 39.02 | 55.47 |
| $\sigma$ | 0.46 | 0.84 | 0.3 | 0.23 |
| $TiO_2$ | b.d.l. | 0.01 | 0.01 | 0.06 |
| $\sigma$ | n.d. | 0.01 | 0.01 | 0.01 |
| $Al_2O_3$ | 0.05 | 0.05 | b.d.l. | 0.47 |
| $\sigma$ | 0.08 | 0.05 | n.d. | 0.03 |
| $Cr_2O_3$ | 0.87 | 0.78 | 0.71 | 1.1 |
| $\sigma$ | 0.43 | 0.12 | 0.02 | 0.02 |
| MgO | 45.55 | 34.03 | 41.95 | 28.33 |
| $\sigma$ | 1.17 | 1.49 | 0.47 | 0.16 |
| FeO | 13.74 | 7.36 | 18.15 | 11.06 |
| $\sigma$ | 0.95 | 1.09 | 0.54 | 0.25 |
| CaO | 0.49 | 0.89 | 0.33 | 3.16 |
| $\sigma$ | 0.79 | 1.15 | 0.01 | 0.05 |
| MnO | 0.47 | 0.34 | 0.42 | 0.41 |
| $\sigma$ | 0.04 | 0.07 | 0.02 | 0.02 |
| $n$ | 24 | 14 | 16 | 18 |
| $D_{Cr}^{oliv\text{-}LCP}$ | n.a. | | 0.647 | |
| $T$ (°C) | n.a. | | 1215 | |

detection limits: Si = 136 ppm, Ti = 173 ppm, Al = 143 ppm,

Fe = 374 ppm, Mn = 361 ppm, Mg = 118 ppm, Ca = 157 ppm,

Cr 294 ppm; b.d.l. = below detection limit, n.d. = not determined.

## 3.5 Discussion

The results confirm that NWA 6871 is a highly shocked ureilite. This can be seen in the recrystallization of 20 µm sized olivine grains forming olivine aggregates but also in the small grain size of pyroxene. Melting and recrystallization of olivine and pyroxene starts at very high pressures of ~60 and ~70 GPa, respectively (Stöffler et al., 2018). Therefore, our observations are in good agreement with the shock classification of S6 by Bunch et al. (2012), although we prefer to classify it as U-S6 after the new classification system by Stöffler et al. (2018). NWA 6871 contains blade-shaped carbon aggregates consisting of nanographite and micro- and nanodiamond (with stacking faults) accompanied by Fe-bearing phases. The blade-shaped morphologies resemble euhedral millimeter-sized graphite crystals, which typically occur in ureilites with very low shock degrees (Berkley and Jones, 1982; Treiman and Berkley, 1994). Generally, the blade-shaped structures appear parallel to the longest dimension of the aggregates and therefore along the (0001) of graphite (Berkley and Jones, 1982; Treiman and Berkley, 1994). Nestola et al. (2020) argued that these morphologies cannot survive static high pressure for long inside a planetary body, because if diamonds had been formed deep inside a large planetary body, they would develop diamond morphologies instead of retaining graphite ones. Hence, what we see in our samples is nanographite and micro- and nanodiamond paramorphing pristine graphite crystals because of a very rapid transformation process such as a shock event.

NWA 3140 is, with a shock degree of U-S3, less shocked than NWA 6871. In NWA 3140, no blade-like structures can be seen in carbon aggregates. Moreover, the carbon aggregates in NWA 3140 show amoeboid shapes, which have also been reported for low-shocked ureilites, for example, ALH 77257 by Nakamuta et al. (2016). Internally however, the carbon aggregates are similar to those in NWA 6871, showing the coexistence of nanographite, nanodiamond, and microdiamond accompanied by Fe-bearing phases. The temperature of ~1215 ± 16 °C recorded by silicates is in good agreement

with equilibrium temperatures of other ureilites from the literature (see Collinet and Grove (2020) and references therein) and clearly shows that silicate-based geothermometers and the graphite-based geothermometer record different temperatures and therefore different events

The occurrence of two carbon polymorphs and therefore the heterogeneous distribution of a shock product on a small scale can better be explained by a heterogeneous propagation of the shock wave rather than by graphitization of diamond (see explanation below). Ogilvie et al. (2011) investigated the distribution of shock metamorphic effects in natural rocks and experiments and demonstrated that the shock distribution depends on the shock impedance contrast between grains and that shock effects can be amplified if the contrast is large. Carbon aggregates in ureilites usually occur interstitially between silicate grains. This can lead to an increased shock pressure on the carbon aggregates in comparison to the more rigid silicate grains surrounding them. Thus, depending on the surrounding material, carbon aggregates can experience different pressures which may be even higher than those recorded by the silicates. This heterogeneity occurs on a submillimeter scale and could be responsible for the different distribution of micro- and nanodiamond in a carbon aggregate.

Figure 3.8: a, b) Two types of Raman spectra for graphite in NWA 3140 and NWA 6871.

### 3.5.1 Graphite

Graphite is the major constituent of carbon aggregates in NWA 6871 and NWA 3140. By MRS, we see the three already mentioned bands, of which the D-band at $\sim 1352\,\mathrm{cm}^{-1}$ indicates disordered graphite. In the X-ray diffractograms of NWA 6871, the graphite peak at $d$-spacing of $3.34\,\mathrm{\mathring{A}}$ is rather broad and shows a peak asymmetry. This could be explained by an overlapping of the graphite peak with the peak of "compressed graphite", which is known to tail toward higher angles with slightly lower $d$-spacings (here $3.20\,\mathrm{\mathring{A}}$; (Endo et al., 1994; Nakamuta and Aoki, 2000)). Generally, compressed graphite is characterized by a smaller interplanar spacing compared to uncompressed graphite (Endo et al., 1994). In ureilites, compressed graphite has been proposed as evidence that ureilitic diamonds formed by transformation of graphite under high pressure and temperature conditions (e.g., Hezel et al., 2008; Nakamuta and Aoki, 2000).

The grain size reduction from micrometer- to nanometer-sized graphite occurred either during the shock event that destroyed the UPB or during one that destroyed a UDB, as discussed by Barbaro et al. (2020). There are three different processes that cause

the grain size reduction: (i) a back transformation from microdiamond, (ii) a back transformation from nanodiamond, or (iii) a grain size reduction from micrographite to nanographite during the impact event.

The back transformation of detonation-obtained microdiamond to nanographite has been investigated by Efremov and Zakatilova (2019). The authors have shown that detonation-produced microdiamond is stable to temperatures >1500 °C and only above these temperatures a graphitization process can be observed. However, this would mean that both the microdiamonds (the precursor of nanographite) and the nanographite were formed during the same event that lasted no longer than a few seconds and after which the parent/daughter body was quenched. Hence, this process is very unlikely. In contrast to that, the back transformation of nanodiamond to nanographite requires lower temperatures of >800 °C (Efremov et al., 2018). If graphitization took place from nanodiamond, it could be verified by TEM, with the aim to check for the presence of an onion graphite structure (Popov et al., 2013). However, this process could account for some of the nanographite in the vicinity of nanodiamonds, but not for all the nanographite that we see today, which would imply that graphite was entirely transformed to diamond and then back to graphite.

More likely, micrographite was reduced in size to nanographite during a shock event. This has been demonstrated by Veysset et al. (2015), who used laser-induced shock waves on highly ordered pyrolytic graphite which led to nanographite. Transferred to ureilites, this would mean that nanographite was simply created during the shock event when micrographite was broken apart by the shock wave.

Finally, we can exclude that the nanometric size is due to polishing. Polishing graphite with abrasive material can reduce its grain size (Lasithiotakis et al., 2020). However, this would only affect the surface and our XRD data clearly show that the fragments consist entirely of nanometric graphite as the X-ray beam probes the whole sample instead of just the surface.

### 3.5.2 Diamond

Diamond can be found in both samples and shows nanometric grain sizes; however, single crystal diffraction spots can be seen in the diffraction images, indicating that both nano- and microdiamond coexist. In NWA 6871, diamond shows stacking disorders in some diffractograms, which are generally considered a shock indicator (Murri et al., 2019; Németh et al., 2014, 2020a,b; Salzmann et al., 2015). In contrast, diffractograms of NWA 3140 do not show such features at all. A possible explanation is that diamond stacking faults are also present in diamond from NWA 3140 and NWA 6871_2, but at a different extent not allowing XRD to detect it. The simultaneous occurrence of micro- and nanodiamond in a carbon aggregate can be explained by the availability of a catalyst. As Varfolomeeva (1971) has shown, using a catalyst for the direct transformation of graphite to diamond, microdiamond forms in the vicinity of the catalyst while nanodiamond forms farther away from the catalyst.

### 3.5.3 Fe-Bearing Phases

The carbon aggregates are accompanied by Fe-bearing phases (e.g., kamacite, taenite, troilite, goethite, and magnetite), of which taenite is very rare and considered to originate from the impactor (Ross et al., 2019). Fe-bearing phases can be observed in many ureilites (e.g., Barbaro et al., 2020, 2021, 2022; Goodrich et al., 2013; Goodrich, 1992; Nakamuta et al., 2016; Nestola et al., 2020; Ross et al., 2019). These phases could act as a catalyst for the direct graphite-to-diamond transformation requiring lower $P,T$-conditions. After Goodrich et al. (2013), Fe-bearing phases in ureilites originate from an Fe-Ni-C melt. In our samples, remnants of this melt can be seen as Fe-bearing phases located in or around carbon aggregates but also in between silicates and in their rims. The important role of Fe-Ni melt for microdiamond (of up to 100 µm in size) formation in ureilites has been discussed by Nestola et al. (2020) and Barbaro et al. (2022), who showed that with the help of a catalyst, microdiamond can be formed at pressures of at

least 15 GPa even within a few seconds of impact duration, which is in agreement with our samples.

### 3.5.4 Origin of Diamond in NWA 6871 and NWA 3140

NWA 6871 shows several shock indicators (olivine crystals are recrystallized, graphite is partly compressed, and stacking faults are present in diamond). The shock indicator in olivine indicates pressure of up to 60–70 GPa, which is more than sufficient to transform graphite to diamond.

While nanosized diamond forms as a product of shock without any catalyst, micro-diamond formed with catalyzing metals. With the availability of a catalyst, there is no necessity for the formation of micrometric diamond under static high pressure over long periods deep inside a large planetary body. The occurrence of diamond in both sizes could be explained by the availability of a catalyst, the short duration of the shock event, and the general heterogeneous distribution of shock effects, which is known from laboratory experiments and natural rocks (Ogilvie et al., 2011, and references therein). According to Ogilvie et al. (2011), such extreme disequilibrium at the micrometer scale can only be explained by extremely short-lived events, that is, shock events.

NWA 3140 is less shocked than NWA 6871 and experienced shock pressures of only up to 15 GPa as seen by its silicates. While 15 GPa is also sufficient to transform graphite directly to diamond, indicative features for this process are absent (compressed graphite, stacking faults in diamond at the scale observable by XRD), but the carbon associations show the same mineralogical composition as in NWA 6871. However, pressure alone does not transform graphite to diamond, also high temperatures must be involved.

Compared to available literature data for temperature records in graphite from ure-ilites (Barbaro et al., 2020, 2021, 2022; Ross et al., 2019), NWA 6871 and NWA 3140 record the highest temperature measured so far (Table 3.4). The temperature obtained by graphite-based geothermometry has been ascribed to the shock event that destroyed

the UPB/UDB and triggered the formation of diamond from graphite (Barbaro et al., 2020, 2021, 2022). The temperatures of 1370 ± 120 °C and 1368 ± 120 °C further prove this assumption as such high temperatures exclude a magmatic origin for this graphite because as silicate and chromite-based geothermometers have shown, the equilibrium temperatures of several ureilites range between 1054 and 1276 °C, a temperature range in which also our data based on the Cr-based geothermometer in NWA 3140 falls. Unfortunately, due to disequilibrium conditions, it was not possible to apply the same geothermometer to NWA 6871. The temperatures of ∼1370 °C as estimated from graphite falls into the catalytic diamond synthesis field as shown in the carbon phase diagram in Dobrzhinetskaya (2012). This makes it very likely that diamond from NWA 3140 also formed during the shock event that destroyed the UPB/UDB. However, NWA 6871 has experienced higher pressures and the peak temperature was probably higher than catalytic synthesis requires. It would be intuitive to assume a correlation between temperatures recorded by graphite and the shock degree of the individual ureilite. However, NWA 3140 shows that this is not the case because here a medium shocked sample shows the same high temperature as the highly shocked sample NWA 6871 and considering the error of 120 °C also the literature temperatures are in relatively good agreement to each other. Hence, no linear correlation can be observed and, as Stöffler et al. (2018) pointed out, the temperature increase during shock depends on multiple factors including porosity and shock impedance of the constituents of the parent body. Especially porosity has a major influence on the temperature increase as shown in Fig. 2 in Stöffler et al. (2018). Here, at a given temperature, the pressure increase can differ on the scale of a magnitude depending on the porosity of the target rock. Unfortunately, we lack information about the current and initial porosities of both samples and the initial porosities in the samples could have been higher before the impact/collision event(s).

In summary, there are four parameters which control the formation of micro- and nanodiamond in ureilites: (i) availability and location of the catalyst that triggers the

graphite to diamond formation at lower pressures and temperatures, (ii) different shock wave propagation, (iii) shock impedance that controls the pressure distribution, and (iv) porosity that controls the temperature increase.

Table 3.4: Average $T_{max}$ in °C as recorded from graphite in different ureilites based on the graphite thermometer by Cody et al. (2008). The temperature uncertainty is $\pm 120$ °C.

| Sample | AhS #7[1] | Kenna[2] | AhS 209[3] | AhS 72[3] | AhS A135A[3] | Y-74123[4] | NWA 6871[5] | NWA 3140[5] |
|---|---|---|---|---|---|---|---|---|
| Shock | medium | medium | medium | medium | medium/high | medium/high | high | medium |
| $T_{max}$ (°C) | 990 | 1180 | 1266 | 1242 | 1332 | 1314 | 1370 | 1368 |

[1]Ross et al. (2011); [2]Barbaro et al. (2021), [3]Barbaro et al. (2020); [4]Barbaro et al. (2022); [5]this study

### 3.5.5 Conclusions

Microdiamond associated with Fe-bearing phases but also nanodiamond and nanographite can be found by single crystal XRD in medium and highly shocked ureilites. Thus, our study further proves the formation of (micro)diamond by shock events. The size of microdiamonds, however, is difficult to determine if the extracted carbon aggregate does not consist entirely of microdiamond as was reported for one aggregate in NWA 7983 by Nestola et al. (2020). With $1370 \pm 120$ °C and $1369 \pm 120$ °C, graphite in the two differently shocked ureilites NWA 6871 and NWA 3140 records the highest temperatures ever reported for ureilites, and the temperature is in good agreement with temperatures required for diamond synthesis through metal catalysis (see carbon phase diagram in Dobrzhinetskaya (2012)). Furthermore, these temperatures exceed the equilibration temperature of $1215 \pm 16$ °C recorded by silicates, which indicates that both thermometers record different events. We conclude that nanographite appears to record temperatures that were reached during the shock event that formed microdiamonds and nanodiamonds. However, the temperature is not correlated with the shock degree of the specific ureilite.

*Data Availability Statement–*The data that support the findings of this study are available from the corresponding author upon reasonable request.

*Editorial Handling–Dr. Christian Koeberl*

## 3.6 References

A. Barbaro, M. C. Domeneghetti, C. A. Goodrich, M. Meneghetti, L. Litti, A. M. Fioretti, P. Jenniskens, M. H. Shaddad, and F. Nestola. Graphite-based geothermometry on almahata sitta ureilitic meteorites. *Minerals*, 10(11):1005, 2020.
 doi.org/10.3390/min10111005

A. Barbaro, M. C. Domeneghetti, K. D. Litasov, L. Ferrière, L. Pittarello, O. Christ, S. Lorenzon, M. Alvaro, and F. Nestola. Origin of micrometer-sized impact diamonds in ureilites by catalytic growth involving Fe-Ni-silicide: The example of Kenna meteorite. *Geochimica et Cosmochimica Acta*, 309:286–298, 2021.
 doi.org/10.1016/j.gca.2021.06.022

A. Barbaro, F. Nestola, L. Pittarello, L. Ferrière, M. Murri, K. D. Litasov, O. Christ, M. Alvaro, and M. C. Domeneghetti. Characterization of carbon phases in Yamato 74123 ureilite to constrain the meteorite shock history. *American Mineralogist: Journal of Earth and Planetary Materials*, 107(3):377–384, 2022.
 doi.org/10.1016/j.gca.2021.06.022

J. L. Berkley and J. H. Jones. Primary igneous carbon in ureilites: Petrological implications. *Journal of Geophysical Research: Solid Earth*, 87(S01):A353–A364, 1982.
 doi.org/10.1029/JB087iS01p0A353

H. Bovenkerk, F. Bundy, H. Hall, H. Strong, and R. Wentorf. Preparation of diamond. *Nature*, 184(4693):1094–1098, 1959.
  🔗 doi.org/10.1038/1841094a0

T. Bunch, J. Wittke, A. Irving, S. Kuehner, and P. Sipiera. Three Very Highly Shocked Ureilites NWA 4165, NWA 6871 and NWA 7195: Evidence for Recrystallization and Melting of Silicates and Vaporization of Graphite and Diamond. *75th Annual Meeting of the Meteoritical Society*, 2012

F. Bundy, H. T. Hall, H. Strong, et al. Man-made diamonds. *Nature*, 176(4471):51–55, 1955.
  🔗 doi.org/10.1038/176051a0

J. Chikami, T. Mikouchi, H. Takeda, and M. Miyamoto. Mineralogy and cooling history of the calcium-aluminum-chromium enriched ureilite, Lewis Cliff 88774. *Meteoritics & Planetary Science*, 32(3):343–348, 1997.
  🔗 doi.org/10.1111/j.1945-5100.1997.tb01277.x

G. Cody, H. Yabuta, A. Kilcoyne, T. Araki, H. Ade, P. Dera, M. Fogel, B. Militzer, B. Mysen, et al. Organic thermometry for chondritic parent bodies. *Earth and Planetary Science Letters*, 272(1-2):446–455, 2008.
  🔗 doi.org/10.1016/j.epsl.2008.05.008

M. Collinet and T. L. Grove. Incremental melting in the ureilite parent body: Initial composition, melting temperatures, and melt compositions. *Meteoritics & Planetary Science*, 55(4):832–856, 2020.
  🔗 doi.org/10.1111/maps.13471

S. Desch, J. O'Rourke, L. Schaefer, T. Sharp, and D. Schrader. Diamonds in ureilites from Mars. In *50th Annual Lunar and Planetary Science Conference*, 2019

L. F. Dobrzhinetskaya. Microdiamonds—frontier of ultrahigh-pressure metamorphism: a review. *Gondwana Research*, 21(1):207–223, 2012.
  🔗 doi.org/10.1016/j.gr.2011.07.014

H. Downes, D. W. Mittlefehldt, N. T. Kita, and J. W. Valley. Evidence from polymict ureilite meteorites for a disrupted and re-accreted single ureilite parent asteroid gardened by several distinct impactors. *Geochimica et Cosmochimica Acta*, 72(19):4825–4844, 2008.
  🔗 doi.org/10.1016/j.gca.2008.06.028

V. Efremov and E. Zakatilova. Spectroscopic methods of investigation and the thermal stability of detonation nanodiamonds. In *Journal of Physics: Conference Series*, volume 1238. IOP Publishing, 2019.
  🔗 doi.org/10.1088/1742-6596/1238/1/012013

V. Efremov, E. Zakatilova, I. Maklashova, and N. Shevchenko. Thermal stability of detonation-produced micro and nanodiamonds. In *Journal of Physics: Conference Series*, volume 946. IOP Publishing, 2018.
  doi.org/10.1088/1742-6596/946/1/012107

S. Endo, N. Idani, R. Oshima, K. J. Takano, and M. Wakatsuki. X-ray diffraction and transmission-electron microscopy of natural polycrystalline graphite recovered from high pressure. *Physical Review B*, 49(1):22, 1994.
  doi.org/10.1103/PhysRevB.49.22

A. C. Ferrari and J. Robertson. Interpretation of Raman spectra of disordered and amorphous carbon. *Physical Review B*, 61(20):14095, 2000.
  doi.org/10.1103/PhysRevB.61.14095

K. Fukunaga, J.-i. Matsuda, K. Nagao, M. Miyamoto, and K. Ito. Noble-gas enrichment in vapour-growth diamonds and the origin of diamonds in ureilites. *Nature*, 328(6126): 141–143, 1987.
  doi.org/10.1038/328141a0

P. Gillet and A. E. Goresy. Shock events in the solar system: the message from minerals in terrestrial planets and asteroids. *Annual Review of Earth and Planetary Sciences*, 41:257–285, 2013.
  doi.org/10.1146/annurev-earth-042711-105538

C. Goodrich, F. Nestola, R. Jakubek, T. Erickson, M. Fries, A. Fioretti, D. Ross, and F. Brenker. The origin of diamonds in ureilites. In *51st Lunar and Planetary Science Conference*, 2020

C. A. Goodrich, R. D. Ash, J. A. Van Orman, K. Domanik, and W. F. McDonough. Metallic phases and siderophile elements in main group ureilites: Implications for ureilite petrogenesis. *Geochimica et Cosmochimica Acta*, 112:340–373, 2013.
  doi.org/10.1016/j.gca.2012.06.022

C. A. Goodrich. Ureilites: A critical review. *Meteoritics*, 27(4):327–352, 1992.
  doi.org/10.1111/j.1945-5100.1992.tb00215.x

C. A. Goodrich, E. R. Scott, and A. M. Fioretti. Ureilitic breccias: clues to the petrologic structure and impact disruption of the ureilite parent asteroid. *Geochemistry*, 64(4): 283–327, 2004.
  doi.org/10.1016/j.chemer.2004.08.001

C. A. Goodrich, G. E. Harlow, J. A. Van Orman, S. R. Sutton, M. J. Jercinovic, and T. Mikouchi. Petrology of chromite in ureilites: Deconvolution of primary oxidation states and secondary reduction processes. *Geochimica et Cosmochimica Acta*, 135: 126–169, 2014.
  doi.org/10.1016/j.gca.2014.02.028

C. A. Goodrich, W. K. Hartmann, D. P. O'Brien, S. J. Weidenschilling, L. Wilson, P. Michel, and M. Jutzi. Origin and history of ureilitic material in the solar system: The view from asteroid 2008 $TC_3$ and the Almahata Sitta meteorite. *Meteoritics & Planetary Science*, 50(4):782–809, 2015.
  doi.org/10.1111/maps.12401

J. S. Herrin, M. E. Zolensky, M. Ito, L. Le, D. W. Mittlefehldt, P. Jenniskens, A. J. Ross, and M. H. Shaddad. Thermal and fragmentation history of ureilitic asteroids: Insights from the Almahata Sitta fall. *Meteoritics & Planetary Science*, 45(10-11): 1789–1803, 2010.
  doi.org/10.1111/j.1945-5100.2010.01136.x

D. C. Hezel, L. Dubrovinsky, L. Nasdala, J. Cauzid, A. Simionovici, M. Gellissen, and T. SCHÖNBECK. In situ micro-Raman and X-ray diffraction study of diamonds and petrology of the new ureilite UAE 001 from the United Arab Emirates. *Meteoritics & Planetary Science*, 43(7):1127–1136, 2008.
  doi.org/10.1111/j.1945-5100.2008.tb01117.x

T. Irifune, A. Kurio, S. Sakamoto, T. Inoue, and H. Sumiya. Ultrahard polycrystalline diamond from graphite. *Nature*, 421(6923):599–600, 2003.
  doi.org/10.1038/421599b

G. F. Kunz. Diamonds in meteorites. *Science*, 11(266):118–119, 1888.
  doi.org/10.1126/science.ns-11.266.118.b

M. Lasithiotakis, J. T. Marrow, and B. J. Marsden. Evaluation of damage induced in graphite due to sample preparation by standard non-destructive techniques. *Materials Physics and Mechanics*, 44(3), 2020.
  doi.org/10.18720/MPM.4432020_1

M. E. Lipschutz. Origin of diamonds in the ureilites. *Science*, 143(3613):1431–1434, 1964.
  doi.org/10.1126/science.143.3613.1431.b

J.-I. Matsuda, A. Kusumi, H. Yajima, and Y. Syono. Noble gas studies in diamonds synthesized by shock loading in the laboratory and their implications on the origin of diamonds in ureilites. *Geochimica et Cosmochimica Acta*, 59(23):4939–4949, 1995.
  doi.org/10.1016/0016-7037(95)00333-9

D. W. Mittlefehldt, T. J. McCoy, C. A. Goodrich, and A. Kracher. Non-chondritic meteorites from asteroidal bodies. In *Planetary materials*, pages 523–718. De Gruyter, 2018.
  doi.org/10.1515/9781501508806-019

M. Miyahara, E. Ohtani, A. El Goresy, Y. Lin, L. Feng, J.-C. Zhang, P. Gillet, T. Nagase, J. Muto, and M. Nishijima. Unique large diamonds in a ureilite from Almahata Sitta 2008 $TC_3$ asteroid. *Geochimica et Cosmochimica Acta*, 163:14–26, 2015.
  doi.org/10.1016/j.gca.2015.04.035

A. Morbidelli, J. I. Lunine, D. P. Obrien, S. N. Raymond, and K. J. Walsh. Building terrestrial planets. *Annual Review of Earth and Planetary Sciences*, 40(1):251–275, 2012.
doi.org/10.1146/annurev-earth-042711-105319

M. Murri, R. L. Smith, K. McColl, M. Hart, M. Alvaro, A. P. Jones, P. Németh, C. G. Salzmann, F. Corà, M. C. Domeneghetti, et al. Quantifying hexagonal stacking in diamond. *Scientific reports*, 9(1):1–8, 2019.
doi.org/10.1038/s41598-019-46556-3

F. Nabiei, J. Badro, T. Dennenwaldt, E. Oveisi, M. Cantoni, C. Hébert, A. El Goresy, J.-A. Barrat, and P. Gillet. A large planetary body inferred from diamond inclusions in a ureilite meteorite. *Nature Communications*, 9(1):1–6, 2018.
doi.org/10.1038/s41467-018-03808-6

Y. Nakamuta and Y. Aoki. Mineralogical evidence for the origin of diamond in ureilites. *Meteoritics & Planetary Science*, 35(3):487–493, 2000.
doi.org/10.1111/j.1945-5100.2000.tb01430.x

Y. Nakamuta, F. Kitajima, and K. Shimada. In situ observation, X–ray diffraction and Raman analyses of carbon minerals in ureilites: Origin and formation mechanisms of diamond in ureilites. *Journal of Mineralogical and Petrological Sciences*, 111(4): 252–269, 2016.
doi.org/10.2465/jmps.150906

P. Németh, L. A. Garvie, T. Aoki, N. Dubrovinskaia, L. Dubrovinsky, and P. R. Buseck. Lonsdaleite is faulted and twinned cubic diamond and does not exist as a discrete material. *Nature Communications*, 5(1):1–5, 2014.
doi.org/10.1038/ncomms6447

P. Németh, K. McColl, L. A. Garvie, C. G. Salzmann, M. Murri, and P. F. McMillan. Complex nanostructures in diamond. *Nature Materials*, 19(11):1126–1131, 2020a.
doi.org/10.1038/s41563-020-0759-8

P. Németh, K. McColl, R. L. Smith, M. Murri, L. A. Garvie, M. Alvaro, B. Pécz, A. P. Jones, F. Corà, C. G. Salzmann, et al. Diamond-graphene composite nanostructures. *Nano letters*, 20(5):3611–3619, 2020b.
doi.org/10.1021/acs.nanolett.0c00556

F. Nestola, C. A. Goodrich, M. Morana, A. Barbaro, R. S. Jakubek, O. Christ, F. E. Brenker, M. C. Domeneghetti, M. C. Dalconi, M. Alvaro, et al. Impact shock origin of diamonds in ureilite meteorites. *Proceedings of the National Academy of Sciences*, 117(41):25310–25318, 2020.
doi.org/10.1073/pnas.1919067117

P. Ogilvie, R. L. Gibson, W. U. Reimold, A. Deutsch, and U. Hornemann. Experimental investigation of shock metamorphic effects in a metapelitic granulite: The importance

of shock impedance contrast between components. *Meteoritics & Planetary Science*, 46(10):1565–1586, 2011.

doi.org/10.1111/j.1945-5100.2011.01250.x

V. Popov, A. Egorov, S. Savilov, V. Lunin, A. Kirichenko, V. Denisov, V. Blank, O. Vyaselev, and T. Sagalova. Features of the transformation of detonation nanodiamonds into onion-like carbon nanoparticles. *Journal of Surface Investigation. X-ray, Synchrotron and Neutron Techniques*, 7(6):1034–1043, 2013.

doi.org/10.1134/S1027451013060153

N. Rai, H. Downes, and C. Smith. Ureilite meteorites provide a new model of early planetesimal formation and destruction. *Geochemical Perspectives Letters*, 14:20–25, 2020.

doi.org/10.7185/geochemlet.2018

A. J. Ross, A. Steele, M. D. Fries, L. Kater, H. Downes, A. P. Jones, C. L. Smith, P. M. Jenniskens, M. E. Zolensky, and M. H. Shaddad. MicroRaman spectroscopy of diamond and graphite in Almahata Sitta and comparison with other ureilites. *Meteoritics & Planetary Science*, 46(3):364–378, 2011.

doi.org/10.1111/j.1945-5100.2010.01157.x

A. J. Ross, H. Downes, J. S. Herrin, D. W. Mittlefehldt, M. Humayun, and C. Smith. The origin of iron silicides in ureilite meteorites. *Geochemistry*, 79(4):125539, 2019.

doi.org/10.1016/j.chemer.2019.125539

A. Ruzicka, J. N. Grossman, and L. Garvie. The meteoritical bulletin, no. 100, 2014 june, 2014

H. Sabbah, A. L. Morrow, P. Jenniskens, M. H. Shaddad, and R. N. Zare. Polycyclic aromatic hydrocarbons in asteroid 2008 TC$_3$: Dispersion of organic compounds inside asteroids. *Meteoritics & Planetary Science*, 45(10-11):1710–1717, 2010.

doi.org/10.1111/j.1945-5100.2010.01103.x

C. G. Salzmann, B. J. Murray, and J. J. Shephard. Extent of stacking disorder in diamond. *Diamond and Related Materials*, 59:69–72, 2015.

doi.org/10.1016/j.diamond.2015.09.007

P. Scherrer. Bestimmung der inneren Struktur und der Größe von Kolloidteilchen mittels Röntgenstrahlen. In *Kolloidchemie Ein Lehrbuch*, pages 387–409. Springer, 1912.

doi.org/10.1007/978-3-662-33915-2_7

S. Singletary and T. Grove. Early petrologic processes on the ureilite parent body. *Meteoritics & Planetary Science*, 38(1):95–108, 2003.

doi.org/10.1111/j.1945-5100.2003.tb01048.x

S. K. Sinha, R. O. Sack, and M. E. Lipschutz. Ureilite meteorites: Equilibration temperatures and smelting reactions. *Geochimica et Cosmochimica Acta*, 61(19):4235–4242,

1997.
  doi.org/10.1016/S0016-7037(97)00254-8

D. Stöffler and K. Keil. Shock metamorphism of ordinary chondrites. *Geochimica et Cosmochimica Acta*, 55(12):3845–3867, 1991.
  doi.org/10.1016/0016-7037(91)90078-J

D. Stöffler, C. Hamann, and K. Metzler. Shock metamorphism of planetary silicate rocks and sediments: Proposal for an updated classification system. *Meteoritics & Planetary Science*, 53(1):5–49, 2018.
  doi.org/10.1111/maps.12912

H. Takeda. Mineralogy of coexisting pyroxenes in magnesian ureilites and their formation conditions. *Earth and Planetary Science Letters*, 93(2):181–194, 1989.
  doi.org/10.1016/0012-821X(89)90067-8

H. Takeda, H. Mori, and H. Ogata. Mineralogy of augite-bearing ureilites and the origin of their chemical trends. *Meteoritics*, 24(2):73–81, 1989.
  doi.org/10.1111/j.1945-5100.1989.tb00947.x

A. H. Treiman and J. L. Berkley. Igneous petrology of the new ureilites Nova 001 and Nullarbor 010. *Meteoritics*, 29(6):843–848, 1994.
  doi.org/10.1111/j.1945-5100.1994.tb01097.x

H. C. Urey. Diamonds, Meteorites, and the Origin of the Solar System. *The Astrophysical Journal*, 124:623, 1956

T. Varfolomeeva. *Synthesis and investigation of polycrystalline diamond.* PhD thesis, PhD thesis, Institute for High Pressure Physics, USSR Academy of Sciences, 1971

D. Veysset, T. Pezeril, S. Kooi, A. Bulou, and K. A. Nelson. Laser-induced versus shock wave induced transformation of highly ordered pyrolytic graphite. *Applied Physics Letters*, 106(16):161902, 2015.
  doi.org/10.1063/1.4918929

J. F. Wacker. Noble gases in the diamond-free ureilite, ALHA 78019: The roles of shock and nebular processes. *Geochimica et Cosmochimica Acta*, 50(4):633–642, 1986.
  doi.org/10.1016/0016-7037(86)90112-2

I. Weber, A. Bischoff, and D. Weber. TEM investigations on the monomict ureilites Jalanash and Hammadah al Hamra 064. *Meteoritics & Planetary Science*, 38(1):145–156, 2003.
  doi.org/10.1111/j.1945-5100.2003.tb01051.x

K. Zhu, F. Moynier, M. Schiller, D. Wielandt, K. K. Larsen, E. M. van Kooten, J.-A. Barrat, and M. Bizzarro. Chromium isotopic constraints on the origin of the ureilite parent body. *The Astrophysical Journal*, 888(2):126, 2020.
  doi.org/10.3847/1538-4357/ab5af7

# 4 Shock-origin of a Microdiamond from a Ureilite Meteorite Derived from its Carbon Isotopic Composition

This manuscript is planned to be submitted to Nature Geoscience. OC and FN designed the study. OC, AB, and FN developed the methods. OC, AB, and FN collected XRD and Raman data. GB and SG developed the method to clean the diamond of graphite. Mass spectroscopy was performed and the data processed by ET.

All the authors discussed the data and agree on their interpretation. OC, AB, FB, MCD, GB, SG, and FN wrote the manuscript. All the co-authors contributed to the final polishing of the manuscript.

Microphotography was done by Matteo Chinellato, who is not an author of the paper but kindly contributed his photo laboratory.

Oliver CHRIST[1][*], Anna BARBARO[1], Giulia BRAGAGGIA[2], Silivia GROSS[2], Emilie Thomassot[3], Frank E. BRENKER[4], M. Chiara DOMENEGHETTI[5], and Fabrizio NESTOLA[1,2]

[1]Department of Geosciences, University of Padova, Via Gradenigo 6, 35131 Padova, Italy

[2]Department of Chemical Sciences, University of Padova, Via Francesco Marzolo 1, 35131 Padova, Italy

[3]3University of Lorraine, CNRS, CRPG, 15 Rue Notre Dame des Pauvres, 54500 Vanduvre-lès-Nancy, France

[4]Geoscience Institute, Goethe-University Frankfurt, Altenhöferallee 1, 60438 Frankfurt, Germany

[5]Department of Earth and Environmental Sciences, University of Pavia, Via A. Ferrata 1, I-27100 Pavia, Italy

*Corresponding author. E-mail: oliver.christ@phd.unipd.it

**Abstract** Carbon isotopic values for ureilitic carbon bearing material has only been reported in a few studies of which one dates to the 1970s. Since a commonly used method was the combustion method, a distinction between graphite and diamond is difficult and only two publications for pure ureilitic diamond and one for pure ureilitic graphite report reliable carbon isotopic data. Here, we report unprecedented carbon isotopic data for a very large (450 µm) single crystal diamond from the highly shocked (U-S6) and fine-grained ureilite NWA 6871, which resulted in $\delta^{13}C$ values of $-2.6\,‰$ to $-3.5\,‰$ ($\delta^{13}C_{mean} = -2.88 \pm 0.42\,‰$). Fine-grained ureilites are thought to have formed by recrystallisation of coarse-grained ureilites upon impact smelting. The impact might have led to a degassing of $^{12}C$ in form of a CO gas which might be the reason for heavier carbon isotopic signatures. X-ray diffraction revealed the presence of compressed graphite and stacking disordered diamond. These shock indicators, in combination with the relatively heavy $\delta^{13}C$ values and the overall shock features of NWA 6871, make it reasonable to assume that this large microdiamond was formed during the shock event which destroyed the ureilite parent body rather than deep inside of it.

## 4.1 Introduction

Diamond has been reported in different types of meteorites including chondrites, iron meteorites, and ureilites. While diamonds in chondrites represent presolar grains (Lewis et al., 1987; Ming and Anders, 1988), diamonds in iron meteorites are rare and have so far been reported in only a few meteorites, e.g., Canyon Diablo, where diamonds were most likely formed when the meteorite hit Earths surface (e.g., Vdovykin, 1973, and references therein). For ureilites, the process which led to diamonds is still discussed. Three major hypothesises have been proposed: (i) the formation inside a planetary body (Miyahara et al., 2015; Nabiei et al., 2018; Urey, 1956), (ii) the direct transformation from graphite to diamond upon shock (Barbaro et al., 2021, 2022; Christ et al., 2022; Hezel et al.,

2008; Lipschutz, 1964; Lorenz et al., 2019; Nakamuta and Aoki, 2000; Nakamuta and Toh, 2013; Nakamuta et al., 2016; Nestola et al., 2020) and (iii) crystal vapor deposition processes (Fukunaga et al., 1987; Tomkins et al., 2022). The direct transformation from graphite to diamond during a shock event is the most accepted one. However, recent studies claimed that ureilitic diamonds have formed by crystal fluid/vapor deposition (Tomkins et al., 2022) and that large ureilitic diamonds have formed inside a large planetary body (Miyahara et al., 2015; Nabiei et al., 2018).

Ureilites are ultramafic carbon-rich achondrites, which originate from the ureilite parent body (UPB) (Goodrich, 1992). The history of the UPB is characterised by various impact events which occurred in an early stage of our Solar System and destroyed the partially differentiated UPB and created multiple ureilite daughter bodies (Rai et al., 2020). During these impact events, high pressure and temperature regimes were reached which led to the direct transformation of graphite to diamond. Evidence for this direct transformation can be seen by X-ray diffraction (XRD) in form of compressed graphite (Nakamuta and Aoki, 2000) and/or diamond with stacking faults (Murri et al., 2019; Németh et al., 2014). Ureilitic diamond usually shows nanometric grainsizes, however, recent studies have shown that nanometric diamond coexists closely with microdiamond (Barbaro et al., 2021, 2022; Christ et al., 2022; Nestola et al., 2020) including a single crystal diamond with a size of up to $100\,\mu m$ its longest dimension (Nestola et al., 2020). However, apart from one single crystal microdiamond, ureilitic microdiamonds were always accompanied by nanographite and often by nanodiamonds forming carbon-aggregates which prevent an exact size estimation of the micrometric diamond. Ureilitic carbon isotopes have long been reported, but since pure ureilitic microdiamonds are very rare, carbon isotopes of microdiamonds have not been reported yet. The literature shows that an often-used technique to analyse ureilitic carbon phases is the combustion method (Barrat et al., 2017; Downes et al., 2015; Grady et al., 1985; Hudon et al., 2004; Russell et al., 1993). Combustion temperatures for graphite and diamond however, over-

lap between $600\,°C$ and $900\,°C$ (Grady et al., 1985) and hence, assigning specific $\delta^{13}C$ values to graphite or diamond and therefore comparisons between these data sets are difficult. For example, the combustion method showed a main release $650\,°C$ and, for some samples, a second minor release at $\sim\!900\,°C$ and $\sim\!1000\,°C$ with almost identical isotopic composition (Downes et al., 2015). This second release was interpreted as a release of either highly crystalline graphite or genetically related diamond (Downes et al., 2015), which shows that a distinction between graphite and diamond is almost impossible.

In the literature there are only two publications which report carbon isotopic values of ureilitic diamond: a pure diamond fraction from the Novo Urei meteorite (Vdovykin, 1970) and diamond FIB cuts from the Almahata Sitta MS-170 fragment (Miyahara et al., 2015). In the case of Novo Urei, the pure diamond fraction was characterised by XRD, however, this publication is from 1970 where instruments were not as sensitive as today which is why it is reasonable to assume that graphite might not have been detected depending on the percentage of diamond to graphite. The $\delta^{13}C$ value of the diamond fraction was reported to be $-5.7\,‰$.

The diamond from MS-170 on the other hand has been characterised by electron backscatter diffraction and transmission electron microscopy (Miyahara et al., 2015). Although the authors report $\delta^{13}C$ values for diamond, the large unique diamond (Miyahara et al., 2015) has already been questioned (Nestola et al., 2020) and the selected area electron diffraction images show that diamond is indeed in very close association with graphite, which might yield to a mixture of $\delta^{13}C$ values of graphite and diamond. And in fact, the $\delta^{13}C$ values of diamond and graphite are very similar: diamond grains showed $\delta^{13}C$ value of $-4 \pm 0.8\,‰$, while fine-grained graphite between diamond grains showed $\delta^{13}C$ value values of $-5.7 \pm 1.4\,‰$. Another large diamond crystal showed $\delta^{13}C$ value of $-5.7 \pm 0.5\,‰$ which were identical to the surrounding graphite (Miyahara et al., 2015).

Recently, pure graphite has also been analysed in regard of its carbon isotopic com-

position (Storz et al., 2021). The authors measured graphite from nineteen different ureilites and found a distinction between $\delta^{13}$C values from graphite in coarse- and fine-grained ureilites. Graphite in coarse-grained ureilites shows a mean $\delta^{13}$C values values of $-5.29\,$‰, which are homogeneous within a specific sample and are in good agreement with the hyperbolae correlation of $\delta^{13}$C values with Fe/Mg ratios of olivine cores (Barrat et al., 2017). In comparison, graphite in fine-grained ureilites shows a heavier mean $\delta^{13}$C of $1.94\,$‰. However, values within one fine grained sample may vary. For example, the authors report $\delta^{13}$C for graphite in MS 20 which range between $-9.29\,$‰ and $4.09\,$‰.

Here we present a new almost non-destructive approach. A carbon aggregate was cut out of the host ureilite, characterised by XRD. The measurement revealed the presence of a large portion of microdiamond accompanied by nanodiamond and graphite. The aggregate was cleaned from matrix material in an ultrasonic ethanol bath and graphite by a hydrothermal approach. The remaining material was again characterised by XRD to ensure that graphite was entirely removed, and that diamond was the only remaining carbon-containing phase. The cleaning process resulted in a microdiamond which has a size of up to $450\,\mu$m and therefore exceeds all previously ureilitic diamonds reported in literature of which grain sizes were reported (Miyahara et al., 2015; Nestola et al., 2020). The diamond was analysed by large geometry-secondary ion mass spectrometry (LG-SIMS) in regard of its carbon isotopic content. Hence, this study provides the very first thorough analysis of a large microdiamond originating from a ureilite. By combining multiple analytical methods, we show that this microdiamond was formed during the shock event which destroyed the UPB and not deep inside of it.

## 4.2 Samples, Preparation and Methods

This study was conducted on a diamond from the Northwest Africa (NWA) 6871 ureilite, which is a highly shocked meteorite (U-S6) (Stöffler et al., 2018). NWA 6871 consists of olivine aggregates with subhedral forms. The space between the olivine aggregates is

filled with opaque material composed of carbon aggregates, metallic phases, and sulfides. The complete petrographic description of this ureilitic fragment is reported in Christ et al. (2022).

The diamond which was analysed was cut out of the bulk sample of NWA 6871, glued on top of a glass fibre (Figure 4.1), and analysed by a multimethodological approach.

Analyses included multiple XRD measurements using a Rigaku Oxford Diffraction SuperNova single-crystal diffractometer at the Department of Geosciences, University of Padua. The instrument is equipped with a 200K Dectris detector and operates with a micro-source MoK$\alpha$ X-ray radiation at a wavelength of 0.710 73 Å (X-ray beam diameter was 0.120 mm, the sample-to-detector distance 69 mm). The diamond was measured in a range of 1360° with a step size of 1° around the $\phi$-axis and an acquisition time of 100 s per frame.

After a first characterization by X-ray diffraction, the diamond was put into a subsonic ethanol bath to eliminate the remaining matrix material. It was measured a second time to ensure that the cleaning process was successful. Subsequentially, a chemical cleaning procedure based on a hydrothermal process was optimised at the Department of Chemical Sciences, University of Padua, to remove remaining graphite from the diamond. A combination of high temperature and pressure in a sealed vessel partially filled with a highly aggressive solution was applied. In particular, 18 ml of a solution of $HNO_3$ 65% and $H_2SO_4$ 96% (1:2 molar ratio) was added in a 150 ml PTFE cup, placed in a Berghof stainless steel Acid-Digestion Bomb (filling ratio of 12%), tightly sealed and heated at 250 °C for 48 hours. After cooling at room temperature, the diamond was recovered, washed several times with deionized water and separated by centrifugation. A third and last XRD measurement was done to ensure that also this cleaning process was successful.

After XRD, micro-Raman spectroscopy (MRS) was performed to obtain the peak centre and the full width half maximum (FWHM) of the cleaned microdiamond. MRS was performed at the Department of Geosciences, University of Padua, where a WITec

99

alpha300 R spectrometer ($\lambda = 532\,\text{nm}$, grating $= 300\,\text{g}\,\text{mm}^{-1}$) was used. The laser power was set to $10\,\text{mW}$ and each measurement was conducted with 5 accumulations and an exposure time of $0.5\,\text{s}$.

Subsequentially, the diamond was detached from the glass fiber and put into indium paste to be analysed by a CAMECA 1280 Large-Geometry Secondary Ion Mass Spectrometer (LG-SIMS) at the Centre de Recherches Pétrographiques et Géochimiques (CRPG), Nancy, France. Cleaned diamond grains were put into Indium-paste (see Figure 4.4). Measurement conditions. The results are reported as $\delta^{13}$C, the used standard was Vienna PeeDee Belemnite (VPDB):

$$\delta^{13}\text{C}(\text{‰}) = \left( \frac{\left(\frac{^{13}\text{C}}{^{12}\text{C}}\right)_{sample}}{\left(\frac{^{13}\text{C}}{^{12}\text{C}}\right)_{VPDB}} - 1 \right) * 10^3 \tag{4.1}$$

## 4.3 Results

Optical microscopy shows that the sample has an irregular shape (Figure 4.1). X-ray diffraction revealed the presence of diffraction rings together with unusually large diffraction spots at $d$-spacings of $2.06\,\text{Å}$, $1.26\,\text{Å}$, and $1.07\,\text{Å}$ (Figure 4.2). In addition, a characteristic shoulder at the highest diamond peak ($d$-spacing of $2.06\,\text{Å}$) can be seen in the corresponding diffractogram, which indicates the presence of stacking disordered diamond (Murri et al., 2019; Németh et al., 2014). Additional phases can be seen in peaks of graphite ($d$-spacing of $3.34\,\text{Å}$), iron ($d$-spacing of $1.17\,\text{Å}$ and $1.43\,\text{Å}$), goethite ($d$-spacing of $4.18\,\text{Å}$) and forsteritic olivine ($d$-spacing of $2.46\,\text{Å}$). In comparison to diamond, all other phases show relatively low intensities. After the ultrasonic bath in ethanol, the goethite peak at $d$-spacing of $4.18\,\text{Å}$ and forsterite peak at $d$-spacing of $2.46\,\text{Å}$ lost intensity (Figure 4.2 c).

X-ray diffraction was repeated after the sample was hydrothermally treated to eliminate the graphite. The corresponding diffractogram can be seen in blue in Figure 4.2 (c).

Here, the graphite diffraction peak at $d$-spacing of $3.34\,\text{Å}$ is absent which demonstrates that graphite was removed from the sample. The elimination of graphite is also shown from Figure 4.2 (a) to (b) where the graphite ring at $d$-spacing of $3.34\,\text{Å}$ is lost. Hence, after cleaning the sample of residing matrix material and graphite, the diffractogram and diffraction image show only diamond, minor forsterite, and iron. However, most of the sample consists solely of diamond, which occurs in two different grainsizes. From the rings at $d$-spacings of $1.26\,\text{Å}$ and $1.07\,\text{Å}$ in the diffractograms, we calculated a crystallite size of $\sim5\,\text{nm}$ using the Scherrer equation (Scherrer, 1912).

MRS measurements were conducted on the surface of the cleaned diamond. We collected nine point analyses, which resulted in an average D-band position at $1330 \pm 2.4\,\text{cm}^{-1}$ and an average FWHM of $33 \pm 13.8\,\text{cm}^{-1}$. D-band positions and FHWMs are summarized in Table 4.1.

Table 4.1: MRS data from the large diamond found in NWA 6871 after the cleaning process.

| Diamond band position in $\text{cm}^{-1}$ | FWHM in $\text{cm}^{-1}$ |
|:---:|:---:|
| 1329 | 35 |
| 1328 | 33 |
| 1332 | 37 |
| 1329 | 34 |
| 1330 | 31 |
| 1328 | 23 |
| 1335 | 65 |
| 1328 | 15 |
| 1331 | 27 |

LG-SIMS measurements were conducted on the diamond. The analysed diamond is the

450 µm sized diamond from Figure 4.1 (Dia 1 in Figure 4.4). Four measurement points were conducted which showed $\delta^{13}$C values of $-2.7\,‰$, $-2.7\,‰$, $-2.6\,‰$ and $-3.5\,‰$ ($\delta^{13}$C$_{\mathrm{mean}} = -2.88 \pm 0.42\,‰$).
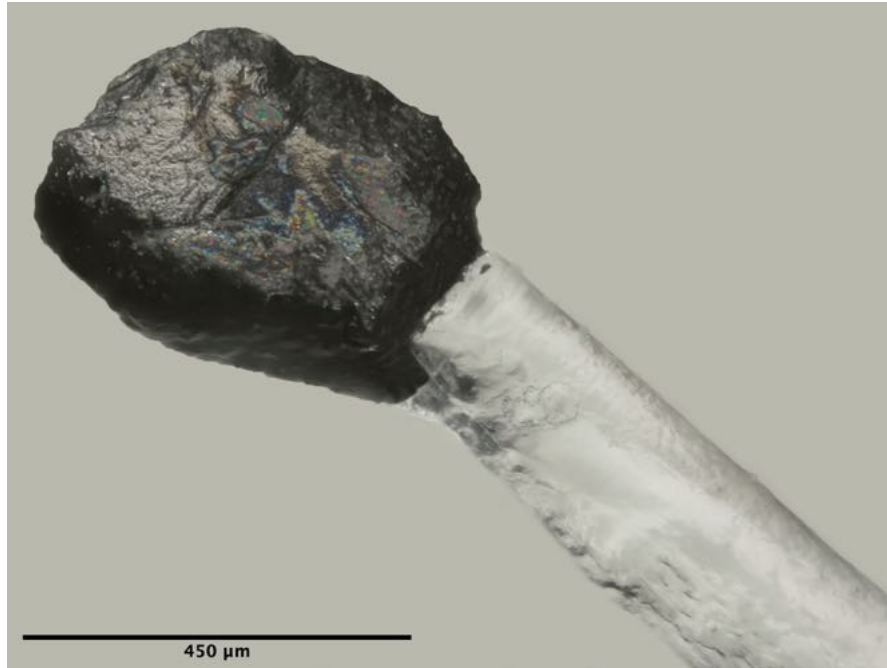


Figure 4.1: Microphotography of the diamond from NWA 6871 after the cleaning process glued on top of a glass fibre (Microphotograph: Matteo Chinellato).
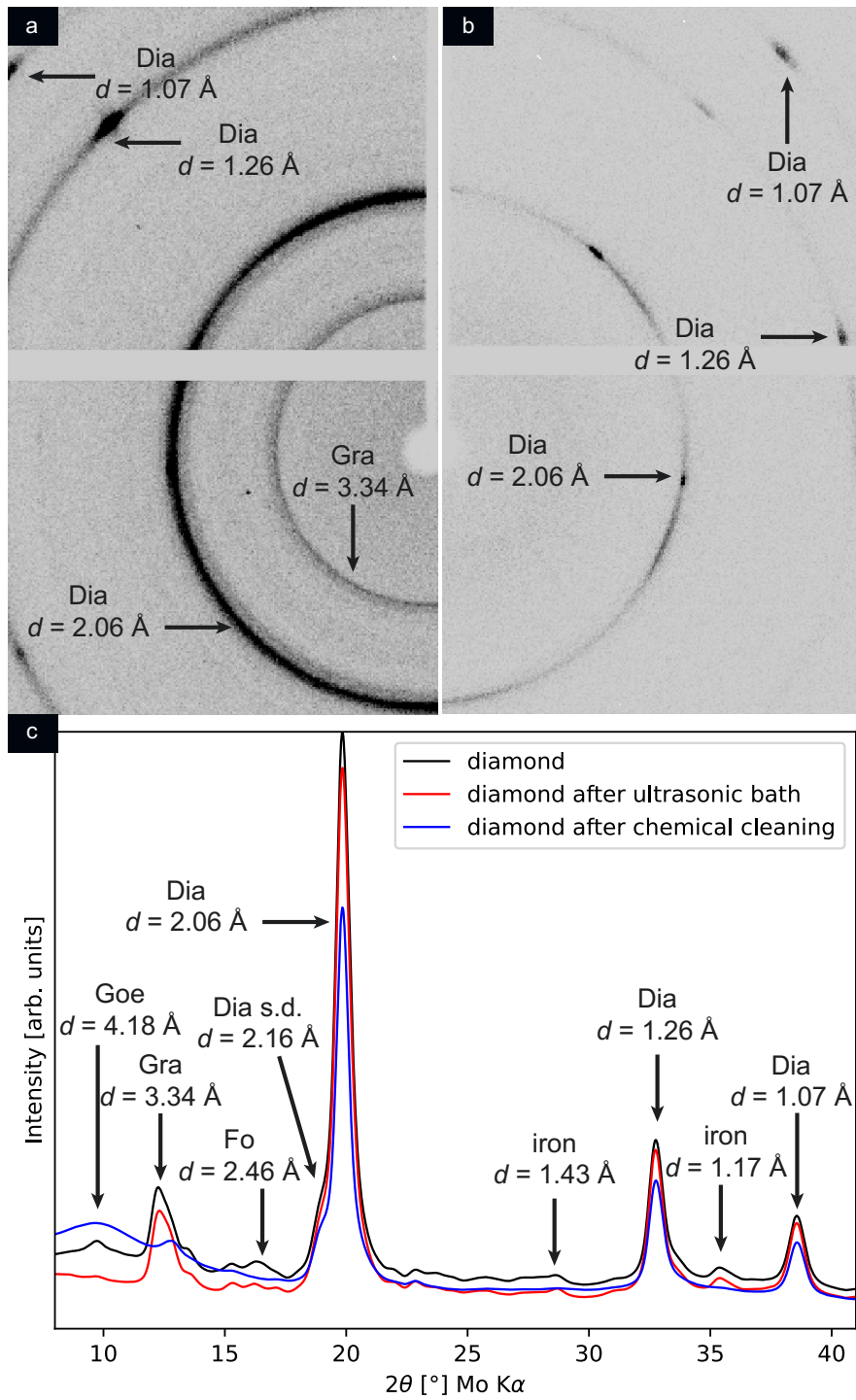
Figure 4.2: Caption on next page.

Figure 4.2: Documentation of the hydrothermal cleaning process (a) Initial, diffraction image of the sample showing both rings and diffraction spots. Here, the large single crystal diffraction spots for diamond are most noteworthy. (b) Diffraction image of the diamond after the cleaning hydrothermal process. The graphite signal at d-spacing 3.34 Å is lost as well as some polycrystalline material as shown by the lower intensities of the rings at d-spacings 2.06 Å and 1.26 Å. (c) The initial diffractogram (black), the diffractogram after the ultrasonic bath (red), and the diffractogram after the chemical hydrothermal cleaning (blue). To provide a better readability, not all small peaks have been labelled. Diffraction rings for iron and forsterite are not visible in (a) and (b) due to their low intensities and the contrast settings of the diffraction images. However, they can be seen in (c). Mineral abbreviations: Dia = diamond, s.d.-Dia = stacking disordered diamond, Gra = graphite, Goe = goethite, Fo = forsterite, Iron = metallic iron/Fe-Ni phases.

## 4.4 Discussion

NWA 6871 is a highly shocked ureilite (US6) which experienced pressures of up to 6064 GPa (Christ et al., 2022; Stöffler et al., 2018). During the shock event which destroyed the parent body, diamond was formed directly from graphite due to the high temperature and pressures (Christ et al., 2022). Previously analysed diamonds in ureilites showed grain sizes of several tens of micrometres up to a size of $\sim$100 µm (Nestola et al., 2020). The diamond, which was analysed here, is four times larger and has been cleaned of any accompanying carbon phases, i.e., graphite. The effectiveness of the hydrothermal cleaning process was carefully checked by XRD (Figure 4.2). Usually, the method is used to clean larger gem diamonds, but as we have shown it is also capable to clean smaller diamond samples from graphite.

Mineralogically, our sample is very similar to carbon aggregates from NWA 7983 (Nestola et al., 2020), Kenna (Barbaro et al., 2021), Yamato-74123 (Barbaro et al., 2022) and other diamonds from NWA 6871 (Christ et al., 2022). These similarities, as seen by the shock indicator lonsdaleite and compressed graphite, indicate that also this large diamond was formed during a shock event. Recently, the occurrence of large ureilitic diamonds had been linked to all discussed formation scenarios: the formation

deep inside a planetary body (Miyahara et al., 2015; Nabiei et al., 2018), the formation by shock (Barbaro et al., 2021, 2022; Christ et al., 2022; Nestola et al., 2020) and the formation from crystal fluid/vapor deposition (Tomkins et al., 2022). The diamonds which were thought to have formed deep inside a planetary body (Miyahara et al., 2015; Németh et al., 2014) however, have never been analysed by XRD. Hence, possible crystallographic shock indicators have never been reported.

The very large ureilitic diamond was analysed in regard of its carbon isotopic composition after being cleaned from graphite. This procedure represents the third carbon isotopic analysis collected solely on ureilitic diamond and the very first on a ureilitic microdiamond. Figure 4.2 a) and b) clearly show large single crystal diffraction spots for this diamond before and after the chemical cleaning procedure, while Figure 4.2 c) shows the powder diffraction pattern of the initial uncleaned sample (in black), after an ultrasonic bath in ethanol (in red), and finally after the chemical hydrothermal cleaning procedure (in blue). The LG-SIMS measurements resulted in an average $\delta^{13}$C of –2.88 $\pm$ 0.42 ‰. A comparison to literature data is rather difficult. Most of the available data originates either from conference abstracts or from publications in which the combustion method was used where ureilitic graphite and diamond were analysed together (Barrat et al., 2017; Downes et al., 2015; Grady et al., 1985; Grady and Pillinger, 1986; Hudon et al., 2004; Russell et al., 1996; Smith et al., 2001). Only two publications report reliable isolated diamond grains. Vdovykin (1970) reported a mean $\delta^{13}$C of $-5.7$‰ for a pure diamond fraction (Vdovykin, 1970), which was characterised by XRD to demonstrate that this investigated sample consisted entirely of diamond. Further diamond grains were analysed by Miyahara et al. (2015) who report $\delta^{13}$C values of two large diamond grains of –4.1 $\pm$ 0.8 ‰ and –5.7 $\pm$ 0.5 ‰ (Miyahara et al., 2015). These authors also measured surrounding graphite which showed a $\delta^{13}$C of –5.7 $\pm$ 1.4 ‰. Our data from NWA 6871 is similar to these values as ureilitic diamonds seem to have heavier carbon isotopic signatures compared to bulk carbon isotopic measurements (see Table 4.2 and

Figure 4.3).

Table 4.2: Available $\delta^{13}$C values of graphite and diamond in ureilites from literature and this study. Bulk carbon isotopic measurements were excluded as it is not possible to distinguish between graphite and diamond. Literature where a distinction between graphite and diamond were excluded, as well as studies where diamond was reported but no sample characterisation.

| Reference | Sample | Analysed carbon phase | Method | $\delta^{13}$C |
|---|---|---|---|---|
| Vdovykin (1970) | Novo Urei | total carbon and diamond graphite intergrowths | not avail- able | $-7.1\,‰$ and $-6.31\,‰$ |
| | | pure diamond | | $-5.7\,‰$ |
| Miyahara et al., (2015) | MS-170 | diamond FIB blocks | nano-SIMS | $-4.1\,‰$ |
| | | | | $-5.6\,‰$ |
| | | fine grained graphite | | $-5.7\,‰$ |
| Storz et al., (2021) | 19 ureilites | Graphite from coarse grained ureilites | nano-SIMS | $-9.2\,‰$ to $-0.1\,‰$ (mean $-5.29\,‰$) |
| | | Graphite from fine grained ureilites | | Up to $+10.4\,‰$ (mean $+1.94\,‰$) |
| This study | NWA 6871 | large diamond | LG-SIMS | $-2.6\,‰$ to $-3.5\,‰$ (mean $-2.88\,‰$) |

As recently demonstrated, the occurrence of nanographite, nanodiamond and microdiamond in ureilites can be ascribed to the shock event that destroyed the UPB (Barbaro et al., 2021, 2022; Christ et al., 2022; Nestola et al., 2020), a process which affected the carbon precursor material present in the UPB and formed the carbon mixture that can be observed in ureilites nowadays. Among the scientific community, carbonaceous chondrites (CC) are considered as the precursor material of the UPB (Rubin, 1988). During the shock event(s), the CC material was affected by the increase of pressure and temperature, underwent partial melting, and was processed which might have led to fractionation of carbon isotopes. As products of the same event, we would expect to have similarities between the $\delta^{13}$C of graphite and diamond as variations would be very small (Maruoka et al., 2003). Storz et al. (2021) report that graphite from fine-grained ureilites shows heavier carbon isotopic compositions and assume that fine-grained ure-

ilites are the result of recrystallisation of coarse-grained ureilites which were affected by impact smelting (Horstmann et al., 2014; Warren and Rubin, 2010). Following Storz et al. (2021), primitive graphite was the carbon precursor of which during the impact smelting on the UPB a CO gas was produced which led to a degassing effect during which a mass-dependent fractionation took place leading to a larger loss of $^{12}$C than $^{13}$C and resulting in heavier carbon isotopic signatures for graphite. This would also affect the carbon isotopic content of shock formed ureilitic diamond and could explain the relatively heavy $\delta^{13}$C value of our ureilitic microdiamond.

The combination of the overall shocked appearance of NWA 6871, the crystallographic shock indicators of our microdiamond (compressed graphite before the cleaning and stacking faults in diamond) make this assumption even more probable. Further, this would imply that a large UPB cannot be interfered from the presence of large diamonds in ureilites.
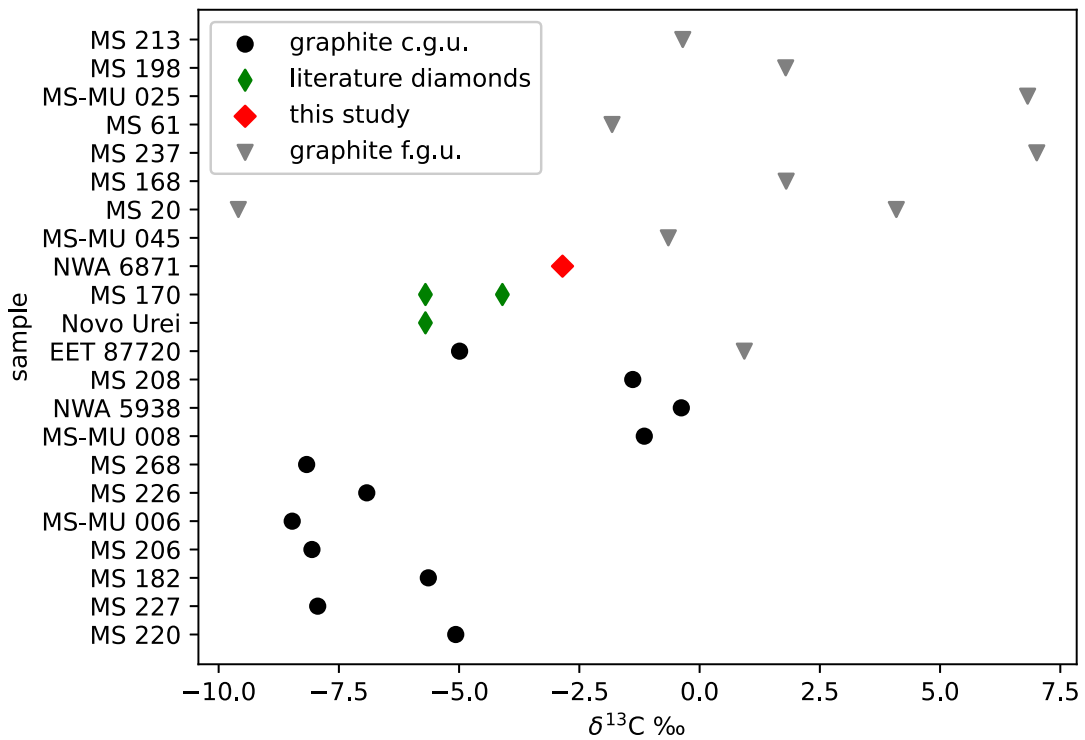
Figure 4.3: Scatter plot of $\delta^{13}$C values graphite from coarse and fine grained ureilites (c.g.u. and f.g.u.) (Storz et al., 2021), ureilitic diamond (Miyahara et al., 2015; Vdovykin, 1970) and this study.

## 4.5 Conclusions

The 450 µm sized diamond from NWA 6871 is the largest ureilitic diamond reported so far and the only ureilitic microdiamond which was analysed in regard of its carbon isotopic composition. We demonstrated that it is possible to clean larger ureilitic diamonds of graphite using a method which is usually used to clean larger gem diamonds. XRD showed that graphite is entirely lost during this cleaning process which enables an almost non-destructive carbon isotopic measurement in-situ solely on ureilitic diamond. However, the diamond needs to have an almost flat surface to ensure reliable isotope measurements. The $\delta^{13}$C values of our large 450 µm sized diamond range from $-2.6$ ‰ to $-3.5$ ‰ (mean $\delta^{13}$C $= -2.88 \pm 0.42$ ‰, $n = 4$). This value is consistent with the few

$\delta^{13}$C values reported in literature for ureilitic diamonds: $\delta^{13}$C $= -5.7\,‰$, $-5.7\,‰$, and $-4.1\,‰$. Generally, ureilitic diamonds seem to show heavier carbon isotopic compositions like the $\delta^{13}$C group of graphite from fine-grained. Fine-grained ureilites, as NWA 6871, can be interpreted as the product of coarse-grained ureilites which experienced recrystallisation during the shock event which destroyed the UPB. Combining XRD and LG-SIMS data, it is reasonable to assume that this large microdiamond was not formed deep inside the UPB but directly from graphite during the shock event which destroyed it.

## 4.6 Supplementary Information
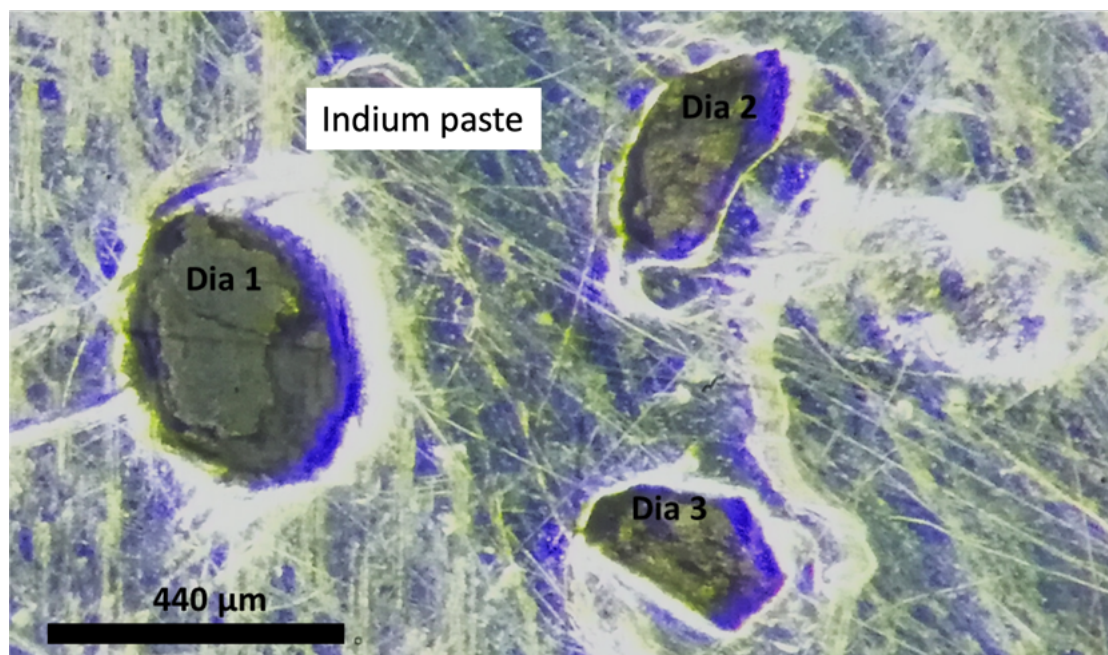


Figure 4.4: Three diamond grains put into Indium paste.

## 4.7 References

A. Barbaro, M. C. Domeneghetti, K. D. Litasov, L. Ferrière, L. Pittarello, O. Christ, S. Lorenzon, M. Alvaro, and F. Nestola. Origin of micrometer-sized impact diamonds in ureilites by catalytic growth involving Fe-Ni-silicide: The example of Kenna meteorite. *Geochimica et Cosmochimica Acta*, 309:286–298, 2021.
  doi.org/10.1016/j.gca.2021.06.022

A. Barbaro, F. Nestola, L. Pittarello, L. Ferrière, M. Murri, K. D. Litasov, O. Christ, M. Alvaro, and M. C. Domeneghetti. Characterization of carbon phases in Yamato 74123 ureilite to constrain the meteorite shock history. *American Mineralogist: Journal of Earth and Planetary Materials*, 107(3):377–384, 2022.
  doi.org/10.1016/j.gca.2021.06.022

J.-A. Barrat, P. Sansjofre, A. Yamaguchi, R. C. Greenwood, and P. Gillet. Carbon isotopic variation in ureilites: Evidence for an early, volatile-rich Inner Solar System. *Earth and Planetary Science Letters*, 478:143–149, 2017.
  doi.org/10.1016/j.epsl.2017.08.039

O. Christ, A. Barbaro, F. E. Brenker, P. Nimis, D. Novella, M. C. Domeneghetti, and

F. Nestola. Shock degree and graphite geothermometry in ureilites NWA 6871 and NWA 3140. *Meteoritics & Planetary Science*, 57(10):1861–1878, 2022.
doi.org/10.1111/maps.13907

H. Downes, F. Abernethy, C. Smith, A. Ross, A. Verchovsky, M. Grady, P. Jenniskens, and M. Shaddad. Isotopic composition of carbon and nitrogen in ureilitic fragments of the Almahata Sitta meteorite. *Meteoritics & Planetary Science*, 50(2):255–272, 2015.
doi.org/10.1111/maps.12413

K. Fukunaga, J.-i. Matsuda, K. Nagao, M. Miyamoto, and K. Ito. Noble-gas enrichment in vapour-growth diamonds and the origin of diamonds in ureilites. *Nature*, 328(6126): 141–143, 1987.
doi.org/10.1038/328141a0

C. A. Goodrich. Ureilites: A critical review. *Meteoritics*, 27(4):327–352, 1992.
doi.org/10.1111/j.1945-5100.1992.tb00215.x

M. Grady, I. Wright, P. Swart, and C. Pillinger. The carbon and nitrogen isotopic composition of ureilites: Implications for their genesis. *Geochimica et Cosmochimica Acta*, 49(4):903–915, 1985.
doi.org/10.1016/0016-7037(85)90306-0

M. M. Grady and C. Pillinger. The ALHA 82130 ureilite: Its light element stable isotope composition and relationship to other ureilites. In *49th Annual Meeting of the Meteoritical Society*, 1986

D. C. Hezel, L. Dubrovinsky, L. Nasdala, J. Cauzid, A. Simionovici, M. Gellissen, and T. SCHÖNBECK. In situ micro-Raman and X-ray diffraction study of diamonds and petrology of the new ureilite UAE 001 from the United Arab Emirates. *Meteoritics & Planetary Science*, 43(7):1127–1136, 2008.
doi.org/10.1111/j.1945-5100.2008.tb01117.x

M. Horstmann, M. Humayun, M. Fischer-Gödde, A. Bischoff, and M. Weyrauch. Si-bearing metal and niningerite in Almahata Sitta fine-grained ureilites and insights into the diversity of metal on the ureilite parent body. *Meteoritics & Planetary Science*, 49(10):1948–1977, 2014.
doi.org/10.1111/maps.12370

P. Hudon, C. Romanek, L. Paddock, and D. Mittlefehldt. Evolution of the ureilite parent body. In *35th Lunar and Planetary Science Conference*, 2004

R. S. Lewis, T. Ming, J. F. Wacker, E. Anders, and E. Steel. Interstellar diamonds in meteorites. *Nature*, 326(6109):160–162, 1987.
doi.org/10.1038/326160a0

M. E. Lipschutz. Origin of diamonds in the ureilites. *Science*, 143(3613):1431–1434, 1964.
doi.org/10.1126/science.143.3613.1431.b

C. Lorenz, A. Shiryaev, I. Vlasov, and S. Borisovsky. Metamorphism of four desert ureilites and luminescence spectroscopy of defects in ureilitic diamonds. *Meteoritics & Planetary Science*, 54(6):1197–1214, 2019.

  doi doi.org/10.1111/maps.13274

T. Maruoka, C. Koeberl, J.-i. Matsuda, and Y. Syono. Carbon isotope fractionation between graphite and diamond during shock experiments. *Meteoritics & Planetary Science*, 38(8):1255–1262, 2003.

  doi doi.org/10.1111/j.1945-5100.2003.tb00311.x

T. Ming and E. Anders. Isotopic anomalies of Ne, Xe, and C in meteorites. II. Interstellar diamond and SiC: Carriers of exotic noble gases. *Geochimica et Cosmochimica Acta*, 52(5):1235–1244, 1988.

  doi doi.org/10.1016/0016-7037(88)90277-3

M. Miyahara, E. Ohtani, A. El Goresy, Y. Lin, L. Feng, J.-C. Zhang, P. Gillet, T. Nagase, J. Muto, and M. Nishijima. Unique large diamonds in a ureilite from Almahata Sitta 2008 TC$_3$ asteroid. *Geochimica et Cosmochimica Acta*, 163:14–26, 2015.

  doi doi.org/10.1016/j.gca.2015.04.035

M. Murri, R. L. Smith, K. McColl, M. Hart, M. Alvaro, A. P. Jones, P. Németh, C. G. Salzmann, F. Corà, M. C. Domeneghetti, et al. Quantifying hexagonal stacking in diamond. *Scientific reports*, 9(1):1–8, 2019.

  doi doi.org/10.1038/s41598-019-46556-3

F. Nabiei, J. Badro, T. Dennenwaldt, E. Oveisi, M. Cantoni, C. Hébert, A. El Goresy, J.-A. Barrat, and P. Gillet. A large planetary body inferred from diamond inclusions in a ureilite meteorite. *Nature Communications*, 9(1):1–6, 2018.

  doi doi.org/10.1038/s41467-018-03808-6

Y. Nakamuta and Y. Aoki. Mineralogical evidence for the origin of diamond in ureilites. *Meteoritics & Planetary Science*, 35(3):487–493, 2000.

  doi doi.org/10.1111/j.1945-5100.2000.tb01430.x

Y. Nakamuta and S. Toh. Transformation of graphite to lonsdaleite and diamond in the Goalpara ureilite directly observed by TEM. *American Mineralogist*, 98(4):574–581, 2013.

  doi doi.org/10.2138/am.2013.4341

Y. Nakamuta, F. Kitajima, and K. Shimada. In situ observation, X–ray diffraction and Raman analyses of carbon minerals in ureilites: Origin and formation mechanisms of diamond in ureilites. *Journal of Mineralogical and Petrological Sciences*, 111(4): 252–269, 2016.

  doi doi.org/10.2465/jmps.150906

P. Németh, L. A. Garvie, T. Aoki, N. Dubrovinskaia, L. Dubrovinsky, and P. R. Buseck. Lonsdaleite is faulted and twinned cubic diamond and does not exist as a discrete

material. *Nature Communications*, 5(1):1–5, 2014.
doi  doi.org/10.1038/ncomms6447

F. Nestola, C. A. Goodrich, M. Morana, A. Barbaro, R. S. Jakubek, O. Christ, F. E. Brenker, M. C. Domeneghetti, M. C. Dalconi, M. Alvaro, et al. Impact shock origin of diamonds in ureilite meteorites. *Proceedings of the National Academy of Sciences*, 117(41):25310–25318, 2020.
doi  doi.org/10.1073/pnas.1919067117

N. Rai, H. Downes, and C. Smith. Ureilite meteorites provide a new model of early planetesimal formation and destruction. *Geochemical Perspectives Letters*, 14:20–25, 2020.
doi  doi.org/10.7185/geochemlet.2018

A. E. Rubin. Formation of ureilites by impact-melting of carbonaceous chondritic material. *Meteoritics*, 23(4):333–337, 1988.
doi  doi.org/10.1111/j.1945-5100.1988.tb00918.x

S. S. Russell, J. W. Arden, and C. Pillinger. A carbon and nitrogen isotope study of diamond from primitive chondrites. *Meteoritics & Planetary Science*, 31(3):343–355, 1996.
doi  doi.org/10.1111/j.1945-5100.1996.tb02071.x

S. Russell, J. Arden, I. Franchi, and C. Pillinger. A carbon and nitrogen isotope study of carbonaceous vein material in ureilite meteorites. In *24th Lunar and Planetary Science Conference*, 1993

P. Scherrer. Bestimmung der inneren Struktur und der Größe von Kolloidteilchen mittels Röntgenstrahlen. In *Kolloidchemie Ein Lehrbuch*, pages 387–409. Springer, 1912.
doi  doi.org/10.1007/978-3-662-33915-2_7

C. Smith, I. Franchi, I. Wright, M. Grady, and C. Pillinger. New data on carbon isotopic compositions of some ureilites. In *32nd Lunar and Planetary Science Conference*, 2001

D. Stöffler, C. Hamann, and K. Metzler. Shock metamorphism of planetary silicate rocks and sediments: Proposal for an updated classification system. *Meteoritics & Planetary Science*, 53(1):5–49, 2018.
doi  doi.org/10.1111/maps.12912

J. Storz, T. Ludwig, A. Bischoff, W. H. Schwarz, and M. Trieloff. Graphite in ureilites, enstatite chondrites, and unique clasts in ordinary chondrites–insights from the carbon-isotope composition. *Geochimica et Cosmochimica Acta*, 307:86–104, 2021.
doi  doi.org/10.1016/j.gca.2021.05.028

A. G. Tomkins, N. C. Wilson, C. MacRae, A. Salek, M. R. Field, H. E. Brand, A. D. Langendam, N. R. Stephen, A. Torpy, Z. Pintér, et al. Sequential lonsdaleite to diamond formation in ureilite meteorites via in situ chemical fluid/vapor deposition.

*Proceedings of the National Academy of Sciences*, 119(38), 2022.
doi.org/10.1073/pnas.22088141

H. C. Urey. Diamonds, Meteorites, and the Origin of the Solar System. *The Astrophysical Journal*, 124:623, 1956

G. Vdovykin. The Canyon Diablo meteorite. *Space Science Reviews*, 14(6), jul 1973.
doi.org/10.1007/bf00224776

G. Vdovykin. Ureilites. *Space Science Reviews*, 10(4):483–510, 1970

P. H. Warren and A. E. Rubin. Pyroxene-selective impact smelting in ureilites. *Geochimica et Cosmochimica Acta*, 74(17):5109–5133, 2010.
doi.org/10.1016/j.gca.2010.05.026

# 5 Micro X-ray Computed Tomography

Micro X-ray CT was performed at ELETTRA, Trieste. However, the conducted measurement was just a test to see whether our diamonds are large enough to use micro X-ray CT or if they are too small and we have to use nano X-ray CT. A first test was conducted using the TomoLab instrument which guarantees a focal spot size of at least $5\,\mu m$. The instrument operates in a voltage range of $40$–$130\,kV$ and with a maximum power of $39\,W$. As a detector a water cooled CCD camera is used. However, as the investigated diamond was of relatively small size ($\sim 200\,\mu m$), see Fig. 5.1 and the resolution of the TomoLab instrument was not sufficient to produce useful 3D reconstructions. Therefore it was decided to use one of the beamlines. Fortunately, we could use the SYRMEP (SYnchrotron Radiation for MEdical Physics) beamline. However, as the name suggests, this beamline is usually used for different samples and has already been set up for a different experiment. This led to non-optimal measurement conditions for our sample which could not be changed that day but despite the non-optimal measurement conditions it was possible to produce a relatively good 3D reconstructions, see Figure 5.2.
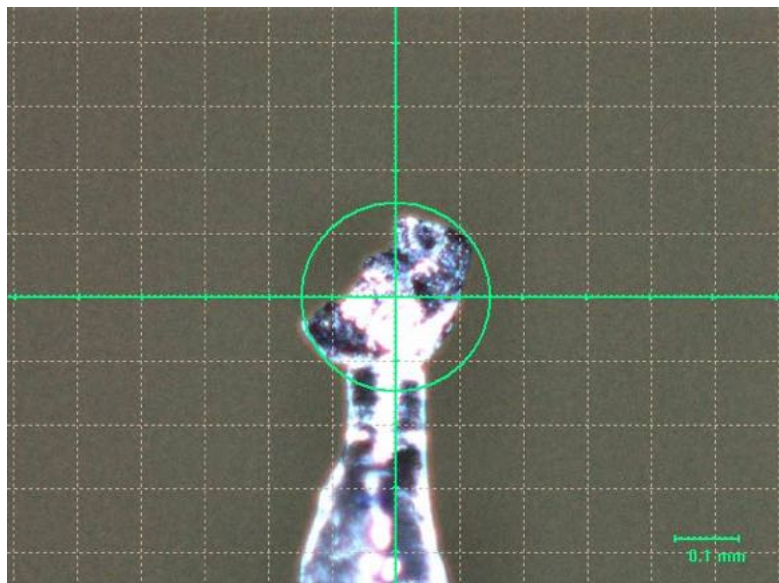
Figure 5.1: Photo of sample NWA6871_xx3, which was analysed by micro X-ray CT. The image was taken with the camera of the XRD instrument at our department.
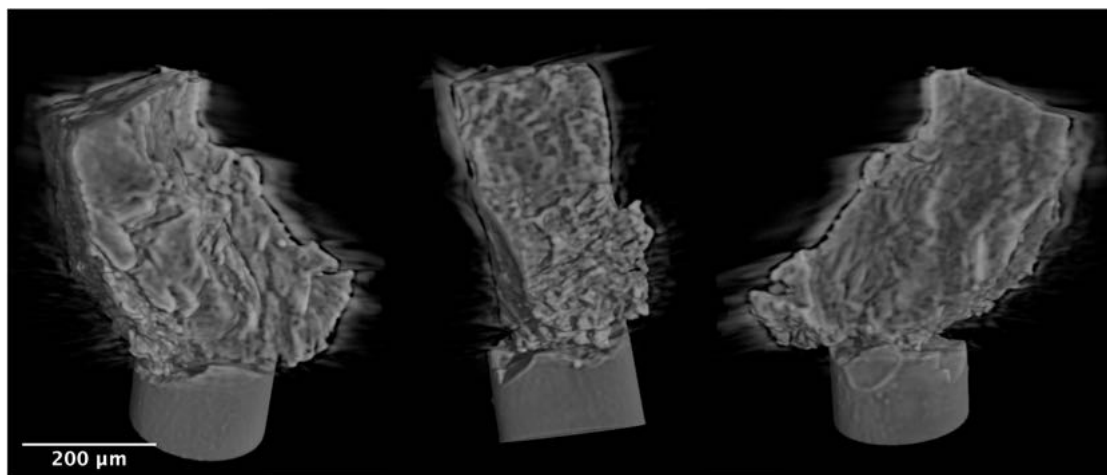


Figure 5.2: 3D reconstruction of NWA6871_xx3 showing the sample on top of the glass fibre from three perspectives. Due to the suboptimal measurement conditions many artefacts are present.

Slicing through the 3D reconstruction revealed the presence of either cracks or segments in the interior of the diamond as well as regions of high absorbance which might be remnants of the metallic catalyst which lowered the $P, T$ conditions needed for the

116

direct transformation of graphite to diamond, see Figure 5.3.
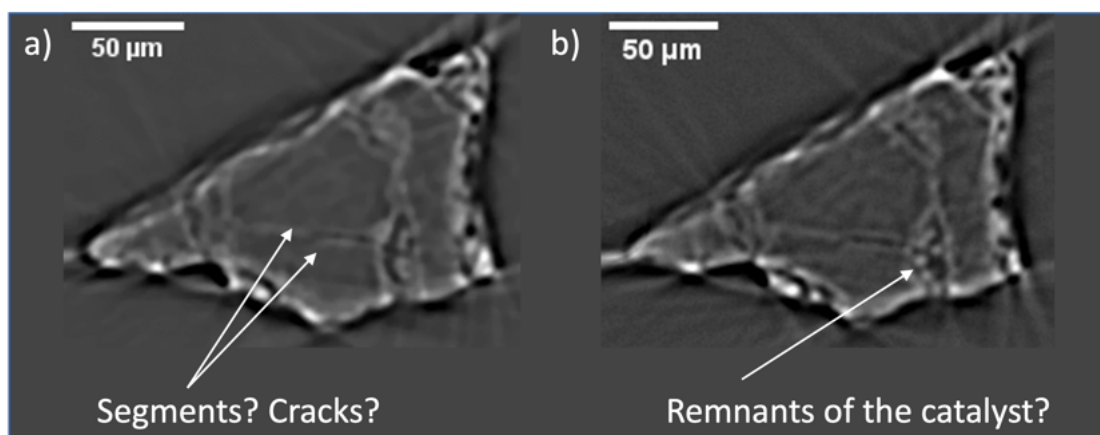


Figure 5.3: Slices of the 3D reconstruction of NWA6871_xx3 showing the internal structure of the sample. Arrows indicate possibe segments or cracks (a) as well as possible remnant of the catalyst (b).

Figure 5.3 clearly shows the potential of future CT scans of microdiamonds from NWA 6871 as the internal structure is intriguing. By localising possible inclusions which might represent the catalyst, FIB cuts could be done very efficiently for subsequent TEM analyses. Of course the measurement conditions have to be optimised for these small samples, however, from this first test a micro X-ray CT facility would be sufficient instead of nano X-ray CT.

# 6 Summary and Future Developments

## 6.1 Summary

The present work consisted of a variety of analytical techniques, i.e., optical microscopy, scanning electron microscopy, Raman-spectroscopy, X-ray diffraction, field emission gun electron probe microanalyser, mass spectrometry, and first tests with micro X-ray computer tomography, which were applied on the two ureilites NWA 6871 and NWA 3140 and carbon aggregates therein. Ureilites represent the second largest group of achondrites and the only samlpes of the mantle of a differntiated planetesimal. These achondrites are known to contain significant amounts of diamond of which some are microdiamonds in the size range of up to 450 µm. All applied techniques in this study indicate that (micro)diamonds from the ureilites NWA 3140 and NWA 6871 were formed during the shock event which destroyed the ureilite parent body during which high pressure and temperature regimes were reached and graphite transformed directly to diamond. A byproduct of this process was "lonsdaleite", or more precisely, stacking faulted diamond and diamond nano twins. The origin of ureilitic diamond is a highly discussed topic as summarised in section 1.4.3. Especially the occurrence of microdiamonds and inclusions therein have recently been ascribed to the formation process deep inside the parent body. However, this hypothesis has been questioned and laid the foundation for this project which showed that diamonds including microdiamonds from the two ureilites were formed during the shock event which destroyed the ureilite parent body.

From both ureilites, thin sections were produced which was essentially difficult due to the presumed abundance of diamond. By optical microscopy, the shock degree of each sample was carefully determined to be U-S3 for NWA 3140 and U-S6 for NWA 6871. Hence, a medium shocked and a highly shocked ureilite were analysed. Low-vacuum scanning electron microscopy was applied to localise carbon bearing aggregates. The

term carbon bearing aggregates was used because as it was shown both samples contain aggregates which consist of both graphite and diamond. After their localisation, carbon aggregates were cut out of the samples using a sharp knife and needle and glued on top of glass fibres to enable X-ray diffraction measurements as well as micro Raman-spectroscopy.

X-ray diffraction revealed close associations of graphite, compressed graphite and diamond with stacking faults and nano twins. Hence, by X-ray diffraction shock indicators could already be seen. For graphite, only diffraction rings could be seen which indicated nanometric crystallite sizes while diamond showed diffraction rings but also diffraction spots indicating both nanometric and mirometre sized diamond.

By applying Raman-spectroscopy on graphite, a geothermometer was used which yield to temperatures of 1368 $\pm$ 120 °C for NWA 3140 and 1370 $\pm$ 120 °C for NWA 6871, respectively. This temperature falls into the catalytic synthesis diamond field in the carbon phase diagram. Considering the nanometric size of graphite in NWA 3140 and NWA 6871 as seen by XRD, I assume that graphite was processed during the shock event in terms of its grain size: micro/millimetre sized graphite got crushed into nano sized graphite because in unshocked ureilites graphite occurs large as euhedral grains. Laboratory experiments from the literature in which laser-induced shock waves were used to confirm this. This link to the shock event combined with the temperature which is sufficient to produce diamond directly from graphite with the help of metals acting as a catalyst, the obtained temperatures were ascribed directly to the shock event. Remnants of the metallic catalyst could be seen in both BSE images of the carbon aggregates as well as in the diffractograms where peaks for iron, goethite and troilite could be seen. Another indicator for the assumption that the graphite-based geothermometer delivers the temperature which was reached during the shock event was delivered by using FEG-EPMA. Olivine and pyroxene from both samples were analysed regarding their Cr content because a recently published geothermometer for ureilites uses

119

the Cr partitioning between low-Ca pyroxene and olivine to determine the equilibrium temperature recorded by these minerals. For NWA 6871 however, the thermometer could not be applied because the data showed large standard deviations and therefore a wide range of temperatures. It was concluded that this sample did not experience a state of equilibrium and therefore is not suitable for geothermometry on its silicates. NWA 3140 on the other hand showed very small standard deviations and was suitable. The obtained temperature for its silicates is $1216 \pm 16\,°C$. This temperature is in agreement with literature data regarding a variety of ureilites and $\sim 150\,°C$ lower than the temperatures recorded by graphite. Hence, the graphite-based geothermometer delivers the temperature which was reached during the ureilite parent body breakup. As optical microscopy has shown, NWA 3140 and NWA 6871 experienced different degrees of shock, i.e, U-S3 and U-S6. Surprisingly, the temperature recorded by graphite during the shock event is not correlated to the shock degree.

A careful search for further carbon bearing aggregates revealed the presence of large carbon aggregates in NWA 6871 which then were extracted. Due to their size, these carbon bearing aggregates were assumed to be suitable for X-ray computed tomography and carbon isotopic analyses by SIMS.

A first test with micro X-ray computer tomography showed that remnants of the metallic catalysts can probably still be seen inside the diamond grains. The tests were performed using the in-house instrument at ELETTRA, Trieste, but the grain sizes were still too small to obtain good data. Fortunately, we could use one of the X-ray CT beamlines of the synchrotron. However, the test was performed with suboptimal measurement conditions as the beamline was already set up for a different experiment. The final reconstruction contains a lot of artefacts due to the non optimised measurement conditions. Nonetheless, even in these relatively bad reconstructions small bright spots can be observed which might be metallic inclusions, i.e., the catalyst which triggered the graphite to diamond transformation at lower pressures. This assumption however,

must be confirmed in future projects involving specific X-ray CT scans with optimised measurement conditions. Doing this would lead to high quality 3D reconstructions which then can be used to localise the inclusions to subsequently extract them by FIB cuts in order to characterise them by transmission electron microscopy.

Among the large carbon bearing aggregates, the largest extraterrestrial single crystal diamond was found. With a size of up to $450\,\mu m$, this diamond exceeds previously reported ureilitic single crystal diamonds. This specific diamond seemed suitable for carbon isotopic measurements. However, it was accompanied by graphite which would have influenced the measurement. To avoid such contamination, a collaboration with the research group of Prof. Dr. Silvia Gross, Department of Chemistry, University of Padova was established who uses a hydrothermal cleaning process to clean gem diamonds. This procedure involves $18\,ml$ of a solution of $HNO_3$ 65% and $H_2SO_4$ 96%. The carbon grains were placed in this solution, added in a $150\,ml$ PTFE cup which then was put into a Berghof stainless steel Acid-Digestion Bomb. The samples were then heated up to $250\,°C$ and held at this temperature for 48 hours. After cooling to room temperature, the samples were recovered and cleaned. To obtain more data, we extracted three large diamond grains. In total, three diamond grains were cleaned efficiently of graphite, which was confirmed by XRD measurements. Subsequently, the grains were put into Indium paste for mass spectrometry and sent to the Centre de Recherches Pétrographiques et Géochimiques (CRPG), Nancy, France. Unfortunately, due to the lack of smooth surfaces only one diamond could be analysed in regard of its carbon isotopic content, but fortunately it was the large $450\,\mu m$ sized one. In total, four measurements were conducted with led to a mean $\delta^{13}C$ value of $-2.8\,‰$. This measurement represents the very first reliable measurement of a single crystal diamond originating from a ureilite. The $\delta^{13}C$ value of $-2.8\,‰$ is relatively heavier in composition than some ureilitic bulk carbon isotopic measurements. A possible explanation was delivered from a publication regarding carbon isotopes from graphite in coarse and fine grained ureilites. Fine grained

121

ureilites are generally assumed to be the product of recrystallisation which was triggered by the shock event. During this shock event which destroyed the ureilitic parent body, a CO gas was formed which ultimately led to a degassing effect. During this degassing effect more $^{12}$C than $^{13}$C was lost which can be seen in heavier $\delta^{13}$C values in graphite from fine grained ureilites. The simultaneous loss of $^{12}$C and the formation of diamond from graphite could be responsible for heavier $\delta^{13}$C signature in ureilitic diamonds as well and in fact, all reported $\delta^{13}$C values for ureilitic diamonds show relatively heavy $\delta^{13}$C compositions, see sections 1.4.3 and 4.

Summarising all used techniques it is clear that ureilitic diamonds, including microdiamonds, were formed during the shock event which destroyed the ureilite parent body. As a consequence, there is no necessity for a large parent body in which deep inside graphite was transformed to diamond.

## 6.2 Future Developments

Future developments should include the search for more ureilitic microdiamonds. Suitable ureilites can be found by using the meteoritical bulletin database with a focus of ureilites which are described as highly shocked and very difficult to polish like NWA 6871. Table 6.1 shows a summary of such ureilites. However, this list is most likely incomplete as many ureilites lack a detailed description. With a larger suite of ureilitic microdiamonds, micro/nano X-ray computed tomography scans should be conducted to search for inclusions. With their location known, FIB cuts can be performed to extract the inclusions from their host diamond in order to analyse them in regard of their chemical composition and crystallographic structure by using TEM. By using TEM, we could learn more about the catalyst which triggered the direct transformation of graphite to diamond during the shock event. Inclusions in diamond have already been used to learn more about the formation of diamond but have been linked to a different formation process.

To expand the data about temperatures in ureilites recorded by graphite, also this method should be applied to more samples. At the point of writing this thesis, only eight different samples are reported in literature including two samples from this study. It has been shown that the temperature range lies between 990–1370 °C. With more samples, this range could be further confirmed as well as the non existent correlation between the shock degree and the recorded temperature. Without the present work, a correlation could have been derived from the literature data. However, a comparison between different samples must include a detailed description of the shock degree.

In addition, synchrotron based X-ray diffraction should be considered. As shown, NWA 3140 is a medium shocked ureilite which contains diamond. However, characteristic shock indicators (i.e., "lonsdaleite" and compressed graphite) were not detectable. Using synchrotron based X-ray diffraction would yield a better resolution and hence enable to detect shock indicators also in very small extents.

Here, it was shown that microdiamonds in ureilites were formed during the shock event which destroyed the ureilite parent body more than 4.5 Ga. However, the occurrence of diamond in ureilites remains an exciting topic with a lot of potential for future work.

Table 6.1: Possible samples for further microdiamonds according to their description in the meteoritical bulletin. All meteorite names are clickable links leading to their specific entry in the meteoritical bulletin database. Sample names written in **bold** represent the most likely ones to find microdiamonds due to similar descriptions to NWA 6871.

| Sample | Shock | Description |
|--------|-------|-------------|
| Acfer 360 | n.a. | diamonds |
| **Al Hawaya 002** | n.a. | Carbon platelets are very common (∼10 vol.%) and consist mainly of diamond |
| **ALHA77257** | n.a. | The meteorite is extremely resistant to cutting and polishing, which probably indicates the presence of diamond |
| ALHA81101 | n.a. | Under crossed polars the olivine crystals are seen as a mosaic of tiny grains averaging 0.05 mm across, evidently a shock effect |
| DaG 084 | high | |

...continued

| Sample | Shock | Description |
|---|---|---|
| DaG 661 | S5 | |
| DaG 897 | S5 | |
| **DaG 1023** | n.a. | A slice of a lithic clast of $3.7 \times 2.7$ cm in size (sub-sample ,02; 6.89 g slice), is one of the most heavily shocked ureilites known. |
| DaG 1066 | n.a. | Ureilite (polymict) with high degree of shock |
| **Dhofar 2115** | n.a. | Carbon platelets (up to 1.5 mm length) consist mainly of diamond |
| **Dhofar 2116** | n.a. | Carbon platelets (up to 1 mm length) consist mainly of diamond and minor microcrystalline graphite |
| **Dhofar 2118** | S2 | Carbon platelets (up to 2 mm length) consist mainly of diamond and minor microcrystalline graphite. |
| **Dhofar 2119** | S2 | Carbon platelets (up to 1 mm length) consist of dominant diamond |
| **Dhofar 2120** | S2 | Carbon platelets up to 1.5 mm, diamond with minor microcrystalline graphite |
| **El Gouanem** | n.a. | graphite and diamond were observed by Raman spectrometry |
| EET 87720 | n.a. | Under crossed polars the olivine grains are seen as a mosaic of tiny crystals, evidently a shock effect. |
| EET 96293 | n.a. | large olivine grains up to 1 mm across with numerous areas of finer-grained ($\sim$200 µm) |
| EET 96314 | n.a. | large olivine grains up to 1 mm across with numerous areas of finer-grained ($\sim$200 µm) |
| EET 96331 | n.a. | large olivine grains up to 1 mm across with numerous areas of finer-grained ($\sim$200 µm) |
| FRO 90168 | n.a. | Olivines are mosaiced, indicating a high degree of shock. |
| FRO 90200 | n.a. | Diamond, positively identified on the basis of its cathodoluminescence, constitutes abundant small grains only within carbonaceous areas. |
| FRO 97013 | n.a. | interstitial carbonaceous material bears tiny diamond crystals, as identified by cathodoluminescence. |
| FRO 01012 | S5 | Abundant diamond is present as small grains within carbonaceous material, as revealed by its cathodoluminescence |

... continued

| Sample | Shock | Description |
| --- | --- | --- |
| **FRO 01088** | S5/6 | Abundant, small diamond grains occur in the carbonaceous material, as revealed by its cathodoluminescence (strong blue-red dispersion) under the beam of the electron microprobe. Most olivine shows a very strong mosaicism, and locally hints of incipient solid-state recrystallisation, corresponding to a shock stage S5/6. |
| FRO 03022 | S5 | Shock varies in the different up to shock stage S5. |
| FRO 10063 | S5 | C-rich material along silicate grain boundaries |
| **GRA 95205** | n.a. | This meteorite is very hard and extremely difficult to break. |
| **GRA 98032** | n.a. | The olivines have been mosaicised by shock. |
| **GRV 021512** | S2/3 | [...] diamond-bearing graphite patches or veins. The presence of diamond was confirmed by Raman spectrum and CL analyses |
| **GRV 022931** | S2/3 | [...] with a few diamond-bearing graphite patches. The occurrence of diamond in graphite patches was confirmed by the Raman spectrum and cathodoluminescence. |
| **GRV 052382** | n.a. | Olivine grains are heavily shocked into small grains of 10-20 $\mu$m and shows fine-grained mosaic or granoblastic texture [...] Diamond and graphite were identified in carbonaceous material by Raman. |
| JaH 054 | n.a. | Aggregates, 100–800 $\mu$min size, composed by graphite and diamond grains, occur between silicate grains. |
| JaH 422 | n.a. | abundant carbon platelets (up to 1 mm) consisting of graphite and diamond and Fe-oxyhydroxides |
| JaH 424 | S2? | Carbon platelets (to 0.8 mm length) consisting of graphite and diamond are abundant along grain boundaries of olivine and pyroxene. |
| **JaH 641** | n.a. | [...] some associated graphite and/or microdiamond. |
| JaH 800 | S2 | Common carbon-platelets (up to 1 mm) contain both graphite and diamond. |
| **JaH 1100** | S5 | the mosaic texture of the olivines suggesting this sample has been highly shocked. |
| JaH 1102 | S5 | The olivine grains show mosaicised texture suggesting a high level of shock. [...] Though diamonds and carbide were not observed within these thin sections, graphite is observed. |

...continued

| Sample | Shock | Description |
|--------|-------|-------------|
| **KaF 018** | n.a. | the presence of diamond platelets |
| **Lahmada 048** | n.a. | significant amount of carbon material, likely diamonds in view of the extreme difficulty to saw the rock. |
| **LEW 86216** | n.a. | The probable presence of accessory diamond is indicated by difficulties in cutting and polishing, and by brightly fluorescent particles in an electron beam. The meteorite is heavily shocked, the large olivines being converted into a mosaic of tiny grains averaging 0.05 mm across. |
| MET 01085 | n.a. | During preparation of this thin section, a large ($\sim$2 mm) patch of carbonado was encountered and it remains in the potted butt. |
| **NEA 027** | high | Composed of very finely recrystallised (mosaicised) olivine and clinopyroxene |
| **NWA 2634** | high | highly shocked |
| **NWA 3135** | n.a. | The difficulties in cutting and polishing this sample suggest the presence of microdiamond. |
| **NWA 4165** | high | Heavily shocked, large areas of recrystallised olivine and pigeonite. Cathodoluminescence imagery shows high diamond density in thermally metamorphosed graphite (mostly amorphous) |
| **NWA 4304** | n.a. | The meteorite contains diamonds. |
| NWA 4507 | n.a. | Microscopic observations and Raman analyses show tiny diamond crystals occurring in blade-shaped graphite crystals. |
| NWA 4742 | n.a. | Carbon ($\sim$3.5 vol.%) is partly amorphous, mostly polycrystalline aggregates of diamond and lonsdaleite (TEM, Raman, XRD) up to several mm |
| **NWA 5144** | n.a. | A dense, dark brown stone that was very difficult to cut |
| **NWA 7195** | high | The complete recrystallisation of silicates is unusual among ureilites, and places this specimen with other very highly shocked ureilites such as NWA 6871 |
| **NWA 7304** | S6 | Partly shock-recrystallised and melted. |
| **NWA 7455** | low | Raman analysis confirms both diamond and graphite phases, though diamond is more prevalent. |

. . . continued

| Sample | Shock | Description |
|---|---|---|
| **NWA 7983** | n.a. | Extremely resistant to grinding and polishing. [...] Diamond ubiquitous, often forming elongate domains up to 500 μm. |
| **NWA 8399** | n.a. | Diamonds occur throughout, often forming elongate domains up to 1000 μm |
| NWA 8622 | n.a. | Carbon (graphite or diamond) clusters are present. |
| NWA 8678 | high | Protogranular aggregate of olivine and pigeonite with accessory blades of graphite. |
| **NWA 10047** | low | This is a diamond-bearing ureilite. The diamonds have elongate habits and aggregates are up to ∼2 mm in length. |
| NWA 10687 | high | Composed of olivine and low-Ca pyroxene with grain boundary zones of blebby Fe metal and microdiamond. |
| NWA 11408 | n.a. | Diamond |
| NWA 11409 | n.a. | Diamond |
| NWA 11410 | n.a. | The veins contain irregularly shaped patches of graphite, partially altered to diamond, 200–1000 μm in length. |
| **NWA 11411** | n.a. | Graphite, partially altered to diamond, is present along some grain boundaries as small domains 50–200 μm in size. |
| **NWA 11412** | n.a. | Graphite, partially altered to diamond, is common along grain boundaries, occurring mainly as small domains 100–200 μm in size but with a few patches up to 1000 μm in length. |
| **NWA 11640** | n.a. | The meteorite contains diamond and shows some foliation. |
| NWA 11890 | low | Si glass, graphite, and diamonds were also identified. |
| NWA 11891 | low | Graphite and diamonds were found. |
| NWA 11892 | low | Graphite and diamonds were found. |
| NWA 11894 | moderate | Graphite and diamonds were found. |
| **NWA 11950** | moderate | Both graphite and diamond are present (as determined by Raman spectroscopy). |
| **NWA 11951** | moderate | The meteorite has a high abundance of diamond. |
| NWA 12191 | low | A carbon polymorph (diamond or graphite) is present. |
| **NWA 12506** | n.a. | diamond (∼50 μm) |
| NWA 12528 | n.a. | intgerstitial graphite, diamond, and metal. |

127

...continued

| Sample | Shock | Description |
|---|---|---|
| NWA 12635 | moderate | Graphite and diamond occur in clots interstitial to the mineral grains |
| **NWA 12939** | moderate | Raman analysis confirms the presence of both graphite and diamond. |
| **NWA 13476** | high | The presence of microdiamond is also inferred from the extreme difficulty in cutting this specimen (the owner reported that several diamond saw blades were severely damaged in attempts to remove the type material). |
| NWA 13914 | high | Highly recrystallised aggregate of finely polygranular olivine |
| NWA 14274 | high | Extensively recrystallised and partially melted assemblage dominated by olivine (>90 vol.%) |
| NWA 14587 | high | Protogranular aggegate of olivine (∼80 vol.%) |
| **NWA 14662** | high | Extremely hard specimen evidently containing a significant amount of diamond (confirmed by electron microprobe analysis). |
| NWA 15307 | high | Grains of both olivine and orthopyroxene consist internally of multiple, small polygonal subgrains |
| **Nova 018** | high | Specimen is very hard and difficult to cut with a diamond saw. |
| **QUE 93336** | relatively un-shocked | During polishing the probable presence of microscopic diamonds in the matrix was noted. |
| **QUE 93341** | relatively un-shocked | During polishing the probable presence of microscopic diamonds in the matrix was noted. |
| RaS 247 | n.a. | The stone contains 16 vol.% of 0.5–1.8 mm size carbon plates consisting of graphite and diamond (confirmed by XRD). |
| RaS 420 | S2 | Carbon platelets (to 0.9 mm length) consisting of graphite and diamond are abundant along silicate grain boundaries of. |
| RaS 517 | n.a. | Carbon platelets (to 0.9 mm length) consist of dominant graphite and minor diamond. |
| **RF 029** | strongly shocked | Carbon platelets (to 1 mm length) consist of dominant diamond and some graphite. |
| RF 516 | S2 | Carbon platelets (up to 3.5 mm in length) consist of diamond |
| RF 517 | S2 | Carbon platelets are irregular in shape, to 0.5 mm, consist of diamond and fine-grained graphite. |

...continued

| Sample | Shock | Description |
| --- | --- | --- |
| RF 518 | S2 | Carbon platelets are irregular in shape, to 1.5 mm, consist of diamond and fine-grained graphite. |
| RF 519 | S2 | Carbon platelets are irregular in shape, to 1 mm, consist of diamond and fine-grained graphite. |
| RF 520 | S2 | Carbon platelets are irregular in shape, to 1 mm, consist of diamond and fine-grained graphite. |
| RF 521 | S2 | Carbon platelets are irregular in shape, to 1 mm, consist of diamond and fine-grained graphite. |
| RF 522 | S1-2 | Carbon platelets are irregular in shape, to 1 mm, consist of diamond and fine-grained graphite. |
| RF 523 | S1-2 | Carbon is present as both coarsely crystalline graphite laths and associated coarse grains of diamond (up to 20 µm). |
| **RF 526** | medium | Carbon platelets are diamond-rich and up to 2.5 mm in size. |
| **RF 527** | S2 | Carbon platelets (up to 1.5 mm length) consist mainly diamond. |
| **RF 528** | S3 | Carbon platelets (up to 1.5 mm length) consist of dominant diamond. |
| SaU 511 | S2 | Common carbon-platelets (up to 0.2 × 2 mm), showing some parallel orientation, consist of graphite and diamond (2Ð10 µm in size) |
| SaU 525 | n.a. | Rare phases are metal Fe, troilite, and diamond. |
| **SaU 559** | medium | Difficult to cut, requiring seven diamond blades and one week to slice the stone in half. [...] Diamond abundant and confirmed by powder X-ray diffraction. Diamond clusters to 20 µm visible with a reflected-light microscope. |
| SaU 563 | n.a. | Carbon (graphite or diamond) is present in elongate clusters up to 500 µm. |
| **SaU 628** | low | Carbon platelets (up to 2 mm in length) consist dominantly of diamond. |
| **UAE 001** | n.a. | Abundant, up to 100 µm size diamonds occur interstitial to silicates, usually associated with graphite. |
| Watson 018 | n.a. | graphite + diamond along grain boundaries |

# 7 Acknowledgments

First of all I would like to thank Prof. Fabrizio Nestola for the opportunity to work on this project at the Department of Geosciences, University of Padua and for the realisation of the project. Further, Prof. Frank E. Brenker for being my co-supervisor during the three years. I would also like to thank both for the supervision and the helpful discussions through which I learned a lot. Further, Anthony Love, Appalachian State University, Department of Geology for providing one of the samples.

Special thanks also to Dr. Lidia Pittarello, Natural History Museum Vienna, where I spent a full month learning everything about the classification of meteorites. At this point I would also like to thank Dr. Uwe Kolitsch, head of the Department for Mineralogy & Petrography, who made this visit possible.

Further, I would like to thank all the colleagues at the Department of Geosciences, University of Padua. Dr. Davide Novella for his help with the new Raman instrument, Leonardo Tauro for preparing the especially difficult thin sections, Dr. Jacopo Nava and Prof. Paolo Nimis for his help with the SEM, again Prof Paolo Nimis for helpful discussion about EPMA data.

Thanks also to Dr. Federico Zorzi, CEASC, University of Padua, for his help with the SEM. Prof. Silivia Gross and her Ph.D. student Giulia Bragaggia, Department of Chemical Sciences, University of Padua with whom we collaborated to clean our small diamonds. Prof. Dominik Hezel, Department of Geosciences, University Frankfurt am Main, for his help with the FEG-EPMA. Emilie Thomassot, CRPG, Nancy who conducted the carbon isotopic measurements.

Special thanks at this point to Dr. Anna Barbaro with who I worked very closely on the topic.

Last but not least I would like to thank all my friends who supported me during the three years of my Ph.D. and everyone who participated in valuable discussions in the

deparment.

Without the help of all the people mentioned above, this project would not have been possible.

# 8 Appendix A - First-Author Paper

## Shock degree and graphite geothermometry in ureilites NWA 6871 and NWA 3140

Oliver CHRIST [1]*, Anna BARBARO[1], Frank E. BRENKER[2], Paolo NIMIS[1], Davide NOVELLA[1], M. Chiara DOMENEGHETTI[3], and Fabrizio NESTOLA[1,2]

[1]Department of Geosciences, University of Padova, Via Gradenigo 6, 35131 Padova, Italy
[2]Geoscience Institute, Goethe-University Frankfurt, Altenhöferallee 1, 60438 Frankfurt, Germany
[3]Department of Earth and Environmental Sciences, University of Pavia, Via A. Ferrata 1, I-27100 Pavia, Italy
*Corresponding author. E-mail: oliver.christ@phd.unipd.it

**Abstract**–Carbon aggregates from two differently shocked ureilites were analyzed to gain insight into the shock transformation of graphite to diamond in ureilites, which happened when the ureilite parent body (UPB) was most likely destroyed by massive impact events. We present data for carbon aggregates from the highly shocked (U-S6) Northwest Africa (NWA) 6871 and the medium shocked (U-S3) NWA 3140. Both samples contain abundant carbon aggregates which were analyzed by X-ray diffraction and micro-Raman spectroscopy revealing the presence of close associations of (compressed) nanographite, micro- and nanodiamond, as well as Fe-rich phases. Graphite and diamond in NWA 6871 show shock indicators that are absent in NWA 3140. Based on Raman geothermometry on graphite, we calculated mean temperatures of 1368 ± 120 °C and 1370 ± 120 °C for NWA 3140 and NWA 6871, respectively. For comparison, a geothermometer based on the partitioning of Cr between olivine and low-Ca pyroxene was applied on NWA 3140, which yielded a temperature of only 1215 ± 16 °C. The graphite-based temperatures are the highest reported for graphite in ureilites so far and exceed calculated magmatic temperatures for ureilites from silicate- and chromite-based geothermometers. Graphite temperatures fall into the temperature field of catalytic diamond synthesis, which supports the hypothesis of direct transformation from graphite to diamond upon shock. Although the temperatures estimated seem to be independent of the shock degree, they can be ascribed to the shock event that destroyed the UPB.

## INTRODUCTION

Ureilites are coarse-grained ultramafic meteorites (Goodrich, 1992). They are the second largest group of achondrites after the howardite–eucrite–diogenite meteorites and have unique properties compared to other achondrites. In particular, ureilites can contain significant amounts of carbon and show features of both planetary differentiation and undifferentiated material as well as very old ages of up to ~4566.7 ± 1.5 Ma (Zhu et al., 2020). Therefore, ureilites originate from the early stages of our solar system, a period characterized by violent collisions among planetesimals, planetary embryos, and protoplanets (Morbidelli et al., 2012). Ureilites represent mantle material of a partially differentiated parent body (Mittlefehldt et al., 1998), the

ureilite parent body (UPB). The UPB was destroyed by one or more large collisions and/or impact events, which led to the formation of ureilite daughter bodies (UDB) and eventually to the distribution of ureilitic material throughout the solar system (Downes et al., 2008; Goodrich et al., 2004, 2015; Herrin et al., 2010; Rai et al., 2020). Consequences of these shock events are preserved in ureilitic silicates, that is, olivine and pyroxene, and are used to characterize different degrees of shock ranging from very low U-S1 to high U-S6, where the "U" stands for ultramafic (Stöffler et al., 2018). The original shock classification based on olivine and plagioclase in chondrites was adapted for ureilites by Nakamuta et al. (2016). Stöffler et al. (2018) updated the original shock classification from Stöffler et al. (1991) to consider also shock effects in different

groups of rocks, including ultramafic rocks, to which ureilites belong.

Ureilites mainly consist of olivine and pyroxene with minor accessory phases of carbon (up to 8 wt%), metal, and sulfides. Carbon may occur as graphite and diamond, cohenite (Goodrich et al., 2015, 2020), or organic compounds (Sabbah et al., 2010). Unshocked ureilites usually contain solely graphite (Nakamuta & Aoki, 2000; Wacker, 1986), which was interpreted to represent the primary form of carbon in ureilites (Berkley & Jones, 1982; Treiman & Berkley, 1994). Shocked samples, however, contain close associations of graphite and diamond (e.g., Nestola et al. [2020] and references therein). They often show blade-shaped structures in their longest dimension (see fig. 1a in Nestola et al., 2020), which resemble the shape of millimeter-sized graphite in low-shocked ureilites. Carbon associations in shocked ureilites are polycrystalline and consist of graphite, diamond, and stacking-disordered diamond (Murri et al., 2019; Németh et al., 2014; Németh, McColl, Garvie, et al., 2020; Németh, McColl, Smith, et al., 2020; Nestola et al., 2020; Salzmann et al., 2015). Despite being known for over a century (Kunz, 1888), the origin of these diamonds remains a strongly debated topic. There are three different major hypotheses: (i) formation under high pressure conditions inside a large planetary body (e.g., Desch et al., 2019; Miyahara et al., 2015; Nabiei et al., 2018; Urey, 1956), (ii) formation from graphite during shock (e.g., Lipschutz, 1964; Nestola et al., 2020), and (iii) formation by chemical vapor deposition (Fukunaga et al., 1987; Matsuda et al., 1995). Of these, formation by shock is the most accepted hypothesis, but recent studies by Miyahara et al. (2015) and Nabiei et al. (2018) claim that "large" diamonds were formed under high pressures in a large planetary body with a size between Mercury ($r \approx 2439$ km) and Mars ($r \approx 3389$ km). In a comprehensive study of three different ureilites, Northwest Africa (NWA) 7983 and Almahata Sitta (AhS 209b and AhS 72), by scanning electron microscopy (SEM), micro X-ray diffraction (XRD), transmission electron microscopy (TEM), and micro-Raman spectroscopy (MRS), Nestola et al. (2020) provided the first clear evidence for the coexistence of large (up to 100 μm) single-crystal diamonds, polycrystalline nanodiamonds, and nanographite in close associations in the carbon matrix of ureilites and concluded that these diamonds were formed by shock. Further proof for this kind of carbon associations and the formation of micro-sized diamonds during a shock event was given by Barbaro et al. (2021, 2022) for the Kenna and Yamato 74123 ureilites.

Following Gillet and El Goresy (2013), the time scale of shock events depends on the type of impactor (e.g., its size, density, speed, and angle of impact) and ranges from a few hundred milliseconds to a few seconds. Despite the short duration, high pressure and temperature regimes can be reached during a shock event (Gillet & El Goresy, 2013). These extreme conditions affect the impacted planetary body in terms of melting and ejection of material and can lead to the formation of high-pressure and high-temperature minerals, which includes the formation of diamond from graphite. The transition from graphite to diamond is well understood and occurs when the $sp^2$ carbon bonds of graphite are unbound to form $sp^3$ carbon bonds of diamond. However, the required energy for this direct transition is high, as shown by Irifune et al. (2003), who produced diamond directly from graphite at pressures ranging from 12 to 25 GPa and temperatures above 2000 °C. To lower the energy barrier, metals (usually Fe, Co, Ni but also Pt, Rh, Ru, Pa, Ir, Os, Mn, Cr, Cu, Ti, and Zr) are added as a catalyst (Bovenkerk et al., 1959; Bundy et al., 1955). These metals have a eutectic or peritectic relationship with C and react easily with C, which leads to a breakup of the $sp^2$ carbon bonds of graphite and subsequentially to diamond nucleation (Dobrzhinetskaya, 2012). This catalyzed reaction starts at $P = 5$ GPa and $T = 1400–1600$ °C with a reaction time ranging between 5 and 20 min (e.g., Bovenkerk et al., 1959; Bundy et al., 1955). A graphical summary of different forms of diamond syntheses from graphite was published by Dobrzhinetskaya (2012). Based on these experimental findings, it is reasonable to assume that Fe-Ni-C melts, formed when the UPB was destroyed, could have acted as a catalyst for the graphite to diamond transition (Nestola et al., 2020).

Geothermometry based on the composition of coexisting silicates has been applied to ureilites. However, since most ureilites contain only olivine and pigeonite, geothermometry on ureilites was limited to specific samples containing further phases like augite or chromite. The two-pyroxene thermometer yielded temperatures of 1070–1280 °C (Chikami et al., 1997; Sinha et al., 1997; Takeda, 1989; Takeda et al., 1989; Weber et al., 2003), the olivine–pigeonite–melt thermometer a range of 1240–1300 °C (Herrin et al., 2010; Singletary & Grove, 2003), and the olivine–chromite thermometer a range of 1040–1060 °C (Goodrich et al., 2014). Application of these geothermometers relies on the availability of the required minerals and is therefore limited. Recently, a new geothermometer was introduced by Collinet and Grove (2020), based on partitioning of Cr between olivine and low-Ca pyroxene and is "applicable to all ureilites" as long as they "contain at least one low-Ca pyroxene." In addition to these geothermometers, a graphite-based geothermometer established for carbonaceous chondrites by Cody et al. (2008) was applied to

ureilitic graphite by Ross et al. (2011) and Barbaro et al. (2020, 2021, 2022) which yielded temperatures of 990 ± 120 °C and 1242 ± 120 to 1314 ± 120 °C, respectively.

The main aim of this work is to further characterize the impact event that destroyed the UPB/UDB and to understand whether the presence of micrometer-sized diamond is a unique feature of NWA 7983, Kenna, and Yamato 74123 or a general feature of every shocked ureilite. Therefore, the ureilites NWA 6871 and NWA 3140 were analyzed using the same multimethodological approach that was applied to NWA 7983, Kenna, and Yamato 74123, combining SEM, XRD, MRS including graphite-based geothermometry and field emission gun electron probe microanalyzer (FEG-EPMA). We will show that applying the graphite-based geothermometer and comparing it to the Cr-based geothermometer helps us to better understand the meaning of the former.

## SAMPLES AND PREPARATION

Sample NWA 6871 was provided by Anthony Love, Appalachian State University, while NWA 3140 is from the collection of Frank Brenker, Goethe-University, Frankfurt am Main.

NWA 6871 is a find from 2011 in Morocco and was described as "very hard to cut" due to a very high abundance of diamond (Ruzicka et al., 2014). NWA 6871 is a unique ureilite because the complete recrystallization of silicates implies that it must have experienced a high shock level (Ruzicka et al., 2014). This is in agreement with Bunch et al. (2012), who reported a shock degree of S6 (Stöffler et al., 1991). We examined two fragments of NWA 6871. The first fragment is an ~2 cm × 2 cm × 0.1 cm thick section. Six carbon-bearing aggregates were extracted from this fragment: NWA6871_1, NWA6871_2, NWA6871_3, NWA6871_4, NWA6871_5, and NWA6871_6.

The second fragment of NWA 6871 is ~0.9 cm × 0.8 cm × 0.1 cm. We used this smaller fragment to produce a thin section for petrographic description by optical microscopy and FEG-EPMA analyses. Probably due to the high abundance of (micro)diamonds, polishing was difficult. To avoid contamination with diamonds from the abrasive, the fragment was polished using SiC paper.

NWA 3140 was found in Morocco in 2004. We examined only a small irregularly shaped fragment, from which it was impossible to directly extract carbon aggregates. Therefore, we cut the sample into two pieces, put one half into epoxy, and polished it to obtain a plane surface. The cutting process was done using a water-cooled diamond saw and was very difficult, presumably due to the presence of diamond. Polishing was done with

SiC paper. The obtained surface covers an area of ~20 mm² from which we extracted two carbon-bearing aggregates: NWA 3140_1 and NWA 3140_2. To prevent sampling diamonds from the diamond saw, we avoided material from the surface. Therefore, we scratched away the uppermost layer and extracted the underlying material. In comparison to NWA 6871, the extraction was more difficult, and the extracted aggregates were very small. Eventually, we produced a thin section of the half, which was already in epoxy, again using SiC paper to avoid contamination.

## METHODS

### Scanning Electron Microscopy

SEM was done in two steps. The first analyses were conducted at the CEASC (Centro di Analisi e Servizi per la Certificazione, University of Padua), with an FEI Quanta 200 instrument operating at 20 keV with a working distance of 12.60 mm under low-vacuum conditions. These conditions allow us to analyze the sample without carbon coating, which otherwise would have prevented the identification of carbon aggregates by energy-dispersive X-ray spectroscopy (EDS). Backscattered electron (BSE) images were taken to characterize the overall appearance of carbon aggregates.

The second step of SEM was done at the Department of Geosciences, University of Padua, using a Tescan Solaris instrument operating at 15 keV with a working distance of 5 mm. For this step, the thin sections were carbon coated. EDS point measurements were conducted for 20 s to qualitatively analyze metal phases accompanying the previously identified carbon aggregates.

### X-Ray Diffraction

XRD analyses were carried out at the Department of Geosciences, University of Padua, using a Rigaku Oxford Diffraction SuperNova single-crystal diffractometer equipped with a 200 K Dectris detector operating with a microsource MoKα X-ray radiation at a wavelength of 0.71073 Å (X-ray beam diameter was 0.120 mm; the sample-to-detector distance was 68 mm). Samples were glued on top of glass fibers and measured in the range of 1–360° with a step size of 1° around the φ-axis. Each measurement had an acquisition time of 100 s per frame. The data were processed using the CrysAlisPro 40_64.67a and Panalytical HighScore Plus Software packages. The crystallite sizes ($L$) on powder material were calculated using the Scherrer Equation 1 (Scherrer, 1918):

$$L = \frac{K \times \lambda}{\beta \times \cos \theta} \tag{1}$$

where $K$ is the shape factor, $\lambda$ is the wavelength, $\beta$ is the integral breadth of the peak, and $\theta$ is the Bragg angle.

### Micro-Raman Spectroscopy

MRS was performed using a WITec alpha300 R spectrometer (wavelength = 532 nm) at the Department of Geosciences, University of Padua. The instrument was calibrated with an Si-disk. Each measurement was accumulated four times with an integration time of 30 s and varying laser powers depending on the investigated grain. Graphite was measured with 1–3 mW, to avoid damaging graphite grains. The grating was set to 300 g mm$^{-1}$. The data were processed using the Thermo-Scientific OMNIC™ for Dispersive Raman Software adopting Gaussian + Lorentzian curves to obtain the best fit.

In addition to phase identification, we used the graphite geothermometer (Equation 2), established by Cody et al. (2008) and modified by Ross et al. (2011):

$$T_{max} (°C) = 1594.4 - 20.4\Gamma_G - 5.8 \times 10^{-2}\Gamma_G^2 \tag{2}$$

The equation is used to calculate the temperature recorded by graphite. Here, $\Gamma_G$ is the full width half maximum (FWHM) of the graphite G-band. The original data from which Equation 2 originates can be seen in Cody et al. (2008), who report a relatively high error $2\sigma$ of $\pm 120$ °C for $T_{max}$ due to the scatter in the original plot. However, data for 25 different chondrites show a relationship between the petrological type and $T_{max}$: the higher the petrological type, the higher the $T_{max}$. Hence, Raman-based geothermometry can be used to classify samples in terms of whether they have experienced low, medium, or high temperatures (Cody et al., 2008).

### Field Emission Gun Electron Probe Microanalysis

FEG-EPMA analyses were performed at the Department of Geosciences, Goethe-University Frankfurt am Main, Germany using a JEOL JXA-8530F Plus Hyperprobe instrument. Measurement conditions were set to an acceleration voltage of 15 kV and a probe current of 20 nA. Wavelength-dispersive X-ray spectroscopy (WDS) point analyses of silicates were measured in spot mode (<100 nm) and collected using a counting time of 20 or 30 s on the peak and half that time on the upper and lower background, respectively.

Both thin sections were carbon coated. For calibration, the following standards were used: Ca, Si (CaSiO$_3$), Mg (Mg$_2$SiO$_4$), Fe (Fe$_2$O$_3$), Al (Al$_2$O$_3$), Cr (Astimex chromite), Mn (Astimex rhodonite), K (KTiOPO$_4$). Elements were calibrated to a <1 rel.% precision. EPMA data were used to apply the Cr-based geothermometer of Collinet and Grove (2020), which gives the temperature of equilibration for a specific ureilite according to the equation:

$$T (°C) = 913.9 + 465.6 \times D_{Cr}^{oliv-LCP} \tag{3}$$

where $D_{Cr}^{oliv-LCP} = Cr_2O_3^{oliv}/Cr_2O_3^{LCP}$ is the partition coefficient of Cr between olivine (oliv) and low-calcium pyroxene (LCP: orthopyroxene or pigeonite).

## RESULTS

### Optical Microscopy

Optical microscopy observations show that NWA 6871 consists of olivine aggregates with subhedral forms of former large olivine crystals and sizes in a range between ~0.3 and ~2 mm in their longest dimensions (bright grains in Fig. 1a). These olivine aggregates are fractured and contain small olivine grains with an average grain size of ~20 μm, which meet in triple junction points (Fig. 1b and 1c). The space between the aggregates is filled with opaque material that contains carbon aggregates, metallic phases, and sulfides. In some areas, veins crosscutting multiple aggregates can be observed. Based on the textural observations, NWA 6871 can be classified as highly shocked with a shock degree of U-S6, which corresponds to a pressure of ~60 to 70 GPa (Stöffler et al., 2018). It was not possible to identify pyroxene grains by optical microscopy. However, both MRS and WDS revealed the presence of ~20 μm sized pyroxene grains.

In contrast to NWA 6871, NWA 3140 contains olivine and pyroxene grains up to 1 mm in their longest dimension (Fig. 2a). From the absence of recrystallization features, it is evident that NWA 3140 experienced a lower shock degree than NWA 6871. All olivine and pyroxene grains are fractured (Fig. 2b and 2c). As reported in Fig. 2b, olivine grains show planar fractures, typical for low–medium shock deformation (Stöffler et al., 2018). No mosaicism can be observed, but some olivine grains exhibit a "sawtooth" texture on their edges. In addition, pyroxene displays twinning (see black arrows). Olivine and pyroxene grains are set into an opaque matrix that consists of carbon aggregates and very fine material (including metal phases and sulfides). Based on the described features, NWA 3140
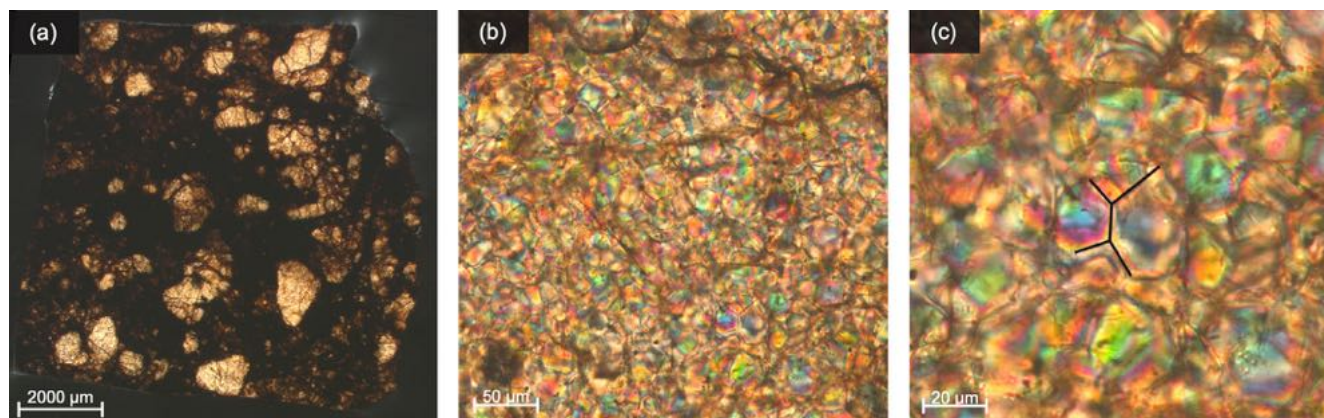
Fig. 1. NWA 6871 in cross polarized light. a) Overview of the sample. b) Close-up of a large bright grain from (a). c) Triple junction points between olivine grains indicated by black lines. (Color figure can be viewed at wileyonlinelibrary.com.)

can be classified as medium shocked with a shock degree of U-S3, which corresponds to peak pressures of ~15 to 20 GPa (Stöffler et al., 2018).

## Scanning Electron Microscopy

Figures 3 and 4 show BSE images of NWA 6871 and NWA 3140, in which silicate phases (light gray), carbon phases (dark gray), and metal-bearing phases (white) can be seen. BSE images of the uncoated NWA 6871 thick section show several dark gray-black areas indicative of carbon. These areas appear irregular or elongated (Fig. 3) and sometimes show blade-shaped structures (Fig. 3c) like those observed in NWA 7983 by Nestola et al. (2020). In NWA 6871, an internally layered aggregate up to 250 μm in length and 80 μm in width is present (Fig. 3c). EDS spectra collected on the brighter areas of the carbon aggregates revealed the presence of Fe, Ni, Si, and S, attributed to Fe,Ni-metal and Fe-sulfides, but also iron-oxides were identified. Additional elements are Mg, Si, and O from the adjacent silicate matrix material. Carbon aggregates are also present in the polished surface of NWA 3140 (Fig. 4a). However, the areas do not show any kind of blade-shaped structures and appear amoeboid (Fig. 4b and 4c).

EDS measurements (Fig. 5) directly on metal phases accompanying carbon aggregates in NWA 3140 revealed the presence of Fe, Ni, and Si. These elements could be ascribed to kamacite, Si-bearing kamacite, and pure taenite. Many grains also showed the presence of oxygen, probably due to terrestrial weathering. In NWA 6871, kamacite, Si-bearing kamacite, troilite, and oxidized metal grains can be found in and around carbon aggregates. Minor elements which occur with Fe and Ni are Cr and P.

## X-Ray Diffraction

*NWA 6871*: As reported in Fig. 6, the XRD analysis revealed the presence of diamond (*d*-spacing of 2.06, 1.26, and 1.07 Å), graphite (*d*-spacing of 3.35 Å), and Fe-metal and Ni-rich Fe-metal (*d*-spacing of 1.78, 1.43, and 1.17 Å). Additional phases are troilite (*d*-spacing of 1.74 Å), goethite (*d*-spacing of 4.17 Å), magnetite (*d*-spacing of 2.53 Å), and olivine with multiple diffraction spots (e.g., *d*-spacing of 2.46 Å in Fig. 6d). For carbon phases, the reconstructed diffraction images (Fig. 6) show rings for both graphite and diamond, indicating polycrystalline material. Figure 6e also shows single crystal diffraction spots of diamond at *d*-spacing of 1.26 Å. The diffractograms (Fig. 6b and 6f) further reveal a shoulder on the highest peak of diamond at *d*-spacing 2.06 Å towards higher *d*-spacings (about 2.15–2.18 Å), ascribed to stacking disordered diamond and is a shock indicator (Murri et al., 2019; Németh et al., 2014, Németh, McColl, Garvie, et al. 2020; Németh, McColl, Smith, et al., 2020).

After a careful line profile analysis for the powdery graphite and diamond, the crystallite sizes were estimated with Equation 1, which yielded sizes of 5–7 nm and 5–9 nm for diamond and graphite, respectively (Table 1). For this calculation, we only used the *d*-spacing at 1.26 and 1.07 Å for diamond and 3.34 Å for graphite (Fig. 6). Graphite, in some spectra, shows 002-diffraction peaks at *d*-spacing of 3.34 Å with a strong asymmetry and the peak centers appear to be shifted toward higher 2θ and therefore lower *d*-spacings (e.g., Fig. 6f), indicative of compressed graphite, which is a further shock indicator (Nakamuta & Aoki, 2000).
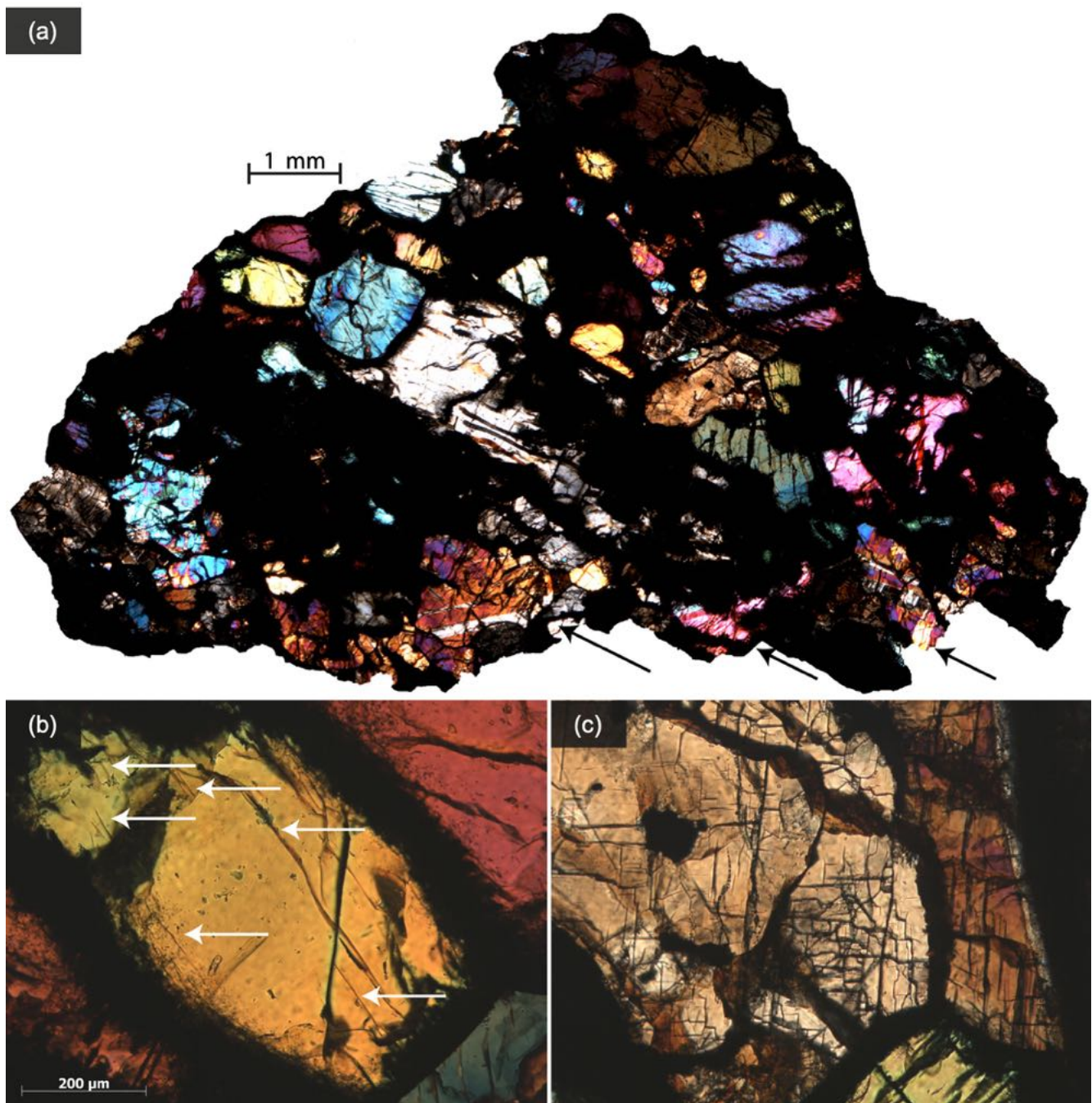
Fig. 2. a) Thin section of NWA 3140 under cross polarized light. b) Close-up of a fractured olivine grain showing planar fractures in the NW–SE direction, white arrows. c) Close-up of a fractured pyroxene grain showing ~90° cleavage structure on the basal section. Mineral identification based on the interference colors was difficult on this sample because of difficulties in the polishing process due to the presence of diamond which led to differences in thickness. (Color figure can be viewed at wileyonlinelibrary.com.)

*NWA 3140*: As reported in Fig. 7, XRD on carbon aggregates from NWA 3140 shows diamond (*d*-spacing of 2.06, 1.26, and 1.07 Å), graphite (*d*-spacing of 3.34 Å), Fe-metal and Fe,Ni-metal (*d*-spacing of 1.78, 1.43, and 1.17 Å). In Fig. 7d, peaks for olivine can be

seen that most likely originate from the matrix material (*d*-spacing of 2.98, 2.76, 2.51, 2.26, 1.74, 1.60, 1.47, and 1.34 Å). In contrast to NWA 6871, no graphite peak asymmetries or diamond peak shoulders can be seen. The diffraction images and powder diffraction patterns
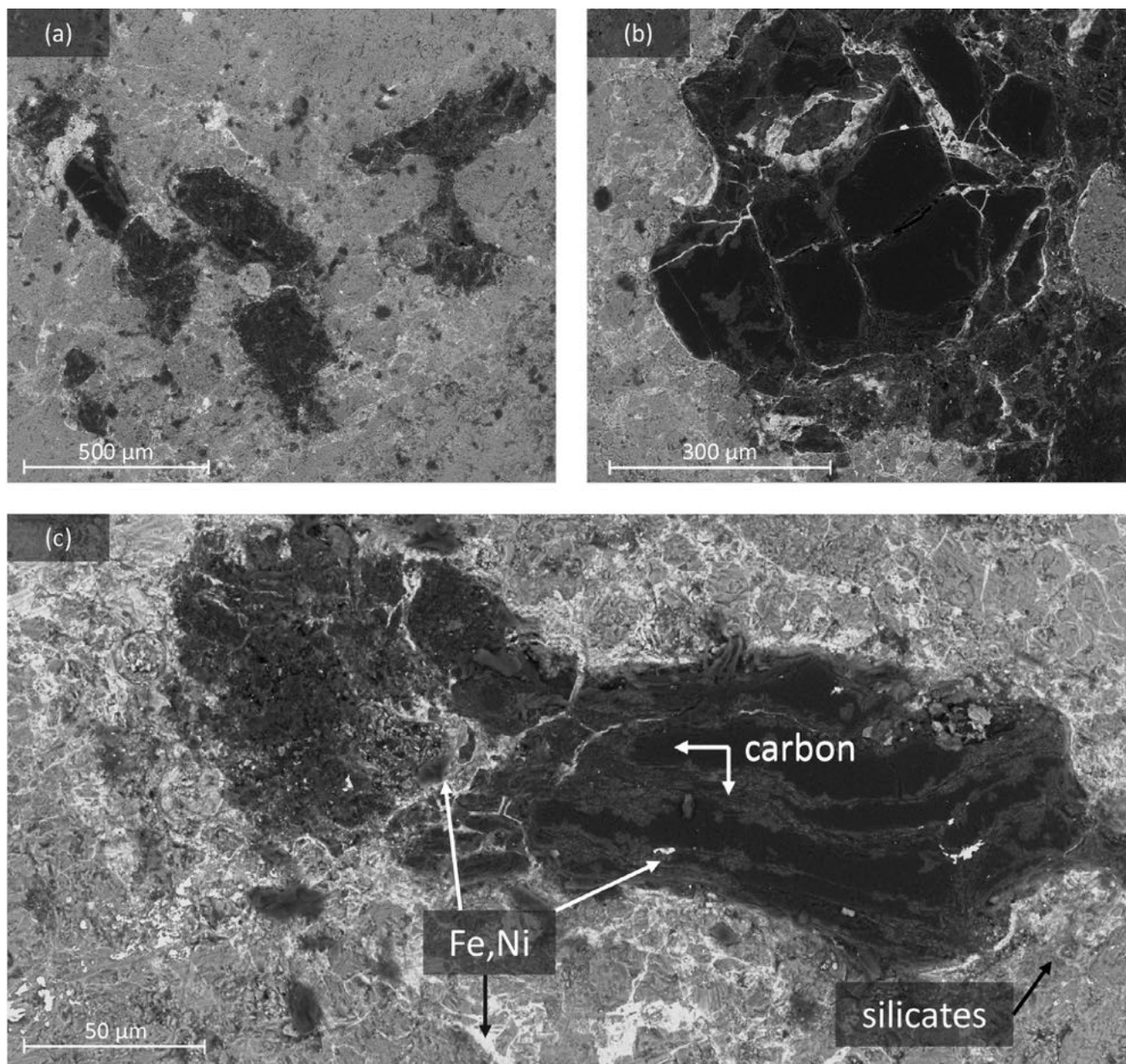
Fig. 3. BSE images of NWA 6871 carbon aggregates (black and dark gray) in a silicate matrix (light gray) and interstitial Fe-Ni alloys (white). In (a), several carbon aggregates in the ureilite silicate matrix are shown. In (b), a close-up image of a carbon aggregate crossed by Fe-Ni veins is reported. In (c), the blade-like structure on the right side of the carbon aggregate is shown, while the left side appears fractured. Fe-bearing veins and blebs can be seen inside the aggregate.

of NWA 3140 are shown in Fig. 7a–d. Carbon-bearing aggregates from NWA 3140 show diffraction rings for graphite and diamond from which the crystallite sizes were calculated using Equation 1. Graphite is about 7–9 nm in size, while diamond crystallites measure 4–10 nm (Table 1). However, NWA 3140 also shows diffraction spots for diamond at $d$-spacing 2.06 Å,

which indicate single-crystal material closely associated with the polycrystalline one in the same aggregate.

Hence, XRD results on NWA 6871 and NWA 3140 showed the coexistence of nanodiamond, microdiamond, and nanographite. In addition, in NWA 6871, compressed graphite and stacking disordered diamond can be observed.
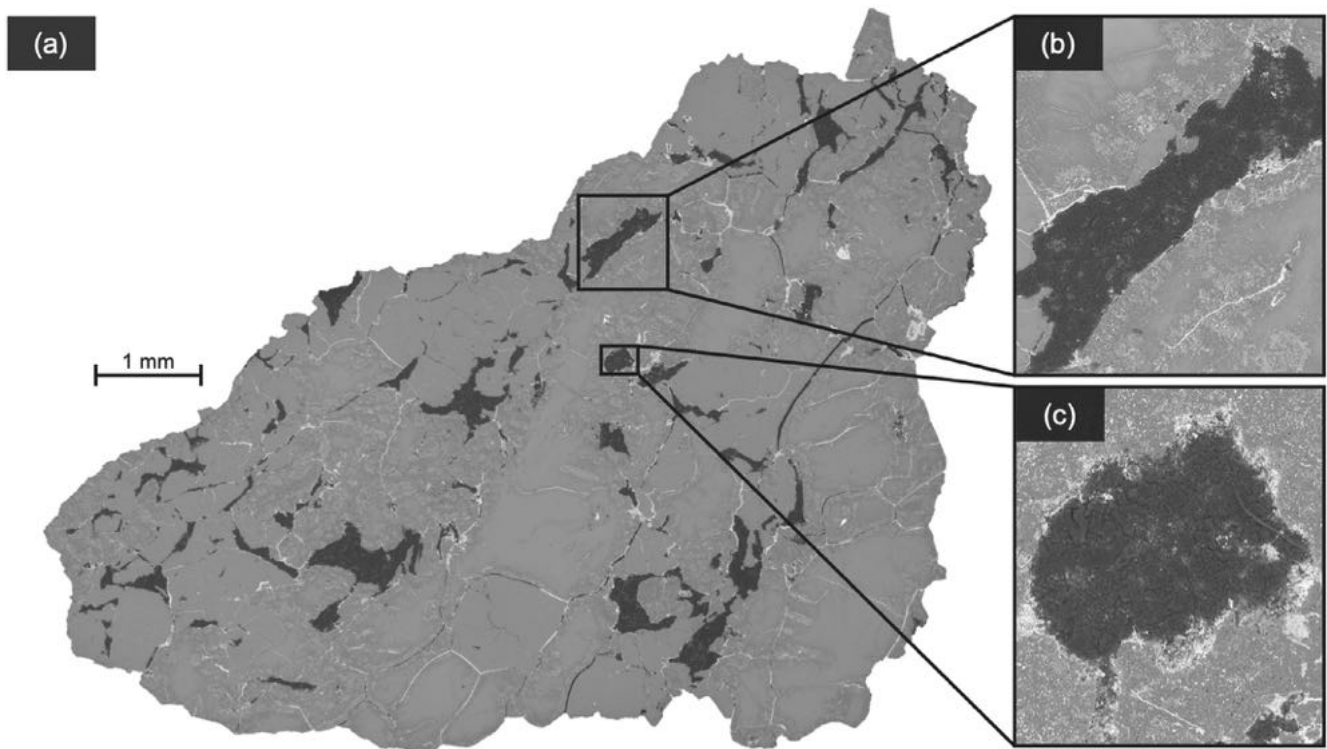
Fig. 4. a) BSE image of NWA 3140 with close-ups of two carbon aggregates showing amoeboid structure in (b) and (c). Although some aggregates are elongated as shown in (b), no blade-like structure can be observed. A notable feature of this sample are the various small Fe-bearing blebs in the rims of silicates, but also in some silicate cores.

**Micro-Raman Spectroscopy**

MRS on carbon aggregates, both within the bulk samples and on the extracted aggregates, shows first-order Raman bands at ~1580 cm$^{-1}$ and ~1352 cm$^{-1}$ and sometimes at ~1620 cm$^{-1}$. These bands are the so-called G-band, D-band, and D′-band of graphite (Ferrari & Robertson, 2000). While the G-band originates from the zone center phonons with $E_{2g}$ symmetry, the D-band is a breathing mode with $A_{1g}$ symmetry, which is forbidden in perfectly ordered graphite and appears only in disordered graphite (Ferrari & Robertson, 2000). Generally, two different types of graphite spectra are observable (see Fig. 8a and 8b). In Fig. 8a, type 1 spectra show a sharp G-band. In addition, a small D-band and often a D′-band as a shoulder of the G-band can be seen. In contrast to type 1 spectra, type 2 (Fig. 8b) spectra show a very high D-band, which seems to affect also the $\Gamma_G$ of the G-band. However, type 2 spectra are very rare in comparison to type 1 spectra.

Temperature calculations using Equation 2 on graphite from NWA 6871 and NWA 3140 were carried out using the data reported in Table 2. To compare our temperatures to the temperatures of Ross et al. (2011)

and Barbaro et al. (2020, 2021, 2022), the G-band $\Gamma_G$ values were corrected for the instrumental peak broadening using the same approach as Barbaro et al. (2020), where a lithospheric diamond of high gem quality was used. Ross et al. (2011) reported an FWHM of 3 cm$^{-1}$ for a kimberlitic diamond, while Barbaro and coauthors reported an FWHM of 6 cm$^{-1}$ (Barbaro et al., 2020) and 5 cm$^{-1}$ (Barbaro et al., 2021, 2022) for lithospheric diamonds. In this work, we used a set of six different lithospheric diamonds from Canada to obtain the correction factor for our instrument. On each diamond, five measurement points were measured five times for 1 s using a magnification of 50×.

Our lithospheric diamonds showed an FWHM of 6.58 ± 0.29 cm$^{-1}$. Divided by the FWHM of Ross et al. (2011), this led to a correction factor of 2.19 ± 0.24. The FWHM values of our graphite were divided by this correction factor, which resulted in average temperatures of 1370 ± 39 °C (±120 °C) for NWA 6871 and 1368 ± 33 °C (±120 °C) for NWA 3140. Here, ±39 °C and ±35 °C are the standard deviations of our data, while the error of ±120 °C is the maximum temperature uncertainty published by Cody et al. (2008). Of course, the correction factor influences
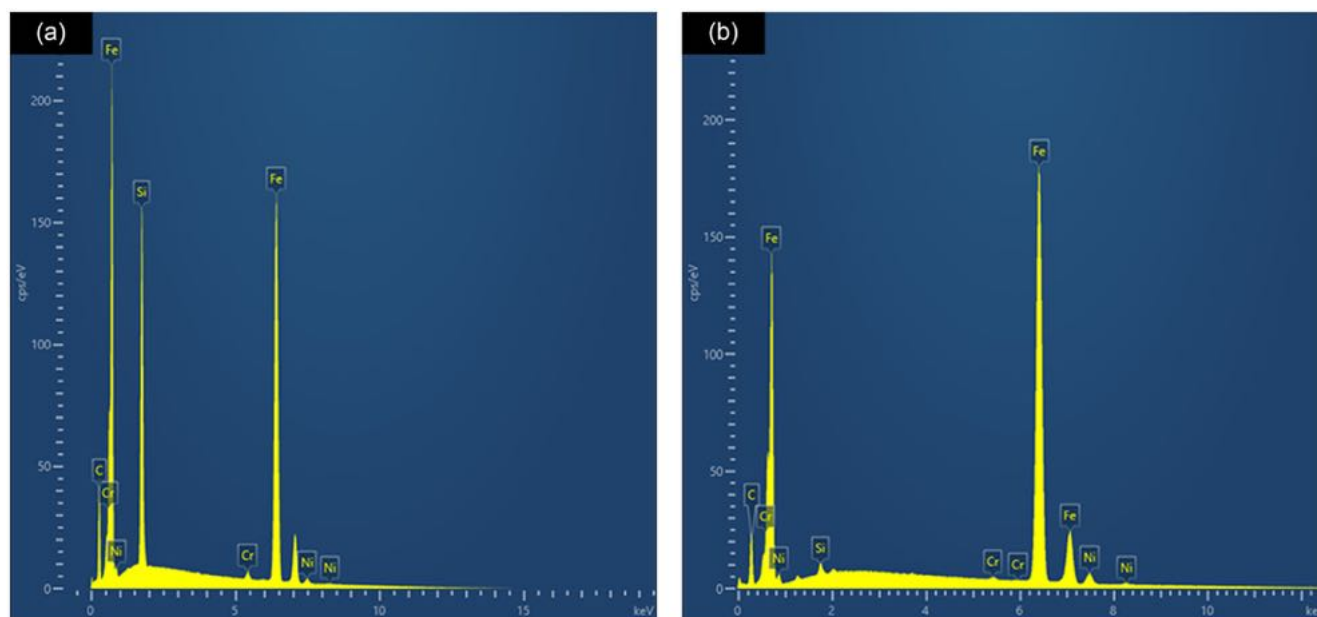
Fig. 5. Examples of EDS spectra of metal-bearing phases accompanying carbon aggregates of NWA 6871 (a) and NWA 3140 (b). Both spectra show possibly Si-bearing kamacite with minor Cr contents. In NWA 6871, many similar EDS spectra were observed with Si-contents of up to ~14 wt%. (Color figure can be viewed at wileyonlinelibrary.com.)

the temperature and the correction factor used in our calculations is slightly higher than the one of Barbaro et al. (2020, 2021, 2022). However, error calculations using Equation 4 with our correction factor $c = 2.19 \pm 0.09$ cm$^{-1}$ and $\Gamma_G = 23 \pm 4$ cm$^{-1}$ ($\Delta\Gamma_G$ of $\pm 4$ cm$^{-1}$ is the standard deviation of the $\Gamma_G$ values) led to an error of $\pm 47$ °C for $T_{max}$, which is lower than the cited error of $\pm 120$ °C by Cody et al. (2008).

$$\Delta T_{max} = \sqrt{\left(\frac{\partial}{\delta c} T_{max}\right)^2 \times \Delta c^2 + \left(\frac{\partial}{\partial \Gamma_G} T_{max}\right)^2 \times \Delta\Gamma_G^2} \quad (4)$$

Type 2 graphite spectra were excluded from the calculations because the high D-band seems to affect the G-band FWHM. This effect on the FWHM could be due to polishing effects, which can lead to an unpredictable increase of the D-band (Lasithiotakis et al., 2020).

### Field Emission Gun Electron Probe Microanalysis

WDS was performed on the cores of silicate grains to identify olivine and low-Ca pyroxene and to measure $Cr_2O_3$ contents for the Cr-based geothermometer by Collinet and Grove (2020).

In NWA 3140, olivine grains show mean composition Fo$_{80.5}$, while low-Ca pyroxenes have a mean composition En$_{77}$Wo$_{6.2}$ (Table 3). The homogeneity of

silicates in NWA 3140 shows that the sample experienced equilibrium and enabled the application of the Cr-based geothermometer, which led to a mean temperature of ~1215 ± 16 °C. Here, the error was calculated using $D_{Cr}^{oliv-LCP}$ from combining the lowest to lowest, highest to highest, lowest to highest, and highest to lowest Cr contents in olivine and pyroxene, respectively, and eventually by calculating a standard deviation of these temperatures.

NWA 6871 contains olivine with mean composition Fo$_{85.5}$. Low-Ca pyroxenes show a composition En$_{88.2}$Wo$_{1.2}$, but also three grains with higher Wo contents of Wo$_{30.1}$, Wo$_{27.3}$, and Wo$_{8.4}$ have been identified. The comparably high standard deviation of the $Cr_2O_3$ content in pyroxenes in NWA 6871 makes the geothermometer inapplicable to this sample, because the sample evidently did not reach equilibrium. Hence, no temperature was calculated for silicates in NWA 6871.

### DISCUSSION

The results confirm that NWA 6871 is a highly shocked ureilite. This can be seen in the recrystallization of 20 μm sized olivine grains forming olivine aggregates, but also in the small grain size of pyroxene. Melting and recrystallization of olivine and pyroxene start at very high pressures of ~60 and ~70 GPa, respectively (Stöffler et al., 2018). Therefore,

Fig. 6. Reconstructed diffraction images (a,c,e) of three carbon aggregates of NWA 6871 with their corresponding diffractograms (b,d,f). a–c) Powder rings for diamond and graphite. In addition to powder rings in (e), diffraction spots can be seen; in detail, see the arrow indicating the *d*-spacing of 1.26 Å for diamond. To provide better readability, not all peaks have been marked. Mineral abbreviations: Dia = diamond, Goe = goethite, Gra = graphite, Mag = magnetite, Ol = olivine, Tro = troilite.

Table 1. 2θ and *d*-spacing of diamond and graphite from carbon-bearing aggregates of NWA 6871 and NWA 3140, which were used to calculate the crystallite sizes using the Scherrer Equation (1).

| Sample | Diamond | | | Graphite | | |
|---|---|---|---|---|---|---|
| | 2θ (°) | *d*-spacing (Å) | *L* (nm) | 2θ (°) | *d*-spacing (Å) | *L* (nm) |
| NWA 6871_1 | n.d. | n.d. | n.d. | 12.11 | 3.36 | 9 |
| NWA 6871_2 | 32.62 | 1.27 | 6 | 12.19 | 3.34 | 7 |
| | 38.46 | 1.07 | 6 | n.d. | n.d. | n.d. |
| NWA 6871_3 | 32.66 | 1.27 | 7 | 12.12 | 3.35 | 9 |
| | 38.52 | 1.07 | 6 | n.d. | n.d. | n.d. |
| NWA 6871_4 | 32.65 | 1.27 | 6 | 12.10 | 3.35 | 7 |
| | 38.47 | 1.07 | 5 | n.d. | n.d. | n.d. |
| NWA 6871_5 | 32.95 | 1.27 | 5 | n.d. | n.d. | n.d. |
| | 38.77 | 1.07 | 7 | n.d. | n.d. | n.d. |
| NWA 6871_6 | 32.69 | 1.27 | 5 | 12.20 | 3.34 | 5 |
| | 38.49 | 1.07 | 5 | n.d. | n.d. | n.d. |
| NWA 3140_1 | 32.61 | 1.27 | 7 | 12.11 | 3.34 | 5 |
| | 38.44 | 1.07 | 4 | n.d. | n.d. | n.d. |
| NWA 3140_2 | 32.61 | 1.26 | 10 | 12.14 | 3.34 | 9 |
| | 38.6 | 1.07 | 4 | n.d. | n.d. | n.d. |

n.d. = not detected.

our observations are in good agreement with the shock classification of S6 by Bunch et al. (2012), although we prefer to classify it as U-S6 after the new classification system by Stöffler et al. (2018). NWA 6871 contains blade-shaped carbon aggregates consisting of nanographite and micro- and nanodiamond (with stacking faults) accompanied by Fe-bearing phases. The blade-shaped morphologies resemble euhedral millimeter-sized graphite crystals, which typically occur in ureilites with very low shock degrees (Berkley & Jones, 1982; Treiman & Berkley, 1994). Generally, the blade-shaped structures appear parallel to the longest dimension of the aggregates and therefore along the (0001) of graphite (Berkley & Jones, 1982; Treiman & Berkley, 1994). Nestola et al. (2020) argued that these morphologies cannot survive static high pressure for long inside a planetary body, because if diamonds had been formed deep inside a large planetary body, they would develop diamond morphologies instead of retaining graphite ones. Hence, what we see in our samples is nanographite and micro- and nanodiamond paramorphing pristine graphite crystals because of a very rapid transformation process such as a shock event.

NWA 3140 is, with a shock degree of U-S3, less shocked than NWA 6871. In NWA 3140, no blade-like structures can be seen in carbon aggregates. Moreover, the carbon aggregates in NWA 3140 show amoeboid shapes, which have also been reported for low-shocked ureilites, for example, ALH 77257 by Nakamuta et al. (2016). Internally however, the carbon

aggregates are similar to those in NWA 6871, showing the coexistence of nanographite, nanodiamond, and microdiamond accompanied by Fe-bearing phases. The temperature of ~1215 ± 16 °C recorded by silicates is in good agreement with equilibrium temperatures of other ureilites from the literature (see Collinet & Grove [2020] and references therein) and clearly shows that silicate-based geothermometers and the graphite-based geothermometer record different temperatures and therefore different events.

The occurrence of two carbon polymorphs and therefore the heterogeneous distribution of a shock product on a small scale can better be explained by a heterogeneous propagation of the shock wave rather than by graphitization of diamond (see explanation below). Ogilvie et al. (2011) investigated the distribution of shock metamorphic effects in natural rocks and experiments and demonstrated that the shock distribution depends on the shock impedance contrast between grains and that shock effects can be amplified if the contrast is large. Carbon aggregates in ureilites usually occur interstitially between silicate grains. This can lead to an increased shock pressure on the carbon aggregates in comparison to the more rigid silicate grains surrounding them. Thus, depending on the surrounding material, carbon aggregates can experience different pressures which may be even higher than those recorded by the silicates. This heterogeneity occurs on a submillimeter scale and could be responsible for the different distribution of micro- and nanodiamond in a carbon aggregate.
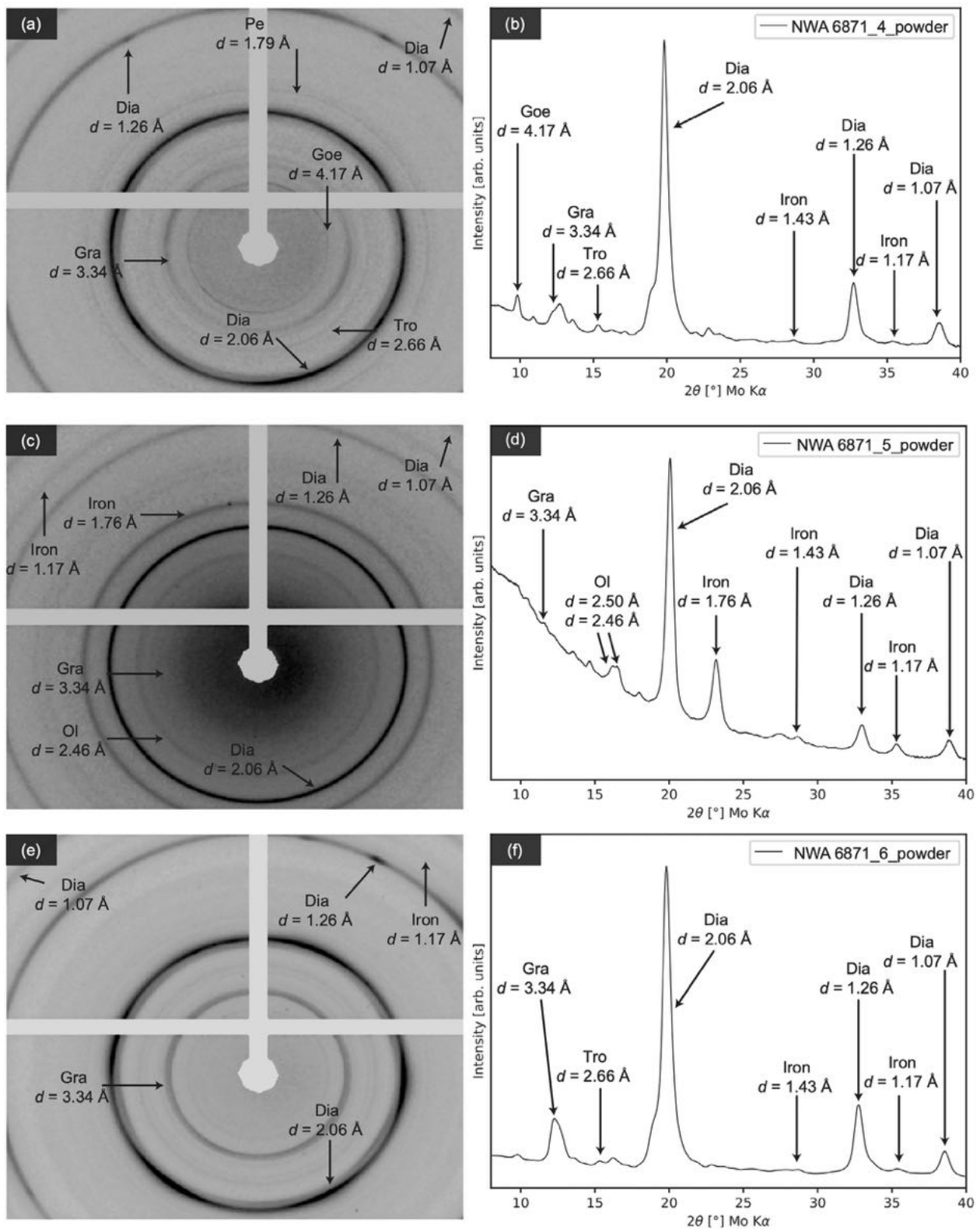
Fig. 7. Reconstructed diffraction images (a,c) of the three carbon aggregates NWA 3140 with their corresponding diffractograms (b,d). a) Diffraction spots can be seen; in detail, see the arrow indicating the *d*-spacing of 2.06 Å for diamond in (c). To provide better readability, not all peaks have been marked. Mineral abbreviations: Dia = diamond, Gra = graphite.

## Graphite

Graphite is the major constituent of carbon aggregates in NWA 6871 and NWA 3140. By MRS, we see the three already mentioned bands, of which the D-band at ~1352 cm$^{-1}$ indicates disordered graphite. In the X-ray diffractograms of NWA 6871, the graphite peak at *d*-spacing of 3.34 Å is rather broad and shows a peak asymmetry. This could be explained by an overlapping of the graphite peak with the peak of "compressed graphite," which is known to tail toward higher angles with slightly lower *d*-spacings (here 3.20 Å; Endo et al., 1994; Nakamuta & Aoki, 2000).

Generally, compressed graphite is characterized by a smaller interplanar spacing compared to uncompressed graphite (Endo et al., 1994). In ureilites, compressed graphite has been proposed as evidence that ureilitic diamonds formed by transformation of graphite under high pressure and temperature conditions (e.g., Hezel et al., 2008; Nakamuta & Aoki, 2000).

The grain size reduction from micrometer- to nanometer-sized graphite occurred either during the shock event that destroyed the UPB or during one that destroyed a UDB, as discussed by Barbaro et al. (2020). There are three different processes that cause the grain size reduction: (i) a back transformation
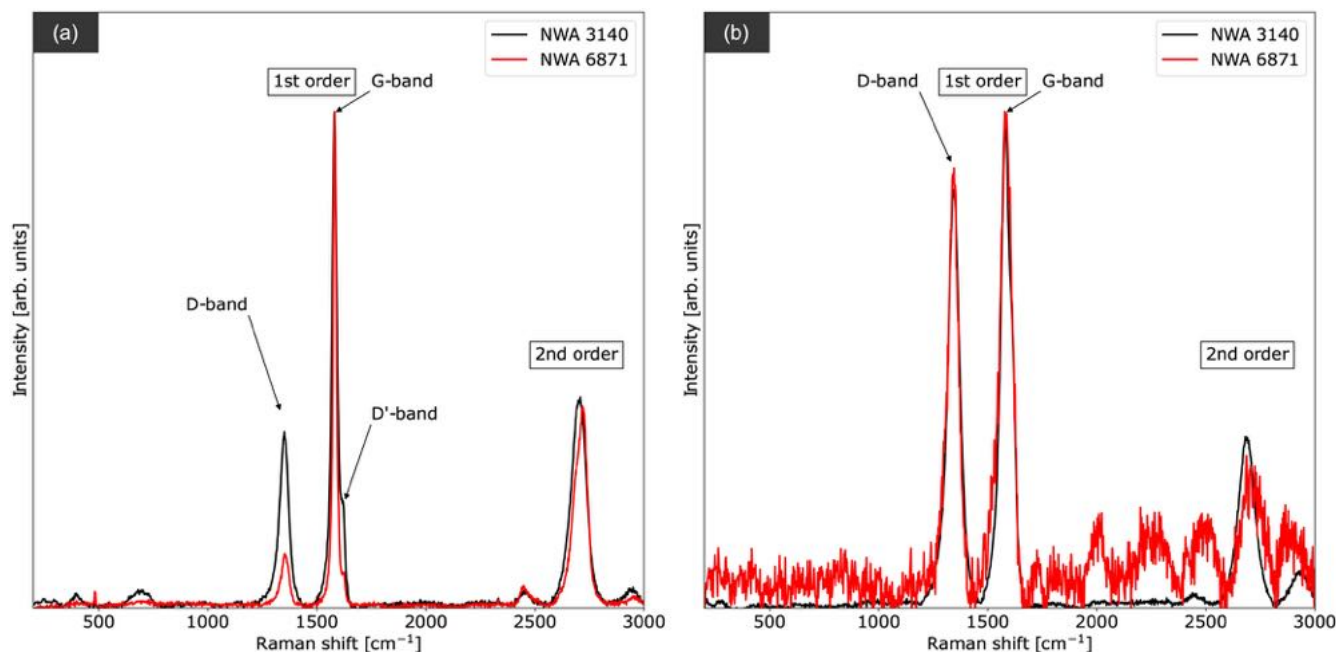
Fig. 8. a, b) Two types of Raman spectra for graphite in NWA 3140 and NWA 6871. (Color figure can be viewed at wileyonlinelibrary.com.)

from microdiamond, (ii) a back transformation from nanodiamond, or (iii) a grain size reduction from micrographite to nanographite during the impact event.

The back transformation of detonation-obtained microdiamond to nanographite has been investigated by Efremov and Zakatilova (2019). The authors have shown that detonation-produced microdiamond is stable to temperatures >1500 °C and only above these temperatures a graphitization process can be observed. However, this would mean that both the microdiamonds (the precursor of nanographite) and the nanographite were formed during the same event that lasted no longer than a few seconds and after which the parent/daughter body was quenched. Hence, this process is very unlikely. In contrast to that, the back transformation of nanodiamond to nanographite requires lower temperatures of >800 °C (Efremov et al., 2018). If graphitization took place from nanodiamond, it could be verified by TEM, with the aim to check for the presence of an "onion graphite structure" (Popov et al., 2013). However, this process could account for some of the nanographite in the vicinity of nanodiamonds, but not for all the nanographite that we see today, which would imply that graphite was entirely transformed to diamond and then back to graphite.

More likely, micrographite was reduced in size to nanographite during a shock event. This has been demonstrated by Veysset et al. (2015), who used laser-induced shock waves on highly ordered pyrolytic graphite which led to nanographite. Transferred to ureilites, this would mean that nanographite was simply created during the shock event when micrographite was broken apart by the shock wave.

Finally, we can exclude that the nanometric size is due to polishing. Polishing graphite with abrasive material can reduce its grain size (Lasithiotakis et al., 2020). However, this would only affect the surface and our XRD data clearly show that the fragments consist entirely of nanometric graphite as the X-ray beam probes the whole sample instead of just the surface.

### Diamond

Diamond can be found in both samples and shows nanometric grain sizes; however, single crystal diffraction spots can be seen in the diffraction images, indicating that both nano- and microdiamond coexist. In NWA 6871, diamond shows stacking disorders in some diffractograms, which are generally considered a shock indicator (Murri et al., 2019; Németh et al., 2014; Németh, McColl, Garvie, et al., 2020; Németh, McColl, Smith, et al., 2020; Salzmann et al., 2015). In contrast, diffractograms of NWA 3140 do not show such features at all. A possible explanation is that diamond stacking faults are also present in diamond from NWA 3140 and NWA 6871_2, but at a different extent not allowing XRD to detect it. The simultaneous occurrence of micro- and nanodiamond in a carbon aggregate can be

Table 2. Data obtained by Raman spectroscopy on carbon aggregates from NWA 6871 and NWA 3140 which were used to calculate the $T_{max}$ by using Equation (2). All data are given in cm$^{-1}$. The reported errors are the standard deviations of the respective sample.

| G-band center | G-band FWHM ($\Gamma_G$) | G-band FWHM ($\Gamma_G$) corrected | D-band center | D-band FWHM | D′-band center | D′-band FWHM | $T_{max}$ (°C) |
|---|---|---|---|---|---|---|---|
| NWA 6871 | | | | | | | |
| 1585 | 29 | 13.2 | 1350 | 43 | 1619 | 28 | 1314 |
| 1582 | 17 | 7.8 | 1353 | 40 | 1624 | 7 | 1432 |
| 1570 | 27 | 12.3 | n.d. | n.d. | 1607 | 24 | 1334 |
| 1579 | 24 | 11.0 | 1354 | 28 | 1616 | 21 | 1363 |
| 1582 | 26 | 11.9 | 1346 | 42 | 1615 | 22 | 1344 |
| 1584 | 26 | 11.9 | 1360 | 28 | 1619 | 20 | 1344 |
| 1584 | 25 | 11.4 | 1350 | 39 | 1621 | 9 | 1353 |
| 1583 | 24 | 11.0 | 1352 | 40 | 1621 | 16 | 1363 |
| 1582 | 18 | 8.2 | 1354 | 37 | 1623 | 8 | 1422 |
| 1581 | 17 | 7.8 | 1352 | 45 | n.d. | n.d. | 1432 |
| 1583 | 23 | 10.5 | 1349 | 51 | 1619 | 23 | 1373 |
| 1572 | 21 | 9.6 | 1341 | 47 | 1610 | 19 | 1393 |
| 1584 | 27 | 12.3 | 1350 | 41 | 1620 | 19 | 1334 |
| | | | | | | | 1370 ± 39 |
| NWA 3140 | | | | | | | |
| 1583 | 22 | 10.0 | 1351 | 38 | 1621 | 18 | 1383 |
| 1584 | 21 | 9.6 | 1344 | 41 | n.d. | n.d. | 1393 |
| 1582 | 25 | 11.4 | 1351 | 41 | n.d. | n.d. | 1353 |
| 1582 | 25 | 11.4 | 1353 | 60 | 1624 | 14 | 1353 |
| 1579 | 27 | 12.3 | 1344 | 69 | 1616 | 21 | 1334 |
| 1581 | 22 | 10.0 | 1349 | 42 | 1620 | 16 | 1383 |
| 1584 | 25 | 11.4 | 1352 | 41 | 1622 | 13 | 1353 |
| 1580 | 23 | 10.5 | 1348 | 39 | 1618 | 16 | 1373 |
| 1574 | 25 | 11.4 | 1347 | 38 | 1613 | 12 | 1353 |
| 1571 | 23 | 10.5 | n.d. | n.d. | n.d. | n.d. | 1373 |
| 1581 | 25 | 11.4 | 1349 | 42 | 1619 | 14 | 1353 |
| 1571 | 23 | 10.5 | 1337 | 48 | n.d. | n.d. | 1373 |
| 1581 | 17 | 7.8 | 1350 | 36 | n.d. | n.d. | 1432 |
| 1574 | 23 | 10.5 | 1346 | 39 | n.d. | n.d. | 1373 |
| 1581 | 19 | 8.7 | 1352 | 36 | 1623 | 7 | 1413 |
| 1582 | 32 | 14.6 | 1347 | 47 | n.d. | n.d. | 1283 |
| | | | | | | | 1368 ± 33 |

n.d. = not detected.

explained by the availability of a catalyst. As Varfolomeeva (1971) has shown, using a catalyst for the direct transformation of graphite to diamond, microdiamond forms in the vicinity of the catalyst while nanodiamond forms farther away from the catalyst.

**Fe-Bearing Phases**

The carbon aggregates are accompanied by Fe-bearing phases (e.g., kamacite, taenite, troilite, goethite, and magnetite), of which taenite is very rare and considered to originate from the impactor (Ross et al., 2019). Fe-bearing phases can be observed in many ureilites (e.g., Barbaro et al., 2020, 2021, 2022; Goodrich, 1992; Goodrich et al., 2013; Nakamuta et al., 2016; Nestola et al., 2020; Ross et al., 2019). These phases could act as a catalyst for the direct graphite-to-diamond transformation requiring lower $P,T$-conditions. After Goodrich et al. (2013), Fe-bearing phases in ureilites originate from an Fe-Ni-C melt. In our samples, remnants of this melt can be seen as Fe-bearing phases located in or around carbon aggregates but also in between silicates and in their rims. The important role of Fe-Ni melt for microdiamond (of up to 100 μm in size) formation in ureilites has been discussed by Nestola et al. (2020) and Barbaro et al. (2022), who showed that with the help of a catalyst, microdiamond can be formed at pressures of at least 15 GPa even within a few seconds of impact duration, which is in agreement with our samples.

Table 3. Mean compositions for olivine and low-Ca pyroxene grains in NWA 6871 and NWA 3140. The temperature was calculated using equation (3).

| Sample | NWA 6871 | | NWA 3140 | |
|---|---|---|---|---|
| Mineral | Olivine | Low-Ca pyroxene | Olivine | Low-Ca pyroxene |
| $SiO_2$ | 39.94 | 57.45 | 39.02 | 55.47 |
| σ | 0.46 | 0.84 | 0.30 | 0.23 |
| $TiO_2$ | b.d.l. | 0.01 | 0.01 | 0.06 |
| σ | n.d. | 0.01 | 0.01 | 0.01 |
| $Al_2O_3$ | 0.05 | 0.05 | b.d.l. | 0.47 |
| σ | 0.08 | 0.05 | n.d. | 0.03 |
| $Cr_2O_3$ | 0.87 | 0.78 | 0.71 | 1.10 |
| σ | 0.43 | 0.12 | 0.02 | 0.02 |
| MgO | 45.55 | 34.03 | 41.95 | 28.33 |
| σ | 1.17 | 1.49 | 0.47 | 0.16 |
| FeO | 13.74 | 7.36 | 18.15 | 11.06 |
| σ | 0.95 | 1.09 | 0.54 | 0.25 |
| CaO | 0.49 | 0.89 | 0.33 | 3.16 |
| σ | 0.79 | 1.15 | 0.01 | 0.05 |
| MnO | 0.47 | 0.34 | 0.42 | 0.41 |
| σ | 0.04 | 0.07 | 0.02 | 0.02 |
| $n$ | 24 | 14 | 16 | 18 |
| $D_{Cr}^{oliv-LCP}$ | n.a. | | 0.647 | |
| $T$ (°C) | n.a. | | 1215 | |

Detection limits: Si = 136 ppm, Ti = 173 ppm, Al = 143 ppm, Fe = 374 ppm, Mn = 361 ppm, Mg = 118 ppm, Ca = 157 ppm, Cr 294 ppm.

b.d.l. = below detection limit, n.d. = not determined.

## Origin of Diamond in NWA 6871 and NWA 3140

NWA 6871 shows several shock indicators (olivine crystals are recrystallized, graphite is partly compressed, and stacking faults are present in diamond). The shock indicator in olivine indicates pressure of up to 60–70 GPa, which is more than sufficient to transform graphite to diamond.

While nanosized diamond forms as a product of shock without any catalyst, microdiamond formed with catalyzing metals. With the availability of a catalyst, there is no necessity for the formation of micrometric diamond under static high pressure over long periods deep inside a large planetary body. The occurrence of diamond in both sizes could be explained by the availability of a catalyst, the short duration of the shock event, and the general heterogeneous distribution of shock effects, which is known from laboratory experiments and natural rocks (Ogilvie et al. [2011] and references therein). According to Ogilvie et al. (2011), such "extreme disequilibrium at the micrometer scale" can only be explained by extremely short-lived events, that is, shock events.

NWA 3140 is less shocked than NWA 6871 and experienced shock pressures of only up to 15 GPa as

seen by its silicates. While 15 GPa is also sufficient to transform graphite directly to diamond, indicative features for this process are absent (compressed graphite, stacking faults in diamond at the scale observable by XRD), but the carbon associations show the same mineralogical composition as in NWA 6871. However, pressure alone does not transform graphite to diamond, also high temperatures must be involved.

Compared to available literature data for temperature records in graphite from ureilites (Barbaro et al., 2020, 2021, 2022; Ross et al., 2011), NWA 6871 and NWA 3140 record the highest temperature measured so far (Table 4). The temperature obtained by graphite-based geothermometry has been ascribed to the shock event that destroyed the UPB/UDB and triggered the formation of diamond from graphite (Barbaro et al., 2020, 2021, 2022). The temperatures of 1370 ± 120 °C and 1368 ± 120 °C further prove this assumption as such high temperatures exclude a magmatic origin for this graphite because as silicate and chromite-based geothermometers have shown, the equilibrium temperatures of several ureilites range between 1054 and 1276 °C, a temperature range in which also our data based on the Cr-based geothermometer in NWA 3140 falls. Unfortunately, due to disequilibrium conditions, it was not possible to apply the same geothermometer to NWA 6871. The temperatures of ~1370 °C as estimated from graphite fall into the catalytic diamond synthesis field as shown in the carbon phase diagram in Dobrzhinetskaya (2012). This makes it very likely that diamond from NWA 3140 also formed during the shock event that destroyed the UPB/UDB. However, NWA 6871 has experienced higher pressures and the peak temperature was probably higher than catalytic synthesis requires. It would be intuitive to assume a correlation between temperatures recorded by graphite and the shock degree of the individual ureilite. However, NWA 3140 shows that this is not the case because here a medium shocked sample shows the same high temperature as the highly shocked sample NWA 6871 and considering the error of ±120 °C, also the literature temperatures are in relatively good agreement to each other. Hence, no linear correlation can be observed and, as Stöffler et al. (2018) pointed out, the temperature increase during shock depends on multiple factors including porosity and shock impedance of the constituents of the parent body. Especially porosity has a major influence on the temperature increase as shown in fig. 2 in Stöffler et al. (2018). Here, at a given temperature, the pressure increase can differ on the scale of a magnitude depending on the porosity of the target rock. Unfortunately, we lack information about the current and initial porosities of both samples and the initial

Table 4. Average $T_{max}$ in °C as recorded from graphite in different ureilites based on the graphite thermometer by Cody et al. ([2008]). The temperature uncertainty is ±120°C.

| Sample | AhS #7[1] | Kenna[2] | AhS 209[3] | AhS 72[3] | AhS A135A[3] | Y-74123[4] | NWA 6871[5] | NWA 3140[5] |
|---|---|---|---|---|---|---|---|---|
| Shock | Medium | Medium | Medium | Medium | Medium/high | Medium/high | High | Medium |
| $T_{max}$ (°C) | 990 | 1180 | 1266 | 1242 | 1332 | 1314 | 1370 | 1368 |

[1]Ross et al. ([2011]); [2]Barbaro et al. ([2021]); [3]Barbaro et al. ([2020]); [4]Barbaro et al. ([2022]); [5]this study.

porosities in the samples could have been higher before the impact/collision event(s).

In summary, there are four parameters which control the formation of micro- and nanodiamond in ureilites: (i) availability and location of the catalyst that triggers the graphite to diamond formation at lower pressures and temperatures, (ii) different shock wave propagation, (iii) shock impedance that controls the pressure distribution, and (iv) porosity that controls the temperature increase.

## CONCLUSIONS

Microdiamond associated with Fe-bearing phases but also nanodiamond and nanographite can be found by single crystal XRD in medium and highly shocked ureilites. Thus, our study further proves the formation of (micro)diamond by shock events. The size of microdiamonds, however, is difficult to determine if the extracted carbon aggregate does not consist entirely of microdiamond as was reported for one aggregate in NWA 7983 by Nestola et al. ([2020]). With $1370 \pm 120$ °C and $1368 \pm 120$ °C, graphite in the two differently shocked ureilites NWA 6871 and NWA 3140 records the highest temperatures ever reported for ureilites, and the temperature is in good agreement with temperatures required for diamond synthesis through metal catalysis (see carbon phase diagram in Dobrzhinetskaya, [2012]). Furthermore, these temperatures exceed the equilibration temperature of $1215 \pm 16$ °C recorded by silicates, which indicates that both thermometers record different events. We conclude that nanographite appears to record temperatures that were reached during the shock event that formed microdiamonds and nanodiamonds. However, the temperature is not correlated with the shock degree of the specific ureilite.

*Editorial Handling*—Dr. Christian Koeberl

## REFERENCES

Barbaro, A., Domeneghetti, M. C., Goodrich, C. A., Meneghetti, M., Litti, L., Fioretti, A. M., Jenniskens, P., Shaddad, M. H., and Nestola, F. 2020. Graphite-Based Geothermometry on Almahata Sitta Ureilitic Meteorites. *Minerals* 10: 1005.

Barbaro, A., Domeneghetti, M. C., Litasov, K. D., Ferrière, L., Pittarello, L., Christ, O., Lorenzon, S., Alvaro, M., and Nestola, F. 2021. Origin of Micrometer-Sized Impact Diamonds in Ureilites by Catalytic Growth Involving Fe-Ni-Silicide: The Example of Kenna Meteorite. *Geochimica et Cosmochimica Acta* 309: 286–98.

Barbaro, A., Nestola, F., Pittarello, L., Ferrière, L., Murri, M., Litasov, K. D., Christ, O., Alvaro, M., and Domeneghetti, M. C. 2022. Characterization of Carbon Phases in Yamato 74123 Ureilite to Constrain the Meteorite Shock History. *American Mineralogist* 107: 377–84.

Berkley, J. L., and Jones, J. H. 1982. Primary Igneous Carbon in Ureilites: Petrological Implications. *Journal of Geophysical Research* 87: A353–64.

Bovenkerk, H. P., Bundy, F. P., Hall, H. T., Strong, H. M., and Wentorf, R. H. 1959. Preparation of Diamond. *Nature* 184: 1094–8.

Bunch, T. E., Wittke, J. H., Irving, A. J., Kuehner, S. M., and Sipiera, P. P. 2012. Three Very Highly Shocked Ureilites NWA 4165, NWA 6871 and NWA 7195: Evidence for Recrystallization and Melting of Silicates and Vaporization of Graphite and Diamond. *Meteoritics & Planetary Science* 47: 5240.

Bundy, F. P., Hall, H. T., and Strong, H. M. 1955. Man-Made Diamonds. *Nature* 176: 51–5.

Chikami, J., Mikouchi, T., Takeda, H., and Miyamoto, M. 1997. Mineralogy and Cooling History of the Calcium-Aluminum-Chromium Enriched Ureilite, Lewis Cliff 88774. *Meteoritics & Planetary Science* 32: 343–8.

Cody, G. D., Alexander, C. M. O'D., Yabuta, H., Kilcoyne, A. L. D., Araki, T., Ade, H., Dera, P., Fogel, M., Militzer, B., and Mysen, B. O. 2008. Organic

Thermometry for Chondritic Parent Bodies. *Earth and Planetary Science Letters* 272: 446–55.

Collinet, M., and Grove, T. L. 2020. Incremental Melting in the Ureilite Parent Body: Initial Composition, Melting Temperatures, and Melt Compositions. *Meteoritics & Planetary Science* 55: 832–56.

Desch, S. J., O'Rourke, J. G., Schaefer, L. K., Sharp, T. G., and Schrader, D. L. 2019. Diamonds in Ureilites from Mars (Abstract #2132). 50th Lunar and Planetary Science Conference. CD-ROM.

Dobrzhinetskaya, L. F. 2012. Microdiamonds—Frontier of Ultrahigh-Pressure Metamorphism: A Review. *Gondwana Research* 21: 207–23.

Downes, H., Mittlefehldt, D. W., Kita, N. T., and Valley, J. W. 2008. Evidence from Polymict Ureilite Meteorites for a Disrupted and Re-Accreted Single Ureilite Parent Asteroid Gardened by Several Distinct Impactors. *Geochimica et Cosmochimica Acta* 72: 4825–44.

Efremov, V. P., and Zakatilova, E. I. 2019. Spectroscopic Methods of Investigation and the Thermal Stability of Detonation Nanodiamonds. *Journal of Physics: Conference Series* 1238: 12013.

Efremov, V. P., Zakatilova, E. I., Maklashova, I. V., and Shevchenko, N. V. 2018. Thermal Stability of Detonation-Produced Micro and Nanodiamonds. *Journal of Physics: Conference Series* 946: 12107.

Endo, S., Idani, N., Oshima, R., Takano, K. J., and Wakatsuki, M. 1994. X-Ray Diffraction and Transmission-Electron Microscopy of Natural Polycrystalline Graphite Recovered from High Pressure. *Physical Review B* 49: 22–7.

Ferrari, A., and Robertson, J. 2000. Interpretation of Raman Spectra of Disordered and Amorphous Carbon. *Physical Review B—Condensed Matter and Materials Physics* 61: 14095–107.

Fukunaga, K., Matsuda, J., Nagao, K., Miyamoto, M., and Ito, K. 1987. Noble-Gas Enrichment in Vapour-Growth Diamonds and the Origin of Diamonds in Ureilites. *Nature* 328: 141–3.

Gillet, P., and El Goresy, A. 2013. Shock Events in the Solar System: The Message from Minerals in Terrestrial Planets and Asteroids. *Annual Review of Earth and Planetary Sciences* 41: 257–85.

Goodrich, C. A. 1992. Ureilites: A Critical Review. *Meteoritics* 27: 327–52.

Goodrich, C. A., Ash, R. D., Van Orman, J. A., Domanik, K., and McDonough, W. F. 2013. Metallic Phases and Siderophile Elements in Main Group Ureilites: Implications for Ureilite Petrogenesis. *Geochimica et Cosmochimica Acta* 112: 340–73.

Goodrich, C. A., Harlow, G. E., Van Orman, J. A., Sutton, S. R., Jercinovic, M. J., and Mikouchi, T. 2014. Petrology of Chromite in Ureilites: Deconvolution of Primary Oxidation States and Secondary Reduction Processes. *Geochimica et Cosmochimica Acta* 135: 126–69.

Goodrich, C. A., Hartmann, W. K., O'Brien, D. P., Weidenschilling, S. J., Wilson, L., Michel, P., and Jutzi, M. 2015. Origin and History of Ureilitic Material in the Solar System: The View from Asteroid 2008 TC$_3$ and the Almahata Sitta Meteorite. *Meteoritics & Planetary Science* 50: 782–809.

Goodrich, C. A., Nestola, F., Jakubek, R., Erickson, T., Fries, M., Fioretti, A. M., Ross, D. K., and Brenker, F. E. 2020. The Origin of Diamonds in Ureilites (Abstract #1411). 51st Lunar and Planetary Science Conference. CD-ROM.

Goodrich, C. A., Scott, E. R. D., and Fioretti, A. M. 2004. Ureilitic Breccias: Clues to the Petrologic Structure and Impact Disruption of the Ureilite Parent Asteroid. *Geochemistry* 64: 283–327.

Herrin, J. S., Zolensky, M. E., Ito, M., Le, L., Mittlefehldt, D. W., Jenniskens, P., Ross, A. J., and Shaddad, M. H. 2010. Thermal and Fragmentation History of Ureilitic Asteroids: Insights from the Almahata Sitta Fall. *Meteoritics & Planetary Science* 45: 1789–803.

Hezel, D. C., Dubrovinsky, L., Nasdala, L., Cauzid, J., Simionovici, A., Gellissen, M., and Schönbeck, T. 2008. In Situ Micro-Raman and X-Ray Diffraction Study of Diamonds and Petrology of the New Ureilite UAE 001 from The United Arab Emirates. *Meteoritics & Planetary Science* 43: 1127–36.

Irifune, T., Kurio, A., Sakamoto, S., Inoue, T., and Sumiya, H. 2003. Materials: Ultrahard Polycrystalline Diamond from Graphite. *Nature* 421: 599–600.

Kunz, G. F. 1888. Diamonds in Meteorites. *Science* 11: 118–9.

Lasithiotakis, M., Marrow, J. T., and Marsden, B. J. 2020. Evaluation of Damage Induced in Graphite Due to Sample Preparation by Standard Non-Destructive Techniques. *Materials Physics and Mechanics* 44: 271–87.

Lipschutz, M. E. 1964. Origin of Diamonds in the Ureilites. *Science* 143: 1431–4.

Matsuda, J.-I., Kusumi, A., Yajima, H., and Syono, Y. 1995. Noble Gas Studies in Diamonds Synthesized by Shock Loading in the Laboratory and Their Implications on the Origin of Diamonds in Ureilites. *Geochimica et Cosmochimica Acta* 59: 4939–49.

Mittlefehldt, D. W., McCoy, T. J., Goodrich, C. A., and Kracher, A. 1998. Non-Chondritic Meteorites from Asteroidal Bodies. *Reviews in Mineralogy and Geochemistry* 36: 1–195.

Miyahara, M., Ohtani, E., El Goresy, A., Lin, Y., Feng, L., Zhang, J.-C., Gillet, P., Nagase, T., Muto, J., and Nishijima, M. 2015. Unique Large Diamonds in a Ureilite from Almahata Sitta 2008 TC$_3$ Asteroid. *Geochimica et Cosmochimica Acta* 163: 14–26.

Morbidelli, A., Lunine, J. I., O'Brien, D. P., Raymond, S. N., and Walsh, K. J. 2012. Building Terrestrial Planets. *Annual Review of Earth and Planetary Sciences* 40: 251–75.

Murri, M., Smith, R. L., McColl, K., Hart, M., Alvaro, M., Jones, A. P., Németh, P., et al. 2019. Quantifying Hexagonal Stacking in Diamond. *Scientific Reports* 9: 10334.

Nabiei, F., Badro, J., Dennenwaldt, T., Oveisi, E., Cantoni, M., Hébert, C., El Goresy, A., Barrat, J.-A., and Gillet, P. 2018. A Large Planetary Body Inferred from Diamond Inclusions in a Ureilite Meteorite. *Nature Communications* 9: 1–6.

Nakamuta, Y., and Aoki, Y. 2000. Mineralogical Evidence for the Origin of Diamond in Ureilites. *Meteoritics & Planetary Science* 35: 487–93.

Nakamuta, Y., Kitajima, F., and Shimada, K. 2016. In Situ Observation, X-Ray Diffraction and Raman Analyses of Carbon Minerals in Ureilites: Origin and Formation Mechanisms of Diamond in Ureilites. *Journal of Mineralogical and Petrological Sciences* 111: 252–69.

Németh, P., Garvie, L. A. J., Aoki, T., Dubrovinskaia, N., Dubrovinsky, L., and Buseck, P. R. 2014. Lonsdaleite Is Faulted and Twinned Cubic Diamond and Does Not Exist as a Discrete Material. *Nature Communications* 5: 1–5.

Németh, P., McColl, K., Garvie, L. A. J., Salzmann, C. G., Murri, M., and McMillan, P. F. 2020. Complex Nanostructures in Diamond. *Nature Materials* 19: 1126–31.

Németh, P., McColl, K., Smith, R. L., Murri, M., Garvie, L. A. J., Alvaro, M., Pécz, B., et al. 2020. Diamond-Graphene Composite Nanostructures. *Nano Letters* 20: 3611–9.

Nestola, F., Goodrich, C. A., Morana, M., Barbaro, A., Jakubek, R. S., Christ, O., Brenker, F. E., et al. 2020. Impact Shock Origin of Diamonds in Ureilite Meteorites. *Proceedings of the National Academy of Sciences* 117: 25310–8.

Ogilvie, P., Gibson, R. L., Reimold, W. U., Deutsch, A., and Hornemann, U. 2011. Experimental Investigation of Shock Metamorphic Effects in a Metapelitic Granulite: The Importance of Shock Impedance Contrast Between Components. *Meteoritics & Planetary Science* 46: 1565–86.

Popov, V. A., Egorov, A. V., Savilov, S. V., Lunin, V. V., Kirichenko, A. N., Denisov, V. N., Blank, V. D., Vyaselev, O. M., and Sagalova, T. B. 2013. Features of the Transformation of Detonation Nanodiamonds into Onion-Like Carbon Nanoparticles. *Journal of Surface Investigation, X-Ray, Synchrotron and Neutron Techniques* 7: 1034–43.

Rai, N., Downes, H., and Smith, C. 2020. Ureilite Meteorites Provide a New Model of Early Planetesimal Formation and Destruction. *Geochemical Perspectives Letters* 14: 20–5.

Ross, A. J., Downes, H., Herrin, J. S., Mittlefehldt, D. W., Humayun, M., and Smith, C. 2019. The Origin of Iron Silicides in Ureilite Meteorites. *Geochemistry* 79: 125539.

Ross, A. J., Steele, A., Fries, M. D., Kater, L., Downes, H., Jones, A. P., Smith, C. L., Jenniskens, P. M., Zolensky, M. E., and Shaddad, M. H. 2011. MicroRaman Spectroscopy of Diamond and Graphite in Almahata Sitta and Comparison with Other Ureilites. *Meteoritics & Planetary Science* 46: 364–78.

Ruzicka, A., Grossman, J. N., and Garvie, L. 2014. The Meteoritical Bulletin, No. 100. *Meteoritics & Planetary Science*, Wiley Online Library 49: E1–E101.

Sabbah, H., Morrow, A. L., Jenniskens, P., Shaddad, M. H., and Zare, R. N. 2010. Polycyclic Aromatic Hydrocarbons in Asteroid 2008 TC$_3$: Dispersion of Organic Compounds Inside Asteroids. *Meteoritics & Planetary Science* 45: 1710–7.

Salzmann, C. G., Murray, B. J., and Shephard, J. J. 2015. Extent of Stacking Disorder in Diamond. *Diamond and Related Materials* 59: 69–72.

Scherrer, P. 1918. Bestimmung der Größe und der inneren Struktur von Kolloidteilchen mittels Röntgenstrahlen. Nachrichten von der Gesellschaft der Wissenschaften zu Göttingen. Mathematisch-Physikalische Klasse.

Singletary, S. J., and Grove, T. L. 2003. Early Petrologic Processes on the Ureilite Parent Body. *Meteoritics & Planetary Science* 38: 95–108.

Sinha, S. K., Sack, R. O., and Lipschutz, M. E. 1997. Ureilite Meteorites: Equilibration Temperatures and Smelting Reactions. *Geochimica et Cosmochimica Acta* 61: 4235–42.

Stöffler, D., Hamann, C., and Metzler, K. 2018. Shock Metamorphism of Planetary Silicate Rocks and Sediments: Proposal for an Updated Classification System. *Meteoritics & Planetary Science* 53: 5–49.

Stöffler, D., Keil, K., and Edward, R. D. S. 1991. Shock Metamorphism of Ordinary Chondrites. *Geochimica et Cosmochimica Acta* 55: 3845–67.

Takeda, H. 1989. Mineralogy of Coexisting Pyroxenes in Magnesian Ureilites and Their Formation Conditions. *Earth and Planetary Science Letters* 93: 181–94.

Takeda, H., Mori, H., and Ogata, H. 1989. Mineralogy of Augite-Bearing Ureilites and the Origin of Their Chemical Trends. *Meteoritics* 24: 73–81.

Treiman, A. H., and Berkley, J. L. 1994. Igneous Petrology of the New Ureilites Nova 001 and Nullarbor 010. *Meteoritics* 29: 843–8.

Urey, H. C. 1956. Diamonds, Meteorites, and the Origin of the Solar System. *The Astrophysical Journal* 124: 623–37.

Varfolomeeva, T. D. 1971. Synthesis and Investigation of Polycrystalline Diamond. Ph.D. thesis, Institute for High Pressure Physics, USSR Academy of Sciences.

Veysset, D., Pezeril, T., Kooi, S., Bulou, A., and Nelson, K. A. 2015. Laser-Induced Versus Shock Wave Induced Transformation of Highly Ordered Pyrolytic Graphite. *Applied Physics Letters* 106: 161902.

Wacker, J. F. 1986. Noble Gases in the Diamond-Free Ureilite, ALHA 78019: The Roles of Shock and Nebular Processes. *Geochimica et Cosmochimica Acta* 50: 633–42.

Weber, I., Bischoff, A., and Weber, D. 2003. TEM Investigations on the Monomict Ureilites Jalanash and Hammadah al Hamra 064. *Meteoritics & Planetary Science* 38: 145–56.

Zhu, K., Moynier, F., Schiller, M., Wielandt, D., Larsen, K. K., Van Kooten, E. M. M. E., Barrat, J.-A., and Bizzarro, M. 2020. Chromium Isotopic Constraints on the Origin of the Ureilite Parent Body. *The Astrophysical Journal* 888: 126.

# 9 Appendix B - Co-Author Papers

Research Paper

# A chondrule formation experiment aboard the ISS: Experimental set-up and test experiments

Dominik Spahr [a,\*], Tamara E. Koch [a], David Merges [a], Anna A. Beck [a], Bernhard Bohlender [b], Johan M. Carlsson [c], Oliver Christ [a], Shintaro Fujita [d], Philomena-Theresa Genzel [a], Jochen Kerscher [d], Tobin Knautz [b], Miles Lindner [a], Diego Mederos Leber [a], Victor Milman [c], Wolfgang Morgenroth [a], Fabian Wilde [e], Frank E. Brenker [a], Björn Winkler [a]

[a] *Institute of Geosciences, Goethe University Frankfurt, Altenhöferallee 1, 60438 Frankfurt, Germany*
[b] *Institute of Applied Physics, Goethe University Frankfurt, Max-von-Laue-Str. 1, 60438 Frankfurt, Germany*
[c] *Dassault Systèmes BIOVIA, 335 Cambridge Science Park Rd, Cambridge, United Kingdom*
[d] *HackerSpace FFM e. V., Ludwig-Erhard-Str. 32, 61440 Oberursel, Germany*
[e] *Helmholtz-Zentrum Geesthacht, Max-Planck Strasse 1, 21502 Geesthacht, Germany*

ARTICLE INFO

ABSTRACT

The formation of chondrules in the solar nebula is still an enigmatic process. In order to reconstruct this process, we performed a chondrule formation experiment aboard the International Space Station (ISS), called EXCISS. The purpose of the EXCISS experiment is to acquire new insights in chondrule formation by "nebular lightnings". During the experiment, forsterite ($Mg_2SiO_4$) particles were repeatedly exposed to arc discharges under long-term micro-gravity conditions. The purpose of this paper is to describe the experimental set-up and establish and benchmark approaches for the analysis of the samples once they are returned from the ISS. We produced aggregates of fused $Mg_2SiO_4$ particles in our Earth-based experiment which we studied by SEM and X-ray microtomography. The results of our preliminary Earth-based experiments indicate that the chosen experimental parameters will likely lead to melting of $Mg_2SiO_4$ particles and the formation of aggregates. The results from the first experiments aboard the ISS revealed that the EXCISS experiment is fully operational.

## 1. Introduction

In order to provide experimental evidence for the formation of chondrules by "nebular lightning" (Whipple, 1966; Horányi et al., 1995; Desch and Cuzzi, 2000; Túnyi et al., 2003; Güttler et al., 2008; Johansen and Okuzumi, 2018), we initiated an experiment aboard the International Space Station (ISS). The experiment is named EXCISS (**Ex**perimental **C**hondrule formation aboard the **ISS**) and was launched on 17th November 2018 with space flight Cygnus NG-10.

### 1.1. Chondrules and their formation

Chondrules are small spherical objects of varying sizes which can be found in many primitive meteorites (Russel et al., 2018). While most of them have diameters in the sub-mm range, also cm-sized chondrules have been found (Weisberg et al., 2001). Chondrules belong, together with calcium-aluminum-rich inclusions, to the oldest material of our solar system. Most of the models for planet and planetesimal formation consider chondrules as the building blocks of our solar system (Russel

et al., 2018). Despite their great abundance and numerous studies carried out for over 150 years, the processes leading to the formation of chondrules are still disputed controversially (Boss, 1996; Kerr, 2013; Connolly and Jones, 2016).

The textures of chondrules indicate that they crystallized from a melt. A realistic model for chondrule formation should be consistent with their typical microstructures, indicating high peak temperatures of 1600–2000 K, and fast cooling rates of 10–10000 $Kh^{-1}$ (Libourel and Portail, 2018). Also, there is a complementarity in the distribution of refractory elements between chondrules and matrix, i.e. while chondrules and matrix have different compositions, the bulk composition is that of CI chondrites, which a realistic model should be able to explain (Hewins and Connolly, 1996; Alexander et al., 2000; Desch and Connolly Jr., 2002; Hezel and Palme, 2010; Palme et al., 2015; Budde et al., 2016; Libourel and Portail, 2018).

Most chondrule formation models assume that the formation occurred in the early solar nebula environment (Youdin and Shu, 2002;

---

Morris et al., 2012; Johansen and Okuzumi, 2018). In the last decades, the formation of chondrules by shock waves (Connolly and Love, 1998; Ciesla and Hood, 2002) or by nebular lightnings (Whipple, 1966; Horányi et al., 1995; Desch and Cuzzi, 2000; Túnyi et al., 2003; Güttler et al., 2008; Johansen and Okuzumi, 2018) has been suggested. Alternatively, their formation by collisions of planetesimals (Krot et al., 2005; Asphaug et al., 2011; Johnson et al., 2015; Lichtenberg et al., 2018) has been proposed. The very young ages of chondrules found in CB chondrites (about 5 Myr younger than chondrules in CV chondrites) and their unique geochemical properties indicate that chondrules of this chondrite type might have formed at a different period and setting during the evolution of our solar system (Krot et al., 2005).

The main strength of the "nebular lightning" theory is the explanation of the inferred fast cooling rates and the strongly varying thermal histories of different chondrules in the same meteorite sample. It is, however, uncertain if lightnings occurred in the solar nebula, and it has been debated whether they have provided enough energy to melt mm-sized particles. Recently, Johansen and Okuzumi (2018) published a study where they conclude that the escape of positrons released in the decay of the short-lived radionuclide $^{26}$Al would lead to charging of dust particles in the solar nebula, which would discharge through lightnings. The amount of energy in this case would be sufficient to melt almost all chondrules.

Fig. 1 shows a schematic illustration of a possible chondrule formation process in the solar nebula by several heating events according to Scott (2007). The suggested multiple heatings may have been caused by lightnings.

### 1.2. Previous chondrule formation experiments

The number of experiments studying chondrule formation is rather limited (Wdowiak, 1983; Lofgren, 1996; Connolly et al., 1998; Hewins et al., 2000; Hewins and Fox, 2004; Güttler et al., 2008; Morlok et al., 2012; Imae and Isobe, 2017). Most of the experimental work focused on changes of textural and geochemical properties as a function of cooling rates (Lofgren, 1996; Connolly et al., 1998; Hewins and Fox, 2004). These experiments reproduced many properties of chondrules, but of course suffered from the influence of gravity. Wdowiak (1983) was the first to expose chondrules from the Allende meteorite to lightnings, while Güttler et al. (2008) subjected dust aggregates to electrical discharges. Both experimental studies did not show compelling evidence for the formation of chondrules due to lightning, but the relevance of these findings is limited due to the influence of gravity and the specific experimental parameters (e. g. energy, duration of the lightnings, gas pressure), which preclude a generalization of their results. Morlok et al. (2012) accelerated a mixture of silicate, sulfide and metal particles (100–500 μm) into a fixed arc plasma, thus studying the role of heated gas produced by a shock wave. The experiment produced a small amount of round, molten objects of different phases with diameters ranging from a few microns to about 100 μm.

### 1.3. Preparation of the EXCISS experiment

Our experiment is designed to study the behavior of $Mg_2SiO_4$ (forsterite) particles in a long-term micro-gravity environment aboard the ISS while they are exposed to repeated arc discharges. Forsterite was chosen as it is the most abundant mineral phase in natural chondrules (Russel et al., 2018). Here we describe the development of the experimental set-up, first laboratory-based experiments, aimed to establish optimal parameters for the ISS-based experiments, and the sample characterization. While our experiments resemble those of Güttler et al. (2008), we assume that by using energies lower by two orders of magnitude and substantially longer duration of the arc discharges we will avoid the fragmentation of aggregates, but will rather observe their fusion. Because of the microgravity conditions aboard the ISS, the particles can move, collide and fuse induced only by the

lightning and its radiation without the influence of gravity or a directed movement caused by e. g. a gas flow. The experimental set-up described below fulfills all NASA safety requirements. Sample characterization included Raman spectroscopy, X-ray powder diffraction, scanning electron microscopy and synchrotron based X-ray microtomography. We also studied natural porphyric chondrules in order to demonstrate that it is possible to visualize the inner structure of chondrules.

## 2. Experimental

### 2.1. Sample preparation

We used two types of sample material in our experiments, namely synthetic forsterite and natural chondrules.

#### 2.1.1. Synthetic forsterite

We synthesized $Mg_2SiO_4$ pellets from the oxides as sample material. They were ground mechanically for a few seconds in an agate mortar. The resulting powder was elutriated with distilled water to remove particles with a grain size much smaller than 80 μm. After drying the powder in an oven at atmospheric conditions at 353(1) K it was sifted with sieves having 80 μm and 120 μm mesh size respectively. The particles which passed through the 120 μm but not the 80 μm sieve were used for the experiment. The sample material was finally washed with isopropyl alcohol and dried again. The melting point of the forsterite end-member is $\approx 2200$ K (Bowen and Schairer, 1925).

#### 2.1.2. Natural chondrules

Individual chondrules were separated from a fragment of the carbonaceous chondrite Allende (CV3) (Clarke Jr. et al., 1971). We used the high-voltage electrical pulse fragmentation system selFrag-Lab from Ammann Schweiz AG to crush the chondrite fragment. The electrical pulse fragmentation technique allows to separate components of rocks along their grain boundaries without being abrasive. The selected chondrite fragment had a dimension of $\approx 1 \times 1 \times 0.5$ cm$^3$. It was placed on a sieve in a vessel filled with water, so the fragmented sample material could sink down and would not be exposed to further discharges. We used a pulse voltage of 110 kV with a repetition rate of 5 Hz for 10 s. The distance between both electrodes was 15 mm. The suspension was filtered and the retrieved fragments were dried at 353(1) K.

### 2.2. Sample characterization

#### 2.2.1. Powder diffraction and Raman spectroscopy

The synthetic $Mg_2SiO_4$ powder was analyzed by X-ray powder diffraction with a PANalytical X'Pert Pro powder diffractometer in Bragg–Brentano geometry. We used a PANalytical PIXcel$^{3D}$ detector and a X-ray tube with a copper anode in combination with a Johansson monochromator to obtain Cu K$_{\alpha 1}$ radiation. All instrument parameters were obtained by measuring and refining a Si-standard (99.999% purity). The sample measurements were performed with 1/4° fixed divergence slits in a range of $10° < 2\Theta < 110°$ with a scan speed of $0.04°$ min$^{-1}$ on an oriented Si single crystal sample holder. Rietveld refinement (Rietveld, 1969) was carried out using the software package GSAS-II (Toby and Von Dreele, 2013).

The $Mg_2SiO_4$ powder was further characterized by Raman spectroscopy with a set-up described in Bayarjargal et al. (2018). The set-up consists of an OXXIUS S.A. LaserBoxx LMX532 laser ($\lambda = 532.14$ nm) and a Pixis256E CCD camera mounted on a Princeton Instruments ACTON SpectraPro 2300i spectrograph. Theoretical Raman spectra were calculated by DFT-based model calculations using the CASTEP-package (Clark et al., 2005).
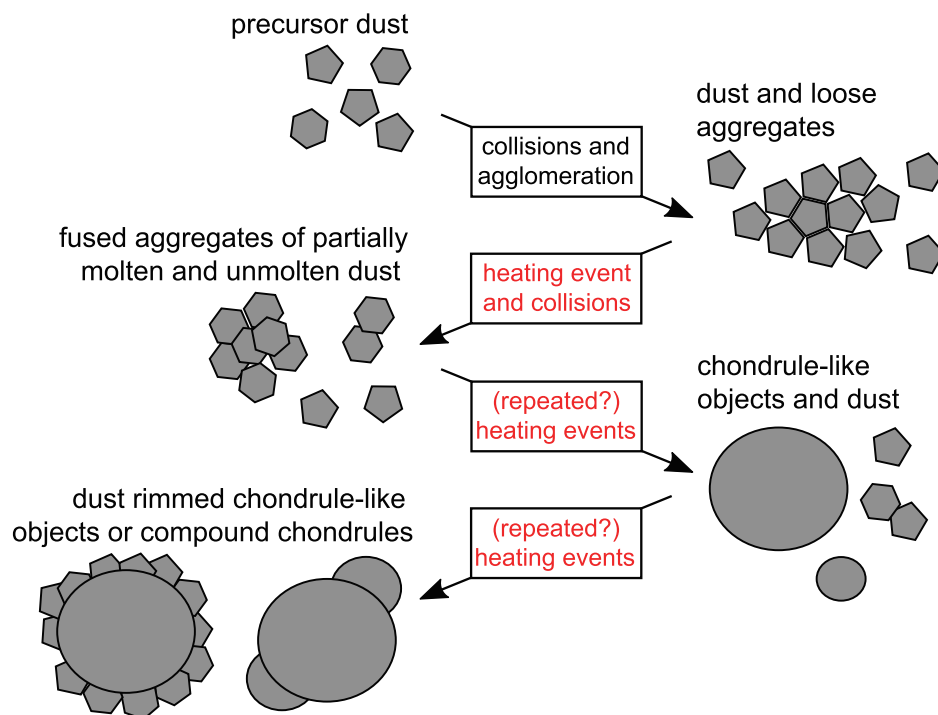
**Fig. 1.** Schematic illustration of the chondrule formation process. Dust particles were exposed to several electrical discharges. The chondrules grow by agglomeration and (partial-)melting of agglomerated particles.
*Source:* Adopted from Scott (2007).

### 2.2.2. Scanning electron microscopy

Scanning electron microscopy (SEM) was performed with a Phenom World ProX desktop SEM using an electron backscatter detector (BSE). Energy dispersive X-ray spectroscopy (EDX) was carried out with an integrated silicon drift detector for a semi-quantitative characterization of the composition. The samples were mounted without coating using sticky carbon tape on aluminum stubs. They were measured under low vacuum conditions to reduce charging effects on the sample. For imaging we used an acceleration voltage of 10 kV while for EDX analysis a voltage of 15 kV was employed. Multiple BSE images were acquired with different focal planes and combined afterwards with the Helicon Focus 7 Pro (Kozub et al., 2018) software from Helicon Soft to obtain images with an improved depth of field using the depth map rendering method with radius 8 (size of the analyzed area around each pixel) and smoothing 4 (value determines how depth map will be smoothed out). EDX data were analyzed using the Phenom Pro Suite software.

### 2.2.3. Synchrotron-based microtomography

Synchrotron-based microtomography was performed at PETRA III (DESY) in Hamburg, Germany. All data were collected on the microtomography beamline P05 (Wilde et al., 2016; Ogurreck et al., 2013), operated by Helmholtz-Zentrum Geesthacht, using a 15 keV beam monochromatized by a double crystal monochromator. The images were acquired using a 24× objective lens with a CMOS camera resulting in a $1.8 \times 1.8$ mm$^2$ field of view. We used an acquisition time of 350 ms. A binning factor of $2 \times 2$ pixel resulted in a binned pixel size of $\approx 0.61 \times 0.61$ μm$^2$. The Mg$_2$SiO$_4$ particles and the experimental products from the discharge experiments were embedded in two component epoxy adhesive UHU Plus Endfest 300 placed on 50 μm Kapton foil. The epoxy was cured under vacuum by heating it up to 333(2) K. The Kapton foil was glued with Henkel LOCTITE 493 on the sample holder. The natural chondrules were directly mounted with LOCTITE 493. Data pre-processing, including tomographic reconstruction was performed using MATLAB scripts provided by Moosmann et al. (2014). The microtomography reconstructions were visualized with the volume exploration software tool Drishti (Limaye, 2012).

## 3. Experimental set-up

We designed two different experimental set-ups, one for Earth-based experiments (sample chamber type I) and one for ISS-based experiments (sample chamber type II). Both set-ups allowed us to expose Mg$_2$SiO$_4$ particles to arc discharges. The experiments on Earth were carried out to design and calibrate the experimental set-up for the ISS experiment. A list of materials (Table S1) and figures of the experimental set-up can be found in the supplementary material section. Further, a detailed description of the calibration of the experimental set-up is provided there.

### 3.1. Sample chamber I

Sample chamber I (Fig. S1) was designed to allow a variation of the experimental conditions, such as gas composition and pressure or electrode material and shape. It consists of two KF-16 cross vacuum flanges connected to a vacuum pump and a gas supply. We used two different types of electrodes, W-electrodes similar to the ISS experiment (Fig. S3) and Cu-electrodes to allow a spectroscopic determination of the plasma temperature. Their distance was adjusted to be $\approx 3$ mm. Optical characterization of the arc discharge was enabled by a transparent window. Most experiments were carried out in a 100(1) mbar Ar atmosphere. A Ar/H$_2$ gas mixture at the same pressure was used for the temperature and electron density measurements. The forsterite dust particles were placed inside a 5 mm quartz glass tube mounted between the tips of the electrodes for the melting experiments.

### 3.2. Sample chamber II

Sample chambers of type II (Fig. S2, Fig. 2 left) made of quartz glass were developed for the ISS-based experiment. W-electrodes were embedded into the glass on opposite sides with $\approx$ 2–3 mm distance between the tips. A vacuum tight connection between electrodes and glass was achieved by a copper galvanization of the electrodes' surface. The Ar gas pressure inside the sample chambers was adjusted to
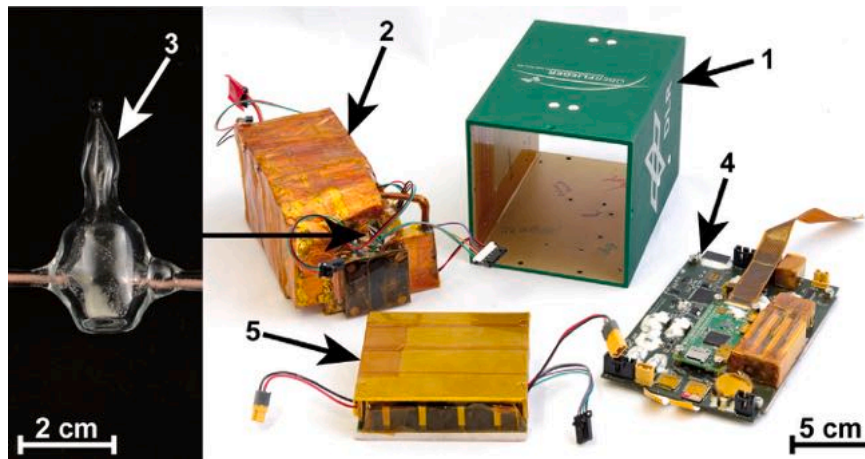
**Fig. 2.** Experimental set-up of the ISS-based experiment with NanoRacks NanoLab housing (1), arc generation unit and Raspberry PI camera with optics (2), a sample chamber of type II (3), EXCISS mainboard with Raspberry Pi Zero and mass storage devices (4) and power supply unit with lithium-ion batteries (5).
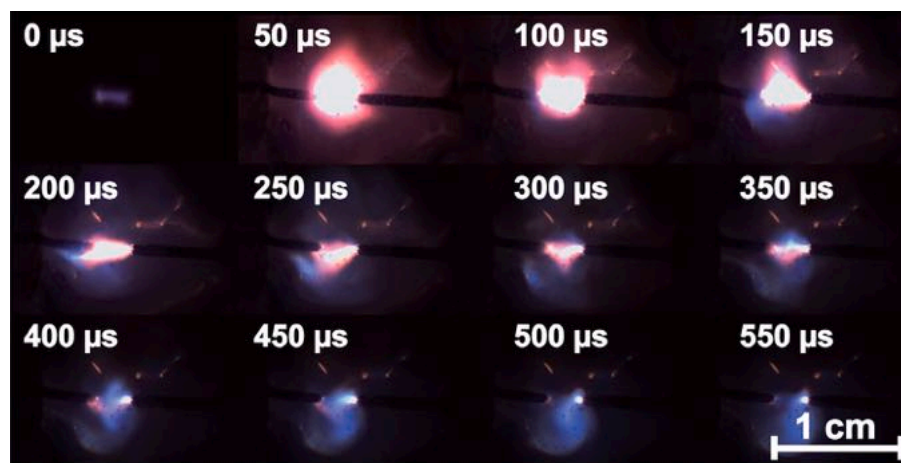


**Fig. 3.** High-speed photographs of an arc discharge where the capacitors were charged to 450 V. Picture one (0 μs) shows the weak ignition spark.

be 100(1) mbar before sealing. They were loaded with 30(1) mg of synthetic $Mg_2SiO_4$ particles.

### 3.3. Arc discharge generation

The experimental set-ups of the Earth-based and ISS-based experiments are very similar. The differences will be explained in the subsequent sections. Figure S4 shows a schematic illustration of sample chamber I and a simplified circuit which includes the most relevant parts of the arc generation unit.

In order to meet the severe constraints for the ISS-based experiment (e. g. NASA safety requirements, limited space, power supply etc.), we developed an electronic circuit with a two-stage process to generate arc discharges. A DC–DC converter charges three parallel capacitors ($C_{arc}$ ≙ 450 μF). An ignition coil is protected from the charging voltage of $C_{arc}$ by the diode $D_{spark}$. After $C_{arc}$ has reached the target voltage, the ignition coil generates a high voltage peak up to 8 kV and produces an ionized channel between the electrodes (ignition spark). Diode $D_{spark}$ becomes conductive while $D_{arc}$ protects $C_{arc}$ from the high voltage peak. After the electrical breakdown the voltage decreases instantaneously. When the voltage has dropped below the charging voltage of $C_{arc}$, the energy stored in $C_{arc}$ is released into the existing ionized channel, causing a high energetic arc discharge. Figure S5 shows the

arc generation unit used for the laboratory experiments on Earth. The circuit diagrams and the components are available on GitHub.[1]

### 3.4. Discharge characterization

The discharges were characterized using the Earth-based experiment. We used a Tektronix TDS 2024B oscilloscope to measure current and voltage in order to quantify the energy of the arc discharges. A Testec TT-SI 50 10:1 test probe was connected to a 10 mΩ shunt in series with the spark gap for current measurements. The voltage across the gap was measured with a Testec HVP-15HF 1000:1 test probe and the charging voltage of the capacitor was measured with a Testec TT-SI 51 100:1 test probe. The configuration of the test probes is illustrated in Figure S4.

We used an ACTON SpectraPro 2500i spectrograph equipped with a Pixis256E CCD camera to measure the Cu-I emission lines from the electrodes and the $H_\beta$ emission lines from the $Ar/H_2$ plasma in the sample chamber I. The spectrograph was connected with a 200 μm optical fiber to the window of sample chamber I.

We employed a pco.dimax HD camera for high-speed video recording of the arc discharge with a frame rate of 20,000 fps and a resolution of $288 \times 248$ pixel. Long-time exposure photography of the arc discharge was performed with a Nikon D7200 single-lens reflex camera.

---

[1] github.com/Geowissenschaften/EXCISS.

### 3.5. Experimental set-up for the ISS-based experiments

The experiment aboard the ISS was carried out inside a 1.5 U NanoRacks NanoLab (e. g. Brisset et al. (2017)). Fig. 2 shows the NanoRacks NanoLab with a dimension of $\approx 10 \times 10 \times 15$ cm$^3$ and the different components of the experimental set-up. This set-up is equipped with a sample chamber of type II loaded with 30(1) mg of $Mg_2SiO_4$ particles.

A camera in combination with a 2.5× objective and a tube lens was utilized to monitor the particle distribution, movement and interaction with the arc discharges and to inspect the condition of the electrodes aboard the ISS. The video recording was controlled by a Raspberry Pi Zero. All optical components were mounted on a microbench system and the focus was adjusted to the tip of the pointed electrode. The sample chamber was illuminated with one LED from the front and one from the back. The field of view (Fig. S3) is $\approx 2.73 \times 3.63$ mm$^2$ with a resolution of $1640 \times 1232$ pixel when a $2 \times 2$ pixel binning is employed. Videos were recorded with a frame rate of 40 fps. The custom designed power supply unit was equipped with four lithium-ion batteries. The PCB design and the software developed here will be available on GitHub.[1]

The NanoLab is connected with an USB3 B port (5 V, 900 mA) to the NanoRacks rack aboard the ISS for power supply and data transfer. We configured two 256 GB USB mass storage devices for redundant long-time data storage and a single 64 GB mass storage device for data transfer between our set-up and the NanoRacks rack. The experiment was designed to operate autonomously.

### 3.6. Calibrating the experimental set-up

#### 3.6.1. Energy of the arc discharge

The arc discharge generation in our sample chamber is initiated by an ignition spark (Fig. 3, $t = 0$ μs) with a breakdown voltage of $\approx 6$–8 kV. The generation of an ignition spark takes $\approx 4$ μs (Fig. S6). The duration of the ignition spark is much shorter than the duration of the following arc discharge and the voltage maximum is two orders of magnitude higher than the burning voltage of the arc discharge. The energy released during the ignition spark can be neglected.

The energy released into the arc discharge in the ISS-based experiment can be varied between $\approx 3.1$–21 J (150–450 V) and for the Earth-based experiment between $\approx 2.6$–17 J. The energy of the arc discharge reaches its maximum $\approx 5$–10 μs after the ignition spark. At this time the voltage is decreasing from the charging voltage to the burning voltage of the arc (usually 60–80 V, see Fig. S7). The duration of an arc discharge varies between 400 μs and 600 μs. We adjusted the arc discharge to an energy level which was sufficient to melt and fuse the $Mg_2SiO_4$ particles, without wearing the electrodes down strongly. Fig. 3 shows frames recorded by a high-speed camera of the arc discharge. The time interval between the frames is 50 μs and the first frame shows the weak ignition spark.

In order to ensure the transferability of parameters between the different types of sample chambers and the ISS- and Earth-based-laboratory set-ups, we performed discharge experiments as a function of charging voltages (Fig. S8). The calibration enables us to approximate the energy released into an arc discharge aboard the ISS for different voltages.

#### 3.6.2. Electron density and temperature of the arc discharge

In addition to its energy the arc discharge can be characterized by its electron density $n_e$ and temperature $T_e$. In the desired range of operation we determined an electron density of $n_e = 1.6(1) \times 10^{16}$ cm$^{-3}$ to $2.0(1) \times 10^{16}$ cm$^{-3}$ and an electron temperature of $k_B T_e \approx 6900(1000)$ K (Fig. S10).
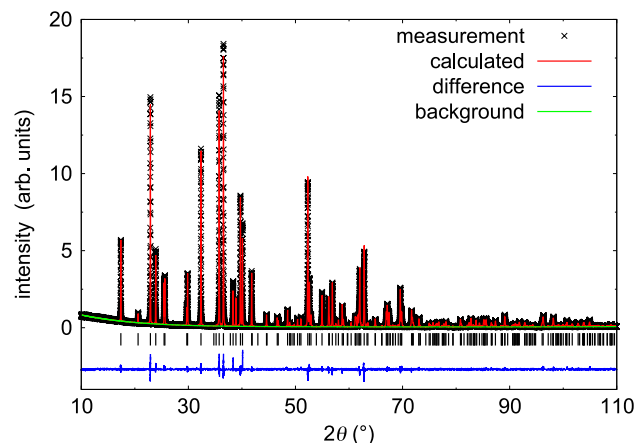


**Fig. 4.** Rietveld refinement of synthetic $Mg_2SiO_4$ powder. The differences between measurement and refinement are represented by the blue line. The Bragg positions are indicated by tick marks.
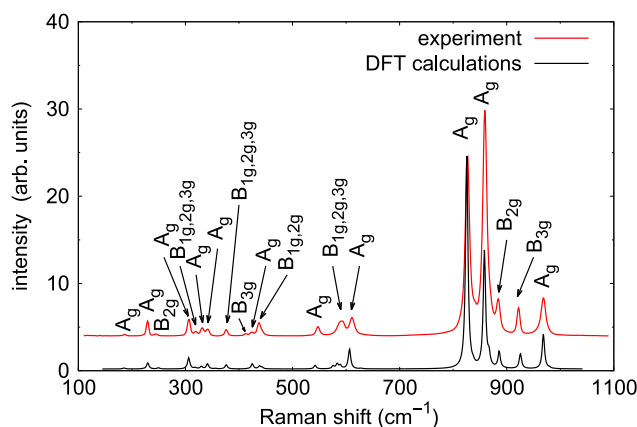


**Fig. 5.** Experimental Raman spectra of synthetic $Mg_2SiO_4$ grains in comparison to DFT calculations for forsterite. The DFT spectrum was scaled by 5%. All Raman modes were assigned to irreducible representations.

## 4. Results & discussion

### 4.1. Characterization of the starting material

#### 4.1.1. X-ray powder diffraction

The phase purity of the synthetic $Mg_2SiO_4$ powder was confirmed by Rietveld refinement and no secondary phase was detected within the experimental error limits of $\approx 3\%$ (Fig. 4). The diffraction pattern also shows that the sample material is very well crystallized.

The results of the Rietveld refinement are listed in the supplementary material section (Table S2). The refinement data confirmed the established structural model of forsterite (Cernik et al., 1990).

#### 4.1.2. Raman spectroscopy

Powder Raman spectroscopy was performed on the $Mg_2SiO_4$ particles. The experimental Raman spectra are in very good agreement with theoretical data from DFT calculations (Fig. 5).

Based on the DFT-based calculations we were able to assign irreducible representations to all observed peaks. Following the factor group analysis (DeAngelis et al., 1972) 36 modes can be Raman active ($\Gamma_{Raman} = 11A_g + 11B_{1g} + 7B_{2g} + 7B_{3g}$) and we observed all $A_g$ modes experimentally. The experimental Raman data also confirmed the very good crystallinity of the $Mg_2SiO_4$ powder as the Raman peaks did not show any broadening.
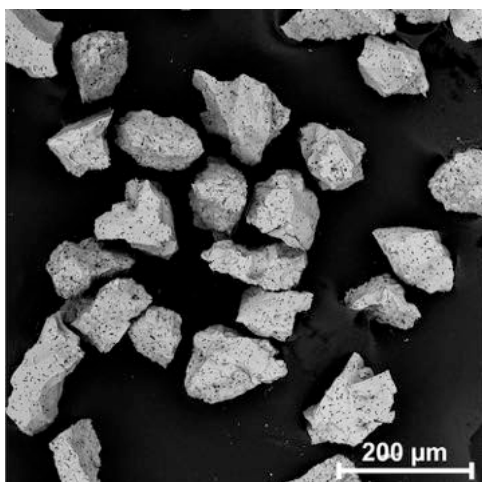
**Fig. 6.** SEM image of multiple $Mg_2SiO_4$ grains after the sample preparation process.

### 4.1.3. SEM

The size, shape and micro-structure of the $Mg_2SiO_4$ grains before exposing them to arc discharges were examined by scanning electron microscopy. The SEM images confirm that all grains of the starting material with a diameter of <80 × 80 $\mu m^2$ and a diameter of >120 × 120 $\mu m^2$ were sorted out during the sample preparation (Fig. 6). The length of the third axis can differ from the range.

The $Mg_2SiO_4$ grains show an irregular shape and fractured surfaces. Some grains have approximately flat surfaces (Fig. 7a), while others have a rough surface (Fig. 7b). Furthermore, the roughness of the surface and the clearly visible cavities in the particles suggest that the grains are highly porous.

We confirmed the expected chemical composition of the $Mg_2SiO_4$ grains by EDX analysis (nominal vs. EDX in atom %): MgO: 66.7/68(5) and $SiO_2$: 33.3/32(2). No other elements were detected within experimental uncertainties.

### 4.1.4. X-ray microtomography

X-ray microtomography (CT) was performed on the starting material. The results show no density differences inside the $Mg_2SiO_4$ grains, which confirms the chemical homogeneity of the grains. Furthermore, the microtomography also confirms the porosity of the $Mg_2SiO_4$ grains (Fig. 8).
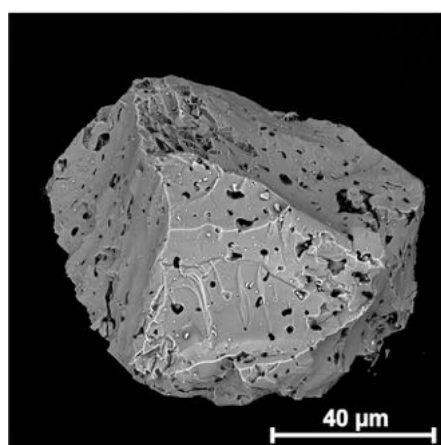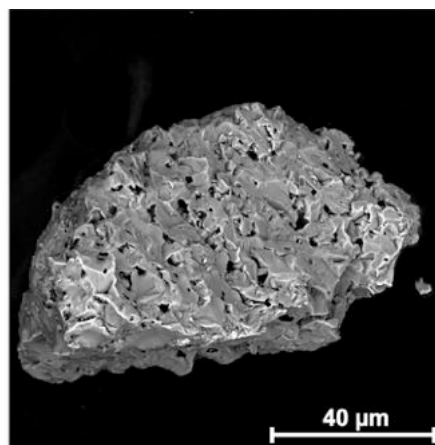
### 4.2. Aggregates formed by arc discharges

### 4.2.1. SEM

We used both sample chambers to expose the $Mg_2SiO_4$ grains to arc discharges on Earth in order to estimate the energy which is sufficient to melt and fuse $Mg_2SiO_4$ particles. In sample chamber of type II the particles were located at the bottom of the chamber close to the electrodes and the turbulence of the arc discharge led to floating particles.

We were able to partially melt and fuse $Mg_2SiO_4$ grains and form aggregates of several grains by arc discharges in sample chamber I and II on Earth. The first melting and aggregation of $Mg_2SiO_4$ particles occurred in experiments with a charging voltage of 350 V ($\approx 11$ J). The SEM image (Fig. 9a) shows a representative fused aggregate of $Mg_2SiO_4$ particles. The surface of the particles of the aggregate is much smoother and homogeneous, the cavities in the surface and the sharp edges have disappeared. Fig. 9b shows a close-up where the molten areas between the fused single grains can be clearly identified. Grain boundaries between the $Mg_2SiO_4$ particles cannot be identified any more. Fig. 9c shows a small $Mg_2SiO_4$ melt droplet between unmolten grains. The surface of the nearly spherical melt droplet is smooth. We studied the aggregates by EDX map analysis to ensure that the $Mg_2SiO_4$ particles are not welded together by sputtered material from the electrode. The EDX spectra showed the absence of any tungsten contamination from the electrodes. An example of a tungsten contamination found in another aggregate is shown in Fig. 9d. A molten tungsten particle from the electrodes impacted into $Mg_2SiO_4$ particles and lead to aggregate formation.

The number of aggregated particles increased with the charging voltage, but the erosion of the electrodes and the contamination of the sample material also increased. EDX analysis clearly shows an enhanced tungsten contamination at higher charging voltages of $C_{arc}$ (450 V to 550 V).

### 4.2.2. X-ray microtomography

We used microtomography to study the grain-grain contacts of the fused aggregates (Fig. 10). Fig. 10a shows the contact of an elongated and partially molten grain to another unmolten $Mg_2SiO_4$ particle. The surface of the partially molten grain is rounded and the molten regions show a slightly higher density than the rest of the grain, especially in the contact area to the other grain. We observed no heavy element contamination in the surface area of the particles. Fig. 10b and c show melt droplets with a size between 30–60 $\mu m$ which fuse $Mg_2SiO_4$ precursor grains together. The microtomography images reveal that these melt droplets are less porous than the initial grains, based on the
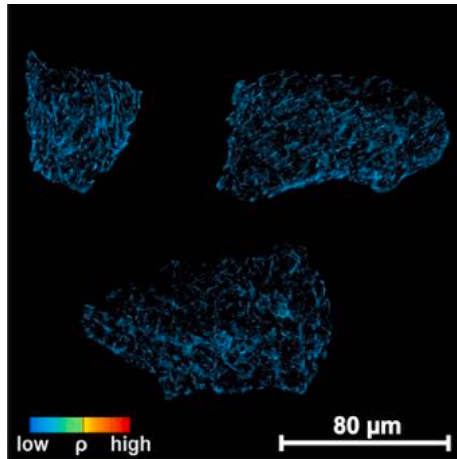


**Fig. 7.** Close-up SEM images of $Mg_2SiO_4$ grains after the sample preparation process: $Mg_2SiO_4$ grain with flat surfaces (a) and grain with a rough surface (b).

**Fig. 8.** Synchrotron microtomography image of three $Mg_2SiO_4$ grains after the sample preparation process.

density contrast in comparison to the unmolten particles. Furthermore, the surface of the melt droplets is smoothed. Fig. 10d shows a close-up of an aggregate with a $Mg_2SiO_4$ melt droplet and heavy element contamination (probably tungsten from the electrodes). We could clearly identify whether fused aggregates were formed due to the impact of molten tungsten particles from the electrodes or by the arc discharge.

### 4.3. X-ray microtomography on natural chondrules

We studied two different types of chondrules from the Allende meteorite by X-ray microtomography to allow a comparison between the samples produced by arc discharges and natural chondrules. The first chondrule has a diameter of about $\approx 935$ μm and is nearly spherical with a flat side (Fig. 11). The chondrule shows a porphyric texture with grain diameters from 48 μm to 196 μm. The grain size increases towards the edges. Metal inclusions are rare and have diameters of less than 40 μm. The structure of these porphyric chondrules is caused by incomplete melting of the chondrule precursors (Connolly et al., 1998; Lofgren, 1996).

The second chondrule represents a compound chondrule (Fig. 12). Compound chondrules consist of two chondrules fused together and represent 4%–5% of all chondrules (Gooding and Keil, 1981). This material is of special interest for our studies as the interfaces between the single chondrules of a compound chondrule can provide information about the temperature and velocities during their fusion. Whether or not collisions of liquid or cooled chondrules lead to the formation of compound chondrules is still discussed controversially (Hubbard, 2015; Arakawa and Nakamoto, 2016).

In the studied compound chondrule, the dominant chondrule has a diameter of 250 μm, while the small one has a size of $\approx 95$ μm. The dominant chondrule shows two regions with distinct textures. The predominant texture type of the chondrule is porphyric. The small chondrule and the interstitial region between the two primary chondrules have a texture typical for a quickly quenched melt. Furthermore,
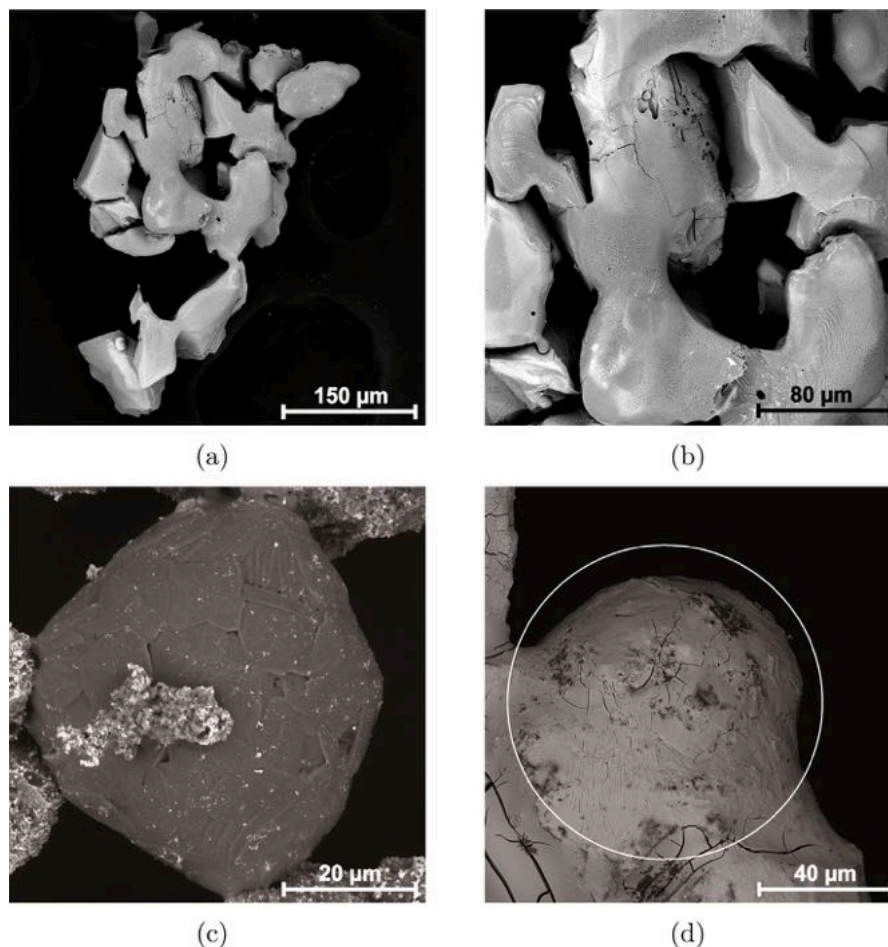


**Fig. 9.** SEM image of an aggregate formed by fusion of multiple $Mg_2SiO_4$ grains with lower (a) and higher (b) magnification. Melt droplet between unmolten $Mg_2SiO_4$ grains (c) and impact of a tungsten particle from the electrodes (white circle) into $Mg_2SiO_4$ grains (d). The particles were exposed to several discharges with 450 V ($\approx 22$ J) in sample chamber II on Earth.
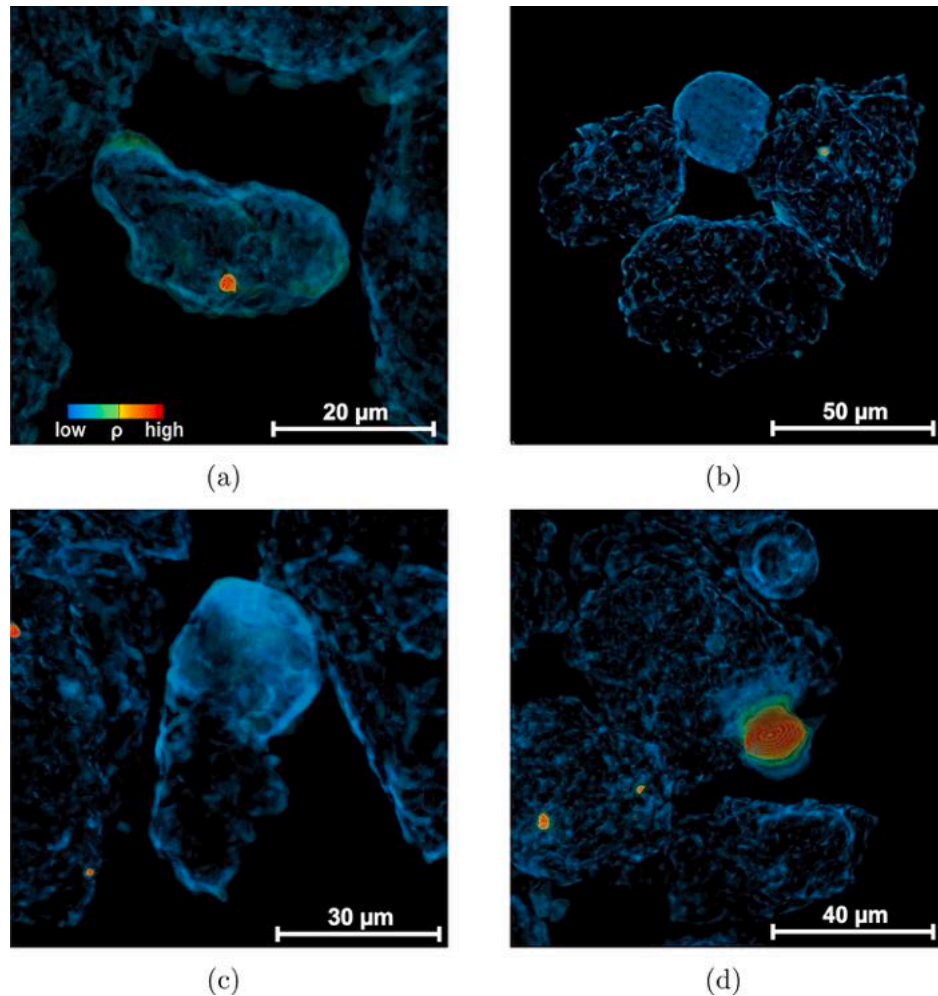
**Fig. 10.** Synchrotron microtomography images of the fused aggregates obtained by Earth-based experiments: contact point between two grains (a), melt droplet between fused $Mg_2SiO_4$ grains (b), partially molten $Mg_2SiO_4$ grain fused to an aggregate (c) and melt droplet with heavy element contamination, probably tungsten from the electrodes (d).

the main chondrule contains a significant amount of spherical metallic inclusions with diameters up to $\approx 44$ μm.

### 4.4. Start of the experiments aboard the ISS

The experiment was initially activated on November 27th 2018 and communication in the daily data transfer time window was possible. In the first weeks we were able to obtain preliminary image and video data which confirmed that we can operate the camera and the micro computers remotely. In addition, we performed ignition sparks without charging the capacitors to test our arc generation unit (Fig. 13). Furthermore, the log files showed that the power supply aboard the ISS worked as planned. Consequently the received images, videos and log files confirmed that the experimental set-up was fully operational.

### 5. Conclusion & outlook

We have developed an experimental set-up for a chondrule forma-tion experiment aboard the ISS to investigate if chondrule formation via nebular lightning is a viable process. With our laboratory-based experi-ments on Earth we were able to find appropriate experimental settings for the experiment aboard the ISS. We will start the experiments aboard the ISS with an energy of $\approx 2.6$ J (150 V) and afterwards increase the released energy to 13–21 J (350–450 V) which was appropriate to fuse and melt particles in the Earth-based test experiments. Therefore, while our experiments resemble those of Güttler et al. (2008), we
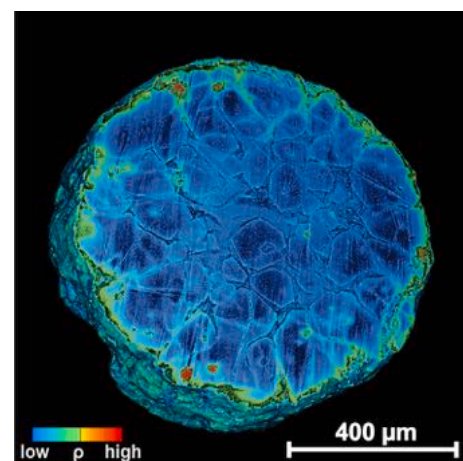


**Fig. 11.** Virtual slice through a single porphyric chondrule obtained by synchrotron microtomography. The chondrule was separated from the Allende meteorite by the selFrag technique.

anticipate that by using energies lower by two orders of magnitude and substantially longer duration of the arc discharges we will avoid the fragmentation of aggregates, but will rather observe the fusion of freely floating particles.

8
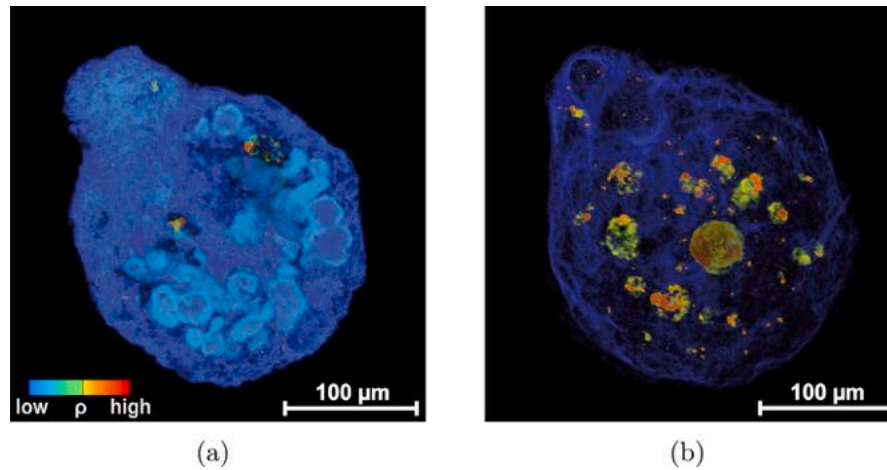
**Fig. 12.** Visualization of a microtomography scan of a compound chondrule separated from the Allende meteorite by the selFrag technique: texture of the silicate crystals inside the chondrule (a) and transparency adjusted to visualize the metallic inclusions (b).
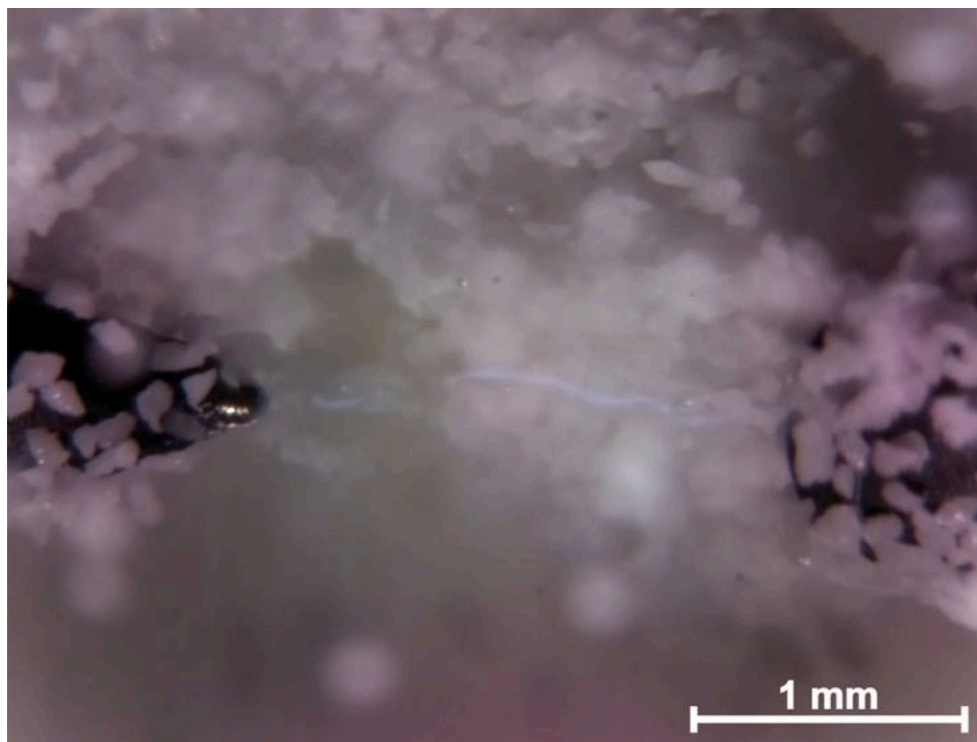


**Fig. 13.** Ignition spark between the electrodes in sample chamber II aboard the ISS, without charging $C_{arc}$. Agglomerated $Mg_2SiO_4$ particles are levitating between the electrodes and many particles are sticking on the electrodes. Field of view with a resolution of 1640 × 1232 pixel.

We have established benchmarks for the characterization of the samples once they have been returned, and shown that synchrotron-based microtomography data are very well suited to detect the density difference due to partial melting. The CT images obtained from the natural Allende chondrules clearly show their complex inner structure and we therefore anticipate that we will be able to study our synthetic samples in similar detail.

The preliminary images received from the ISS show that $Mg_2SiO_4$ particles agglomerate and accumulate between electrodes in micro-gravity. While finalizing this manuscript, we performed about 80 electrical discharges aboard the ISS and acquired approximately 16 h of video material and 15,000 pictures. Sample return was scheduled with SpaceX CRS-17 and took place on the 3rd June 2019. The samples are now studied with the techniques described above and will then be compared to the results of the laboratory-based experiments on Earth and a variety of natural chondrules.

**Data availability**

The circuit diagrams, the PCB designs and the software of the experiment are available on github.com/Geowissenschaften/EXCISS, an open-source online data repository hosted at GitHub.

**Acknowledgments**

the whole Institute of Applied Physics (Plasmaphysics) Frankfurt of Prof. J. Jacoby. The authors are grateful for financial support by the Dr. Rolf M. Schwiete Stiftung, DFG, Germany (Wi1232/44-1), the BMWi, Germany (50JR1704), the BMBF, Germany (05K16RFB), the German Aerospace Center (DLR), ZEISS, Germany, Dassault Systèmes BIOVIA, European Company, DreamUp, USA, NanoRacks, USA and Nordlicht, Germany. We acknowledge DESY (Hamburg, Germany), a member of the Helmholtz Association HGF, for the provision of experimental facilities. Parts of this research were carried out at PETRA III.

## Appendix A. Supplementary data

Supplementary material to this article includes Figures S1–S10 and Tables S1 and S2.

Supplementary material related to this article can be found online at https://doi.org/10.1016/j.icarus.2020.113898.

## References

Alexander, C.M.O., Grossmann, J.N., Wang, J., Zanda, B., Bourot-Denise, M., Hewins, R.H., 2000. The lack of potassium-isotopic fractionation in Bishunpur chondrules. Meteorit. Planet. Sci. 35, 859–868.

Arakawa, S., Nakamoto, T., 2016. Compound chondrule formation via collision of supercooled droplets. Icarus 276, 102–106.

Asphaug, E., Jutzi, M., Movshovitz, N., 2011. Chondrule formation during planetesimal accretion. Earth Planet. Sci. Lett. 308, 369–379.

Bayarjargal, L., Fruhner, C.-J., Schrodt, N., Winkler, B., 2018. CaCO₃ phase diagram studied with Raman spectroscopy at pressures up to 50 GPa and high temperatures and DFT modeling. Phys. Earth Planet. Inter. 281, 31–45.

Boss, A.P., 1996. A concise guide to chondrule formation models. In: Hewins, R.H., Jones, R.H., Scott, E.R.D. (Eds.), Chondrules and the Protoplanetary Disk. pp. 257–263.

Bowen, N.L., Schairer, J.F., 1925. The system MgO-FeO-SiO₂. Am. J. Sci. 29, 151–217.

Brisset, J., Colwell, J., Dove, A., Maukonen, D., 2017. NanoRocks: Design and performance of an experiment studying planet formation on the International Space Station. Rev. Sci. Instrum. 88, 074502.

Budde, G., Burkhardt, C., Brennecka, G.A., Fischer-Gödde, M., Kruijer, T.S., Kleine, T., 2016. Molybdenum isotopic evidence for the origin of chondrules and a distinct genetic heritage of carbonaceous and non-carbonaceous meteorites. Earth Planet. Sci. Lett. 454, 293–303.

Cernik, R.J., Murray, P.K., Pattison, P., Fitch, A.N., 1990. A two-circle powder diffractometer for synchrotron radiation with a closed loop encoder feedback system. J. Appl. Cryst. 23, 292–296.

Ciesla, F.J., Hood, L.L., 2002. The nebular shock wave model for chondrule formation: Shock processing in a particle–gas suspension. Icarus 158, 281–293.

Clark, S.J., Segall, M.D., Pickard, C.J., Hasnip, P.J., Probert, M.I.J., Refson, K., Payne, M.C., 2005. First principles methods using CASTEP. Z. Kristallogr. 220, 567–570.

Clarke Jr., R.S., Jarosewich, E., Mason, B., Nelen, J., Gomez, M., Hyde, J.R., 1971. The Allende, Mexico, meteorite shower. Smithson. Contrib. Earth Sci. 5, 1–53.

Connolly, H.C., Jones, R.H., 2016. Chondrules: The canonical and noncanonical views. J. Geophys. Res. Planets 121, 1885–1899.

Connolly, H.C., Jones, B.D., Hewins, R.H., 1998. The flash melting of chondrules: an experimental investigation into the melting history and physical nature of chondrule precursors. Geochim. Cosmochim. Acta 62, 2725–2735.

Connolly, H.C., Love, S.G., 1998. The formation of chondrules: Petrologic tests of the shock wave model. Science 280, 62–67.

DeAngelis, B.A., Newnham, R.E., White, W.B., 1972. Factor group analysis of the vibrational spectra of crystals: A review and consolidation. Am. Mineral. 57, 255–268.

Desch, S.J., Connolly Jr., H.C., 2002. A model of the thermal processing of particles in solar nebula shocks: Application to the cooling rates of chondrules. Meteorit. Planet. Sci. 37, 183–207.

Desch, S.J., Cuzzi, J.N., 2000. The generation of lightning in the solar nebula. Icarus 143, 87–105.

Gooding, J.L., Keil, K., 1981. Relative abundances of chondrule primary texture types in ordinary chondrites and their bearing on chondrule formation. Meteorit. Planet. Sci. 16, 17–43.

Güttler, C., Poppe, T., Wasson, J.T., Blum, J., 2008. Exposing metal and silicate charges to electrical discharges: Did chondrules form by nebular lightning? Icarus 195, 504–510.

Hewins, R.H., Connolly, Jr., H.C., 1996. Peak temperatures of flash-melted chondrules.. In: Hewins, R.H., Jones, R.H., Scott, E.R.D. (Eds.), Chondrules and the Protoplanetary Disk. pp. 197–204.

Hewins, R.H., Fox, G.E., 2004. Chondrule textures and precursor grain size: an experimental study. Geochim. Cosmochim. Acta 68, 917–926.

Hewins, R.H., Zanda, R.H., Horányi, M., Robertson, S., Den Hartog, D.J., Fiksel, G., 2000. The trouble with flash heating. In: 31St Lunar and Planetary Science Conference, Abstract #1675.

Hezel, D.C., Palme, H., 2010. The chemical relationship between chondrules and matrix and the chondrule matrix complementarity. Earth Planet. Sci. Lett. 294, 85–93.

Horányi, M., Morfill, G., Goertz, C.K., Levy, E.H., 1995. Chondrule formation in lightning discharges. Icarus 114, 174–185.

Hubbard, A., 2015. Compound chondrules fused cold. Icarus 254, 56–61.

Imae, N., Isobe, H., 2017. An experimental study of chondrule formation from chondritic precursors via evaporation and condensation in Knudsen cell: Shock heating model of dust aggregates. Earth Planet. Sci. Lett. 473, 256–268.

Johansen, A., Okuzumi, S., 2018. Harvesting the decay energy of ²⁶Al to drive lightning discharge in protoplanetary discs. Astron. Astrophys. 609, A31.

Johnson, B.C., Minton, D.A., Melosh, H.J., Zuber, M.T., 2015. Impact jetting as the origin of chondrules. Nature 517, 339–341,.

Kerr, R.A., 2013. Meteorite mystery edges closer to an answer — Or the end of a field. Science 341, 126–127.

Kozub, D., Khmelik, V., Shapoval, J., Chentsov, V., Yatsenko, S., Litovchenko, B., Starikh, V., 2018. Helicon focus 7.0.2 pro. Available: https://www.heliconsoft.com/heliconsoft-products/helicon-focus/. [2018, Septemper 27].

Krot, A.N., Amelin, Y., Cassen, P., Meibom, A., 2005. Young chondrules in CB chondrites from a giant impact in the early solar system. Nature 436, 989–992.

Libourel, G., Portail, M., 2018. Chondrules as direct thermochemical sensors of solar protoplanetary disk gas. Sci. Adv. 4, eaar3321.

Lichtenberg, T., Golabek, G.J., Dullemond, C.P., Schönbächler, M., Gerya, T.V., Meyer, M.R., 2018. Impact splash chondrule formation during planetesimal recycling. Icarus 302, 27–43.

Limaye, A., 2012. Drishti: A volume exploration and presentation tool. In: Developments in X-ray tomography VIII, vol. 8506, SPIE, pp. 1–9.

Lofgren, G.E., 1996. A dynamic crystallization model for chondrule melts. In: Hewins, R.H., Jones, R.H., Scott, E.R.D. (Eds.), Chondrules and the Protoplanetary Disk. pp. 187–196.

Moosmann, J., Ershov, A., Weinhardt, V., Baumbach, T., Prasad, M.S., LaBonne, C., Xiao, X., Kashef, J., Hofmann, R., 2014. Time-lapse x-ray phase-contrast micro-tomography for in vivo imaging and analysis of morphogenesis. Nat. Protoc. 9, 294–304.

Morlok, A., Sutton, Y.C., Braithwaite, N.S.J., Grady, M.M., 2012. Chondrules born in plasma? Simulation of gas–grain interaction using plasma arcs with applications to chondrule and cosmic spherule formation. Meteorit. Planet. Sci. 47, 2269–2280.

Morris, M.A., Boley, A.C., Desch, S.J., Athanassiadou, T., 2012. Chondrule formation in bow shocks around eccentric planetary embryos. Astrophys. J. 752, 27.

Ogurreck, M., Wilde, F., Herzen, J., Beckmann, F., Nazmov, V., Mohr, J., Haibel, A., Müller, M., Schreyer, A., 2013. The nanotomography endstation at the PETRA III imaging beamline. J. Phys. Conf. Ser. 425, 182002.

Palme, H., Hezel, D.C., Ebel, D.S., 2015. The origin of chondrules: Constraints from matrix composition and matrix-chondrule complementarity. Earth Planet. Sci. Lett. 411, 11–19.

Rietveld, H.M., 1969. A profile refinement method for nuclear and magnetic structures. J. Appl. Cryst. 2, 65–71.

Russel, S., Connolly Jr., H.C., Krot, A.N. (Eds.), 2018. Chondrules: Records of proto-planetary disk processes. In: Cambridge Planetary Science, Cambridge University Press.

Scott, E.R.D., 2007. Chondrites and the protoplanetary disk. Annu. Rev. Earth Planet. Sci. 35, 577–620.

Toby, B.H., Von Dreele, R.B., 2013. GSAS-II: the genesis of a modern open-source all purpose crystallography software package. J. Appl. Cryst. 46, 544–546.

Túnyi, I., Guba, P., Roth, L.E., Timko, M., 2003. Electric discharges in the protoplanetary nebula as a source of impulse magnetic fields to promote dust aggregation. Earth Moon Planets 93, 65–74.

Wdowiak, T.J., 1983. Experimental investigation of electrical discharge formation of chondrules. In: King, E.A. (Ed.), Chondrules and their Origins. Lunar and Planetary Institute, Houston, pp. 279–283.

Weisberg, M.K., Prinz, M., Clayton, R.N., Mayeda, T.K., Sugiura, N., Zashu, S., Ebihara, M., 2001. A new metal-rich chondrite grouplet. Meteorit. Planet. Sci. 36, 401–418.

Whipple, F.L., 1966. Chondrules: Suggestion concerning the origin. Science 153, 54–56.

Wilde, F., Ogurreck, M., Greving, I., Hammel, J.U., Beckmann, F., Hipp, A., Lottermoser, L., Khokhriakov, I., Lytaev, P., Dose, T., Burmester, H., Müller, M., Schreyer, A., 2016. Micro-CT at the imaging beamline P05 at PETRA III. AIP Conf. Proc. 1741, 030035.

Youdin, A.N., Shu, F.H., 2002. Planetesimal formation by gravitational instability. Astrophys. J. 580, 494–505.

# Impact shock origin of diamonds in ureilite meteorites

Fabrizio Nestola[a,b,1], Cyrena A. Goodrich[c,1], Marta Morana[d], Anna Barbaro[d], Ryan S. Jakubek[e], Oliver Christ[a], Frank E. Brenker[b], M. Chiara Domeneghetti[d], M. Chiara Dalconi[a], Matteo Alvaro[d], Anna M. Fioretti[f], Konstantin D. Litasov[g], Marc D. Fries[h], Matteo Leoni[i,j], Nicola P. M. Casati[k], Peter Jenniskens[l], and Muawia H. Shaddad[m]

[a]Department of Geosciences, University of Padova, I-35131 Padova, Italy; [b]Geoscience Institute, Goethe University Frankfurt, 60323 Frankfurt, Germany; [c]Lunar and Planetary Institute, Universities Space Research Association, Houston, TX 77058; [d]Department of Earth and Environmental Sciences, University of Pavia, I-27100 Pavia, Italy; [e]Astromaterials Research and Exploration Science Division, Jacobs Johnson Space Center Engineering, Technology and Science, NASA, Houston, TX 77058; [f]Institute of Geosciences and Earth Resources, National Research Council, I-35131 Padova, Italy; [g]Vereshchagin Institute for High Pressure Physics RAS, Troitsk, 108840 Moscow, Russia; [h]NASA Astromaterials Acquisition and Curation Office, Johnson Space Center, NASA, Houston, TX 77058; [i]Department of Civil, Environmental and Mechanical Engineering, University of Trento, I-38123 Trento, Italy; [j]Saudi Aramco R&D Center, 31311 Dhahran, Saudi Arabia; [k]Swiss Light Source, Paul Scherrer Institut, 5232 Villigen, Switzerland; [l]Carl Sagan Center, SETI Institute, Mountain View, CA 94043; and [m]Department of Physics and Astronomy, University of Khartoum, 11111 Khartoum, Sudan

The origin of diamonds in ureilite meteorites is a timely topic in planetary geology as recent studies have proposed their formation at static pressures >20 GPa in a large planetary body, like diamonds formed deep within Earth's mantle. We investigated fragments of three diamond-bearing ureilites (two from the Almahata Sitta polymict ureilite and one from the NWA 7983 main group ureilite). In NWA 7983 we found an intimate association of large monocrystalline diamonds (up to at least 100 μm), nanodiamonds, nanographite, and nanometric grains of metallic iron, cohenite, troilite, and likely schreibersite. The diamonds show a striking texture pseudomorphing inferred original graphite laths. The silicates in NWA 7983 record a high degree of shock metamorphism. The coexistence of large monocrystalline diamonds and nanodiamonds in a highly shocked ureilite can be explained by catalyzed transformation from graphite during an impact shock event characterized by peak pressures possibly as low as 15 GPa for relatively long duration (on the order of 4 to 5 s). The formation of "large" (as opposed to nano) diamond crystals could have been enhanced by the catalytic effect of metallic Fe-Ni-C liquid coexisting with graphite during this shock event. We found no evidence that formation of micrometer(s)-sized diamonds or associated Fe-S-P phases in ureilites require high static pressures and long growth times, which makes it unlikely that any of the diamonds in ureilites formed in bodies as large as Mars or Mercury.

diamond | impact shock | ureilitic diamonds | ureilites | carbon phases

The origin of diamonds in ureilite meteorites is a highly controversial topic among planetary geologists with three main hypotheses being debated: 1) formation by impact shock conversion from graphite (1–7), 2) formation at low pressure in the solar nebula by chemical vapor deposition (8–10), and 3) formation at high static pressures in a planetary-sized body (11–13).

The ureilites form the second largest group of achondrites. They are ultramafic rocks mainly composed of olivine and pyroxene, with interstitial carbon, metal, and sulfide phases (14–19). They represent the mantle of a partially differentiated parent body (the ureilite parent body, or UPB) that experienced igneous processing at temperatures up to 1,200 to 1,300 °C (18). The UPB was catastrophically disrupted by a major impact before it had completely cooled, with ureilites being derived from daughter bodies that reassembled in the aftermath of the disruption (17, 19–21).

Carbon abundances are notably high in ureilites, ranging up to 8.5 wt % (19, 22), with the carbon occurring principally as graphite (18). In ureilites of very low shock level (based on shock indicators in the silicates), the graphite occurs as millimeter-sized euhedral (blade-shaped or tabular) crystals showing prominent (0001) cleavage, closely associated with Fe, Ni metal, and sulfides (23, 24) (SI Appendix, Fig. S1). Diamonds have not been reported in the lowest-shock samples (2, 25). Most ureilites, however, are shocked

to various degrees and in these samples the graphite areas, though still having external blade-shaped morphologies, are internally polycrystalline (18). Diamonds and lonsdaleite [diamond with stacking faults and twinning defects (26)] occur embedded in these areas, constituting a volumetrically minor (thus disproportionately illustrious) component of ureilites.

Although the presence of diamonds in these meteorites was reported more than a century ago, the process by which the diamonds formed has been hotly debated and is still controversial. The first hypothesis on the origin of diamond in ureilites dates back to 1956, when Urey (11) proposed that diamonds may form under static high-pressure conditions in the interior of large meteorite parent bodies. A few years later, in his seminal work on diamonds from the Goalpara and Novo Urei ureilites, Lipschutz (1) proposed that diamonds in ureilites were formed by shock conversion of graphite, a hypothesis that has been supported by many subsequent studies (2–7). A third hypothesis that has been discussed is that diamonds in ureilites formed at low pressure in the solar nebula by chemical vapor deposition (8–10).

## Significance

The origin of diamonds in ureilites is still a debated issue among the scientific community, with significant implications for the sizes of early Solar System bodies. We investigated three diamond-bearing ureilites by a multimethodological approach using scanning electron microscopy, micro X-ray diffraction, transmission electron microscopy, and micro-Raman spectroscopy, with the aim of determining the origin of the diamonds. Our results show that formation of both microdiamonds and nanodiamonds in ureilites can be explained by impact shock events on a small planetesimal and does not require long growth times at high static pressures within a Mercury- or Mars-sized body.

EARTH, ATMOSPHERIC, AND PLANETARY SCIENCES

Recent work on the Almahata Sitta (AhS) polymict ureilite (12, 13) reported the presence of large diamonds (with inclusions of chromite and Fe-S-P phases) in a ureilitic clast and suggested that such diamonds could only be formed at static pressures higher than 20 GPa. This would imply either that the UPB was similar in size to Mercury or Mars (13), or that diamonds in ureilites are exogenous to the UPB (27).

In order to provide insight into the origin of diamonds in ureilites, we investigated carbon phases in two ureilitic stones from AhS, samples AhS 209b and AhS 72, and also the NWA 7983 main group ureilite (28), by single-crystal micro X-ray diffraction (XRD) both in-house at the University of Padova (all three samples) and using synchrotron radiation at Paul Scherrer Institute, Villigen, Switzerland (AhS samples only). In addition, micro-Raman spectroscopy was performed on several carbon areas in NWA 7983 at ARES (Astromaterials Research and Exploration Science), Johnson Space Center, NASA, Houston, TX. Our results cast reasonable doubt on purported evidence for formation of ureilitic diamonds under high static pressures and provide strong evidence for their formation by impact shock at pressure peaks possibly as low as 15 GPa.

## Results

**Samples.** AhS 209b and 72 are two stones from the AhS meteorite, which fell in the Nubian desert in 2008 (19, 29–31). They are fine-grained, porous ureilites showing various degrees of "impact smelting" and shock metamorphism as previously described for fine-grained AhS ureilites and a few main group ureilites (32, 33). Olivine areas in AhS 209b are completely mosaicized (*SI Appendix*, Fig. S2). They consist of aggregates of ~5- to 20-μm-sized equigranular tiles (adopting the terminology of ref. 32) with tiny amounts of interstitial pyroxene and Si+Al-rich glass, which are inferred to represent recrystallized versions of originally ~0.5- to 1-mm-sized primary grains (e.g., refs. 32 and 33). The olivine largely preserves a typical ureilite olivine core composition of Fo ~79, except in reduction rims near inferred original grain boundaries and/or carbon areas. Reduction rim compositions range up to Fo ~93. Pigeonitic pyroxene areas in AhS 209b also show complete mosaicism with extensive in situ reduction and porosity. They consist of aggregates of ~5- to 10-μm-sized subhedral to anhedral grains, with varying amounts of interstitial Ca-enriched pyroxenes and Si-Al–enriched glass. Pores and small grains of metal and sulfide among the pyroxene grains are common. The pyroxene tiles show reverse zoning. Cores are reduced (core Mg#s up to ~93) relative to inferred primary compositions (~Mg# 81, such as would have been in equilibrium with Fo ~79 olivine in a typical lower-shock ureilite) with varying Wo contents (~2 to 8). Pyroxene textures such as these were described by Warren and Rubin (32) in several main group and AhS ureilites and attributed to "impact smelting" (concomitant melting and chemical reduction by carbon) of originally larger primary pigeonite grains. Elongated masses of carbon phases and metal grains are dispersed throughout the sample, commonly occurring along inferred primary silicate grain boundaries (Fig. 1 *A* and *B* and *SI Appendix*, Fig. S3).

The fragment of AhS 72 that we examined is dominated by olivine and shows a higher degree of shock metamorphism than 209b. Olivine is completely recrystallized to ~1- to 20-μm-sized equigranular (anhedral to subhedral) grains in a groundmass (of varying proportions relative to the amount of olivine) of pyroxene. The olivine grains are highly reduced (Fo ~99) and nearly free of inclusions, suggesting recrystallization from a melt (or at least at very high temperatures) under highly reducing conditions. Interstitial pyroxene compositions range from Wo 0.8 to Wo 34 and are also reduced (Mg# 88 to 99). Pores, masses of carbon phases (~20 to hundreds of micrometers), and grains of metal are abundant throughout the section.

The NWA 7983 meteorite was found in 2013 in Morocco. The stone has a total mass of 424.3 g and was classified as a main group ureilite (28). The original description noted that the meteorite was extremely resistant to cutting and polishing and suggested that diamond was abundant (28), and our work confirms this. We studied four polished sections of NWA 7983. A polished thick section with an area of about 2 cm$^2$ was used for scanning electron microscopy (SEM) observations (not carbon-coated; see *SI Appendix*, sections 1.1 and 1.2) followed by micro XRD. Three polished thin sections were used for optical microscopy and additional SEM observations (both carbon-coated and not carbon-coated). NWA 7983 consists mainly of olivine, minor pyroxene, and ~6 vol % masses of carbon phases. Metal, Fe-oxides/hydroxides (presumed terrestrial replacements of metal), troilite, and Cr-rich sulfides occur cross-cutting silicates and as blebs. The olivine shows a high degree of shock metamorphism, with textures similar to those in AhS 72 (*SI Appendix*, Fig. S4). All olivine areas are either mosaicized with ~2- to 12-μm-sized euhedral tiles and very minor interstitial feldspathic material, or recrystallized to ~1- to 20-μm-sized equigranular (anhedral to subhedral) grains in a groundmass of minor pyroxene. The degree of reduction of the olivine varies greatly. Some areas (inferred original grains) are dominantly Fo 82 to 83, which may be close to the primary composition, while others are strongly reduced with Fo ~90 to 98. The interstitial pyroxenes vary in Wo from ~2 to 33 and Mg# ~84 to 92. Elongated masses of carbon phases, as well as metal ± sulfide grains (wholly or partly altered to terrestrial Fe-hydroxides), are dispersed throughout the sample. Similar to AhS 72, the degree of recrystallization of the silicates is so high that the outlines of primary silicate grain boundaries are difficult to discern.

The carbon masses typically occur as elongated (blade-shaped), internally layered structures of up to 1 mm in length and 300 μm in width (Fig. 1 *C–E* and *SI Appendix*, Figs. S5 and S6). In one of the sections that we studied, such blades form a nearly continuous vein ~1 cm long. In reflected light, the carbon masses contain elongated, highly reflective, high-relief stripes that are parallel to the external morphology of the carbon mass in the long dimension and are inferred to be diamond, based on their optical properties and fluorescence under an electron beam (Fig. 1*D* and *SI Appendix*, Figs. S5 *A–C* and S6*A*). Some of these contain structures that resemble {111} crystal faces of octahedral diamonds. In back-scattered electron images (BEI), the carbon masses also show a striped appearance (parallel to the external morphology of the carbon mass), which is defined by light and dark areas (Fig. 1*C* and *SI Appendix*, Figs. S5 *D* and *E* and S6*B*). The lighter areas contain numerous tiny, bright grains of what appears to be metallic Fe and Fe-sulfides, based on energy-dispersive X-ray spectroscopy (EDS) spectra showing peaks for C, Fe, and S. The darker areas appear to be largely free of inclusions and have EDS spectra showing only C. Based on fluorescence under the electron beam, diamonds are abundant in both the light and the dark areas. In general, the high-reflectance, high-relief areas observed in reflected light correspond closely to the darker areas in BEI (Fig. 1 *C* and *D* and *SI Appendix*, Fig. S6 *A* and *B*).

None of the samples studied in this work shows any high-pressure polymorphs of olivine such as wadsleyite and ringwoodite, even in veins or fractures where we specifically searched for them by micro-Raman spectroscopy.

**Micro XRD.** Using reflected light and/or back-scattered electron images of thick sections that were not carbon-coated we located carbon areas for micro XRD in the three samples. We gently removed portions of such carbon areas (*SI Appendix*, section 1.3) and analyzed them by micro XRD.
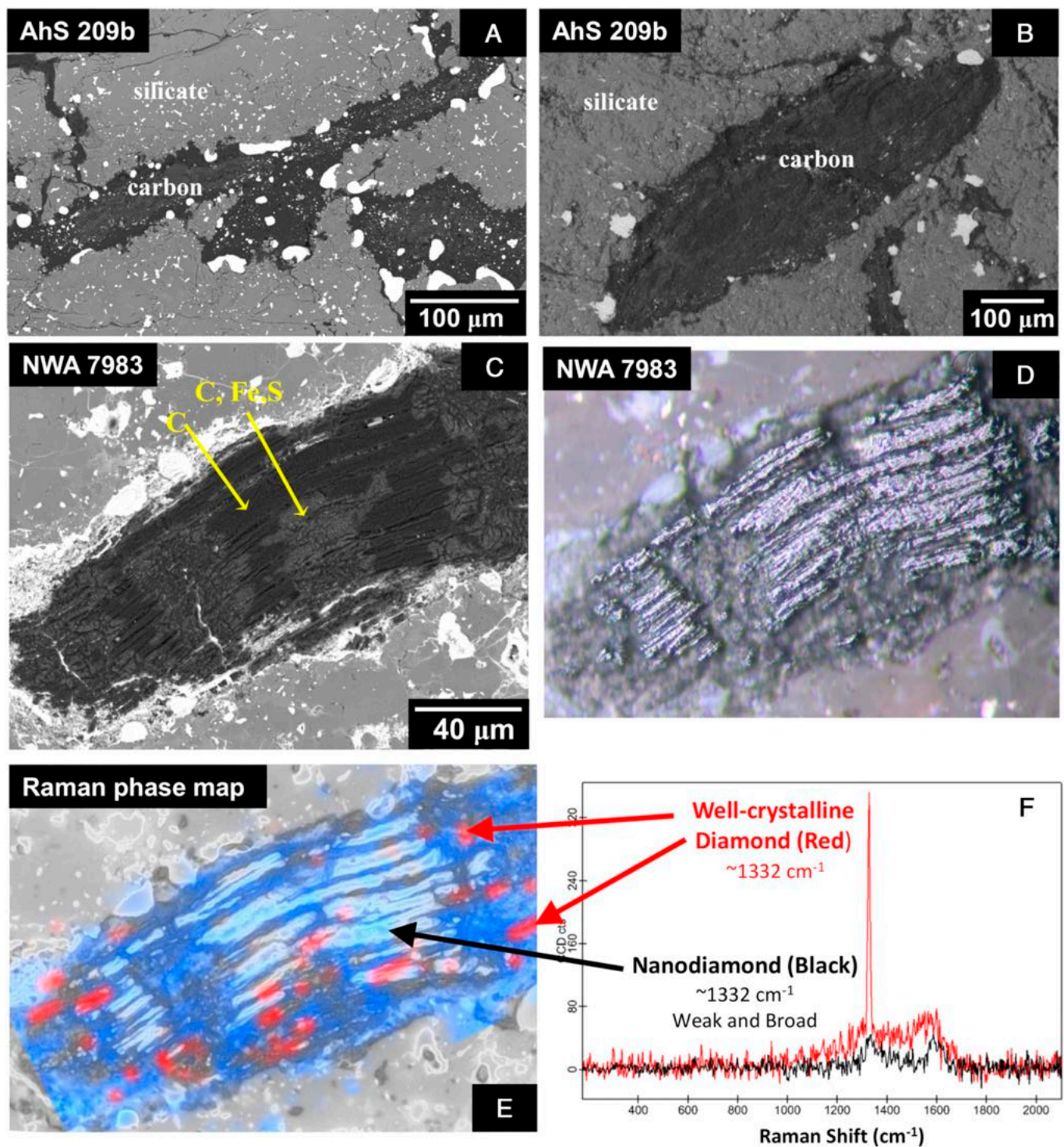
**Fig. 1.** Carbon masses in polished sections of AhS 209b and NWA 7983. (*A*) BEI of AhS 209b, showing elongated masses of carbon phases located along inferred primary silicate grain boundaries (see also *SI Appendix*, Fig. S3 for a lower-magnification view). (*B*) BEI of non-carbon-coated section of AhS 209b in low-vacuum mode (hence low contrast). BEI of other carbon areas in AhS 209b are shown in *SI Appendix*, Fig. S3. (*C*) BEI of carbon-coated section of NWA 7983 in high-vacuum mode. Carbon masses in this sample tend to have elongated, blade-like morphology and internally show a structure of dark and light stripes parallel to the long edges of the carbon mass (see also *SI Appendix*, Fig. S4). Dark areas show only C, whereas lighter areas show C, Fe, and S peaks in EDS spectra. (*D*) Reflected light image of same area as in *C*. Highly reflective, high-relief stripes correlate with dark areas in BEI and are inferred to be diamond from their optical properties, as well as fluorescence under the electron beam. (*E*) Raman phase map of area in *C* and *D*. The intensity of the red color corresponds to the intensity of the diamond ~1,332-cm$^{-1}$ band. The intensity of the blue color corresponds to the intensity of the graphite G band (~1,575 cm$^{-1}$). In nanodiamonds, the ~1,332-cm$^{-1}$ band is broad, has low intensity, and is downshifted, making it difficult to detect. Thus, the Raman image is predominantly sensitive to large diamonds (red) while most nanodiamonds likely go undetected (38, 39). In this Raman image, nanodiamonds were detected only in a few areas, although XRD results indicate that they are present throughout the carbon mass. (*F*) Raman spectra of large diamonds (red) and nanodiamonds (black) from *E*.

**AhS 72 and AhS 209b.** The sections of carbon materials removed from the AhS 209b and AhS 72 samples were two irregularly shaped grains of 320 μm and 380 μm, respectively, along their longest dimension (*SI Appendix*, Fig. S7). Synchrotron radiation micro XRD showed that these two fragments are both composed mainly of diamonds, graphite and metallic iron (minor troilite was also detected; see *SI Appendix*, section 1.4). Fig. 2*A* shows the X-ray diffractogram and the diffraction image of the AhS 209b fragment. As demonstrated by the diffraction rings (rather than individual diffraction spots), the sample is polycrystalline. A similar observation was made for the AhS 72 sample (the diffractogram and diffraction images for AhS 72 are shown in *SI Appendix*, Fig. S8). Diffraction line profile analysis (34) using the High Score Plus software package (Panalytical) was applied to estimate the crystallite size of the carbon phases (*SI Appendix*, section 1.4). The results of this analysis are given in *SI Appendix*, Table S1 and show that diamonds in both AhS 209b and AhS 72 are nanometric with crystal size of 17 to 19 nm for AhS 209b and 18 to 25 nm for AhS 72. However, both of the AhS samples show a typical feature of diamond stacking faults (see the shoulder of the 2.06 Å peak of diamond in Fig. 2*A*, more evident in the magnification in *SI Appendix*, Fig. S9) and in order to take into account any defects in diamond and eventually graphite (which shows a significant peak asymmetry and broadening) not considered in the previous profile analysis, we performed a further profile analysis by using DIFFaX+ software (35) (*SI Appendix*, sections 1.4 and 1.5 and Fig. S10) which provides more reliable results for defect-bearing powder materials. This revealed that the samples are characterized by two diamond domain sizes: Smaller domains are on average 3 to 12 nm, whereas the larger ones are larger than 50 nm; for sizes >100 nm, diffraction is no longer reliable for the determination of size and defects in materials. The average graphite crystal size was estimated to be 20 nm. These analyses indicate that in the AhS ureilite fragments studied here diamonds are nanometric with an average size of about 25 nm.

**NWA 7983.** The BEI observations described above revealed that the carbon masses in NWA 7983 show distinct internal stripes of dark and light areas (Fig. 1 *C* and *D* and *SI Appendix*, Figs. S5 and S6), correlating with stripes of high reflectance and high relief and low reflectance and low relief (respectively) in reflected light. We removed fragments from both dark and light areas within five different carbon masses and investigated them by micro XRD in-house (*SI Appendix*, section 1.5 and S11). The XRD images of dark areas in several of the carbon masses (e.g., Fig. 2) showed no evidence of diffraction rings but only diffraction spots typical of monocrystals. Based on the sizes of the removed fragments, the monocrystals that we investigated ranged from ~20 to at least 100 μm in size (longest dimensions). The diffraction image for the largest monocrystal that we observed is shown in Fig. 2*B* (BEI and reflected light images of this carbon mass, indicating the area removed and analyzed, are given in *SI Appendix*, Fig. S12). The unit-cell edge length that we determined for this crystal is $a = 3.569$ Å (*SI Appendix*, Table S1), typical of cubic diamond. The absence of evidence for any other phases in the diffractogram of this crystal (or similar ones that we analyzed) is consistent with the observations from EDS analyses in the SEM that only C was detected in dark areas of the carbon masses in this sample. In other fragments removed from dark areas, the diffractograms showed the simultaneous presence of diffraction spots (indicating single crystal diamonds) and diffraction rings (e.g., *SI Appendix*, Fig. S13), indicating that in some of the darker areas large diamond monocrystals are intimately intermixed with nanodiamonds on a scale below that detectable in reflected light or BEI imaging.

The diffraction results for fragments removed from the lighter carbon areas (as seen in BEI) in NWA 7983 yielded results very similar to those obtained on the AhS ureilite fragments. Fig. 2*C* shows that such areas are polycrystalline and mainly composed of diamond, graphite, cohenite (ideally $Fe_3C$), troilite, and minor metallic iron, consistent with EDS spectra showing the presence of Fe and S in addition to C in such areas. The small shoulder at higher *d*-spacing (e.g., 2.18 Å) with respect to the main peak of diamond at 2.06 Å is characteristic of lonsdaleite as already observed for the AhS 209b and AhS 72 samples. The profile analysis for polycrystalline diamonds in both the light areas and the dark areas indicates that the polycrystalline diamond is nanometric and even smaller than diamonds in the AhS fragments with a size of 9 nm (*SI Appendix*, Table S1). Although it was not possible to model the diffraction peaks of graphite, based on the peak broadening of its most intense peak it is likely that the graphite is also nanometric.

In this study an intimate association of micro- and nanodiamonds has been reported in natural samples, either terrestrial or extraterrestrial. Unfortunately, it was not possible to distinguish microdiamonds from nanodiamonds in either reflected light or BEI, and so our principal method of locating microdiamonds was a "hit-or-miss" approach of removing fragments from sections and X-raying them. This approach was time-consuming, thus limiting the number of areas that could be studied, and resulted in loss of textural context of the diamonds. In order to get an idea of the distribution, shapes, and relative abundance of microdiamonds in situ, we used micro-Raman imaging on several areas using 488-nm excitation (Fig. 1 *E* and *F* and *SI Appendix*, Fig. S6 *C–E*). Raman mapping of these areas easily identifies larger diamond grains [>~45 nm (36)] from the narrow, high intensity band at ~1,332 cm$^{-1}$ (37), although it does not allow definitive determination of their sizes (38). These Raman maps show clearly that in a number of places the large diamond grains are elongated along the direction of the stripes seen in BEI and reflected light (parallel to external morphology of the carbon mass) and (as shown particularly in *SI Appendix*, Fig. S6) are concentrated along the stripes, that is, forming stripes of their own. We note that nanodiamonds are not easily identified in Raman spectra (38, 39) and so the Raman images (Fig. 1 *E* and *F*) are less useful for showing their distribution. Nevertheless, the XRD analyses showed clearly that nanodiamonds are present in both light and dark areas of the carbon masses.

**Transmission Electron Microscopy.** The same fragments of AhS 209b and AhS 72 investigated by XRD were analyzed by transmission electron microscopy (TEM) with the main goal being to verify the crystallite size compared with the results from synchrotron micro XRD. The presence of diamond stacking faults (lonsdaleite), as predicted by micro XRD showing the typical shoulders at higher *d*-spacing with respect to the 2.06 Å peak of diamond (*SI Appendix*, Fig. S9), was confirmed by TEM.

Sections of AhS 72 and AhS 209b suitable for TEM analyses were prepared by focused ion beam and investigated by a Philips 200 CM transmission electron microscope (*SI Appendix*, section 1.6). A typical bright-field image of the AhS 72 sample (Fig. 3, *Left*) shows diamond domains with size between about 20 and 150 nm. At the same time, electron diffraction images (Fig. 3, *Right*) indicate that nanodiamonds are associated with graphite (see the ring at about 3.35 Å) and lonsdaleite (see ring at about 2.18 Å), confirming the XRD results. In addition to these main phases, TEM analyses of the AhS 72 sample also revealed the presence of nanometric metallic iron (evident by XRD) and other phases including cohenite $Fe_3C$, iron sulphide, and Fe-Ni-P compounds. By XRD we determined the iron sulphide to be troilite, but unfortunately due to the extremely small crystal size between 50 and 100 nm we were unable to determine the identity or stoichiometry of the Fe-Ni-P compounds, which could for example be schreibersite $(Fe,Ni)P_3$. Due to the nanometric
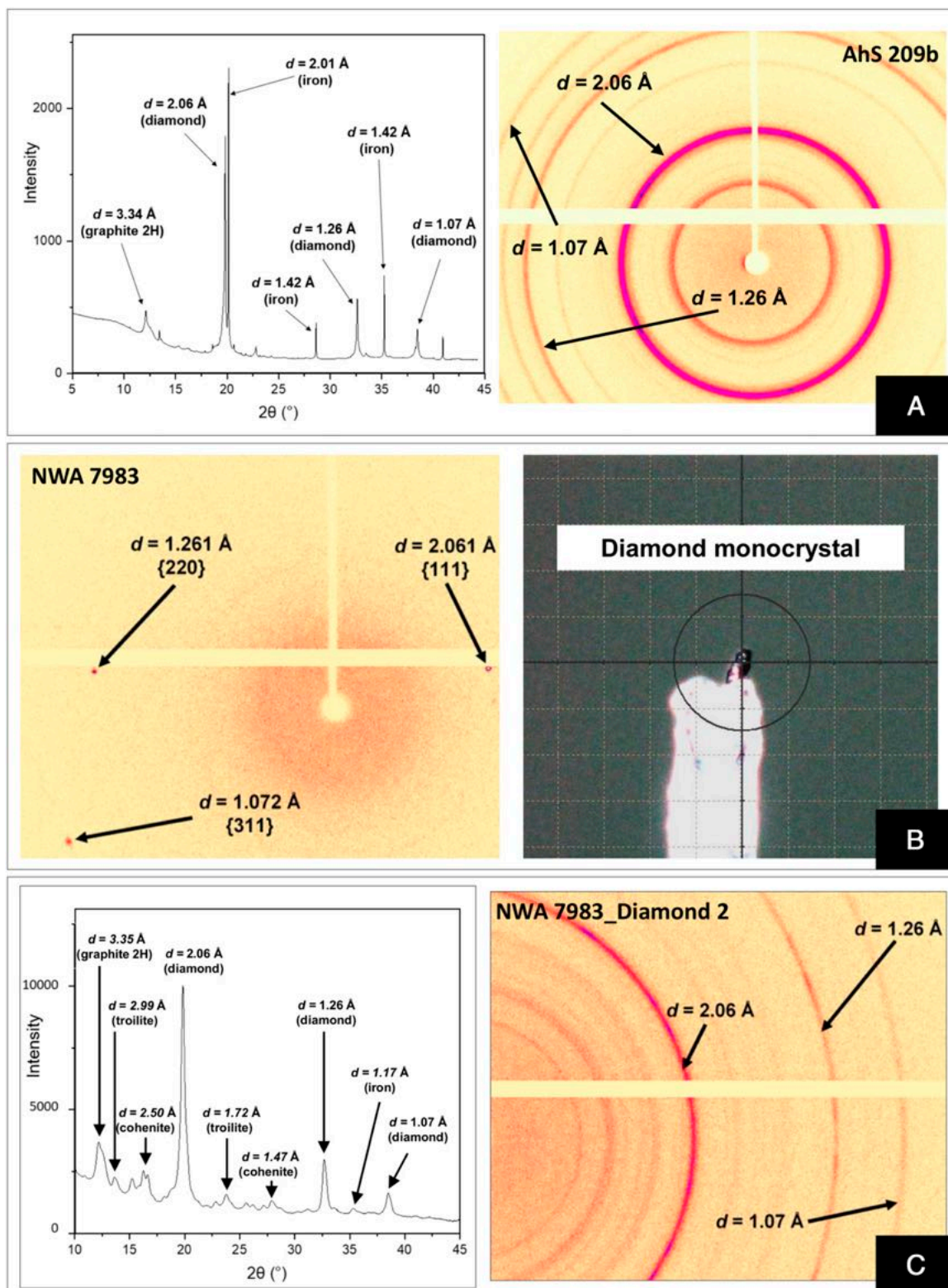
**Fig. 2.** (*A*) The diffractogram (*Left*) and the diffraction image (*Right*) of the AhS 209b sample, analyzed by micro X-ray powder diffraction at the Paul Scherrer Institute, Villigen, Switzerland. In the diffractogram the most abundant phases found in the carbon-bearing aggregate, polycrystalline diamond, graphite, and iron metal are shown. (*B*) Diffraction image (*Left*) for a fragment of a carbon area in NWA 7983 (from an area that was dark in BEI), showing only diffraction spots typical of a monocrystalline diamond. This monocrystal must be at least 100 μm (the size of the whole fragment removed along its longest dimension). We determined its unit-cell edge length, $a$ = 3.569 Å, typical of diamond. (*C*) Diffractogram (*Left*) and the diffraction image (*Right*) of another fragment of NWA 7983, this one from an area that was lighter in BEI. This sample was analyzed by the Rigaku-Oxford Diffraction Supernova kappa-geometry goniometer at the Department of Geoscience, University of Padova. In this fragment polycrystalline diamond, graphite, iron, cohenite, and a minor abundance of troilite are detected.

Nestola et al.

size of the diamonds in this sample, we cannot state definitively whether these other phases are inclusions in diamonds or just coexist with diamonds in the carbon masses.

## Discussion

**AhS 72 and AhS 209b.** The results from synchrotron diffraction and TEM analyses of the AhS ureilites studied in this work show nanodiamonds associated with nanographite. In addition, they show metallic iron, troilite, cohenite, and nanometric grains of Fe-Ni-P (likely schreibersite) associated with the diamond phases. The diamond–metal–sulfide–carbide–phosphide association in these AhS stones is the same phase assemblage as that reported in AhS stone MS-170 (13), which argues that the diamond had a common origin in all three stones. However, AhS 72 and AhS 209b are highly shocked ureilites, based on shock features in their silicates (complete mosaicism of olivine). This strongly suggests that the diamonds formed as a result of the same shock event that affected the silicates.

The association of metal, sulfide, carbide, and phosphide phases with diamonds in AhS 72 and AhS 209b is especially significant because Nabiei et al. (13) argued that these phases were definitive evidence of diamond formation at $\geq 21$ GPa static pressure within a parent body with size comparable to Mercury or Mars. Nabiei et al. (13) base this interpretation on the measured molar $(Fe+Ni)/(S+P)$ ratios of the bulk composition of multiphase (metal–sulfide–phosphide) inclusions in diamond, which were close to 3:1. They argue that this implies that the inclusions were trapped as crystals of the phase $(Fe,Ni)_3(S,P)$, which (for $P/[P+S] < 0.2$) is only stable at pressures above 21 GPa. However, this argument is flawed, because at temperatures above 1,275 °C (or lower if S is present) the $(Fe,Ni)_3(S,P)$ phase melts (40, 41). This temperature is almost certainly much lower than temperatures in a Mars-sized body 4.55 Ga ago at depths equivalent to 21 GPa (42). This means either that the interpretation that the inclusions were trapped as $(Fe,Ni)_3(S,P)$ solids is incorrect and their apparent stoichiometry is only a coincidence, or that the proposed formation in a Mars-sized body is incorrect, or both. In fact, the $(Fe,Ni)_3(P,S)$ phase can be formed simultaneously with diamonds by shock compression and quenching, as in shock melt veins in IIE iron meteorite Elga (43). Therefore, the presence of these inclusions does not in any way require a static pressure (large parent body) origin.

With respect to AhS 209b and AhS 72, based on the highly shocked nature of the silicates, and the association of nanodiamond, lonsdaleite, and nanographite, we argue that diamonds in these two ureilites most likely formed by a shock event (44–46) with a peak pressure possibly as low as 15 GPa, based on mosaicism of olivine (47). The presence of the same phase assemblage (diamond–metal–sulfide–carbide–phosphide) in AhS stone MS-170 (13) as in the highly shocked AhS stones studied here strongly suggests that diamond had a common origin in all three samples. However, based on these samples alone, it cannot be ruled out that preexisting, large, defect-poor diamonds [formed, e.g., at high static pressures (12,13)] were reduced in grain size and acquired stacking faults during the shock event that affected the silicates, and that in MS-170 some of these preexisting diamonds happened to survive. Nevertheless, additional evidence provided by NWA 7983 (discussed below) leads to the conclusion that this possibility would be extremely unlikely.

**NWA 7983.** NWA 7983 is a crucial sample for understanding the origin of diamonds in ureilites because its silicates record a high degree of shock (again, complete mosaicism of olivine) and yet it contains large diamonds (i.e., single crystal diamonds up to at least 100 μm in size) in addition to the nanodiamonds that are accepted to be a common product of shock (44–46). This discovery suggests the possibility that the large diamonds in this ureilite were also formed by the shock process, rather than simply having fortuitously survived it.

A first-order argument supporting this interpretation is the predominantly blade-shaped morphology of the carbon masses in which the diamonds are embedded along with graphite (Fig. 1 and *SI Appendix*, Fig. S5). This external morphology of the carbon areas is the same as that of millimeter-sized euhedral laminate (or tabular) graphite crystals that occur in very-low-shock-level ureilites (*SI Appendix*, Fig. S1) and have been argued to represent the primary form of carbon in all ureilites (23, 24). If the diamonds in NWA 7983 were only remnants of larger diamonds that had formed at high static pressures during long residence times in a planetary mantle, the external shapes of the carbon areas would not be those of graphite crystals (even if graphite laths had been the precursor material) but would be those of typical diamonds formed deep within the Earth's mantle (48). Instead, their shapes, and the prominent striped texture (Fig. 1 and *SI Appendix*, Figs. S5 and S6) of both the nanodiamond aggregates and the larger
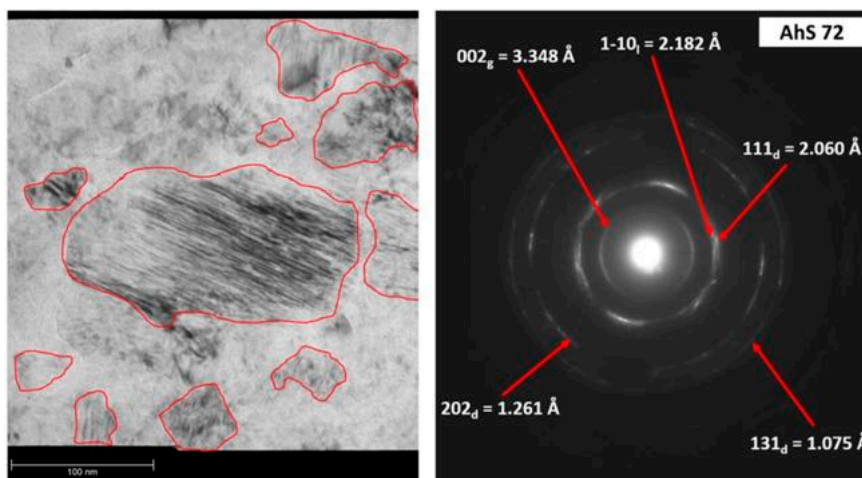


**Fig. 3.** (*Left*) A typical bright-field image of the AhS 72 sample, which shows diamond domains with size ranging from 20 to 150 nm. The corresponding electron diffraction image (*Right*) indicates that nanodiamonds are associated with graphite (see the ring at about 3.35 Å) and diamond with stacking faults, that is, lonsdaleite (see ring at about 2.18 Å), confirming the XRD results. The diffraction line indicators are represented by the (hkl) planes of diamond (indicated with the subscript "d") and graphite (indicated with the subscript "g") and give the spacing in angstroms. These images were obtained with a Philips CM200 transmission electron microscope.

diamonds within these blade-shaped regions, parallel to the long dimension of the laths which likely represents the trace of (0001) in original graphite (23, 24), strongly suggests that the diamonds are pseudomorphing original graphite crystals and formed in a rapid process that did not allow time for external graphite morphology to be replaced by diamond morphology. In fact, diamonds pseudomorphing original graphite forms is what is observed for diamonds formed in the Popigai impact crater (49, 50) in which aggregates of submicron-sized diamonds show external tabular shapes preserving the crystal habit of precursor graphite flakes (though we note that the primary graphite morphologies inferred for ureilites differ from those at Popigai).

As emphasized above, our observations of NWA 7983 represent an astonishing intimate association of micro- and nanodiamonds reported in a natural sample. The nanodiamond aggregates in NWA 7983 are especially abundant and render this ureilite even more resistant to cutting and polishing than most ureilites, similar to industrially produced ultrahard nanodiamonds (51, 52). As discussed by refs. 44–46, nanodiamonds of this type are the typical product of shock compression of disordered graphite, and nanodiamonds in ureilites and other meteorites are widely interpreted to be the product of impact shock (1, 4, 53, 54).

However, the formation mechanism of the large diamonds observed in NWA 7983, and the question of whether they formed at the same time as the nanodiamonds, are the critical issues in this investigation, as refs. 12 and 13 argue that such large sizes require long growth times under static high-pressure conditions. Hezel et al. (3) reported diamonds up to 5 μm in size (identified by in situ XRD) in a ureilite, and based on their close association with compressed graphite and secondary, polycrystalline graphite argued for formation of the diamonds by shock. The diamonds observed in this work are even larger and may require additional evidence to support formation in a shock event, the principal objections being the extremely short duration of peak pressure conditions during a shock event (45, 51, 55) and the kinetic/energetic limitations associated with direct transformation from graphite (45). We address both of these issues.

First, although the effective duration of a typical laboratory shock experiment is on the order of a microsecond, and so does not allow time for the growth of diamonds beyond very small (less than micrometer) sizes (46), large natural impacts have a significantly longer duration of high-pressure conditions (45). The largest craters on asteroid 4 Vesta, with a diameter of 400 to 500 km, could have formed from a 25- to 30-km impactor, with peak shock pressure during the compression stage lasting for 4 to 5 s (56). During the major impact event of UPB disruption, which is the most likely event in the history of ureilites to explain the majority of their shock features (17, 21, 32), the duration of the compression stage could have been comparably long, based on the impact parameters of ref. 57 for catastrophic disruption of the UPB and equations of ref. 56.

Second, although the direct transformation of graphite to diamond may require higher pressures and/or longer duration of pressure than those of many shock events (44, 45, 58) the catalyzed formation of diamonds in metallic (Fe,Ni,Co)-C melts proceeds at notably lower pressures and higher reaction rates and has long been used in industrial production of diamonds (59–64). Catalysis by metallic melts (referred to as the solvent method or solvent-catalysis in some literature) is likely to have been a significant factor in formation of diamonds in ureilites. As shown in *SI Appendix*, Fig. S1, the millimeter-sized euhedral graphite crystals in ureilites of very low shock level are intimately associated with Fe,Ni metal. Such metal is a common interstitial component associated with carbon in most ureilites (18, 65). Goodrich et al. (65) argued that the metal in ureilites represents Fe-Ni-C melt that was present at $T \geq 1,150$ °C and remained after extraction of lower-temperature Fe,S-enriched melt during the igneous stage of ureilite formation. The presence in ureilite silicates of ~5- to 150-μm-diameter metallic spherules, consisting of cohenite ($Fe_3C$), metal, schreibersite ($Fe_3P$), and sulfide, constitute direct evidence for the presence of such melts at magmatic temperatures (65, 66). The impact disruption of the UPB occurred while the silicates were still hot, ~1,050 ± 50 °C (18, 21). The temperature increase associated with this impact shock event, assuming a 5 km·s$^{-1}$ relative velocity, would have been on the order of 200 to 300 °C (67). Thus, grain boundary metal would have been remelted to create Fe-Ni-C liquids, and it seems inescapable that they would have had a large effect on the growth rate of diamonds forming during the shock event. The importance of such metallic liquids in catalyzing the formation of diamonds from graphite in ureilites was previously suggested by ref. 6 though not discussed for diamonds of such large sizes as those observed here.

There is, in fact, a vast literature on the formation of diamonds via the catalytic method, because of the industrial importance of diamond. In general, the catalyzed formation of diamonds from graphite occurs in a very thin film of molten metal in contact with graphite (62, 64, 68), with reported diamond growth rates ranging from 0.2 to 0.4 μm/s at 5.4 GPa and 1,127 °C (62) to 30 to 60 μm/s (in the first 20 s) at 4.5 GPa and 1,100 to 1,200 °C (59). The latter rates would easily permit formation of a 100-μm-sized diamond, as observed in NWA 7983, in the ~4 to 5 s estimate made above for the duration of peak pressure during the catastrophic disruption of the UPB. This evidence is sufficient to show that formation of large diamonds in ureilites during shock events is plausible and to cast reasonable doubt on the necessity for much longer growth times under static high-pressure conditions (12, 13).

Catalyzed formation of diamonds during a shock event can also account for simultaneous formation of micro- and nanodiamonds in ureilites. For example, using a technique of pulsed heating of a graphite-metal experimental charge in a static high-pressure apparatus at 8 to 14 GPa, which simulates natural impact processes (45, 55) with respect to duration of peak pressures and temperatures, Varfolomeeva (60) reported formation of up to 10-μm-sized diamonds near the catalyst and nanodiamonds in other parts of the experimental charge (*SI Appendix*, Fig. S14).

Catalysis of diamond formation from graphite via metallic melts may also explain other features of the diamonds in NWA 7983. For example, we hypothesize that the striped internal textures of the carbon areas, defined by stripes of concentrated (higher abundance of larger) diamonds and C-dominated (Fe,S-absent) chemistry (darker in BEI) alternating with stripes of dominantly nanodiamonds and C+Fe+S chemistry, could have formed if the metallic melts were injected between (0001) graphite platelets [assuming the long dimensions of the carbon masses to represent the trace of (0001) in original large graphite crystals]. Growth of larger diamonds then proceeded to form the largely Fe-free dark stripes adjacent to the metallic liquids, while the lighter stripes retain concentrations of residual Fe intermixed with nanodiamonds. In addition, ref. 59 suggested that the growth of diamonds from metallic liquids proceeded through the intermediate step of carbide formation, which could explain the association of cohenite ($Fe_3C$) with diamonds observed in this work (Fig. 2C). Another type of inclusion, chromite, reported by ref. 13 in ureilite diamonds, could also support catalytic formation of diamonds during a shock event. Nabiei et al. (13) noted that the nearly pure (Al-Ti-Mg-free) compositions of the chromite required crystallization from metallic melts (references 22 and 23 in ref. 13). We agree with this interpretation, which is strongly supported by the presence of similarly pure chromite in the metallic metal–cohenite–sulfide–phosphide spherules in ureilite silicates mentioned above (65, 66). However, in contrast to Nabiei et al. (13), who argued that the presence of such melts was inconsistent with the low-pressure igneous setting of ureilite

formation, we note that the metallic spherules provide direct evidence that such melts were present in the primary ureilite silicate assemblage (65, 66) and so could have been remobilized to catalyze the formation of diamonds in an impact shock event.

**Additional Evaluation of Proposed Evidence for High Static Pressure.** The 100-μm-sized single diamond crystal that we observed in NWA 7983 constitutes the first definite report of diamonds of this size in a ureilite. Nabiei et al. (13) did not determine the sizes of the diamonds they studied in MS-170 (e.g., no micro XRD was performed showing diffraction spots) but rather relied on the previous report by Miyahara et al. (12) of large diamonds in this sample. In fact, the "large" diamonds reported by Miyahara et al. (12) in MS-170 were not actually large single crystals but rather aggregates of many individual (unconnected) segments having almost the same crystallographic orientation. These aggregates were interpreted (12, 13) to have originally been large single crystals. However, this is not the only possible interpretation. In fact, an aggregate of similarly oriented small crystals is what is expected for diamonds formed by shock compression of oriented graphite (50, 69, 70), as noted also by ref. 6. Miyahara et al. (12) stated that they did not observe the predicted crystallographic relationship between diamond and graphite, and used this as an argument against a shock origin. However, if originally large single graphite crystals had been internally recrystallized in a shock event to nanometric, randomly oriented grains (like those observed in the samples studied here), which is likely (71), their current orientations relative to the diamond are irrelevant. Instead, the orientation of the diamonds would have to be compared with the original orientation of the graphite precursors.

By contrast, the presence of a truly single-crystal 100-μm-sized diamond in a highly shocked ureilite (NWA 7983) makes it more likely that such diamonds actually formed as a result of the shock process, rather than just having survived it. The shock state of silicates in MS-170 was not investigated by refs. 12 and 13 but was classified as S3 by ref. 31, which implies shock pressures of 5 to 10 GPa (47), sufficient to produce diamonds (see ref. 6). Critically, the external morphologies of the carbon masses in MS-170 are no different from those in NWA 7983 or other ureilites—that is, they are elongated masses along silicate grain boundaries, suggesting that they were originally large, single crystals of graphite, as discussed above for all ureilites. This can be observed from inspection of figure 1 of ref. 13 compared with *SI Appendix*, Fig. S1 and was confirmed by recent studies of our own on MS-170. This makes it extremely unlikely that the diamonds formed during long residence times at high pressures, because if they had then external diamond morphologies would have formed. In other words, there is no evidence that MS-170 is an unusual ureilite preserving diamonds formed in a planetary mantle.

Finally, Miyahara et al. (12) also reported the observation of sector zoning of nitrogen in diamond assemblages in MS-170 and argued that this required "sluggish growth" as in a static high-pressure setting. However, the evidence they present for sector zoning (e.g., figure 5 of ref. 12) is at best ambiguous. Heterogeneous nitrogen distribution is clearly shown, but its relationship to diamond crystal morphology is unclear, given that the diamond consists of several unconnected segments separated by areas of graphite (as discussed above) and no crystal orientation information is given. Furthermore, even if sector zoning of nitrogen is present in large ureilite diamonds, this would not require long, slow growth. For example, diamonds grown by the DeBeers Diamond Research Laboratory using an Fe-Ni metal catalyst for diamond growth developed strong sector zonation of nitrogen in 15 to 20 s (*SI Appendix*, Fig. S15), which is hardly "sluggish." The distribution of nitrogen in large ureilite diamonds, and what it implies for their formation, warrants further investigation, but at this time there is no evidence that it supports a high static pressure.

## Conclusions

In conclusion, the results from combined micro XRD, TEM, SEM, EMPA, and micro-Raman spectroscopy of three highly shocked ureilites suggest that the most likely process by which both microdiamonds and nanodiamonds in ureilites formed is in a shock event characterized by a peak pressure possibly as low as 15 GPa, the shock level recorded by the silicates. Micrometer-sized diamonds can form from crystalline graphite in shock events when catalyzed by metallic Fe-Ni-C liquid, which was demonstrably present during the major shock events that occurred on the UPB, and do not require high static pressures and long growth times. None of the minor Fe-S-P phases associated with the diamonds in ureilites require high static pressures either, nor does sector zonation of nitrogen in diamonds. We find no compelling evidence that diamonds in ureilites formed in large planetary bodies or planetary embryos (13).

## Methods

Petrological and mineralogical features of silicate and carbon phases in ureilites AhS 209b, AhS 72, and NWA 7983 were studied in polished sections by optical microscopy and electron microscopy (SEM) at the Lunar and Planetary Institute (Universities Space Research Association, Houston, TX), the ARES division at NASA, JSC, and the University of Padova. Carbon phases were additionally studied by XRD at the University of Padova, synchrotron-radiation X-ray microdiffraction at the Paul Scherrer Institute, TEM at Goethe University in Frankfurt, and micro-Raman spectroscopy at JSC. Contamination of the samples by diamond from the cutting and polishing was avoided by polishing the samples with silicon carbide paper. Further details of the techniques used in this work are provided in *SI Appendix*.

**Data Availability.** All study data are included in the paper, *SI Appendix*, and Datasets S1–S3. The three diffractograms for AhS 209b, AhS 72, and NWA 7983 Diamond 2 are available in a .txt format (intensity vs. 2θ angle) and can be visualized using any graphical software (Datasets S1–S3).

1. M. E. Lipschutz, Origin of diamonds in the ureilites. *Science* **143**, 1431–1434 (1964).
2. Y. Nakamuta, Y. Aoiko, Mineralogical evidence for the origin of diamond in ureilites. *Meteorit. Planet. Sci.* **35**, 487–493 (2000).
3. D. C. Hezel *et al.*, In situ micro-Raman and X-ray diffraction study of diamonds and petrology of the new ureilite UAE 001 from the United Arab Emirates. *Meteorit. Planet. Sci.* **43**, 1127–1136 (2008).
4. C. Le Guillou, J. N. Rouzaud, L. Remusat, A. Jambon, M. Bourot-Denise, Structures, origin and evolution of various carbon phases in the ureilite Northwest Africa 4742 compared with laboratory-shocked graphite. *Geochim. Cosmochim. Acta* **74**, 4167–4185 (2010).
5. A. J. Ross *et al.*, MicroRaman spectroscopy of diamond and graphite in Almahata Sitta and comparison with other ureilites. *Meteorit. Planet. Sci.* **46**, 364–378 (2011).
6. Y. Nakamuta, F. Kitajima, K. Shimada, In situ observation, X-ray diffraction and Raman analyses of carbon minerals in ureilites: Origin and formation mechanisms of diamond in ureilites. *J. Mineral. Petrol. Sci.* **111**, 252–269 (2016).
7. C. A. Lorenz, A. A. Shiryaev, I. I. Vlasov, S. E. Borisovsky, Metamorphism of four desert ureilites and luminescence spectroscopy of defects in ureilitic diamonds. *Meteorit. Planet. Sci.* **54**, 1197–1214 (2019).
8. K. Fukunaga, J. Matsuda, K. Nagao, K. Miyamoto, K. Ito, Noble-gas enrichment in vapour-growth diamonds and the origin of diamond in ureilites. *Nature* **328**, 141–143 (1987).
9. J. I. Matsuda, K. Fukunaga, K. Ito, Noble gas studies in vapor-growth diamonds: Comparison with shock produced diamonds and the origin of diamonds in ureilites. *Geochim. Cosmochim. Acta* **55**, 2011–2023 (1991).

10. J. I. Matsuda, A. Kusumi, H. Yajima, Y. Syono, Noble gas studies in diamonds synthesized by shock loading in the laboratory and their implications on the origin of diamonds in ureilites. *Geochim. Cosmochim. Acta* **59**, 4939–4949 (1995).
11. H. C. Urey, Diamonds, meteorites, and the origin of the solar system. *Astrophys. J.* **124**, 623–637 (1956).
12. M. Miyahara *et al.*, Unique large diamonds in a ureilite from Almahata Sitta 2008 TC$_3$ asteroid. *Geochim. Cosmochim. Acta* **163**, 14–26 (2015).
13. F. Nabiei *et al.*, A large planetary body inferred from diamond inclusions in a ureilite meteorite. *Nat. Commun.* **9**, 1327 (2018).
14. G. Vdovykin, Ureilites. *Space Sci. Rev.* **10**, 483–510 (1970).
15. J. L. Berkley, G. J. Taylor, K. Keil, G. E. Harlow, M. Prinz, The nature and origin of ureilites. *Geochim. Cosmochim. Acta* **44**, 1579–1597 (1980).
16. C. A. Goodrich, Invited review. Ureilites: A critical review. *Meteorit. Planet. Sci.* **352**, 327–352 (1992).
17. C. A. Goodrich, E. R. D. Scott, A. M. Fioretti, Ureilitic breccias: Clues to the petrologic structure and impact disruption of the ureilite parent body. *Chem. Erde* **64**, 283–327 (2004).
18. D. W. Mittlefehldt, T. J. McCoy, C. A. Goodrich, A. Kracher, Non-chondritic meteorites from asteroidal bodies. *Rev. Mineral. Geochem.* **36**, 4.1-4.195 (1998).
19. C. A. Goodrich *et al.*, Origin and history of ureilitic material in the solar system: The view from asteroid 2008 TC$_3$ and the Almahata Sitta meteorite. *Meteorit. Planet. Sci.* **50**, 782–809 (2015).
20. H. Downes, D. W. Mittlefehldt, N. T. Kita, J. W. Valley, Evidence from polymict ureilites for a disrupted and re-accreted single ureilite parent asteroid gardened by several distinct impactors. *Geochim. Cosmochim. Acta* **72**, 4825–4844 (2008).
21. J. S. Herrin *et al.*, Thermal and fragmentation history of ureilitic asteroids: Insights from the Almahata Sitta fall. *Meteorit. Planet. Sci.* **45**, 1789–1803 (2010).
22. E. A. Cloutis *et al.*, Spectral reflectance properties of ureilites. *Meteorit. Planet. Sci.* **45**, 10–11 (2010).
23. J. L. Berkley, J. H. Jones, Primary igneous carbon in ureilites: Petrological implications. *J. Geophys. Res.* **87**, A353–A364 (1982).
24. A. H. Treiman, J. L. Berkley, Igneous petrology of the new ureilites Nova 001 and Nullarbor 010. *Meteoritics* **29**, 843–848 (1994).
25. J. F. Wacker, Noble gases in the diamond-free ureilite ALHA78019: The roles of shock and nebular processes. *Geochim. Cosmochim. Acta* **50**, 633–642 (1986).
26. M. Murri *et al.*, Quantifying hexagonal stacking in diamond. *Sci. Rep.* **9**, 10334 (2019).
27. S. J. Desch, J. G. O'Rourke, L. K. Schaefer, T. G. Sharp, D. L. Schrader, Diamonds in ureilites from Mars. *Lunar Planet. Sci. Conf. Abstr* **50**, 1646 (2019).
28. A. Ruzicka, J. Grossman, A. Bouvier, D. K. Herd, B. Agee, The Meteoritical Bulletin, No. 102. *Meteorit. Planet. Sci.* **50**, 1662 (2015).
29. P. Jenniskens *et al.*, The impact and recovery of asteroid 2008 TC$_{(3)}$. *Nature* **458**, 485–488 (2009).
30. M. H. Shaddad *et al.*, The recovery of asteroid 2008 TC$_3$. *Meteorit. Planet. Sci.* **45**, 1557–1589 (2010).
31. M. Horstmann, A. Bischoff, The Almahata Sitta polymict breccia and the late accretion of asteroid 2008 TC$_3$. *Chem. Erde* **74**, 149–183 (2014).
32. P. H. Warren, A. E. Rubin, Pyroxene-selective impact smelting in ureilites. *Geochim. Cosmochim. Acta* **74**, 5109–5133 (2010).
33. J. L. Berkley, Four Antarctic ureilites: Petrology and observations on ureilite petrogenesis. *Meteoritics* **21**, 169–189 (1981).
34. R. Delhez, E. J. Mittemeijer, Determination of crystallite size and lattice distortions through X-ray diffraction line profile analysis. *Anal. Chem.* **312**, 1–16 (1982).
35. M. Leoni, F. Gualtieri, N. Roveri, Simultaneous refinement of structure and microstructure of layered materials. *J. Appl. Cristallogr.* **37**, 166–173 (2004).
36. V. I. Korepanov, H. Witek, H. Okajima, E. Ōsawa, H. O. Hamaguchi, Communication: Three-dimensional model for phonon confinement in small particles: Quantitative bandshape analysis of size-dependent Raman spectra of nanodiamonds. *J. Chem. Phys.* **140**, 041107 (2014).
37. S. A. Solin, A. K. Ramdas, Raman spectrum of diamond. *Phys. Rev. B* **1**, 1687–1698 (1970).
38. S. Osswald, V. N. Mochalin, M. Havel, G. Yushin, Y. Gogotsi, Phonon confinement effects in the Raman spectrum of nanodiamond. *Phys. Rev. B* **80**, 75419 (2009).
39. A. C. Ferrari, J. Robertson, Raman spectroscopy of amorphous, nanostructured, diamond-like carbon, and nanodiamond. *Philos. Trans. A Math. Phys. Eng. Sci.* **362**, 2477–2512 (2004).
40. D. A. Minin, A. Shatskiy, K. D. Litasov, H. Ohfuji, The Fe–Fe$_2$P phase diagram at 6 GPa. *High Pressure Res.* **39**, 50–68 (2019).
41. A. J. Stewart, M. W. Schmidt, Sulfur and phosphorus in the Earth's core : The Fe-P-S system at 23 GPa. *Geophys. Res. Lett.* **34**, 5–9 (2007).
42. K. Righter, N. L. Chabot, Moderately and slightly siderophile element constraints on the depth and extent of melting in early Mars. *Meteorit. Planet. Sci.* **176**, 157–176 (2011).
43. K. D. Litasov, S. N. Teplyakova, A. Shatskiy, K. E. Kuper, Fe-Ni-P-S melt pockets in Elga IIE iron meteorite: Evidence for the origin at high-pressures up to 20 GPa. *Minerals* **9**, 616 (2019).
44. P. S. De Carli, Shock wave synthesis of diamond and other phases. *MRS Proc.* **383**, 21–31 (1995).
45. P. S. De Carli *et al.*, "Laboratory impact experiments versus natural impact events" in *Catastrophic Events and Mass Extinctions: Impacts and Beyond*, C. Koeberl, K. G. MacLeod, Eds. (GSA Special Paper, Geological Society of America, Boulder, CO, 2002), Vol. 356, pp. 595–605.
46. P. S. Decarli, J. C. Jamieson, Formation of diamond by explosive shock. *Science* **133**, 1821–1822 (1961).
47. D. Stöffler, C. Hamann, K. Metzler, Invited Review, Shock metamorphism of planetary silicate rocks and sediments: Proposal for an updated classification system. *Meteorit. Planet. Sci.* **49**, 5–49 (2018).
48. F. Nestola *et al.*, CaSiO$_3$ perovskite in diamond indicates the recycling of oceanic crust into the lower mantle. *Nature* **555**, 237–241 (2018).
49. C. Koeberl *et al.*, Diamonds from the Popigai impact structure, Russia. *Geology* **25**, 967–970 (1997).
50. H. Ohfuji *et al.*, Natural occurrence of pure nano-polycrystalline diamond from impact crater. *Sci. Rep.* **5**, 14702 (2015).
51. T. Irifune, A. Kurio, S. Sakamoto, T. Inoue, H. Sumiya, Materials: Ultrahard polycrystalline diamond from graphite. *Nature* **421**, 599–600 (2003). Correction in: *Nature* **421**, 806 (2003).
52. F. Isobe, H. Ohfuji, H. Sumiya, T. Irifune, Nanolayered diamond sintered compact obtained by direct conversion from highly oriented graphite under high pressure and high temperature. *J. Nanomater.* **2013**, 380165 (2013).
53. L. A. J. Garvie, P. Németh, P. R. Buseck, Transformation of graphite to diamond via a topotactic mechanism. *Am. Mineral.* **99**, 531–538 (2014).
54. S. Mostefaoui, A. El Goresy, P. Hoppe, Ph. Gillet, U. Ott, Mode of occurrence, textural settings and nitrogen-isotopic compositions of in situ diamonds and other carbon phases in the Bencubbin meteorite. *Earth Planet. Sci. Lett.* **204**, 89–100 (2002).
55. F. P. Bundy, J. S. Kasper, Hexagonal diamond–A new form of carbon. *J. Chem. Phys.* **46**, 3437–3446 (1967).
56. P. Gillet, A. El Goresy, Shock events in the solar system: The message from minerals in terrestrial planets and asteroids. *Annu. Rev. Earth Planet. Sci.* **41**, 257–285 (2013).
57. P. Michel *et al.*, Selective sampling during catastrophic disruption: Mapping the location of reaccumulated fragments in the original parent body. Proceedings of the 8$^{th}$ Catastrophic Disruption Workshop. *Planet. Space Sci.* **107**, 24–28 (2015).
58. C. Le Guillou, F. Brunet, T. Irifune, H. Ohfuji, J.-N. Rouzaud, Nanodiamond nucleation below 2273 K at 15 GPa from carbons with different structural organizations. *Carbon* **45**, 636–648 (2007).
59. G. N. Bezrukov *et al.*, "Kinetic features of diamond crystallization" in *Growth of Crystals*, N. N. Sheftal', E. I. Givargizov, Eds. (Consultants Bureau, New York,, 1975), Vol. 9, pp. 74–77.
60. T. D. Varfolomeeva, "Synthesis and investigation of polycrystalline diamond," PhD thesis, Institute for High Pressure Physics, USSR Academy of Sciences (1971), p. 154.
61. L. F. Trueb, An electron-microscope study of shock-synthesized diamond. *J. Appl. Phys.* **39**, 4707–4716 (1968).
62. H. M. Strong, R. E. Hanneman, Crystallization of diamond and graphite. *J. Chem. Phys.* **45**, 3668–3676 (1967).
63. I. I. Fedorov, A. A. Chepurov, J. M. Dereppe, Redox conditions of metal-carbon melts and natural diamond genesis. *Geochem. J.* **36**, 247–253 (2002).
64. F. P. Bundy *et al.*, The pressure-temperature phase and transformation diagram for carbon; updated through 1994. *Carbon* **34**, 141–153 (1996).
65. C. A. Goodrich, R. D. Ash, J. A. Van Orman, K. Domanik, W. F. McDonough, Metallic phases and siderophile elements in main group ureilites: Implications for ureilite petrogenesis. *Geochim. Cosmochim. Acta* **112**, 340–373 (2013).
66. C. A. Goodrich, J. L. Berkley, Primary magmatic carbon in ureilites: Evidence from cohenite-bearing metallic spherules. *Geochim. Cosmochim. Acta* **50**, 681–691 (1986).
67. D. Stöffler, E. R. D. Klaus Keil, Scott, Shock metamorphism of ordinary chondrites. *Geochim. Cosmochim. Acta* **55**, 3845–3867 (1991).
68. H. P. Bovenkerk, F. P. Bundy, H. M. Strong, R. H. Wentorf Jr., H. T. Hall, Preparation of diamond. *Nature* **184**, 1094–1098 (1959).
69. D. J. Erskine, W. J. Nellis, Shock-induced martensitic phase transformation of oriented graphite to diamond. *Nature* **349**, 317–319 (1991).
70. H. Ohfuji, M. Nakaya, A. P. Yelisseyev, V. P. Afanasiev, K. D. Litasov, Mineralogical and crystallographic features of polycrystalline yakutite diamond. *J. Mineral. Petrol. Sci.* **112**, 46–51 (2017).
71. A. N. Dremin, O. N. Breusov, "Dynamic synthesis of superhard materials" in *Shock Waves in Materials Science*, A. B. Sawaoka, Ed. (Springer, Tokyo, 1993), pp. 17–34.

# Origin of micrometer-sized impact diamonds in ureilites by catalytic growth involving Fe-Ni-silicide: The example of Kenna meteorite

Anna Barbaro [a,*], Maria Chiara Domeneghetti [a], Konstantin D. Litasov [b,c], Ludovic Ferrière [d], Lidia Pittarello [d], Oliver Christ [e], Sofia Lorenzon [e], Matteo Alvaro [a], Fabrizio Nestola [e,f]

[a] *Dipartimento di Scienze della Terra e dell'Ambiente, Università degli Studi di Pavia, Via Ferrata 1, I-27100 Pavia, Italy*
[b] *Vereshchagin Institute for High Pressure Physics RAS, Troitsk, Moscow 108840, Russia*
[c] *Fersman Mineralogical Museum RAS, Moscow 115162, Russia*
[d] *Natural History Museum, Department of Mineralogy and Petrography, Burgring 7, 1010 Vienna, Austria*
[e] *Dipartimento di Geoscienze, Università degli Studi di Padova, Via G. Gradenigo 6, I-35131 Padova, Italy*
[f] *Geoscience Institute, Goethe-University Frankfurt, Altenhöferalee 1, 60323 Frankfurt, Germany*

## Abstract

The occurrence of shock-induced diamonds in ureilite meteorites is common and is used to constrain the history of the ureilite parent bodies. We have investigated a fragment of the Kenna ureilite by micro-X-ray diffraction, micro-Raman spectroscopy and scanning electron microscopy to characterize its carbon phases. In addition to olivine and pigeonite, within the carbon-bearing areas, we identified microdiamonds (up to about 10 μm in size), nanographite and magnetite. The shock features observed in the silicate minerals and the presence of microdiamonds and nanographite indicate that Kenna underwent a shock event with a peak pressure of at least 15 GPa. Temperatures estimated using a graphite geothermometer are close to 1180 °C. Thus, Kenna is a medium-shocked ureilite, yet it contains microdiamonds, which are typically found in highly shocked carbon-bearing meteorites, instead of the more common nanodiamonds. This can be explained by a relatively long shock event duration (in the order of 4–5 s) and/or by the catalytic effect of Fe-Ni alloys known to favour the crystallization of diamonds. For the first time in a ureilite, carletonmooreite with formula $Ni_3Si$ and grain size near 4–7 nm, was found. The presence of nanocrystalline carletonmooreite provides further evidence to support the hypothesis of the catalytic involvement of Fe-Ni bearing phases into the growth process of diamond from graphite during shock events in the ureilite parent body, enabling the formation of micrometer-sized diamond crystals.
© 2021 Elsevier Ltd. All rights reserved.

*Keywords:* Kenna meteorite; Ureilite; Diamond; Graphite; Carletonmooreite; Shock metamorphism

## 1. INTRODUCTION

Ureilites are achondritic meteorites, which consist of ultramafic rocks mainly composed of olivine and pigeonite (an exhaustive review about the ureilite group can be found in Goodrich, 1992). Ureilites contain up to ~8 wt% of car-

* Corresponding author at: Dipartimento di Scienze della Terra e dell'Ambiente, Università degli Studi di Pavia, Via Ferrata 1, I-27100 Pavia, Italy.
*E-mail address:* anna.barbaro01@universitadipavia.it (A. Barbaro).

bon (e.g. Cloutis et al., 2010; Goodrich et al., 2015), which is mostly present as diamond and graphite, located in the interstitial space between silicate grains. Diamond and graphite are commonly accompanied by iron-nickel metal, troilite and other accessory phases (e.g. Berkley et al., 1976).

The origin of diamonds in ureilites is still debated within the scientific community. Lipschutz (1964) proposed that diamonds were formed by shock conversion of graphite during the catastrophic breakup of the ureilitic parent body (UPB), while Fukunaga et al. (1987) suggested that diamonds could grow from a dilute gas phase by chemical vapour deposition process (CVD). Another hypothesis by Urey (1956) excludes the shock origin of diamond and instead proposes a process similar to that observed for Earth's mantle diamonds, which is that diamonds are formed under high static pressure conditions in the deep interior of the UPB. This last hypothesis was re-evaluated in some works on the Almahata Sitta ureilite by Miyahara et al. (2015) and Nabiei et al. (2018).

On the other hand, a recent study by Nestola et al. (2020), based on combined data obtained by micro X-ray diffraction (XRD) and transmission electron microscopy (TEM) on three highly-shocked ureilitic samples, Almahata Sitta 209b and 72, and NWA 7983, suggests that diamond formation in ureilites is most likely related to shock, probably characterized by a peak pressure of at least 15 GPa. These authors report on the coexistence of both nanodiamonds and microdiamonds (with single crystals up to 100 μm in size) as well as nanographite intergrown with iron-nickel alloys. According to these authors, the co-occurrence of large monocrystalline diamonds and nanodiamonds can be explained by transformation from graphite during an impact event due to peak pressure with a local duration of up to a few seconds (De Carli et al. 2002). The formation of such "large" diamonds have been favoured by the catalytic effect of metallic Fe-Ni-C liquid interacting with graphite during impact events.

The Kenna ureilite meteorite (Berkley et al., 1976) had a mass of 10.9 kg. Several studies on Kenna have provided data on petrography (Berkley, et al. 1976), noble gases

and fossil particles tracks (Wilkening and Marti,1976), magnetism (Brecher and Fuhrman, 1979), oxygen isotope composition (Clayton et al., 1976), reflectance properties (Cloutis et al., 2010) and carbon content (Nakamuta and Aoki 2000). The occurrence of diamond and graphite, reported by Nakamuta and Aoki (2000) based on X-ray powder diffraction data, showed an intimate coexistence of diamond and graphite, similar to that reported for other ureilites by Nestola et al. (2020) and Barbaro et al. (2021).

Concerning carbon phases, Nakamuta and Aoki (2000) reported on the occurrence of diamond and graphite based on X-ray powder diffraction data obtained using a Gandolfi camera and showed an intimate coexistence of diamond and graphite. Similar intimate coexistence was reported by Nestola et al. (2020) for Almahata Sitta and NWA 6873, and by Barbaro et al. (2021) for Yamato 74123 ureilite.

The aim of this study is the analysis of carbon-bearing aggregates (diamond, graphite and other minor phases) in Kenna ureilite in order to understand their origin, following the same experimental approaches adopted by Nestola et al. (2020) and Barbaro et al. (2021). During our investigations, we found, for the first time in an ureilite (and the second occurrence in a natural sample), a recently discovered $Ni_3$-Si phase called carletonmooreite (IMA 2018-068; Garvie et al., 2021), originally reported by Ma et al. (2018) within the Norton County aubrite meteorite. Using a multi-methods approach [by scanning electron microscopy (SEM), energy dispersive X-ray spectroscopy (EDS), X-ray diffraction (XRD) and micro-Raman spectroscopy (MRS)] we have characterized the carbon phases and estimated the shock pressure and temperature experienced by the Kenna meteorite. Our new observations are discussed in terms of shock metamorphism and compared with observations reported from other ureilites.

## 2. MATERIALS AND ANALYTICAL PROCEDURES

The polished thin section NHMW-O1972 (Fig. 1) and fragment of Kenna (Fig. 2) here investigated are from the Natural History Museum, Vienna (NHMW, Austria) meteorite collection (note that thin section NHMW-O1972 was
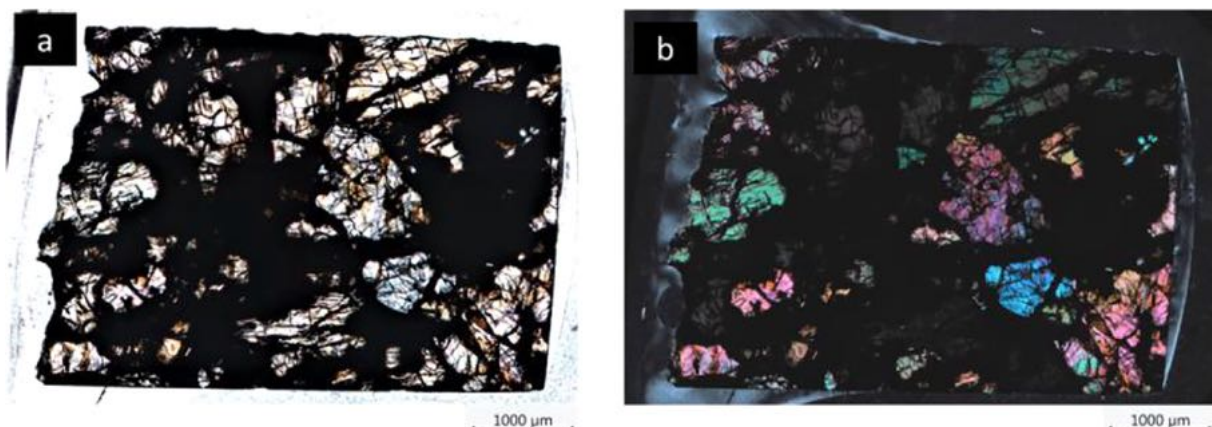


Fig. 1. Thin section of Kenna ureilite in (a) plane polarized light and (b) cross polarized light; the opaque material (mainly composed by carbon material, Fe-Ni alloys and fine silicate crystals) around the large silicate crystals of olivine and pigeonite is shown.
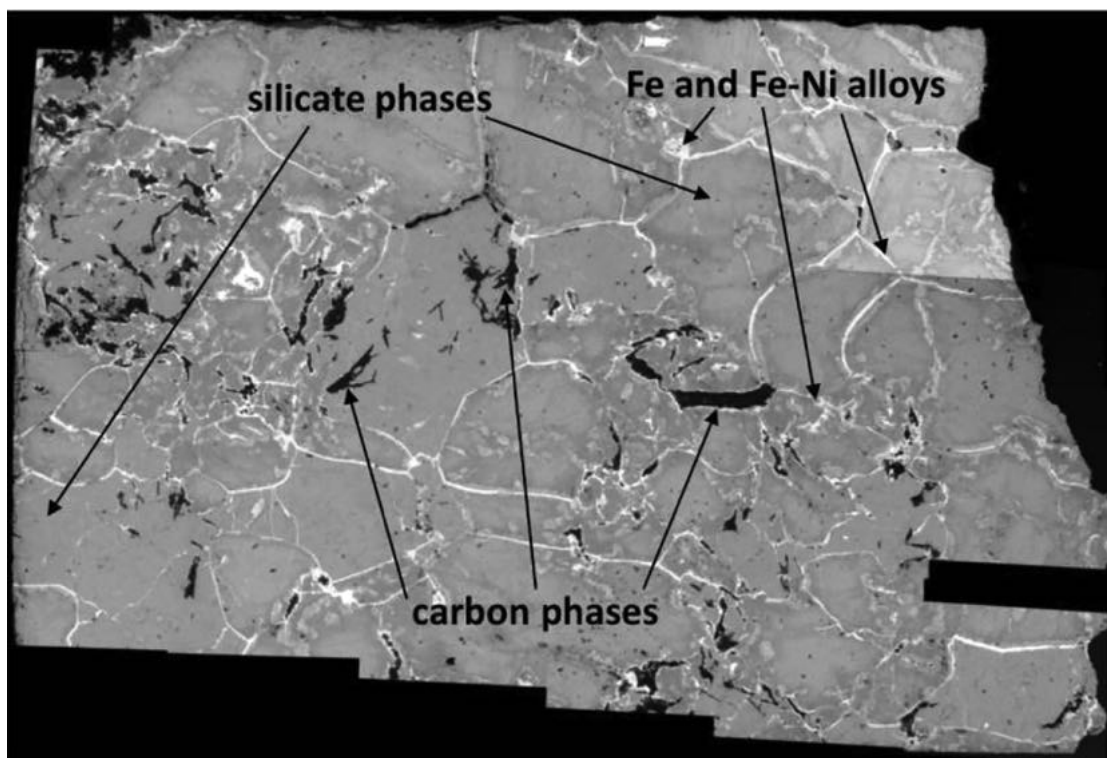
Fig. 2. Mosaic of BSE images of a Kenna ureilitic fragment. Silicate phases (light grey 91%), carbon phases (black 4%) and Fe, Fe-Ni alloys and Fe oxides (white 5%) are easily distinguishable. Relative abundance estimated by image analysis.

prepared from the fragment of Kenna investigated here). Petrographic characterization of the thin section (Fig. 1) was carried out at the "Fiorenzo Mazzi" Experimental Mineralogy Lab at the Earth and Environmental Department of University of Pavia (Italy) using a conventional petrographic microscope in transmitted light.

The non-carbon coated fragment of Fig. 2 was analysed using low vacuum FEI Quanta 200 equipped with an EDS, at CEASC (Centro di Analisi e Servizi per la Certificazione) at the University of Padova (Italy). The working distance was 14 mm, with an emission current of 93 mA, and a voltage of 20 kV. From this fragment we gently removed a small grain from the dark areas in Fig. 2. This grain was then mounted at the tip of a glass fibre for EDS, SEM, micro-XRD and MRS analyses. Unfortunately, we could not perform electron microprobe analysis on the carbon-bearing aggregate sample due to the softness of the material that prevented embedding it in epoxy and subsequent polishing.

A back-scattered electron (BSE) image (collected with a working distance of 13.8 mm, emission current of ca.100 mA and voltage of about 20 kV) of the grain is shown in Fig. 3. The grain, an aggregate fragment, with its longest dimension reaching about 100 μm, was investigated using a Rigaku-Oxford Diffraction Supernova kappa-geometry diffractometer (at the Department of Geosciences, University of Padova) equipped with an X-ray Mo micro-source and a Pilatus 200 K Dectris detector, con-

trolled with the CrysAlis-Pro™ software. Diffraction profile of the powder pattern was analysed using the High Score Plus Software package (from Panalytical). We also performed line profile analysis fitting to the diffraction pattern obtained on the carbon-bearing aggregate with the aim to estimate the crystallite size of the carletonmooreite ($Ni_3Si$) present in this sample using the same High Score Plus software.

To estimate the crystallite size of graphite and carletonmooreite, we applied line profile analysis fitting to the diffraction pattern obtained on the carbon bearing samples of Fig. 3. The crystallite size is different from grain size, a grain may be made up of different crystallites. According to Scherrer (1918) crystallite size represents the crystal domain which produces diffraction. The values of the integral breadth, which were obtained by line profile analysis method, were inserted into the Scherrer equation (Eqs. (1) and (2), Scherrer 1918) to estimate the crystallite size, as follows:

(1) $\beta(2\theta) = \dfrac{K_\beta \times \lambda}{<D>_V \cos\theta_{hkl}}$

(2) $\dfrac{D_V}{K_\beta} = \dfrac{\lambda}{\cos\theta_{hkl} \times \beta(2\theta)}$

Scherrer equation provides a correlation between peaks broadening β, the dimension of diffracted domain and the crystallite size ($D_V$). K is a constant value ranging between 0.5 and 1, describing the contribution of crystallites shape
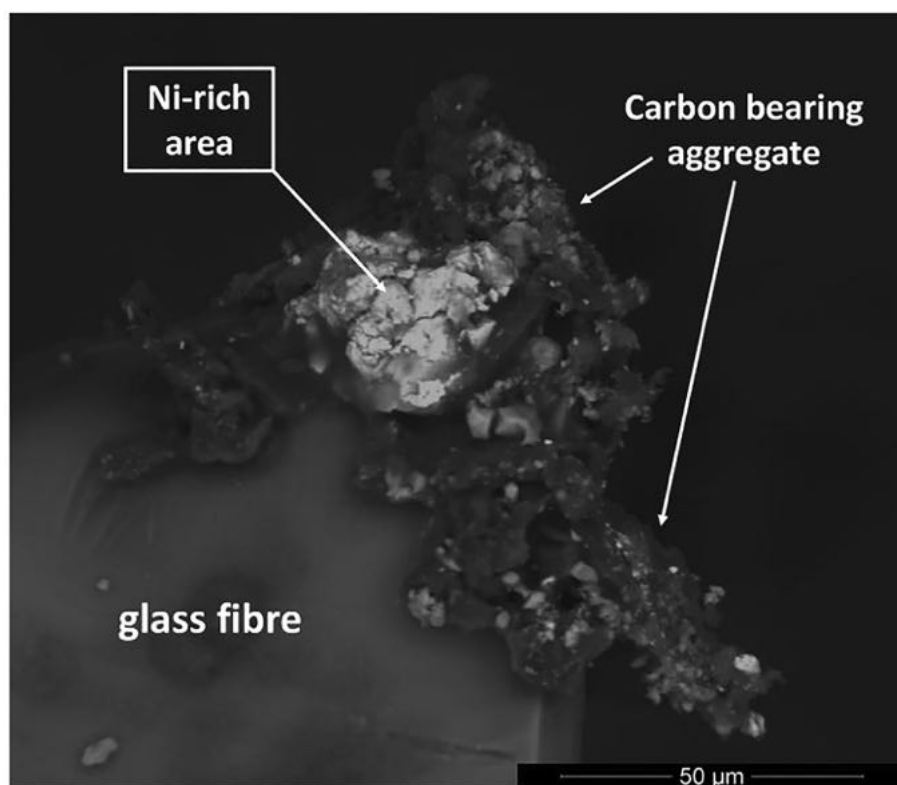
Fig. 3. Backscattered electron image of carbon bearing sample of Kenna ureilite on which we performed EDS, XRD and MRS analyses. In the middle of the sample, it is possible to observe light-grey/white coloured areas, referred to high content of nickel.

and dependent upon the relative orientation of the scattering vector with respect to the external shape of the crystallite (Scherrer 1918).

The same fragment of Fig. 3 studied by XRD was also analysed by MRS using a Horiba LabRam HR Evolution spectrometer equipped with an Olympus BX41 confocal microscope at the controlled temperature of 20(1) °C at the "Fiorenzo Mazzi" Experimental Mineralogy Lab at the Department of Earth and Environmental Science of the University of Pavia. We used a laser excitation of 532 nm with an operating low power of 1–2 mW (in order to avoid any graphite damage), a grating of 600 and a 50x objective magnification. The spectrometer was calibrated to the silicon Raman peak at 520.7 $cm^{-1}$. The spectral resolution was 2 $cm^{-1}$ and we used a 30 s integration time with four accumulations for each spectrum. Curve fitting of the spectra was carried out using the software OMNIC for dispersive Raman (from Thermo Fisher Scientific) adopting Gaussian + Lorentzian curves to obtain the best fit.

The carbon-bearing fragment on which we performed all the analyses was detached from the glass fibre, was carbon-coated and then analysed in high vacuum mode using a CamScan MX3000 electron microscope equipped with a $LaB_6$ four-quadrant solid-state backscattered-electron detector and an EDAX EDS system for micro-analysis (at the Department of Geosciences, University of Padova).

## 3. RESULTS

### 3.1. Petrographic description and SEM characterization

The petrographic analysis of the thin section of Fig. 1 shows that silicates in Kenna meteorite are mainly olivine and low-Ca pyroxene. The olivine crystals in the investigated fragment of Kenna ranges from 0.2 to 2 mm in size. In general, anhedral grains display triple junctions. Anhedral pyroxenes, with size ranging from 0.1 to 1.4 mm, are homogeneously distributed throughout the studied thin section, in agreement with observations made on another thin section of Kenna as reported in Berkley et al. (1976). Possible shock-induced features in Kenna silicates include fracturing and local (weak) mosaicism. In particular, in some olivine grains, it is possible to observe undulatory extinction and kinking due to a slip parallel to [001] (Berkley et al. 1976). As already reported by these authors, twin and translation gliding parallel to (100) were observed in clinopyroxene. In some silicates, it is possible to observe darkening due to the dispersion of metallic Fe-Ni and sulphides within the grains, which is commonly associated to shock effects (Rubin, 2006). All these observations on silicates suggest that Kenna ureilite recorded a medium shock level which could be ascribed to a shock level S3-S4, according to the shock classification by Stöffler et al. (1991, 2018). This assignment to a medium shock level

agrees with the shock level as reported by Berkley et al. (1976), who provided a detailed study of the petrography of Kenna. All our observations agree with those reported by these authors in their petrographic description.

In Fig. 4, SEM images of the analysed fragment (Fig. 2) show that carbon phases mixed together with Fe-Ni phases occur in the interstitial space between silicate grains. The carbon phases are present as relatively thin vein-like aggregates of micrometer-sized, but also, more or less regularly, they are found as elongated laths with thickness around 0.3 mm and length up to 0.7 mm (Fig. 4). Pores and small grains of metal and sulphide localized in the interstitial spaces are relatively abundant. Secondary electron (SE) images collected in the central portion of the carbon aggregates of Fig. 4a at progressively higher magnification (Fig. 4b, c) clearly show that the carbon aggregate is made of an assemblage of individual grains, likely not larger than 10 μm in size.

The SEM-EDS analysis of the non-carbon-coated Kenna fragment of Fig. 2 confirmed the presence of olivine, pigeonite, interstitial carbon phases intermixed with Fe-Ni metals and minor magnetite. The presence of magnetite indicates the oxidation of Fe metal dispersed within the carbon material and is likely related to terrestrial weathering (Lee and Bland, 2004).

Furthermore, we have also analysed by SEM-EDS (low vacuum mode) the carbon-bearing aggregate of Fig. 3. In addition to the carbon phases, we unexpectedly detected the presence of high Ni content often associated with Si peaks (Fig. 5). With the aim to totally exclude the possibility that the detected Si content was from the glass fibre on which the grain was mounted, we detached the carbon-bearing aggregate and analysed it again, after carbon coating, by EDS (in high vacuum mode) (Fig. 6a). During the detachment procedure, the carbon-bearing aggregate was accidentally broken into three fragments (Fig. 6b). The EDS spectrum collected on fragment 1 (Fig. 6c) definitively confirmed our previous observation of the presence of Si, with an Ni/Si ratio close to 3, and a minor amount of Fe.

In order to further characterize the above-mentioned carbon phases and to understand the origin of the anomalous high Ni content detected during EDS analysis of the carbon-bearing fragments of Fig. 3, we investigated the same grain by micro-XRD.
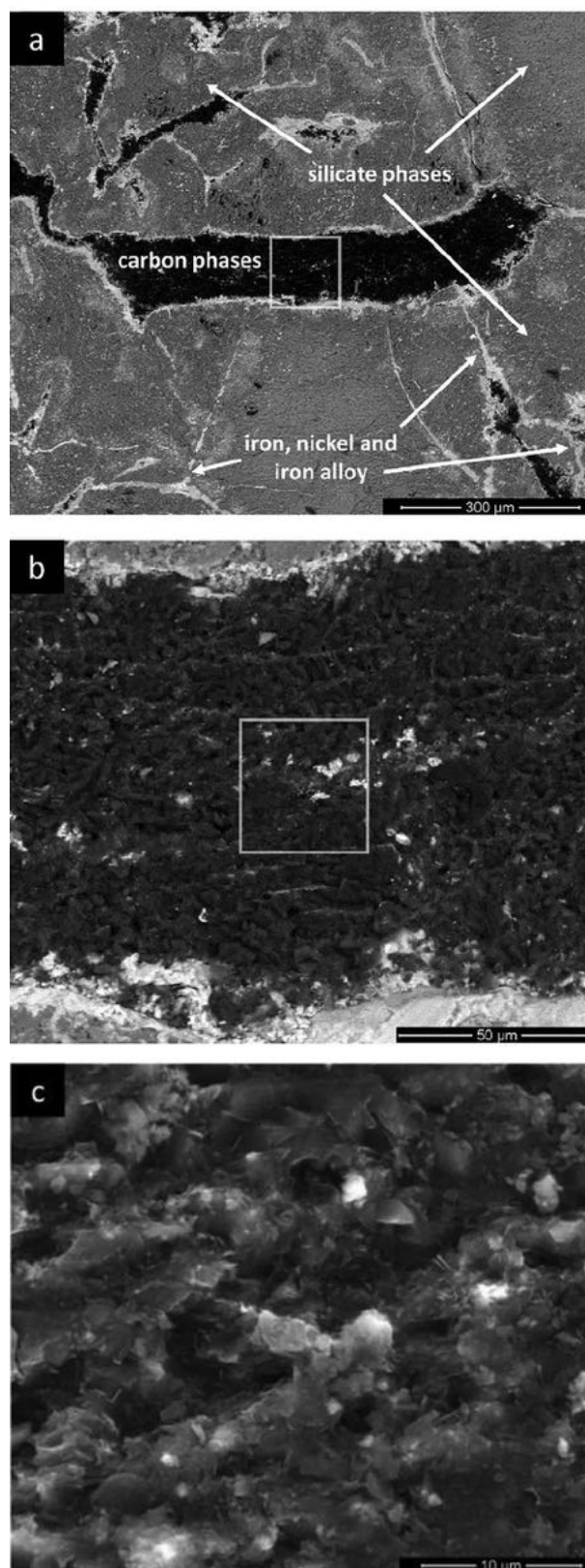


Fig. 4. The carbon material of Kenna ureilite fragments (represented by the dark grey portions). In (a) the carbon aggregate from which we gently removed the carbon bearing sample, that we used for XRD and MRS analyses, is shown (Fig. 3); in (b) a detail from (a) in BSE is shown; in (c) a detail from (b) in SE is reported, showing that the grain size is not larger than 10 μm.
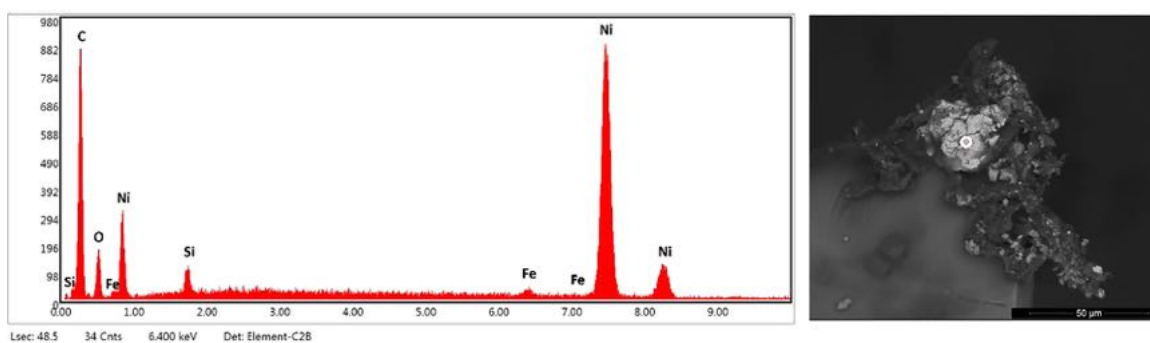
Fig. 5. EDS spectrum collected on the carbon bearing sample of Fig. 3 extracted from Kenna ureilite and attached at the top of the glass fibre. The EDS spectrum corresponds to the spot on the right side of the image (BSE image). This spectrum shows a high content of Ni and the presence of C, Si, Fe, O. The ratio between Ni and Si intensities is close to 3:1.
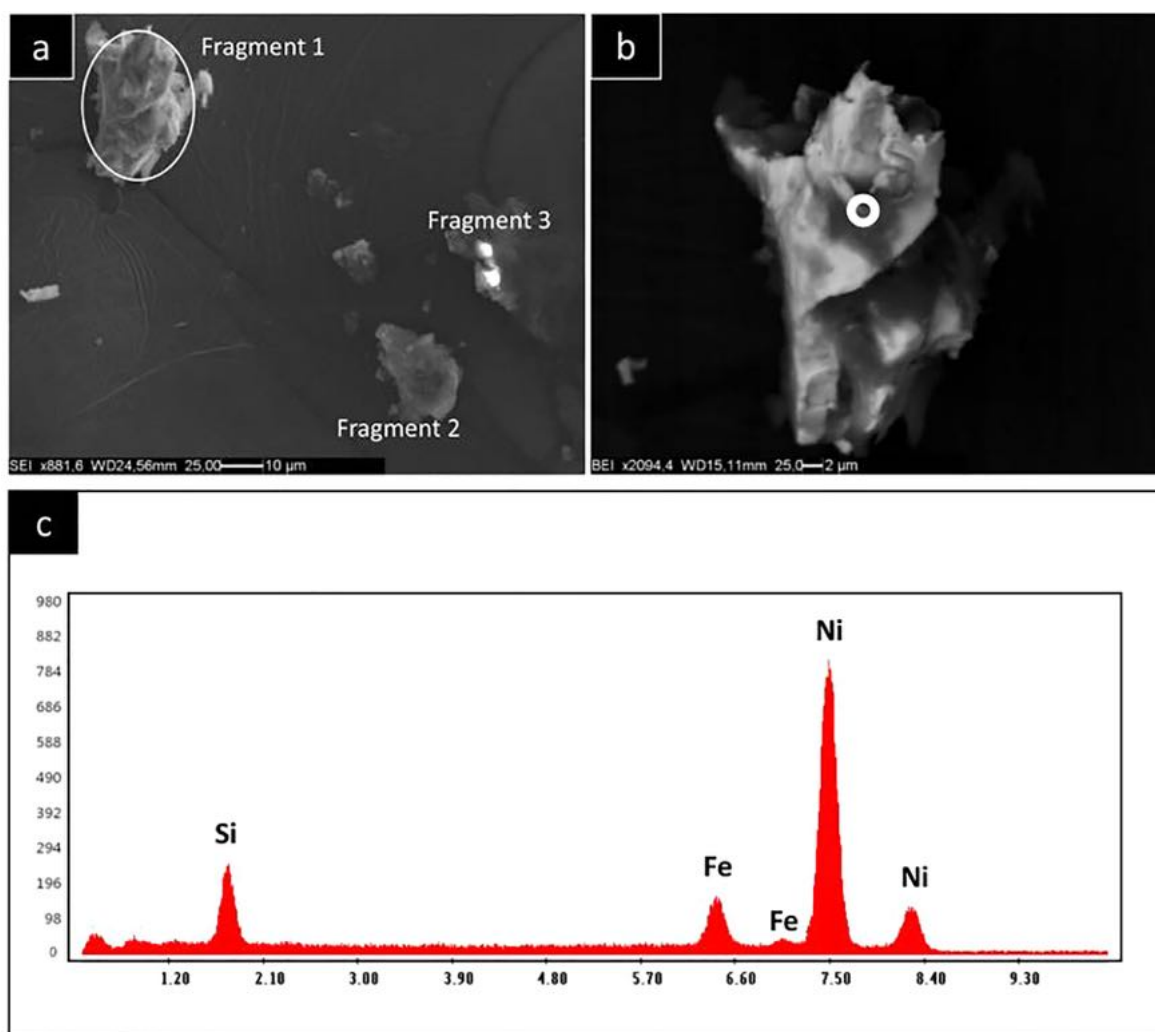


Fig. 6. In (a) three carbon bearing fragments removed from the original carbon bearing aggregate of Fig. 3 are shown; in (b), it is possible to observe the spot on Fragment 1 on which we performed the EDS analysis; in (c) the spectrum collected on the spot reported in (b) is shown.

### 3.2. Micro-X-ray diffraction

Micro X-ray diffraction of the Kenna fragment mounted on glass fibre (see Fig. 3) confirmed the presence of monocrystalline diamonds, as indicated by the presence of an intense peak at 2.06 Å and the two further less intense peaks at 1.26 and 1.07 Å (see spots in Fig. 7). Combining such information with the SEM images from Fig. 4b, c,
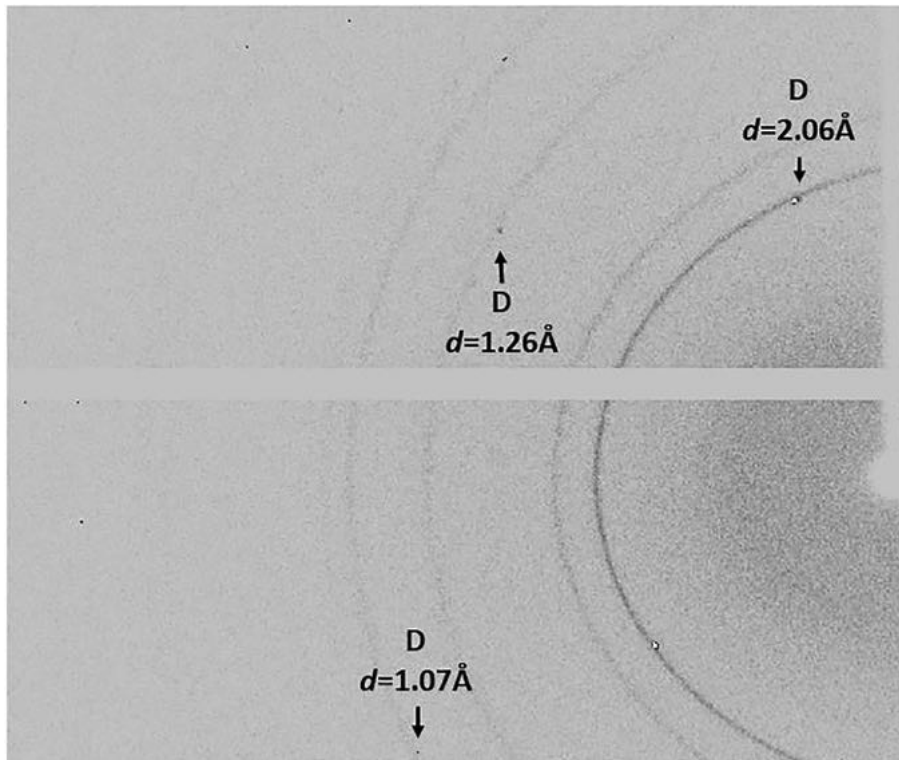
Fig. 7. Diffraction image for the carbon-bearing fragment of Kenna ureilite of Fig. 3, showing diffraction spots (marked with arrows) typical of a monocrystalline diamond and a few diffraction rings typical of polycrystalline materials (see the text).
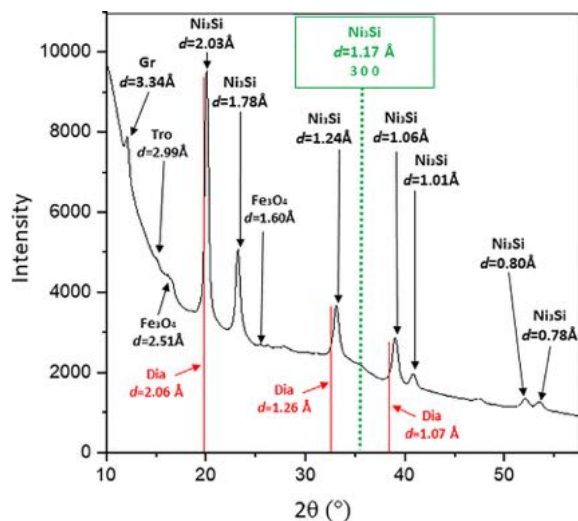


Fig. 8. X-ray powder diffraction patterns reconstructed from the XRD data of Fig. 7 (using the Crysalis software). The diffractogram shows the presence of carletonmooreite (Ni₃Si), and the occurrence of graphite (Gr), magnetite (Fe₃O₄) and troilite (Tro). The other minor peaks are referred to minor Ni sulphides. The dotted green line highlights the presence of a minor peak at $d$-spacing 1.17 Å, which is referred to Ni₃Si phase. The red lines point out the difference of the $d$-spacings position in the diffraction pattern with respect to those of diamond (Dia).

we can further assess that the monocrystalline diamonds in the investigated fragment are not larger than 10 μm in size. In addition to the diamond spots, Fig. 7 also shows diffraction rings, which at first seem to overlap with the $d$-spacings of diamonds, but their position indicates $d$-spacing values systematically shorter. In order to assign such shorter $d$-spacings, we analysed the reconstructed powder diffraction pattern (Fig. 8) collected over 0–360° phi rotation of the grain in Fig. 3. The pattern shows the main peak of graphite ($d = 3.34$ Å) which indeed looks strongly asymmetric. Based on the diffraction pattern peak profile broadening from Fig. 8, we can ascertain that graphite in our sample is definitively nanometric in size. In addition to graphite, the powder pattern indicates the presence of minor magnetite (its main peak is at $d = 2.56$ Å), whose occurrence is also supported by SEM observations and EDS results (see Fe and O in Fig. 5). As reported before, the $d$-spacings observed in the powder diffraction profile do not match those of diamond. Indeed, as it is possible to observe on Fig. 8, the $d$-spacings (in Å) are at 2.03, 1.76, 1.24, 1.06, 1.01, 0.81 and 0.78. The mineralogical phases ascribed to these $d$-spacings could be either metallic Ni (ICDS 98-006-2897, *Fm-3m*) or carletonmooreite Ni₃Si (*Pm-3m*, Ma et al., 2018). However, it was also possible to identify in the diffraction powder data a low intensity peak at $d$-spacing 1.17 Å, which is indexed as (3 0 0) and ascribed to Ni₃Si. Indeed, as metal Ni belongs to the *Fm-3m* space group, we can exclude that the $d$-spacing at 1.17 Å, "forbid-

Table 1

Integrated intensities of the D- and G-bands, I(D)/I(G) ratio of the integrated D- and G-bands and the crystallite size of graphite ($L_a$) of all MRS acquisition of Kenna sample. For the intensity ratios, I(D)/I(G), the standard deviation is 0.08. For $L_a$, the estimated uncertainty is in the order of 20 nm.

| D-band | G-band | I(D)/I(G) | $L_a$(nm) |
|--------|--------|-----------|-----------|
| **Kenna** | | | |
| 263.589 | 255.746 | 1.03 | 43 |
| 141.757 | 318.349 | 0.44 | 99 |
| 1,093.290 | 630.303 | 1.73 | 25 |
| 52.855 | 117.656 | 0.45 | 98 |
| 62.323 | 162.959 | 0.38 | 115 |
| 200.743 | 805.442 | 0.25 | 177 |

den" in this space group, together with those reported above could refer to metallic Ni. In addition, according to Nash and Nash (1987) if we consider the EDS analysis, the homogeneity range obtained for Si is of 20.3 at% which, if we exclude the presence of Fe, is of 22.0 at%. This value of Si at% homogeneity range is not ascribable to either Ni (0.0–15.8Si at%) phase or to $Ni_3Si$ $\beta_1$ (22.8–24.5Si at%) phase, but it is closer to the second one.

The combination of semiquantitative EDS analyses and the diffraction data support the identification of carletonmooreite ($Ni_3Si$), with minor Fe, in the investigated sample. Raghavan (2010) reported that the solubility of Fe in $Ni_3Si$ $\beta_1$ is up to 7.6 at%, which is the same value as obtained for Fe in our EDS analysis (Fig. 6). We refined the lattice parameter for carletonmooreite and, as reported in Table 1, the obtained value is $a = 3.527$ Å with a volume of 43.87 Å$^3$. The peak line profile analysis of the carletonmooreite diffraction pattern shows that such phase is definitively nanometric in size, with a crystallite size of around 4–7 nm.

### 3.3. Micro-Raman spectroscopy

Results of micro-Raman investigations are reported in Tables 1 and 2. In Fig. 9, a typical Raman spectrum obtained for graphite is shown. Table 1 shows the I(D)/I(G) ratio (where I = integrated intensity; D = D-band; G = G-band), which represents the ratio of the integrated D- and G-band intensities. Tuinstra and
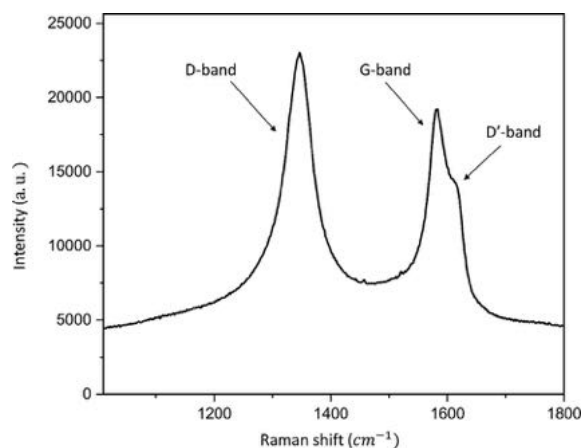


Fig. 9. A typical Raman spectrum of graphite of Kenna ureilite. The G-band (close to 1580 cm$^{-1}$), D-band (close to 1350 cm$^{-1}$) and the D'-band (close to 1620 cm$^{-1}$) are indicated in the figure. The intensity and the positions of the peaks are expressed in arbitrary units (a.u.) and Raman shift (cm$^{-1}$), respectively.

Koenig (1970) observed an important relationship between the ratio of the intensity of D-band and G-band [I(D)/I(G)] and crystallite size of graphite ($L_a$). This relationship was then validated by Ferrari and Roberson (2000) as follows:

$$\frac{I(D)}{I(G)} = \frac{C(\lambda_L)}{L_a} \tag{1}$$

The wavelength-dependent prefactor parameter $C(\lambda_L)$ is equal to $C_0 + \lambda_L C_1$, where $C_0 = -12.6$ nm and $C_1 = 0.033$, is valid for 400 nm $< \lambda_L <$ 700 nm. The wavelength dependency of C parameter is expressed by Eq. (1) (Barbaro et al. 2020 and references therein). The C ($\lambda_L = 532$ nm) parameter corresponds to ~44 Å. The crystallite size results obtained for our sample by applying Eq. (1) are reported in Table 1. The average crystallite size is 84 nm, with a range between 43 and 177 nm. Such data are consistent with the XRD data collected on graphite, which also exhibits a nanometric size.

We applied the geothermometer by Ross et al. (2011) based on the Raman G-band full width at half maximum of graphite [$\Gamma_G$] as follows:

$$T_{max}(^{\circ}C) = 1594.4 - 20.4\Gamma_G - 5.8 \times 10^{-2}\Gamma_G^2 \tag{2}$$

Table 2

Centre positions for G, D and D' bands and FWHM (both in cm$^{-1}$) of Kenna ureilite. Calculated crystallization temperature, $T_{max}$, is reported in the last column and was obtained using Eq. (2). The uncertainty on $T_{max}$ is ±120 °C.

| G-band centre | G-band FWHM | G-band FWHM corrected | D-band centre | D-band FWHM | D'-band centre | D'-band FWHM | $T_{max}$ (°C) |
|------|------|------|------|------|------|------|------|
| **Kenna** | | | | | | | |
| 1579 | 36 | 23 | 1346 | 49 | 1614 | 27 | 1102 |
| 1573 | 28 | 18 | 1346 | 45 | 1609 | 23 | 1215 |
| 1582 | 37 | 23 | 1346 | 53 | 1615 | 27 | 1090 |
| 1572 | 27 | 17 | 1345 | 50 | 1607 | 20 | 1228 |
| 1573 | 25 | 16 | 1342 | 52 | 1608 | 20 | 1256 |
| 1571 | 31 | 19 | 1350 | 40 | 1609 | 20 | 1175 |

In Table 2 we report the graphite Raman peaks positions (G-band, D-band and D′-band), the relevant $\Gamma_G$ values for all studied samples and the $T_{max}$ estimated using Eq. (2). In order to compare obtained $\Gamma_G$ data with those published by Ross et al. (2011) and Barbaro et al. (2020, 2021), we corrected our data for the instrumental peak broadening using a high-quality gemstone natural diamond (which resulted in $\Gamma_G = 5$ cm$^{-1}$), following the same procedure as in Ross et al. (2011) (Table 2). In the same Table 2, the values of $\Gamma_G$ used in Eq. (2) to obtain the $T_{max}$ are reported for each acquirement. The obtained temperature values range between 1102 and 1300 °C, with an uncertainty of ±120 °C (this is a 2σ uncertainty as indicated by Cody et al., 2008).

# 4. DISCUSSION

## 4.1. Comparison with other ureilites: The origin of carbon phases

Unlike in the case of recent XRD studies on diamond in ureilites (Nestola et al., 2020; Barbaro et al., 2021), Kenna only contains μm-size diamonds. Indeed, in the fragments studied by these authors, namely, Almahata Sitta 209b and 72, NWA 7983 and Y-74123, the presence of only nm-diamond (for Almahata Sitta samples) or the coexistence of both μm and nano-diamonds (in NWA 7983 and Y-74123) was observed. It is noteworthy that, even if Kenna was classified as a medium shock level ureilite (this work and Berkley et al., 1976), similarly to Yamato 74123, it contains only μm-size diamonds, whereas Y-74123 contains both μm- and nano-diamonds. In the conditions of a natural shock event (with a shock pulse duration up to 4–5 s, as reported by De Carli et al. 2002) the formation of micrometer-sized diamond could either result from higher shock pressure in the graphite due to shock impedance contrast between contiguous olivine and graphite (e.g. Ogilvie et al., 2011; Gillet and El Goresy, 2013) and/ or to the catalytic effect of Fe-Ni-bearing phases, which are particularly abundant in Kenna (compared to the above mentioned ureilites) and could favour the growth of larger diamonds.

In the XRD pattern obtained for Kenna meteorite, graphite highest peak shows the same asymmetry as that observed in the carbon-bearing samples studied in Nestola et al. (2020) and Barbaro et al. (2021) in Almahata Sitta, NWA 7983 and Y-74123 samples, respectively. This graphite was defined as "compressed graphite", which usually occurs at the initial stage of the direct transformation from graphite to diamond during shock compression. The presence of this type of graphite and the shock-formation hypothesis of diamond for Kenna was proposed for the first time by Nakamuta and Aoki (2000), who interpreted it as a typical indicator of shock event.

The temperature range we estimated on graphite from Kenna, averaging at about 1180 °C, is higher than the values reported by Ross et al. (2011) for graphite in Almahata Sitta #7 ureilitic fragment ($T_{max}$ of 990 ± 120 °C), but slightly lower than values by Barbaro et al. (2020, 2021) for Almahata Sitta (209b, 72 and A135A) and Y-74123 ureilites,

which provided an average $T_{max}$ of 1275 ± 120 °C and 1314 ± 120 °C, respectively. Considering that our method is affected by about ±120 °C uncertainty, it is evident that the $T$-values measured on the above mentioned five samples is very close, providing an average value at about 1200 °C. Such similar temperature could suggest that all these ureilites of medium shock level recorded a common event, such as the UPB breakup. It is unlikely that this $T$-value can refer to pre-shock temperature as it was measured on nano-sized compressed graphite, which must result from an impact event and cannot be pristine graphite from the UPB.

## 4.2. The occurrence of carletonmooreite

The results from XRD measurements carried out on the carbon-bearing aggregates show the presence of micrometer-sized diamond (up to 10 μm), nanographite (average crystal size around 80 nm as determined by micro-Raman spectroscopy), nanocrystals of carletonmooreite, and minor magnetite. In Table 3, some $a$ lattice parameter values for synthetic Ni$_3$Si, natural Ni$_3$Si and metallic Ni are reported to make a comparison with our estimated value for carletonmooreite (see references in Table 3). The $a$ and $V$ parameters we obtained appear to be slightly larger than those reported by Garvie et al. (2021). These authors reported on the chemical composition of (Ni$_3$Si) in Norton County aubrite, as obtained with electron-microprobe, which is Ni 82.8 ± 0.4, Fe 4.92 ± 0.09 and Si 13.08 ± 0.08 wt.%. Garvie et al. (2021) also reported on carletonmooreite grains with an average composition of Ni 81.44 ± 0.82, Fe 5.92 ± 0.93, Cu 0.13 ± 0.02 and Si 13.01 ± 0.1 wt.%. Considering that in our EDS spectrum of Fig. 6c the presence of Fe together with Ni is evident, we can assume that carletonmooreite in the Kenna meteorite contains higher amounts of Fe replacing Ni, compared to carletonmooreite characterized by Garvie et al. (2021). This could justify the slight difference between our cell volume and that reported for carletonmooreite by Ma et al. (2018) and Garvie et al. (2021).

The analyses by SEM revealed an intimate textural association between the carbon aggregates and the Fe-Ni compounds (Fe-Ni metal, carletonmooreite and magnetite) as reported for other ureilitic fragments in the recent studies by Nestola et al. (2020) and Barbaro et al. (2021). These authors did not report on the presence of carletonmooreite or of other silicides (Ross et al., 2019), but reiterated the fundamental role played by Fe-Ni phases in the shock transformation from graphite to diamond of different sizes in ureilites. In particular, the debated formation process of μm-sized diamond crystals present in ureilites was ascribed by Nestola et al. (2020), for diamonds found in NWA 7983, to shock event with the catalytic involvement of Fe-Ni phases and long duration peak pressure stage (up to 4–5 s). Even if the effective duration of a typical laboratory shock experiment for diamond formation is too short to allow the growth of diamonds beyond a few μm sizes (De Carli, 1995), a catastrophic impact event is expected to ensure a sufficient duration of high-pressure conditions (De Carli et al., 2002; Fritz et al., 2017). However, it has been established (Dremin and Breusov, 1993) that the for-

Table 3
Comparison of the value of the *a* cell parameter for $\beta_1$-$Ni_3Si$ and metal Ni.

| $\beta1$-$Ni_3Si$ *a*-cell (Å) | References | Ni metal *a*-cell (Å) | References |
|---|---|---|---|
| 3.482–3.500 | Zhou and Bakker (1994) (milled) Ackerbauer et al. (2009) (Fe = 4 at%) | | |
| 3.496 | Osawa and Okamoto (1938) | 3.516 | Osawa and Okamoto (1938) |
| 3.497 | Ohira et al. (2005) | | |
| 3.506 | Oya and Suzuki (1983) | | |
| 3.506 | Pigozzi et al. (2006) | | |
| 3.507–3.510 | Suzuki et al. (1984) | 3.523 | Suzuki et al. (1984) |
| 3.51 | Zhang et al. (2009) | 3.45 | Zhang et al. (2009) |
| 3.51 | Garvie et al. (2021) (aubrite) (cell volume = 43.24 Å$^3$) | | |
| 3.512 | Connétable and Thomas (2011) (ab initio) | | |
| 3.516 | Cao et al. (2013) (ab initio) | | |
| 3.52 | This work (ureilite, nano) (cell volume = 43.87 Å$^3$) | 3.5186 | ICDS 98-006-2897 |
| | | 3.5231 | Jović et al. (2006) (nano) |
| | | 3.528–3.541 | Wei et al. (2007) (nano) |

Notes: nano – nanocrystalline; milled – ball milled (deformed structures); ab initio – calculated from ab initio; other – experimental synthesis.

mation of diamonds catalysed by metal-bearing (Fe,Ni, Co)-C melts proceeds at lower pressures and higher reaction rates compared to those in absence of these phases, as reported in many studies on industrial synthesis of diamonds (e.g. Bundy et al., 1996; Fedorov et al., 2002). In particular, a description of how the catalysed formation of diamonds by metallic melts during a shock event can also account for simultaneous formation of micro- and nanodiamonds in ureilites is well explained in Nestola et al. (2020). In this work the pulsed heating experiments performed by Varfolomeeva (1971) on a graphite-metal charge in a static high-pressure apparatus, which roughly simulates natural impact processes (De Carli et al. 2002; Bundy and Kasper, 1967), are discussed. In these experiments diamonds up to 10 µm-sized were produced near to the catalyst, while nanodiamonds occurred in other parts of the experimental charge (Fig. S14 of Nestola et al. 2020). The use of Ni as a catalyst for the formation of diamonds is widely discussed in the literature (e.g. Strong, 1963; Tsuzuki et al., 1985) and the anomalous content of Ni in this meteorite, due to the presence of an Ni-rich mineral as carletonmooreite ($Ni_3Si$) in our interpretation can favour the growth process of diamond from graphite during a shock event, thus also enabling the formation of micrometer-sized diamonds. Indeed, in Kenna carbon aggregates, we observed by XRD analysis micrometer-sized diamond alone, in contrast with what is observed in others ureilites (e.g. Yamato 74123 by Barbaro et al. 2021 and NWA 7983 by Nestola et al. 2020), where both micro- and nano-diamonds are present and a lower Ni-content was measured.

At any rate, according to static experiments, very reduced conditions at which this silicide $Ni_3Si$ can form (silicide would be few log units below Fe-FeO buffer) would not be compatible with diamond crystallization, which is commonly associated to relatively oxidizing (Fe-FeO) conditions (see Litasov et al., 2013, their Table 2.1). However, in the case of Kenna ureilite, the formation of diamond is ascribed to shock and is not coeval with the formation of $Ni_3Si$ silicide.

Garvie et al. (2021) reported that in Norton County aubrite, carletonmooreite occurred as euhedral to subhedral crystals of 1–14 µm in size. Furthermore, these authors did not emphasize any shock feature in this meteorite. On the contrary, in Kenna, carletonmooreite occurs as nanometric sized grains, associated with nanographite and diamond, thus indicating that its nanometric size could be related to shock event(s), similarity to nanographite as it is unlikely that nanometric $Ni_3Si$ is of pristine origin.

The iron analogue of carletonmooreite, suessite ($Fe_3Si$), has been already found in ureilites (Ross et al., 2019 and references therein), suggesting that silicides are not so rare in ureilites. Suessite ($I\,m\text{-}3m$) was discovered for the first time in the North Haig ureilite (Keil et al., 1982). As reported by Ikeda (2007), suessite was produced at temperatures around 1200 and 1100 °C and oxygen fugacity of $10^{-18}$ $-10^{-20}$ bars from FeO-bearing olivine and Ni-bearing kamacite. Suessite can contain very low amounts of Ni (<5.6 wt.%) compared to carletonmooreite.

Based on one of the hypotheses proposed by Ross et al. (2019) for the formation of natural suessite, carletonmooreite could also have formed in ureilite in a very reduced

environments, with $fO_2$ significantly below iron-wüstite buffer. Such conditions are quite common in extraterrestrial material and consistent with the general redox state of ureilites. On the other hand, it is hard to expect such reduced conditions in terrestrial environments. However, some unusual findings of Fe- and Mn-silicides were reported. There are several locations where Fe-silicides were identified along with other super-reduced phases, including: (a) in chromitite and peridotite from Luobusa (Tibet) (e.g. Nicheng et al., 2012); (b) in the Yakutian kimberlites (Shiryaev et al., 2011); (c) in the alluvial rocks near Mt. Carmel (Israel) (Griffin et al., 2016); (d) in mantle xenoliths from Kamchatka volcanics (Ishimaru et al., 2009); and (e) in fulgurites (Stefano et al., 2020). Mn-silicides are additionally reported in lamproite from Uzbekistan (Yusupov et al., 2009) and as inclusions in polycrystalline diamond aggregates from Kamchatka placers (Kaminsky et al., 2020). The origin of terrestrial Fe-silicides is, in some cases, questionable, because in the reported locations, a contamination by industrial abrasive or slag materials cannot be excluded (e.g. Litasov et al., 2019, 2020).

In summary, the small size of the carletonmooreite reported here in Kenna, its occurrence in close relationship with carbon phases, and the natural reducing conditions typical for ureilites, other than the rare occurrence of similar reduced phases in terrestrial environments, allow us to exclude that the observed carletonmooreite derives from terrestrial contamination.

## 5. CONCLUSIONS

Microdiamonds (up to about 10 μm in size), nanographite and magnetite were found within the carbon-bearing areas in the Kenna meteorite. The temperature ($T_{max}$) recorded by nanographite using the geothermometer by Cody et al. (2008) is close to 1180 °C. This temperature is ascribable to a shock event which reduced graphite to nanometric in size. In addition to these phases, we identified nanocrystalline carletonmooreite (Ni$_3$Si). This rare phase, reported for the first time in a ureilite, could be formed, in agreement with Ikeda (2007) and Ross et al. (2019), under extreme reducing condition by reaction of Fe-Ni melt, with silicate as a source of silicon (Ikeda, 2007), and graphite as a reducing agent. The shock features observed in olivine and in pyroxene (S3-S4), together with the presence of microdiamonds and nanographite indicate that the Kenna meteorite underwent a shock event with a peak pressure of at least 15 GPa, which could have reduced to nanometric size both pristine graphite and carletonmooreite.

Our results further demonstrate how the role of Fe-Ni metals (and eventually their compounds) is crucial in favouring diamond to grow directly from graphite during a shock event. It is well established that a direct graphite-to-diamond transformation, in absence of any catalytic process, would require very high pressure and temperature conditions. In addition, it is expected that for shock event of limited magnitude (15–20 GPa, as supported by textural features observed in the silicates) such direct transforma-

tion could only produce diamonds of nanometric size (Nestola et al. 2020 and references therein).

Here we show that, combining a long shock pulse with the presence of Fe-Ni phases, in particular Ni as demonstrated by carletonmooreite, diamond growing from graphite can reach micrometer-size even for relatively low shock pressures (ca. 15–20 GPa).

## Declaration of Competing Interest

The authors declare that they have no known competing financial interests or personal relationships that could have appeared to influence the work reported in this paper.

## APPENDIX A. SUPPLEMENTARY MATERIAL

Supplementary data to this article can be found online at https://doi.org/10.1016/j.gca.2021.06.022.

### REFERENCES

Ackerbauer S., Krendelsberger N., Weitzer F., Hiebl K. and Schuster J. C. (2009) The constitution of the ternary system Fe–Ni–Si. *Intermetallics* **17**(6), 414–420.

Barbaro A., Domeneghetti M. C., Goodrich A. C., Meneghetti M., Litti L., Fioretti A. M., Jenniskens P., Shaddad M. H., Alvaro M. and Nestola F. (2020) Graphite based geothermometry on Almahata Sitta ureilites meteorites. *Minerals* **10**(11), 1005.

Barbaro A., Nestola F., Pittarello L., Ferrière L., Murri M., Litasov D. K., Christ O., Alvaro M. and Domeneghetti M. C. (2021) Characterization of carbon phases in Yamato 74123 ureilite to constrain the meteorite shock history. *Am. Mineral.*. doi.10.2138/am 2021 7856 (in Press).

Berkley J. L., Brown, IV, H. G., Keil K., Carter N. L., Mercier J.-C. C. and Huss G. (1976) The Kenna ureilite: an ultramafic rock with evidence for igneous, metamorphic, and shock origin. *Geochim. Cosmochim. Acta* **40**, 1429–1437.

Brecher A. and Fuhrman M. (1979) The magnetic effects of brecciation and shock in meteorites: II. The ureilites and evidence for strong nebular magnetic fields. *Moon Planets* **20**(3), 251–263.

Bundy F. P., Bassett W. A., Weathers M. S., Hemley R. J., Mao H. U. and Goncharov A. F. (1996) The pressure-temperature phase and transformation diagram for carbon; updated through 1994.. *Carbon* **34**(2), 141–153.

Bundy F. P. and Kasper J. S. (1967) Hexagonal diamond–A new form of carbon. *J. Chem. Phys.* **46**, 3437–3446.

Cao Y., Zhu J., Liu Y., Nong Z. and Lai Z. (2013) First-principles studies of the structural, elastic, electronic and thermal properties of Ni$_3$Si. *Comput. Mater. Sci.* **69**, 40–45.

Clayton R. N., Mayeda T. K., Onuma N. and Shearer J. (1976) Oxygen isotopic composition of minerals in the Kenna ureilite. *Geochim. Cosmochim. Acta* **40**(12), 1475–1476.

Cloutis E. A., Hudon P., Romanek C. S., Bishop J. L., Reddy V., Gaffey M. J. and Hardersen P. S. (2010) Spectral reflectance properties of ureilites. *Meteorit. Planet. Sci.* **45**, 10–11.

Cody G. D., Alexander C. M. O'. D., Yabuta H., Kilcoyne A. L. D., Araki T., Ade H., Dera P., Fogel M., Militzer B. and Mysen B. O. (2008) Organic thermometry for chondritic parent bodies. *Earth Planet. Sci. Lett.* **272**, 446–455.

Connétable D. and Thomas O. (2011) First-principles study of nickel-silicides ordered phases. *J. Alloys Compd.* **509**(6), 2639–2644.

De Carli P. S. (1995) Shock wave synthesis of diamond and other phases. *Mat. Res. Soc. Symp. Proc.* **383**, 21–31.

De Carli P. S., Bowden E., Jones A. P. and Price G. D. (2002) Laboratory impact experiments versus natural impact events. In Catastrophic Events and Mass Extinctions: Impacts and Beyond, Geological Society of America Special Paper 356, 595–605.

Dremin A. N. and Breusov O. N. (1993) Dynamic synthesis of superhard materials. In *Shock Waves in Materials Science* (ed. A. B. Sawaoka). Springer, Tokyo, pp. 17–34.

Fukunaga K., Matsuda J., Nagao K., Miyamoto M. and Ito K. (1987) Noble-gas enrichment in vapour-growth diamonds and the origin of diamond in ureilites. *Nature* **328**, 141–143.

Fedorov I. I., Chepurov A. A. and Dereppe J. M. (2002) Redox conditions of metal-carbon melts and natural diamond genesis. *Geochem. J.* **36**, 247–253.

Ferrari A. C. and Roberson J. (2000) Interpretation of Raman spectra of disordered and amorphous carbon. *Phys. Rev. B* **61**, 14095–14107.

Fritz J., Greshake A. and Fernandes V. A. (2017) Revising the shock classification of meteorites. *Meteorit. Planet. Sci.* **52**(6), 1216–1232.

Garvie L. A. J., Ma C., Ray S., Domanik K., Wittman A. and Wadhwa M. (2021) Carletonmooreite, $Ni_3Si$, a new silicide from the Norton County, aubrite meteorite. *Am. Mineral.*. doi.10.2138/am-2021-7645 (in press).

Goodrich C. A. (1992) Ureilites: A critical review. *Meteorit. Planet. Sci.* **27**, 327–352.

Goodrich C. A., Hartmann W. K., O'Brien D. P., Weidenschilling S. J., Wilson L., Michel P. and Jutzi M. (2015) Origin and history of ureilitic material in the solar system: The view from asteroid 2008 $TC_3$ and the Almahata Sitta meteorite. *Meteorit. Planet. Sci.* **50**, 782–809.

Gillet P. and El Goresy A. (2013) Shock Events in the Solar System: The message from minerals in Terrestrial Planets and Asteroids. *Annu. Rev. Earth Planet. Sci.* **41**, 247–285.

Griffin W. L., Gain S. E. M., Adams D. T., Huang J.-X., Saunders M., Toledo V., Pearson N. J. and O'Reilly S. Y. (2016) First terrestrial occurrence of tistarite ($Ti_2O_3$): ultra-low oxygen fugacity in the upper mantle beneath Mount Carmel, Israel. *Geology* **44**, 815–818.

Ikeda Y. (2007) Petrology of an unusual ureilite NWA 1241. *Polar. Sci.* **1**, 45–53.

Ishimaru S., Arai S. and Shukuno H. (2009) Metal-saturated peridotite in the mantle wedge inferred from metal-bearing peridotite xenoliths from Avacha volcano, Kamchatka. *Earth Planet. Sci. Lett.* **284**, 352–360.

Jović V. D., Maksimović V., Pavlović M. G. and Popov K. I. (2006) Morphology, internal structure and growth mechanism of electrodeposited Ni and Co powders. *J. Solid State Electrochem.* **10**(6), 373–379.

Lee M. R. and Bland P. A. (2004) Mechanisms of weathering of meteorites recovered from hot and cold deserts and the formation of phyllosilicates. *Geochim. Cosmochim. Acta* **68**(4), 893–916.

Litasov K. D., Bekker T. B. and Kagi H. (2020) "Kamchatite" diamond aggregate from northern Kamchatka, Russia: New find of diamond formed by gas phase condensation or chemical vapor deposition – Discussion. *Am. Mineral.* **105**, 144–145.

Litasov K. D., Kagi H. and Bekker T. B. (2019) Enigmatic super-reduced phases in corundum from natural rocks: Possible contamination from artificial abrasive materials or metallurgical slags. *Lithos* **340–341**, 181–190.

Litasov K. D., Shatskiy A. and Ohtani E. (2013) Earth's mantle melting in the presence of COH-bearing fluid. *Physics and chemistry of the deep Earth*. Shun-ichiro Karato, pp. 38–65.

Lipschutz M. E. (1964) Origin of Diamonds in the Ureilites. *Science* **143**, 1431–1434.

Kaminsky F. V., Wirth R., Anikin L. P. and Schreiber A. (2020) On "Kamchatite" diamond aggregate from northern Kamchatka, Russia: New find of CVD-formed diamond in nature— Reply to KD Litasov, TB Bekker and H. Kagi. *Am. Mineral.* **105**(1), 144–145.

Keil K., Berkley J. L. and Fuchs L. H. (1982) Suessite, $Fe_3Si$: a new mineral in the North Haig ureilite. *Am. Mineral.* **67**(1–2), 126–131.

Ma C., Garvie L. A. J. and Wittmann A. (2018) Carletonmooreite, IMA 2018-068. CNMNC Newsletter No. 45, October (2018), page 1042. *Europ. J. Mineral.* **30**, 1037–1043.

Miyahara M., Ohtani E., El A., Lin Y., Feng L., Zhang J., Gillet P., Nagase T. and Muto J. (2015) Unique large diamonds in a ureilite from Almahata Sitta 2008 $TC_3$ asteroid. *Geochim. Cosmochim. Acta* **163**, 14–26.

Nabiei F., Badro J., Dennenwaldt T., Oveisi E., Cantoni M., Hébert C., El Goresy A., El Barrat J. and Gillet P. (2018) A large planetary body inferred from diamond inclusions in a ureilite meteorite. *Nat. Commun.* **9**, 1–6.

Nakamuta Y. and Aoki Y. (2000) Mineralogical evidence for the origin of diamond in ureilites. *Meteorit. Planet. Sci.* **35**, 487–493.

Nash P. and Nash A. (1987) The Ni–Si (Nickel-Silicon) system. *Bull. Alloy Phase Diagrams* **8**(1), 6–14.

Nestola F., Goodrich C. A., Morana M., Barbaro A., Jakubek R. S., Chris O., Brenker F. E., Domeneghetti M. C., Dalconi M. C., Alvaro M., Fioretti A. M., Litasov K. D., Fries M. D., Leoni M., Casati N. P. M., Jenniskens P. and Shadad M. H. (2020) Impact shock origin of diamond in ureilite meteorites. *PNAS* **117**(41), 25310–25318.

Nicheng S., Wenji B. A. I., Guowu L. I., Ming X. I. O. N. G., Jingsu Y. A. N. G., Zhesheng M. A. and He R. (2012) Naquite, FeSi, a new mineral species from Luobusha, Tibet, western China. *Acta Geolog. Sinica – English Ed.* **86**(3), 533–538.

Ogilvie P., Gibson R. L., Reimold W. U., Deutsch A. and Hornemann U. (2011) Experimental investigation of shock metamorphic effects in a metapelitic granulite: The importance of shock impedance contrast between components. *Meteorit. Planet. Sci.* **46**, 1565–1586.

Ohira K., Kaneno Y. and Takasugi T. (2005) Microstructure, mechanical property and oxidation property in $Ni_3Si$–$Ni_3Ti$–$Ni_3Nb$ multi-phase intermetallic alloys. *Mater. Sci. Eng.* **399**(1–2), 332–343.

Osawa A. and Okamoto M. (1938) An X-ray analysis of the alloys of the nickel-silicon system. *Nippon Kinzoku. Gakkai-Shi* **2**, 378–388 (in Japanese).

Oya Y. and Suzuki T. (1983) The nickel-rich portion of the Ni-Si phase diagram. *Z. Metallkd.* **74**(1), 21–24.

Pigozzi G., Mukherji D., Gilles R., Barbier B. and Kostorz G. (2006) $Ni_3Si$ (Al)/a-$SiO_x$ core-shell nanoparticles: characteriza-

tion, shell formation, and stability. *Nanotechnology* **17**, 4195–4203.

Raghavan V. (2010) Fe-Ni-Si (iron-nickel-silicon). *J. Phase Equilibria Diffus.* **31**(2), 184–185.

Ross A. J., Steele A., Fries M. D., Kater L., Downes H., Jones A. P., Smith C. L., Jenniskens P. M., Zolensky M. E. and Shaddad M. H. (2011) MicroRaman spectroscopy of diamond and graphite in Almahata Sitta and comparison with other ureilites. *Meteorit. Planet. Sci.* **46**, 364–378.

Ross A. J., Downes H., Herrin J. S., Mittlefehldt D. W., Humayun M. and Smith C. (2019) The origin of iron silicides in ureilite meteorites. *Geochemistry* **79**(4) 125539.

Rubin A. (2006) Shock, post-shock annealing, and post-annealing shock in ureilites. *Meteorit. Planet. Sci.* **41**, 125–133.

Scherrer P. (1918) Estimation of the size and internal structure of colloidal particles by means of röntgen. *J. Math. Phys.* **2**, 98–100.

Shiryaev A. A., Griffin W. L. and Stoyanov E. (2011) Moissanite (SiC) from kimberlites: polytypes, trace elements, inclusions and speculations on origin. *Lithos* **122**, 152–164.

Stefano C. J., Hackney S. A. and Kampf A. R. (2020) The occurrence of iron silicides in a fulgurite: implication for fulgurite genesis. *Can. Mineral.* **58**(1), 115–123.

Stöffler D., Keil K. and Scott E. R. D. (1991) Shock metamorphism of ordinary chondrites. *Geochim. Cosmochim. Acta* **55**(12), 3845–3867.

Stöffler D., Hamann C. and Metzler K. (2018) Shock metamorphism of planetary silicate rocks and sediments: Proposal for an updated classification system. *Meteorit. Planet. Sci.* **53**(1), 5–49.

Strong H. M. (1963) Catalytic effects in the transformation of graphite to diamond. *J. Chem. Phys.* **39**(8), 2057–2062.

Suzuki T., Oya Y. and Ochiai S. (1984) The mechanical behavior of nonstoichiometric compounds $Ni_3Si$, $Ni_3Ge$, and $Fe_3Ga$. *Metall. Trans. A* **15**(1), 173–181.

Tsuzuki A., Hirano S. I. and Naka S. (1985) Influencing factors for diamond formation from several starting carbons. *J. Mater. Sci.* **20**(6), 2260–2264.

Tuinstra F. and Koenig J. L. (1970) Raman spectrum of graphite. *J. Chem. Phys.* **53**, 1126–1130.

Urey H. C. (1956) Diamond, meteorites, and the origin of the solar system. *American Astronom. Soc.* **124**, 623–637.

Varfolomeeva T. D. (1971) Synthesis and investigation of polycrystalline diamond, PhD thesis. Institute for High Pressure Physics, USSR Academy of Sciences. p. 154.

Wei Z., Xia T., Ma J., Feng W., Dai J., Wang Q. and Yan P. (2007) Investigation of the lattice expansion for Ni nanoparticles. *Mater. Charact.* **58**(10), 1019–1024.

Wilkening L. L. and Marti K. (1976) Rare gases and fossil particle tracks in the Kenna ureilite. *Geochim. Cosmochim. Acta* **40**(12), 1465–1473.

Yusupov R. G., Stanley C. J., Welch M. D., Spratt J., Cressey G., Rumsey M. S., Seltmann R. and Igamberdiev E. (2009) Mavlyanovite, $Mn_5Si_3$: a new mineral species from a lamproite diatreme, Chatkal Ridge, Uzbekistan. *Mineral. Mag.* **73**, 43–50.

Zhang W. W., Xu H. H., Liang J. L., Xiong W. and Du Y. (2009) Phase equilibria of the Fe–Ni–Si system at 850 °C. *J. Alloys Compd.* **481**(1–2), 509–514.

Zhou G. F. and Bakker H. (1994) Atomic disorder and phase transformation in L12-structure $Ni_3Si$ by ball milling. *Acta Metall. Mater.* **42**(9), 3009–3017.

*Associate editor:* Christian Koeberl

**ORIGINAL PAPER**

# A chondrule formation experiment aboard the ISS: microtomography, scanning electron microscopy and Raman spectroscopy on $Mg_2SiO_4$ dust aggregates

Dominik Spahr[1] · Tamara E. Koch[1] · David Merges[1] · Lkhamsuren Bayarjargal[1] · Philomena-Theresa Genzel[1] · Oliver Christ[1] · Fabian Wilde[2] · Frank E. Brenker[1] · Björn Winkler[1]

**Abstract**

We performed an experiment under long-term microgravity conditions aboard the International Space Station (ISS) to obtain information on the energetics and experimental constraints required for the formation of chondrules in the solar nebula by 'nebular lightning'. As a simplified model system, we exposed porous forsterite ($Mg_2SiO_4$) dust particles to high-energetic arc discharges. The characterization of the samples after their return by synchrotron microtomography and scanning electron microscopy revealed that aggregates had formed, consisting of several fused $Mg_2SiO_4$ particles. The partial melting and fusing of $Mg_2SiO_4$ dust particles under microgravity conditions leads to a strong reduction of their porosity. The experimental outcomes vary strongly in their appearance from small spherical melt-droplets ($\varnothing \approx 90\,\mu m$) to bigger and irregularly shaped aggregates ($\varnothing \approx 350\,\mu m$). Our results provided new constraints with respect to energetic aspects of chondrule formation and a roadmap for future and more complex experiments on Earth and in microgravity conditions.

**Keywords** Microgravity · Arc discharges · International Space Station ISS · Chondrule formation · Microtomography

## Introduction

Experiments performed under extreme conditions such as high pressures or high temperatures have been carried out in very large number during the last decades leading to a better understanding of, e.g. physical properties of minerals or phase relations. Another much less explored extreme condition is microgravity, which can be achieved by parabolic flights, drop-tower experiments or outside the Earth's atmosphere. Currently, long-term microgravity is only available outside the Earth's atmosphere, either aboard the International Space Station (ISS) or using other satellite-based experimental platforms. As commercial payloads for the ISS were made accessible for researchers, we developed the first chondrule formation experiment, which was carried out in long-term microgravity aboard the ISS, with the acronym EXCISS (**Ex**perimental **C**hondrule formation aboard the **ISS**) (Spahr et al. 2020).

Chondrules have been considered to be the building blocks of our solar system in most of the models for planet and planetesimal formation, but their formation process is debated controversially (Russel et al. 2018; Boss 1996; Kerr 2013; Connolly and Jones 2016). Different scenarios for chondrule formation have been proposed, for example formation by shock waves (Connolly and Love 1998; Ciesla and Hood 2002), by nebular lightnings (Whipple 1966; Horányi et al. 1995; Desch and Cuzzi 2000; Túnyi et al. 2003; Güttler et al. 2008; Johansen and Okuzumi 2018) or by collisions of planetesimals (Krot et al. 2005; Asphaug et al. 2011; Johnson et al. 2015; Lichtenberg et al. 2018). Since there is no single theory which can explain all chondrule characteristics, different events could contribute to chondrule formation (Morris and Boley 2018).

✉ Dominik Spahr
  d.spahr@kristall.uni-frankfurt.de

[1] Institute of Geosciences, Goethe University Frankfurt, Altenhöferallee 1, 60438 Frankfurt, Germany

[2] Institute of Materials Physics, Helmholtz-Zentrum Hereon, Max-Planck-Straße 1, 21502 Geesthacht, Germany

Experiments can help to test proposed formation conditions and mechanism, but previous chondrule formation experiments only partially successfully reproduced properties of chondrules as they were affected by the gravity on Earth (Wdowiak 1996; Lofgren 1996; Connolly et al. 1998; Hewins et al. 2000; Hewins and Fox 2004; Güttler et al. 2008; Morlok et al. 2012; Imae and Isobe 2017). Therefore, we developed the EXCISS experiment which was focused on the chondrule formation by 'nebular lightning'. The long-term microgravity conditions aboard the ISS enable us to expose the $Mg_2SiO_4$ particles to arc discharges without the influence of gravity. The hypothesis of chondrule formation by nebular lightnings was recently supported by, e. g. Johansen and Okuzumi (2018). This study provided evidence that the decay of short-lived $^{26}Al$ ($\tau = 7 \times 10^5$ years) may lead to the charging of dust particles in the solar nebular with subsequent discharges through lightning bolts. This finding implies that lightnings can provide enough energy to melt mm-sized particles, which is one of the main uncertainties of the nebular lightning theory. The fast cooling rates assumed for the thermal history of chondrules formed by 'nebular lightning' contradict the previously expected cooling rates for the formation of the most common chondrules. However, Libourel and Portail (2018) presented new constraints on chondrule formation and their thermal history, which may be consistent with cooling rates up to $10^6 \, \mathrm{K \, h^{-1}}$.

In the EXCISS experiment, freely floating forsterite ($Mg_2SiO_4$) dust particles were exposed to high energetic arc discharges which can reach electron temperatures up to $k_B T_e \approx 6900$ K (Spahr et al. 2020). We chose $Mg_2SiO_4$ as a model system for our experiments as it is the most abundant phase in natural chondrules and has a relatively high melting point of $\approx 2200$ K (Russel et al. 2018; Bowen and Schairer 1925). The experiments were observed by a camera and the sample material was analyzed after sample return. The analysis of the video material revealed the particle behavior of agitated particles in electric field in long-term microgravity environment (Koch et al. 2021a). In this study, we have shown that the electric fields influence the aggregation process, the aggregate morphology and the internal structure. These observations can help to understand different aggregation processes in the early Solar System. The experiment also caused the formation of fused aggregates and melt spherules. In our investigations on the small spherical melt droplets, we have shown that the sample material can be completely melted by arc discharges into melt spherules (Koch et al. 2021b). The analysis of these droplets with scanning electron microscopy and electron-back-scattered diffraction showed, that the micro-textural properties of these spherules, such as crystal sizes and orientations, morphologies and metal inclusions, are very similar to those observed in natural chondrules. The microstructure is probably the result of crystallization under microgravity conditions. In

addition, the fused aggregates show similarities to different types of Ca,Al-rich inclusions, the oldest material of our Solar System (Koch et al. 2022). These results imply that a (flash-)heating event with subsequent aggregation could have been involved in the formation of different morphological CAI-characteristics.

In the study presented here we investigated the behavior of $Mg_2SiO_4$ dust particles exposed to high energetic electrical discharges under long-term microgravity conditions. In contrast to the test experiments on Earth (Spahr et al. 2020) the $Mg_2SiO_4$ particles levitated without gravitational influence in the sample chamber during the whole experimental procedure aboard the ISS. $Mg_2SiO_4$ dust particles or already formed aggregates may then be exposed to multiple discharges, which was not possible in the test experiments. We used synchrotron based X-ray microtomography as a tool to study the density contrast in fused dust aggregates and melt-droplets received from experiments aboard the ISS after sample return. Furthermore, we visualized their inner structures and grain-grain boundaries. The microtomography data were complemented by high-resolution scanning electron microscopy images and the phase content was studied by Raman spectroscopy.

## Materials and experimental methods

### Sample material

The initial $Mg_2SiO_4$ pellets were obtained by high-temperature synthesis using pressed pellets of the oxides as starting material, resulting in a sintered $Mg_2SiO_4$ ceramic. The pellets were then ground in an agate mortar and sieved. The chemical composition and the phase purity of the resulting powder was confirmed by scanning electron microscopy and Rietveld refinement on the X-ray powder diffraction data, respectively. The $Mg_2SiO_4$ particles selected after the grinding by sieving had a mean diameter of 126(23) μm and hence can easily be observed by the microscope camera in the experimental setup (Spahr et al. 2020). The high porosity of the initial dust particles allows to unambiguously determine if a melting process took place and which amount of the initial grains was molten. After sample return from the ISS the sample chamber was opened and $Mg_2SiO_4$ dust aggregates and melt-droplets were hand-picked from the received powder and sorted under a microscope.

### Experiments aboard the ISS

The experimental setup and its calibration is described in Spahr et al. (2020) in great detail. The experiment was carried out inside a $10 \times 10 \times 15 \, cm^3$ sized NanoRacks NanoLab aboard the ISS. The $Mg_2SiO_4$ dust particles were

freely levitating inside a glass sample chamber while they were exposed to high energetic electrical discharges with an adjustable energy between 3.1 J and 21 J. The sample chamber was made of quartz glass and we used tungsten electrodes with a diameter of 1 mm and a spark gap of $\approx$ 2–3 mm for the discharges. The chamber was loaded with 30(1) mg of the $Mg_2SiO_4$ powder and the argon gas pressure inside the chamber was adjusted to be 100(1) mbar. The arc discharges between the W-electrodes can have a duration between 400 and 600 $\mu$s and reach electron temperatures up to $k_B T_e \approx 6900$ K with electron densities up to $n_e \approx 2 \times 10^{16}$ cm$^{-3}$. The changes in particle size and morphology after the discharges were recorded with a Raspberry Pi camera. Figure 1 shows frames recorded with a high-speed camera of a typical arc discharge in the sample chamber during the test experiments on Earth. The first frame shows the weak ignition spark. The time interval between the frames is 20 $\mu$s. The released energy during this arc discharge was $\approx$ 8 J.

Aboard the ISS the EXCISS experiment was operated for 30 days. It was connected by USB to the ISS for power supply and data transfer. During this time the initial $Mg_2SiO_4$ dust particles in the sample chamber were exposed to 81 arc discharges. Based on our previous calibration the estimated energy of the released arc discharges was between 5 J and 8 J. Figure 2 shows the field of view in the sample chamber aboard the ISS after 30 arc discharges. The light transmission through the sample chamber is reduced due to the formation of a thin film of tungsten, deposited on the inner glass surface after being sputtered from the electrodes. The aggregates, which were freely levitating in microgravity and later found on the bottom of the sample chamber without sticking to the inner walls or electrodes, were used for the subsequent microtomography, SEM and Raman analysis. The tips of the electrodes are eroded by the arc discharges.
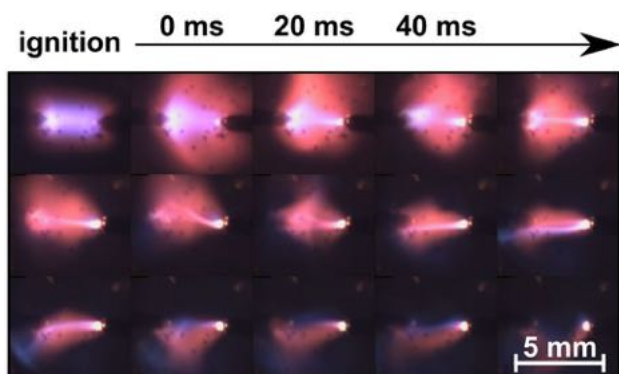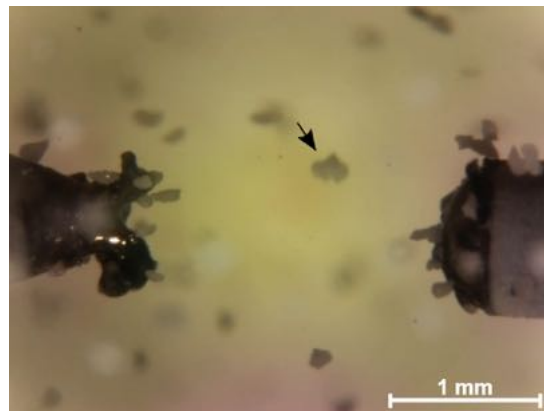


**Fig. 2** Field of view aboard the ISS after 30 arc discharges. Bigger agglomerated objects stick to the electrodes and are levitating in between

## Synchrotron microtomography

Synchrotron microtomography was performed on the microtomography beamline P05 (Wilde et al. 2016; Ogurreck et al. 2013), operated by Helmholtz-Zentrum Geesthacht at PETRA III (DESY) in Hamburg, Germany. All data were collected using a 15 keV beam and the double crystal monochromator. The high quality absorption contrast tomograms were acquired using a 24× objective lens with a CMOS camera resulting in a 1.8 × 1.8 mm$^2$ field of view. A $CdWO_4$ single crystal scintillator with 100 $\mu$m thickness was employed for the X-ray to visible light conversion. We used an acquisition time of 350 ms per frame. A binning factor of 2 × 2 pixel resulted in a binned pixel size of $\approx$ 0.61 × 0.61 $\mu$m$^2$ and the spatial resolution was estimated to be 1 $\mu$m. Data pre-processing, including tomographic reconstruction was performed using MATLAB scripts provided by Moosmann et al. (2014). The microtomography reconstructions were visualized with the volume exploration software tool Drishti (Limaye 2012). The samples were embedded in Araldite epoxy resin and afterwards dried at 333 K under vacuum for 24 hours to ensure their stability during transport and measurement. The high density contrast between the Araldite epoxy ($\rho \approx 1$ g cm$^{-1}$) and the forsterite ($\rho \approx 3.3$ g cm$^{-1}$) prevented a deterioration of the tomographic reconstruction of the embedded aggregates. All objects were embedded and measured individually.

## Scanning electron microscopy

We used a Phenom World ProX desktop SEM equipped with an back-scattered Electron detector (BSE) for scanning electron microscopy (SEM). The samples were used as received and mounted without coating using sticky carbon tape on aluminum stubs. They were measured under low vacuum



**Fig. 1** High-speed photographs of an arc discharge where $\approx$ 8 J are released into the spark gap. The first picture shows the weak ignition spark. The time interval between the frames is 20 $\mu$s

conditions to reduce charging effects on the sample with 10 kV for imaging. We used the software Helicon Focus 7 Pro (Kozub et al. 2018) from Helicon Soft to combine multiple BSE images acquired with different focal planes to obtain images with an improved depth of field. We used the depth map rendering method with radius = 8 (size of the analyzed area around each pixel) and smoothing = 4 (value determines how depth map will be smoothed out). Energy-dispersive X-ray spectroscopy (EDX) was carried out using 15 kV and the obtained data were analyzed using the Phenom Pro Suite software.

## Raman spectroscopy

Raman spectroscopy was performed using an OXXIUS S.A. LaserBoxx LMX532 laser ($\lambda = 532.14$ nm) in combination with a Pixis256E CCD camera mounted on a Princeton Instruments ACTON SpectraPro 2300i spectrograph. The Raman setup is described in Bayarjargal et al. (2018) in more detail and the Raman spectra were background corrected using the software Fityk (Wojdyr 2010).

## Results

### Starting material

The $Mg_2SiO_4$ dust particles which were used as starting material for the ISS-based experiment had a mean diameter of 126(23) μm (Fig. 3a). The SEM and synchrotron microtomography images (Fig. 3) show that they were irregularly shaped and have rough surfaces. In addition, the microtomography reconstruction also shows a homogeneous density distribution inside the grains confirming the structural and chemical homogeneity of the starting material (Fig. 3b). The high porosity of the dust particles can also be observed which is in good agreement with our earlier investigations (Spahr et al. 2020). In addition, the expected chemical

composition was confirmed by EDX analysis within the experimental uncertainties and no unexpected elements were detected.
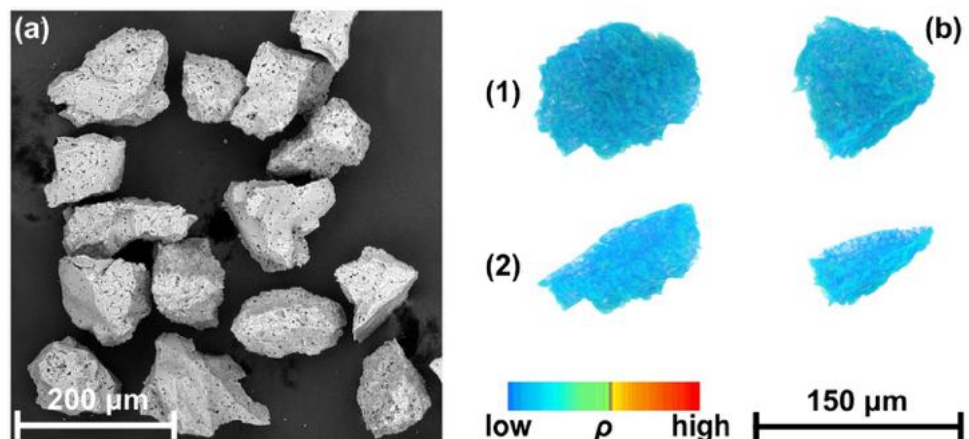
## Aggregates formed aboard the ISS

### Synchrotron microtomography

Aboard the ISS we successfully melted $Mg_2SiO_4$ dust particles or fused them together to bigger objects. We used synchrotron microtomography as a tool to study their inner structure and density distribution. After the sample return, the samples display a morphological diversity as we obtained small and spherical melt-droplets (Fig. 4) and fused aggregates which can have many different shapes (Fig. 5). The spherical objects or melt-droplets ($\approx 90$ μm) have a smooth surface and a strongly reduced porosity in comparison to the initial dust particles (Fig. 3). The melt-droplets must have been melted by the lightnings induced in the experiment and afterwards cooled down without gravitational influence. The melt-droplet (Fig. 4) shows a region with strongly increased density (orange). This is probably caused by an impact of a very hot tungsten particle from the electrode. Other parts of the melt-droplet show a lower density, which can be explained by unmolten regions with pores. The scale bar of the reconstructed absorption contrast tomograms was adjusted to show only objects with a density larger than the surrounding Araldite epoxy resin. Hence, the 3D-reconstruction of the surface of the particles and aggregates is assumed to be the area where the density is higher than the epoxy.

We found by SEM and EBSD analysis in a related study (Koch et al. 2021b) that microtextural properties of the melt-droplets partially resemble those of natural chondrules, e.g. with respect to crystal sizes, crystal orientations, or morphologies. They seem to have a texture comparable to porphyritic chondrules which is the most abundant chondrule type (Russell et al. 2018). Very recent studies reveal that



**Fig. 3** **a** SEM image of different $Mg_2SiO_4$ particles after the sample preparation process. **b** Synchrotron microtomography on representative $Mg_2SiO_4$ dust particles with a 3D-reconstruction of the surface (1) and virtual cross-section through the grains (2)
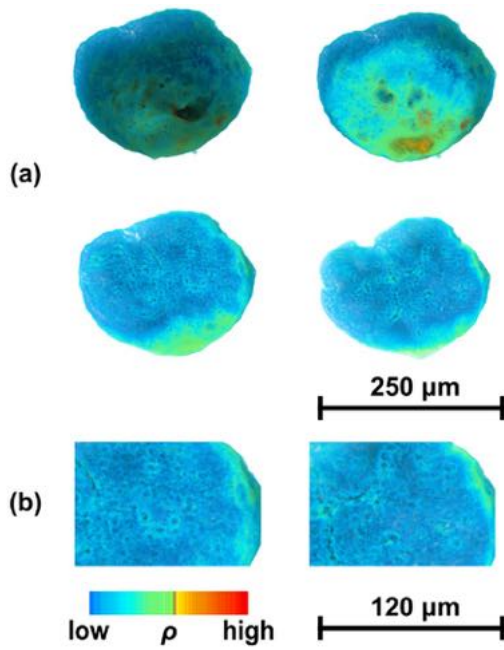
**Fig. 4** Synchrotron microtomography image of a spherical melt-droplet formed aboard the ISS: **a** 3D-reconstruction of the surface (left top) and three virtual cross-sections through the same melt-droplet. **b** Close-ups of selected regions in the cross-sections

porphyritic textured chondrules may be obtained by experiments with very high cooling rates (3000–6000 K h$^{-1}$) (Greenwood and Herbst 2021), in agreement with the very fast cooling rates in our discharge experiment. A columnar crystal morphology was observed in some parts of the melt-droplets (Koch et al. 2021b) which has also been observed in natural porphyritic chondrules (Libourel and Portail 2018). However, due to the use of a the single phase $Mg_2SiO_4$ starting material, the glassy mesostasis typical for porphyritic chondrules was not observed in our experiments.

The size of the melt droplets is significantly smaller than from the fused dust aggregates formed of several $Mg_2SiO_4$ grains. Their size ranges from $\approx$ 150–350 μm depending on the number of participating $Mg_2SiO_4$ dust grains and on their shape. Figure 5 shows four representative aggregates. Aggregate #1 consists of 2–3 $Mg_2SiO_4$ dust particles. Half of this aggregate was completely molten and shows an increased density while in the rest of the aggregate regions with low density and high porosity can be identified. The very high density (orange) is probably caused by the impact of a hot/molten tungsten particle from the electrodes. Other aggregates consist of more initial dust particles. Aggregate #2 is much bigger with $\approx$ 350 μm diameter. This aggregate is still irregularly shaped but molten areas on the surface can clearly be identified. Furthermore, the virtual cross-section through the

**Fig. 5** Synchrotron microtomography images of differently shaped and sized aggregates #1–4 formed aboard the ISS (**a**), corresponding virtual cross-sections (**b**) and close-ups of selected regions in the cross-sections (**c**)
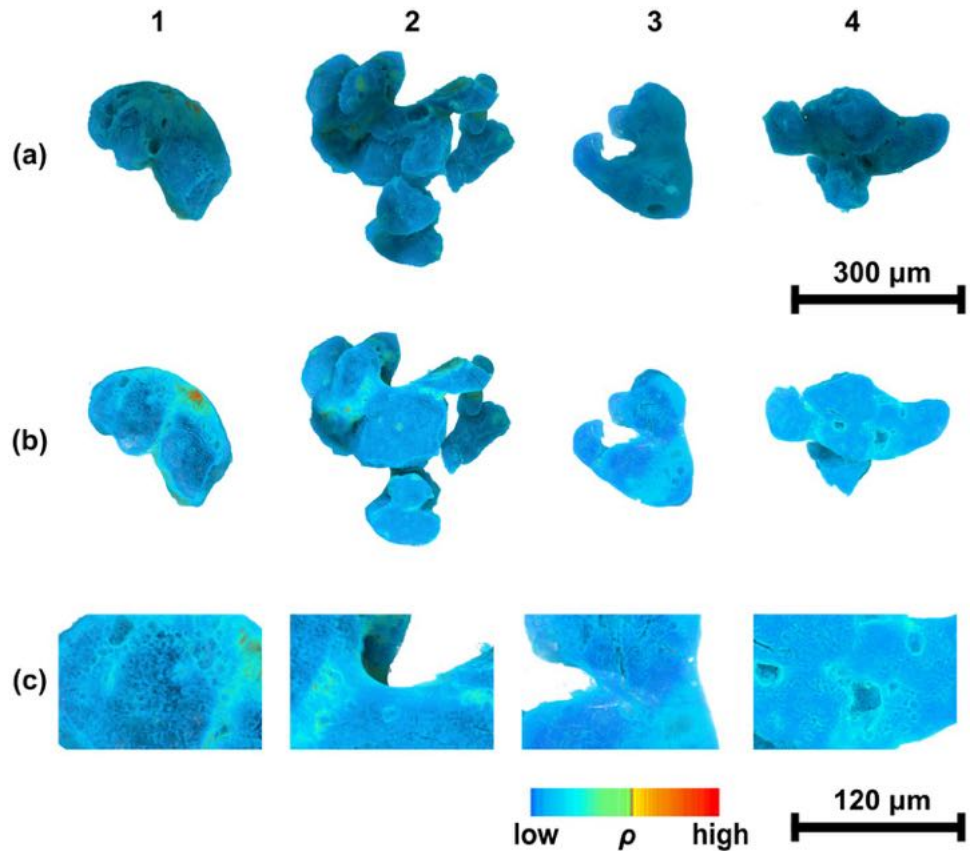
aggregate clearly shows an increased density (green) on the grain boundaries of the former dust particles which corresponds to molten regions. In this area, the high porosity of the starting material has disappeared. Small regions with very high density (orange) indicate tungsten contamination from the electrodes.

Aggregate #3 is not completely spherically shaped but has the shape of a hemisphere. The whole surface is smooth and rounded, which indicates that the surface was completely molten. In the surface reconstruction (a) the initial $Mg_2SiO_4$ dust particles cannot be identified any more. However, the virtual cross-section (b) shows that the inner part in the upper region is still unmolten while the bottom part of the aggregate was molten. In addition, larger pores grow during the melting process. Enlarged pores can also be observed in the cross-section of aggregate #4. These pores were surrounded by molten regions with higher (green) density. In the surface reconstruction of aggregate #4 the increased density can also be observed in the region where the former $Mg_2SiO_4$ melted together, but here the initial $Mg_2SiO_4$ can still be identified. These observations are in good agreement with our test experiments on Earth (Spahr et al. 2020) were we observed increased density on the contact points between grains or in the regions where tungsten from the electrodes impacts into $Mg_2SiO_4$ grains.

The relatively small differences in the density contrast (Fig. 5 aggregates #2–#4) are caused by the homogeneous chemical composition of the starting material. This confirms that the fused aggregates were chemically uniform and not formed e. g. around hot tungsten particles as observed for aggregate #1 or during the Earth based experiments (Spahr et al. 2020). Small changes in the contrast only occur due to a slightly increased density in the molten regions, confirming that the aggregates were formed in the arc discharge and not by the impact of hot tungsten particles. The role of a small amount of tungsten vapor from the electrodes, which cannot be detected by microtomography, during the melting and fusing process of the aggregates is unknown.

## Scanning electron microscopy

We used scanning electron microscopy to obtain high-resolution images of the surfaces of the fused aggregates (Fig. 6). With lower magnification (a) the initial $Mg_2SiO_4$ dust particles can be identified in some regions of the aggregates, but it is obvious that the dimensions of the dust aggregates formed during the experiment (up to 400 µm) are much bigger than of the starting material.

Aggregate #5 is elongated in one direction and in the outer part the $Mg_2SiO_4$ dust particles seem to be pristine. In contrast to the enlarged part in the center of the aggregate where a large amount of melt covers at least the surface of one or two $Mg_2SiO_4$ grains and connects them to the surrounding particles. The surface of aggregate #6 is smooth and rounded in many regions. These areas of the aggregate were molten before, and in the left part of the aggregate the initial $Mg_2SiO_4$ grains and their contact points cannot be identified any more. Furthermore, a spherical melt-droplet is part of the aggregate. The melt-droplet connects the left and molten part with a nearly unchanged $Mg_2SiO_4$ grain on the opposite side. The surface of this melt-droplet varies widely from the surfaces of the other aggregates. A similar melt-droplet within an aggregate was also found in our test experiments on Earth (Spahr et al. 2020). In aggregate #7 only a few parts are molten and with increased magnification it can be observed that some regions of the initial $Mg_2SiO_4$ grains were completely molten and rounded while other parts of the same grain were untouched. Aggregate #7 is held together by the molten areas of a few grains which connects them to the surrounding unmolten particles. In contrast to aggregate #7, in aggregate #8 large parts of the aggregate were molten. The bottom part is covered with a coherent layer of molten material. In some parts the layer is incomplete and unveils an inside look on the unmolten bottom layer.

**Fig. 6** SEM images of different aggregates #5–8 formed aboard the ISS with lower (**a**) and higher (**b**) magnification. Characteristic pristine and melt regions are marked
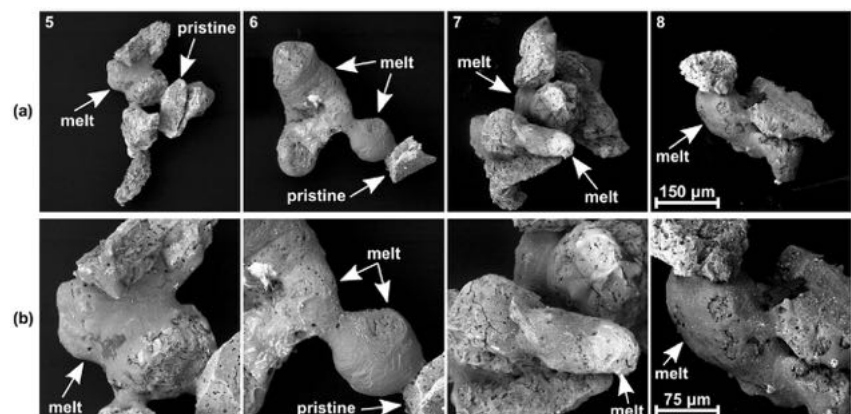
The EDX measurements on the aggregates reveal, that the expected chemical composition of the $Mg_2SiO_4$ dust particles does not change during the melting process. In contrast to the starting material, we found a slight tungsten contamination in some regions of the fused dust aggregates. This is in good agreement with the small regions having a very high density, observed by microtomography.

### Raman spectroscopy

We used Raman spectroscopy to determine the mineral phases occurring in the dust aggregates. Figure 7 shows line measurements through selected aggregates. A picture section of the corresponding SEM image (Fig. 6b) shows the position where the Raman spectra were acquired. It is clear to see that even in the molten regions crystalline forsterite is present, the predominant phase and has not decomposed. No significant peak broadening can be observed in the molten regions and all Raman modes of the pristine areas can still be observed. Only minor peaks of an additional phase can be observed in a few Raman spectra.

## Discussion and conclusion

As we successfully demonstrated that melting of $Mg_2SiO_4$ dust particles is possible with our experimental setup within the chosen experimental conditions, we cross-checked the required energy for melting our $Mg_2SiO_4$ precursor particles. The discharge energy was adjusted up to the $\approx 8$ J, while below no significant changes in the particle texture or



**Fig. 7** Raman spectra measured at different points of aggregate #6 in comparison to those of pristine $Mg_2SiO_4$ dust particles. A section of the corresponding SEM image (Fig. 6b) for the Raman line is shown

morphology had been observed with the integrated camera. After several discharges with energies between 5 J and 8 J first changes were observed in the particle texture and morphology (Fig. 2). Therefore, we chose to not further increase the energy of the arc discharge. The precursor dust particles with a diameter of $d = 0.126(23)$ mm and a density of $\rho = 3.2$ g cm$^{-3}$ have a mass of $m_{dust} \approx 2.5 \times 10^{-5}$ g approximating them as spheres. We calculated the required melting energy ($Q_{melt}$) for the chosen precursor material using the enthalpy of fusion ($\Delta H_{fus} = 114(20)$ kJ mol$^{-1}$ Navrotsky et al. 1989) and the molar mass ($M = 140.7$ g mol$^{-1}$) of $Mg_2SiO_4$:

$$Q_{melt} = \Delta H_{fus} \cdot \frac{m_{dust}}{M_{Mg_2SiO_4}}. \tag{1}$$

The required melting energy is $\approx 0.02$ J per dust particle for a complete melting in the arc discharge. The highest energy used for the discharge experiments aboard the ISS was $\approx 8$ J and the volume heated by the arc discharge can be approximated to be $\approx 1.6$ mm$^3$ resulting in an energy density of $w = 5$ J mm$^{-3}$ in the arc (Spahr et al. 2020). With the known size of the precursor dust particles the provided energy per grain in an arc is $\approx 0.04$ J. Therefore, it is plausible that the arc discharges provided the required energy $Q_{melt}$ for a complete melting of the dust particles.

We demonstrated that our experimental setup for a chondrule formation experiment aboard the ISS worked as planned. With this experimental setup we were able to obtain dust aggregates with very different sizes and shapes. In contrast to the pristine starting material we observed a strongly reduced porosity of the experimental outcomes. A quantitative interpretation of the porosity may be achieved by small-angle scattering techniques such as SANS (Kahle et al. 2004) in future investigations. With the analyses on eight different aggregates presented here we extended our analysis of micro-structure of the small ($\varnothing \approx 90$ μm) melt droplets by investigations on much bigger and complex shaped fused aggregates with lateral dimensions up to $\varnothing \approx 350$ μm (Koch et al. 2021b). Our results show that using relatively low discharge energy of 5–8 J, which is much lower than the energies employed in the chondrule formation experiments of e. g. Wdowiak (1996) (5000 J) or Güttler et al. (2008) (123–490 J), leads to the formation of fused aggregates instead of their destruction.

In comparison to our pre-experiments on Earth (Spahr et al. 2020) the fused aggregates obtained aboard the ISS show an increased amount of molten regions which do not only dominate the surface of the $Mg_2SiO_4$ grains. Molten regions, i. e. reduced porosity, missing grain boundaries and higher density in the contact points of the $Mg_2SiO_4$ particles reveal that the melting processes aboard the ISS affect also the insides of the aggregates, which was not observed during
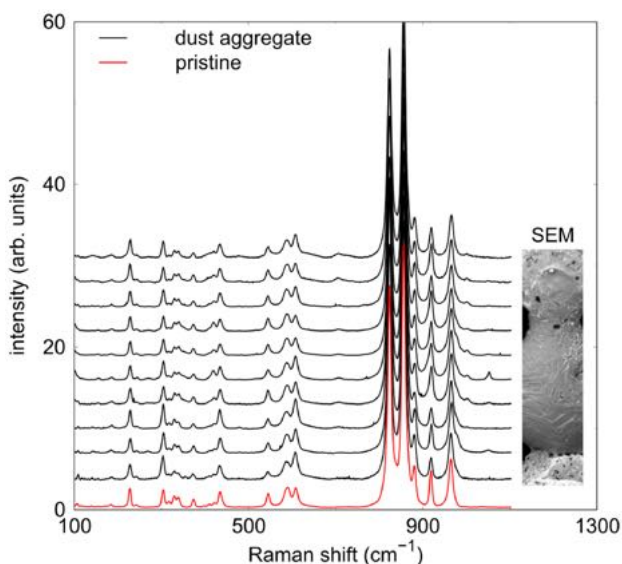
the test experiments on Earth. In addition, some parts of the aggregates were molten completely and hence are almost round. This was not observed during the Earth based experiments, were the aggregates only stick together by molten layers covering several $Mg_2SiO_4$ particles or were fused together by the impact of hot tungsten from the electrodes. It is possible that the aggregates formed aboard the ISS were exposed to more than one discharge while levitating between the electrodes. Therefore, very different morphologies and structures of the aggregates can be observed. This was only possible due to the long-term microgravity conditions aboard the ISS. Here, $Mg_2SiO_4$ particles and already formed aggregates can be exposed to repeated heating events without suffering from gravity influence. The video recordings obtained from the ISS give evidence that the free levitating dust particles and yet formed aggregates (Fig. 2) are in position between the electrodes and therefore hit by the arc discharges without any contact to the inner walls of the sample chamber, while during the test experiments on Earth these results could not be obtained due to gravitational influences. Implications of the formation of the aggregates for the relation to early Solar System processes are provided by Koch et al. (2022).

In summary, we have obtained further information on the energetics and experimental constraints required for chondrule formation experiments under microgravity conditions aboard the ISS. This provides a roadmap for future experiments on Earth and in microgravity, as it now seems timely and relevant to address the role of the chemical complexity in chondrule formation by lightning experiments by extending the chemical simplicity of the $Mg_2SiO_4$ model system.

## References

Asphaug E, Jutzi M, Movshovitz N (2011) Chondrule formation during planetesimal accretion. Earth Planet Sci Lett 308:369–379. https://doi.org/10.1016/j.epsl.2011.06.007

Bayarjargal L, Fruhner CJ, Schrodt N et al (2018) $CaCO_3$ phase diagram studied with Raman spectroscopy at pressures up to 50 GPa and high temperatures and DFT modeling. Phys Earth Planet Inter 281:31–45. https://doi.org/10.1016/j.pepi.2018.05.002

Boss AP (1996) A concise guide to chondrule formation models. In: Hewins RH, Jones RH, Scott ERD (eds) Chondrules and the Protoplanetary Disk, pp 257–263

Bowen NL, Schairer JF (1925) The system $MgO-FeO-SiO_3$. Am J Sci 29:151–217

Ciesla FJ, Hood LL (2002) The nebular shock wave model for chondrule formation: shock processing in a particle-gas suspension. Icarus 158:281–293. https://doi.org/10.1006/icar.2002.6895

Connolly HC, Jones RH (2016) Chondrules: the canonical and non-canonical views. J Geophys Res-Planets 121:1885–1899. https://doi.org/10.1002/2016JE005113

Connolly HC, Love SG (1998) The formation of chondrules: petrologic tests of the shock wave model. Science 280:62–67. https://doi.org/10.1126/science.280.5360.62

Connolly HC, Jones BD, Hewins RH (1998) The flash melting of chondrules: an experimental investigation into the melting history and physical nature of chondrule precursors. Geochim Cosmochim Acta 62(15):2725–2735. https://doi.org/10.1016/S0016-7037(98)00176-8

Desch SJ, Cuzzi JN (2000) The generation of lightning in the solar nebula. Icarus 143:87–105. https://doi.org/10.1006/icar.1999.6245

Greenwood RC, Herbst W (2021) New constraints on chondrule formation from experimental reproduction of aluminum and titanium in chondrule olivine (abstract # 1617). In: 52nd Lunar and Planetary Science Conference

Güttler C, Poppe T, Wasson JT et al (2008) Exposing metal and silicate charges to electrical discharges: Did chondrules form by nebular lightning? Icarus 195:504–510. https://doi.org/10.1016/j.icarus.2007.11.021

Hewins RH, Fox GE (2004) Chondrule textures and precursor grain size: an experimental study. Geochimica et Cosmochimica Acta 68(4):917–926. https://doi.org/10.1016/S0016-7037(03)00494-0

Hewins RH, Zanda RH, Horanyi M et al (2000) The trouble with flash heating. Lunar Planet Sci 31:1675 (**abstract**)

Horányi M, Morfill G, Goertz CK et al (1995) Chondrule formation in lightning discharges. Icarus 114:174–185. https://doi.org/10.1006/icar.1995.1052

Imae N, Isobe H (2017) An experimental study of chondrule formation from chondritic precursors via evaporation and condensation in Knudsen cell: Shock heating model of dust aggregates. Earth Planet Sci Lett 473:256–268. https://doi.org/10.1016/j.epsl.2017.05.040

Johansen A, Okuzumi S (2018) Harvesting the decay energy of $^{26}$Al to drive lightning discharge in protoplanetary discs. Astron Astrophys 609:1–22. https://doi.org/10.1051/0004-6361/201630047

Johnson BC, Minton DA, Melosh HJ et al (2015) Impact jetting as the origin of chondrules. Nature 517:339–341. https://doi.org/10.1038/nature14105

Kahle A, Winkler B, Radulescu A et al (2004) Small-angle neutron scattering study of volcanic rocks. Eur J Mineral 16:407–417. https://doi.org/10.1127/0935-1221/2004/0016-0407

Kerr RA (2013) Meteorite mystery edges closer to an answer—or the end of a field. Science 341:126–127. https://doi.org/10.1126/science.341.6142.126

Koch TE, Spahr D, Merges D et al (2021a) $Mg_2SiO_4$ particle aggregation aboard the ISS—influence of electric fields on aggregation

behavior, particle velocity and shape-preferred orientation. Astron Astrophys 651:A1. https://doi.org/10.1051/0004-6361/202141330

Koch TE, Spahr D, Tkalcec BJ et al (2021b) Formation of chondrule analogs aboard the international space station. Meteorit Planet Sci 56:1669–1684. https://doi.org/10.1111/maps.13731

Koch TE, Spahr D, Tkalcec BJ et al (2022) Formation of fused aggregates under long-term microgravity conditions aboard the iss with implications for early solar system particle aggregation. Meteorit Planet Sci (accepted). https://doi.org/10.1111/maps.13815

Kozub D, Khmelik V, Shapoval J, et al (2018) Helicon Focus 7.0.2 Pro. Helicon Soft Ltd. Available: https://www.heliconsoft.com/heliconsoft-products/helicon-focus/ (2018, Septemper 27)

Krot AN, Amelin Y, Cassen P et al (2005) Young chondrules in CB chondrites from a giant impact in the early Solar System. Nature 436:989–992. https://doi.org/10.1038/nature03830

Libourel G, Portail M (2018) Chondrules as direct thermochemical sensors of solar protoplanetary disk gas. Sci Adv 4:eaar3321. https://doi.org/10.1126/sciadv.aar3321

Lichtenberg T, Golabek GJ, Dullemond CP et al (2018) Impact splash chondrule formation during planetesimal recycling. Icarus 302:27–43. https://doi.org/10.1016/j.icarus.2017.11.004

Limaye A (2012) Drishti: a volume exploration and presentation tool. Proc. SPIE 8506, Developments in X-Ray Tomography VIII, 85060X. https://doi.org/10.1117/12.935640

Lofgren G (1996) A dynamic crystallization model for chondrule melts. In: Hewins RH, Jones RH, Scott ERD (eds) Chondrules and the Protoplanetary Disk, pp 187–196

Moosmann J, Ershov A, Weinhardt V et al (2014) Time-lapse X-ray phase-contrast microtomography for in vivo imaging and analysis of morphogenesis. Nat Protoc 9:294–304. https://doi.org/10.1038/nprot.2014.033

Morlok A, Sutton YC, Braithwaite NSJ et al (2012) Chondrules born in plasma? Simulation of gas-grain interaction using plasma arcs with applications to chondrule and cosmic spherule formation. Meteorit Planet Sci 47:2269–2280. https://doi.org/10.1111/maps.12043

Morris MA, Boley AC (2018) Formation of Chondrules by Shock Waves, vol 1. Cambridge University Press, chap 15:1–17

Navrotsky A, Ziegler D, Oestrike R et al (1989) Calorimetry of silicate melts at 1773 K: measurement of enthalpies of fusion and of mixing in the systems diopside-anorthite-albite and anorthite-forsterite. Contrib Mineral Petrol 101:122–130. https://doi.org/10.1007/BF00387206

Ogurreck M, Wilde F, Herzen J et al (2013) The nanotomography endstation at the PETRA III Imaging Beamline. J Phys Conf Ser 425(18):182002. https://doi.org/10.1088/1742-6596/425/18/182002

Russel S, Connolly HC Jr, Krot AN (eds) (2018) Chondrules: records of protoplanetary disk processes. Cambridge Planetary Science, Cambridge University Press, Cambridge

Russell SS, Connolly HC, Krot AN (eds) (2018) Chondrules: records of protoplanetary disk processes. Cambridge University Press, Cambridge

Spahr D, Koch TE, Merges D, et al (2020) A chondrule formation experiment aboard the ISS: experimental set-up and test experiments. Icarus 350(113):898. https://doi.org/10.1016/j.icarus.2020.113898

Túnyi I, Guba P, Roth LE et al (2003) Electric discharges in the protoplanetary nebula as a source of impulse magnetic fields to promote dust aggregation. Earth Moon Planets 93:65–74. https://doi.org/10.1023/B:MOON.0000034502.21911.22

Wdowiak TJ (1996) Experimental investigation of electrical discharge formation of chondrules. Lunar and Planetary Institute, Houston. In: King EA (ed) Chondrules and their originsk, pp 279–283

Whipple FL (1966) Chondrules: suggestion concerning the origin. Science 153:54–56. https://doi.org/10.1126/science.153.3731.54

Wilde F, Ogurreck M, Greving I et al (2016) Micro-CT at the imaging beamline P05 at PETRA III. AIP Conf Proc 1741(030):035. https://doi.org/10.1063/1.4952858

Wojdyr M (2010) Fityk: a general-purpose peak fitting program. J Appl Cryst 43:1126–1128. https://doi.org/10.1107/S0021889810030499

# Characterization of carbon phases in Yamato 74123 ureilite to constrain the meteorite shock history

Anna Barbaro[1,*], Fabrizio Nestola[2,3], Lidia Pittarello[4], Ludovic Ferrière[4], Mara Murri[5], Konstantin D. Litasov[6], Oliver Christ[2], Matteo Alvaro[1], and M. Chiara Domeneghetti[1]

[1]Department of Earth and Environmental Sciences, University of Pavia, Via A. Ferrata 1, I-27100 Pavia, Italy
[2]Department of Geosciences, University of Padova, Via Gradenigo 6, 35131 Padova, Italy
[3]Geoscience Institute, Goethe-University Frankfurt, Altenhöferallee 1, 60323 Frankfurt, Germany
[4]Department of Mineralogy and Petrography, Natural History Museum, Burgring 7, 1010 Vienna, Austria
[5]Department of Earth and Environmental Sciences, University of Milano-Bicocca, I-20126 Milano, Italy
[6]Vereshchagin Institute for High Pressure Physics RAS, Troitsk, Moscow, 108840 Russia

## Abstract

The formation and shock history of ureilite meteorites, a relatively abundant type of primitive achondrites, has been debated for decades. For this purpose, the characterization of carbon phases can provide further information on diamond and graphite formation in ureilites, shedding light on the origin and history of this meteorite group. In this work, we present X-ray diffraction and micro-Raman spectroscopy analyses performed on diamond and graphite occurring in the ureilite Yamato 74123 (Y-74123). The results show that nano- and microdiamonds coexist with nanographite aggregates. This, together with the shock-deformation features observed in olivine, such as mosaicism and planar fractures, suggest that diamond grains formed by a shock event ($\geq$15 GPa) on the ureilitic parent body (UPB). Our results on Y-74123 are consistent with those obtained on the NWA 7983 ureilite and further support the hypothesis that the simultaneous formation of nano- and microdiamonds with the assistance of a Fe-Ni melt catalysis may be related to the heterogeneous propagation and local scattering of the shock wave. Graphite geothermometry revealed an average recorded temperature ($T_{max}$) of 1314 °C ($\pm$120 °C) in agreement with previously estimated crystallization temperatures reported for graphite in Almahata Sitta ureilite.

**Keywords:** Carbon phases, diamond, graphite, ureilite meteorites, shock, impact event

## Introduction

Ureilites represent the second largest group of achondrite meteorites (Goodrich 1992), with about 570 individuals with distinct names but only six observed falls (Meteoritical Bulletin Database 2020). Their formation, origin, and history are still under discussion among the scientific community. The debate about the formation of carbon phases contained in these meteorites has been going on for 80 years (see Nestola et al. 2020, and references therein).

As reported by Goodrich (1992), ureilites appear to be fractionated ultramafic igneous rocks, either magmatic cumulates (Berkley et al. 1980; Goodrich et al. 1987) or partial melt residues (Boynton et al. 1976; Scott et al. 1992) and, thus, the products of planetary differentiation processes. These conclusions were based on mineralogy, textures, fabrics, lithophile element chemistry, and on some aspects of Sm-Nd isotopic systematics (Berkley et al. 1976) observed in these meteorites (Goodrich 1992). Ureilites strongly differ from the other groups of stony meteorites (i.e., due to a high content of carbon phases and distinct oxygen isotopic composition) and, compared to chondrites, they are enriched in Mg but depleted in metal, troilite, and alkalis.

Ureilites typically contain large olivine grains and a few smaller low-Ca-clinopyroxene (pigeonite) aggregates in a fine-grained, carbon-rich matrix. Minor phases are kamacite (1–3 vol% with the Ni content up to 7.3%), troilite (1–2%), chromite (1–2%), and carbon material (up to 8.5%) (Cloutis et al. 2010; Goodrich et al. 2015). Carbon is present as diamond, usually with stacking disorder and nanotwins (Németh et al. 2014, 2020a, 2020b; Salzmann et al. 2015; Murri et al. 2019), graphite, and organic material (e.g., Sabbah et al. 2010).

The different shock levels observed in ureilites are very important for constraining their history. Shock level determination in meteorites was first proposed by Stöffler et al. (1991, 2018) and is subdivided in six stages of shock for ordinary chondrites, from low (S1) to high (S6) level of shock, based on: (1) shock effects in olivine and plagioclase (e.g., extinction, fractures, planar elements), and (2) the presence of glass and/or of high-pressure silicate phases. Recently, Nakamuta et al. (2016) adapted the shock classification based on olivine in chondrites to the observations in ureilites. For this reason, we will apply this classification in this work.

The occurrence of diamonds in ureilites poses the question of how this high-pressure mineral formed and whether diamonds in ureilites are similar or not to those formed by shock in terrestrial impact structures (e.g., Masaitis 1998; Hough et al. 1995; Koeberl

* E-mail: anna.barbaro01@universitadipavia.it

et al. 1997; Ohfuji et al. 2015; Murri et al. 2019). Three main hypotheses have been proposed for the formation of diamonds in ureilites: (1) static high-pressure conditions in the deep interior of large parent bodies (Urey 1956); (2) direct transformation from graphite due to shock (e.g., Lipschutz 1964; Bischoff et al. 1999; Grund and Bischoff 1999; Nakamuta and Aoki 2000, 2016; Hezel et al. 2008; Le Guillou et al. 2010; Ross et al. 2011; Lorenz 2019), also strongly supported by De Carli (1995) and De Carli et al. (2002); and (3) growth from a dilute gas phase, i.e., at low pressure in the solar nebula by a chemical vapor deposition (CVD) process (Fukunaga et al. 1987). The hypothesis of formation under static high-pressure conditions was recently supported by Miyahara et al. (2015) and Nabiei et al. (2018), who concluded that the size of a hypothetical ureilitic parent body (UPB) could be comparable to the size of Mars since static high-pressure conditions would be required for the formation of micrometer-scaled-diamond crystallites. The shock hypothesis was instead supported by the results obtained by Nakamuta et al. (2016). Indeed, these authors proposed that diamonds in ureilites could have formed at high-pressure (above 12 GPa) by spontaneous shock transformation from graphite and at low pressure (6–10 GPa) by a solid-state catalytic transformation from graphite in presence of a Fe-Ni melt. Additional support to the shock hypothesis is provided in a recent work by Nestola et al. (2020) on Almahata Sitta samples (AhS 72 and AhS 209 b), as well as on NWA 7983. In their study, graphite associated with nano- and (in NWA 7983) microdiamonds was reported, suggesting that the conversion from graphite to diamond was triggered by an impact event and was favored by the catalytic effect of Fe-Ni melts.

Yamato 74123 (Y-74123) ureilite is a meteorite that was found in Antarctic in 1974 by the Japanese expedition on the Yamato mountains. The first detailed study of Y-74123 dates back to 1978, when Hintenberger et al. (1978) measured its noble gas contents as well as several major and minor element bulk rock abundances. Takeda et al. (1980) have reported the petrological description and a chemical characterization of pyroxenes, which revealed Fe-bearing augite compositions ($En_{75}Fs_{18}Wo_7$). In addition, the magnetic properties of Y-74123 were studied by Nagata (1980). Moreover, Grady et al. (1985) carried out a C-isotopic study on Y-74123 reporting values of about $\delta^{13}C_{PDB} = -1.7$, well inside the range of ureilites. However, the carbon phases of Y-74123 have not been extensively studied yet.

In this work, we present the results of a multi-methodological study carried out on diamond and graphite aggregates observed in Yamato 74123 to understand the carbon phases formation in ureilites. In addition, a comparison with similar carbon phases in other meteorites, based on a literature survey and a discussion on their possible formation hypothesis, are also presented.

## METHODS

The fragment of Y-74123 (NHMV-#7636_A) and a corresponding polished thin section (NHMV-L9822) investigated in this study were kindly provided by the Natural History Museum Vienna (Austria). The thin section was investigated by optical and electron microscopy at the Department of Earth and Environmental Sciences, University of Pavia (Italy). Scanning electron microscopy (SEM) of the uncoated fragment of Y-74123 was performed using a FEI Quanta 200 SEM equipped with an energy-dispersive X-ray spectrometry (EDS) in low-vacuum mode at the Centro di Analisi e Servizi per la Certificazione (CEASC) of the University of Padova (Italy). Backscattered electron (BSE) images of Y-74123 were

obtained in low-vacuum mode analytical conditions, at the working distance of 10.6 mm, with an emission current of 93 mA, and a voltage of 20 kV, with the aim to identify the graphite beds in which diamonds were probably located. The BSE images collected by SEM were merged and analyzed with ImageJ and MultiSpec software to estimate the relative percentages of each phase of interest observed on the surface of the investigated meteorite fragment.

Carbon phases were manually extracted from the fragment and mounted on the tip of a 100 μm diameter glass fiber (Fig. 1) and investigated using micro-Raman spectroscopy (MRS) followed by X-ray diffraction (XRD).

Micro-Raman spectroscopy analyses were performed on the graphite material occurring in the extracted carbon-bearing subsample of Figure 1 to estimate the recorded temperature using the geothermometer of Cody et al. (2008), modified by Ross et al. (2011). The analysis of Y-74123 graphite was performed by high-resolution MRS using a Horiba LabRam HR Evolution spectrometer equipped with an Olympus BX41 confocal microscope at the controlled temperature of 20 (±1) °C at the Department of Earth and Environmental Sciences of the University of Pavia. A 532 nm laser excitation with an operating power of 1–2 mW (to prevent damage to the graphite), a grating of 600 g/mm, and a magnification of 50× were used. The spectrometer was calibrated using the silicon Raman peak at 520.5 cm$^{-1}$. The spectral resolution was 2 cm$^{-1}$ and the acquisition time for each spectrum was 30 s with four accumulations. Curve fitting of the spectra was carried out using the OMNIC software for dispersive Raman (Thermo-Fisher Scientific) adopting Gaussian + Lorentzian curves to obtain the best fit. XRD analyses were then performed on the same carbon-bearing subsample (Fig. 1) using a Rigaku-Oxford Diffraction Supernova κ-geometry goniometer with an X-ray Mo microsource equipped with a Pilatus 200 K Dectris detector in transmission mode, controlled by the CrysAlis-Pro software at the Department of Earth and Environmental Sciences in University of Pavia. Line profile analysis fitting of the obtained diffraction pattern was performed using the High Score Plus Software package (Panalytical) to estimate the crystallite size.

## RESULTS

### Petrographic description and observation by scanning electron microscopy

The investigated polished thin section of Y-74123 consists of aggregates of subhedral to anhedral olivine mineral grains, with varying amounts of interstitial pyroxenes and Si-Al-rich glass. The sample contains coarse-grained olivine and minor pigeonite crystals, ranging from 0.1 to 1.5 mm in size, surrounded by a large amount of opaque material (Fig. 2), composed of carbon mixed with different sulfides and metal phases. Pores and small grains of metal and sulfide (≤100 μm in size) commonly occur in the interstitial space between pyroxene and olivine grains.
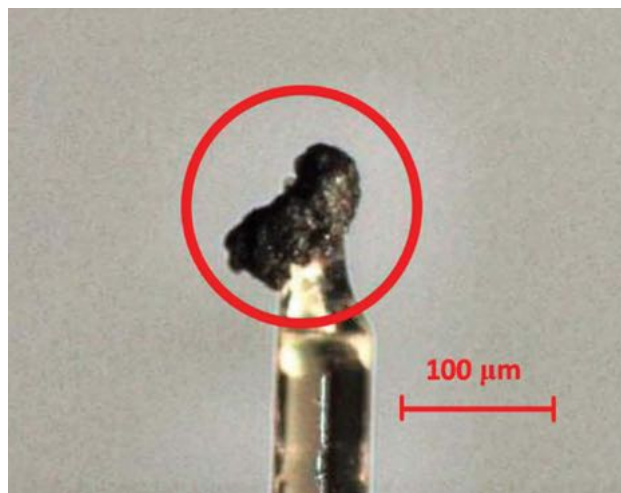


**FIGURE 1.** Carbon-bearing subsample of Y-74123 attached at the top of a glass fiber. Micro-Raman spectroscopy and XRD analyses were performed on this subsample. (Color online.)
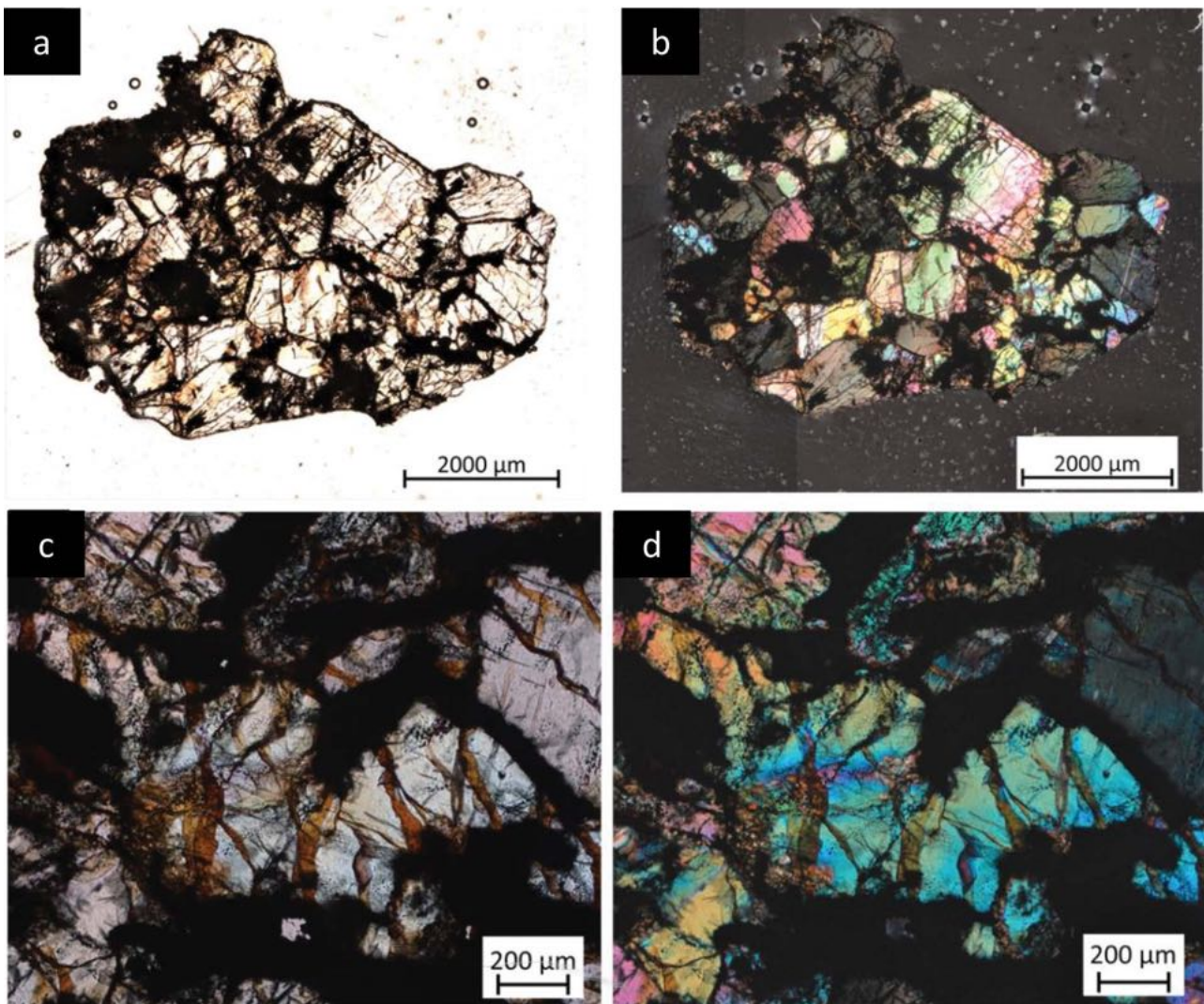
**Figure 2.** Yamato 74123 polished thin section (NHMV-L9822) overview in plane-polarized light (**a**) and between crossed polarizers (**b**); detailed structure of olivine grains in Y-74123 in plane-polarized light (**c**); and between crossed polarizers (**d**) are also presented. Note the presence of interstitial opaque material and the size of olivine grains, which dominate the thin section. (Color online.)

The shock level of Y-74123 was determined using optical microscope observations on shock microstructures in olivine crystals in transmitted light and following the criteria of Stöffler et al. (1991, 2018) and Nakamuta et al. (2016). Olivine crystals show undulate extinction, planar fractures, and, locally, mosaicism. The concurrent observation of undulate extinction and mosaicism in olivine indicates pressure in the range of 15–20 GPa, corresponding to shock level S4 (Stöffler et al. 2018). In addition, both silicates, i.e., olivine and clinopyroxene, show darkening caused by the dispersion of Fe-Ni metal and sulfides within the grains, which is commonly associated with shock metamorphism (e.g., Rubin 2006). In the investigated sample, even after a careful inspection by optical and electron microscopy, high-pressure polymorphs of olivine, such as wadsleyite or ringwoodite, were not found.

A fragment of Y-74123, about 8 × 5 × 5 mm in size, was analyzed by SEM. Figure 3a shows a BSE image of a typical carbon aggregate, which occurs as an interstitial phase in silicates. The size of the carbon phases in Y-74123 is evident in Figure 3b, where carbon phases are about 10 μm wide.

In Figure 3a, it is possible to see that locally, metal phases, indicated as "Fe-Ni metal," occur next to silicates. These metal phases are extremely fine-grained, partly mixed with the carbon phases.

The relative abundances, expressed in percentages, of the main mineralogical components present on the surface of the investigated sample of Y-74123 are 91% of silicate phases (olivine and pyroxene), 7% of carbon phases, and 2% of Fe-Ni metal and alloys, respectively (Fig. 4). The image analysis performed on the surface of the fragment of Y-74123 was important to find the best carbon aggregate zone from which to extract the carbon-bearing aggregate to be analyzed by MRS and XRD. The investigated fragment of Y-74123 turned out to be relatively easy to be cut and polished in comparison with many other studied ureilites, indicating a relatively low amount of diamonds.

### X-ray diffraction

The reconstructed XRD image of the carbon-bearing aggregate of Yamato 74123 and its powder diffraction pattern are shown in Figures 5a and 5b. Instead, Figure 5c clearly shows the presence of spots referred to micrometer-sized diamond.

In particular, Figure 5a shows both rings and spots at $d$-spacing characteristic of cubic diamond ($d$-spacing at 2.06, 1.26, and 1.07 Å) and hexagonal graphite (highest peak at $d$-spacing at 3.34 Å, while the peaks at $d$-spacing 2.03 and 1.15 Å are overlapped by the diamond peaks). In Figure 5b, the highest peak of diamond (at $d$-spacing 2.06 Å) shows a slight asymmetry. This asymmetry could be ascribed, at higher $d$-spacing ($d \approx 2.18$ Å), to the presence of cubic and hexagonal sp$^3$ stacked layers or nanotwins (Murri et al. 2019) and, at lower $d$-spacing ($d \approx 2.02$ Å), to the main peak of Fe metal (which also shows peaks at $d$-spacing 1.42 and 1.17 Å). In addition to diamond, graphite, and Fe metal, a few other peaks can be assigned to troilite ($d$-spacing at 2.99, 2.66, 1.72, and 1.68 Å), and also to minor silicate matrix components. The presence of cubic Ni, common in ureilites, cannot be excluded, as its peaks overlap those of metallic Fe and troilite.

To estimate the crystallite size of the carbon phases, we applied line profile analysis fitting to the diffraction pattern reported in Figure 5b. The integral breadth values, which were obtained by this method, were then inserted into the Scherrer equation (Eqs. 1 and 2; Scherrer 1918) to estimate the crystallite size, as follows:

$$\beta(2\theta) = \frac{K_\beta \times \lambda}{\langle D \rangle_V \cos\theta_{hkl}} \quad (1)$$

$$\frac{D_V}{K_\beta} = \frac{\lambda}{\cos\theta_{hkl} \times \beta(2\theta)} \quad (2)$$

The Scherrer equation provides a correlation between peaks broadening β, the dimension of diffracted domain, and the crys-

tallite size ($D_V$). K is a constant value ranging between 0.5 and 1, describing the contribution of crystallites shape and dependent upon the relative orientation of the scattering vector with respect to the external shape of the crystallite (Scherrer 1918).

For diamond, to obtain a reliable estimate of the crystallite size, we only used the two peaks at $d$-spacing 1.26 and 1.07 Å, as they do not exhibit any overlap with peaks of other phases within the analyzed carbon fragment. A similar approach was
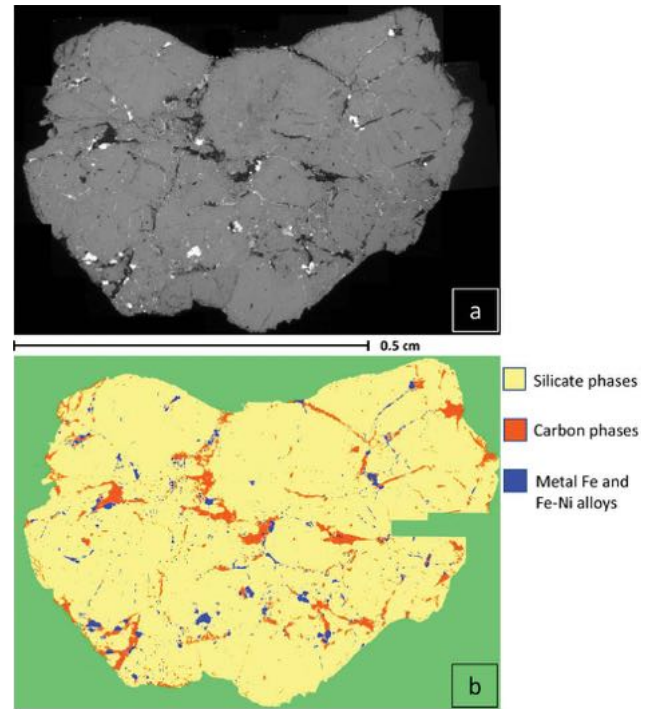


**FIGURE 4. (a)** BSE mosaic of the Yamato 74123 fragment (NHMV-7636_A) showing the typical texture of the meteorite. **(b)** Image analysis applied to **a** with the percentage referred to silicate phases, carbon phases, Fe-Ni metal, Fe-Ni alloys, and Fe-oxides. (Color online.)
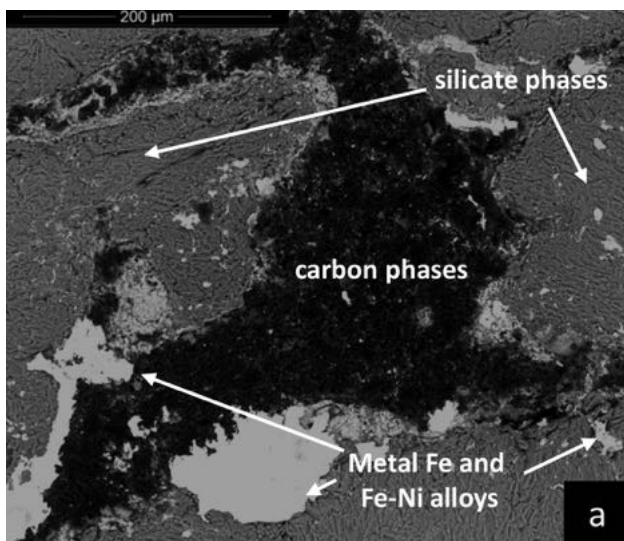


**FIGURE 3. (a)** BSE image of a carbon aggregate from which the investigated carbon-bearing subsample was extracted. Also note the presence of silicate phases and Fe-Ni metal and alloys (metal + troilite + oxide). **(b)** Detail of **a** in secondary electron (SE). As visible on this image, the aggregates in the carbon phases beds are not larger than 10 μm in size.

**FIGURE 5.** X-ray diffraction images of the carbon-bearing subsample from Y-74123. (**a**) Reconstructed powder diffraction image and (**b**) X-ray diffraction pattern of the investigated sample, analyzed by micro-X-ray powder diffraction are shown. The most abundant phases found in the carbon-bearing aggregate are diamond (Dia), graphite (Gr), Fe metal (Fe), and troilite (Tro). (**c**) A diffraction image shows the spots corresponding to micrometer-sized diamonds.

**TABLE 1.** The unit-cell parameters for the micrometer-sized cubic diamond single crystal found in Y-74123

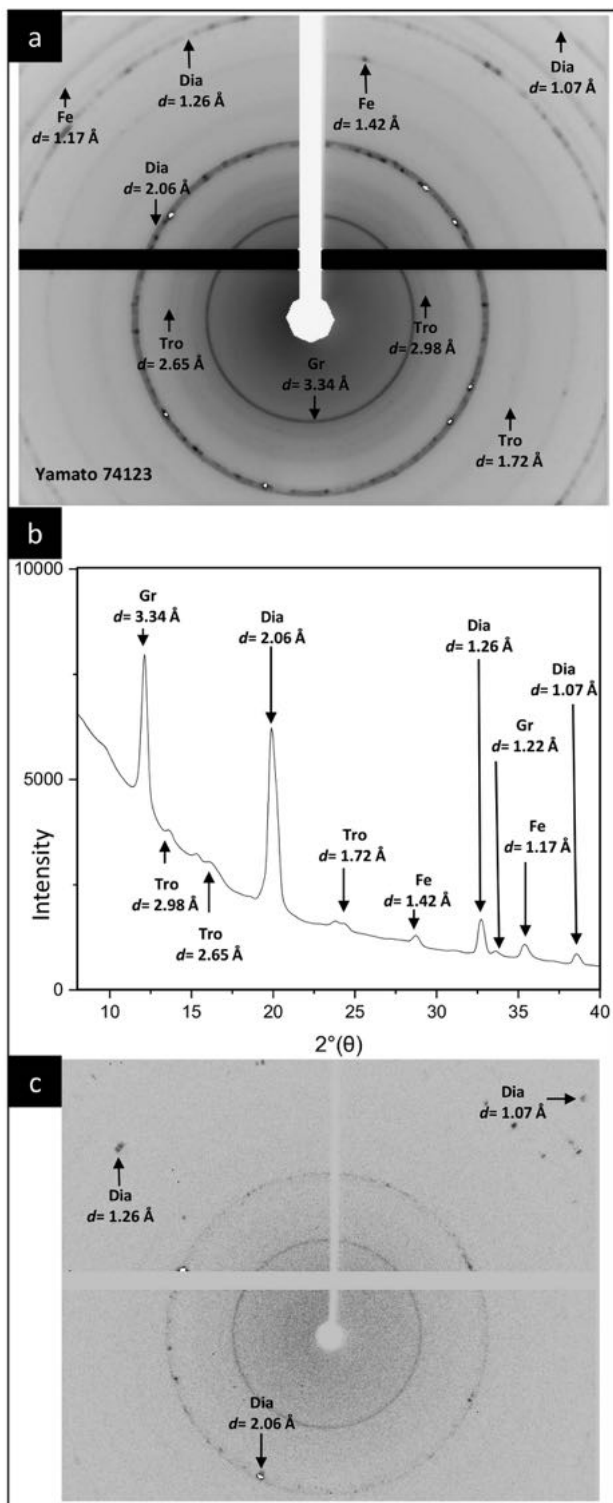| Single-crystal micrometer-sized cubic diamond (space group $Fd\overline{3}m$) | | |
|---|---|---|
| | $a = 3.569(1)$ Å | |
| | $V = 45.46(2)$ Å$^3$ | |
| **Polycrystalline diamond** | | |
| Pos. (2θ°) | $d$-spacing (Å) | $D_V$ (nm) |
| 32.65 | 1.26 | 15 |
| 38.50 | 1.07 | 11 |
| **Polycrystalline graphite** | | |
| Pos. (2θ°) | $d$-spacing (Å) | $D_V$ (nm) |
| 12.10 | 3.34 | 8 |

*Notes*: Mo λ ≈ 0.71. 2θ° positions of the graphite and diamond diffraction peaks, $d$-spacings, and the crystallite size ($D_V$) are reported. The crystallite size was calculated using the most intense peak of graphite at 3.34 Å, and the two peaks of diamond at 1.26 and 1.07 Å.

**TABLE 2.** Center positions for G, D, and D′ bands and FWHM (both in cm$^{-1}$) of Y-74123

| G-band center | G-band FWHM | G-band FWHM corrected | D-band center | D-band FWHM | D′-band center | D′-band FWHM | $T_{max}$ (°C) |
|---|---|---|---|---|---|---|---|
| | | | **Y-74123** | | | | |
| 1582 | 24 | 15 | 1356 | 49 | 1618 | 21 | 1286 |
| 1580 | 22 | 13 | 1354 | 46 | 1618 | 19 | 1310 |
| 1579 | 21 | 13 | 1349 | 37 | 1611 | 22 | 1329 |
| 1579 | 18 | 11 | 1356 | 22 | 1618 | 17 | 1365 |
| 1579 | 20 | 12 | 1351 | 40 | 1616 | 23 | 1334 |
| 1581 | 25 | 16 | 1350 | 50 | 1617 | 22 | 1265 |

*Notes*: Calculated crystallization temperature, $T_{max}$, is reported in the last column and was obtained using the Equation 3. The uncertainty on $T_{max}$ is (2σ) ±120 °C.

used to estimate the crystallite size of graphite, using the peak at $d$-spacing 3.34 Å (see Table 1). The results are reported in Table 1, along with the unit-cell parameters and the space group for the diamond single crystal found in Y-74123. The possibility to estimate the unit-cell parameters for the investigated diamond in Y-74123 implies that micrometer-sized diamonds (i.e., spots in the diffraction image) are present. As it appears from the XRD images (Figs. 5a and 5c), i.e., on the basis of the presence of spots and rings, we can state that nanographite coexists with micro- and nanodiamonds in Y-74123, as also observed by Goodrich et al. (2020) and Nestola et al. (2020) in the NWA 7983 ureilite.

**Micro-Raman spectroscopy**

We applied the geothermometric approach by Cody et al. (2008) and Ross et al. (2011), following the same procedure as reported in Barbaro et al. (2020a, 2020b) for Almahata Sitta samples (AhS 209 b, AhS 72, and AhS A135A), to determine the $T_{max}$ recorded by graphite. The temperature was estimated using Equation 3, expressed in terms of Raman G-band full-width at half maximum (FWHM) ($\Gamma_G$):

$$T_{max}(°C) = 1594.4 - 20.4\Gamma_G - 5.8 \times 10^{-2}\Gamma_G^2 \qquad (3)$$

In Table 2, we list the graphite peaks positions (G, D, and D′ band), the relevant $\Gamma_G$ values (G, D, and D′ bands FWHM) for Y-74123, as well as the $T_{max}$ estimated using Equation 3.

To compare our $\Gamma_G$ data with those published by Ross et al. (2011) and Barbaro et al. (2020b), we corrected our data for the instrumental peak broadening using a high-quality gem-quality lithospheric diamond (with $\Gamma_G = 5$ cm$^{-1}$), following the same procedure as in Ross et al. (2011) (see Table 2). In Table 2, for each set of acquisitions, the values of $\Gamma_G$ used in Equation 3 to obtain the $T_{max}$, are reported. $T_{max}$ values range between 1265 and

**TABLE 3.** Comparison among the $T_{max}$ recorded by graphite in different ureilites using the geothermometer by Cody et al. (2008)[a]

| | AhS 7 (Ross et al. 2011) | AhS 209 (Barbaro et al. 2020b) | AhS 72 (Barbaro et al. 2020b) | AhS (Barbaro et al. 2020b) | A135AY-74123 (This work) |
|---|---|---|---|---|---|
| Average $T_{max}$ (°C) | 990 ± 120 | 1266 ± 120 | 1242 ± 120 | 1332 ± 120 | 1314 ± 120 |

[a] See Cody et al. (2008) and Ross et al. (2011) for a detailed description of the applied geothermometry. The temperature values recorded by graphite in AhS 7 sample are after Ross et al. (2011) and those recorded for AhS 209, AhS 72, and AhS A135A are from Barbaro et al. (2020b).

1334 (±120) °C. These temperatures are slightly higher than those obtained by Ross et al. (2011) on graphite in AhS #7 ureilitic fragment ($T_{max}$ of 990 ± 120 °C), whereas they are very similar to those obtained by Barbaro et al. (2020b) on other Almahata Sitta samples (average $T_{max}$ of 1266 °C for graphite in AhS 209 b, 1242 °C in AhS 72, and 1332 °C in AhS A135A). A comparison between the average temperatures recorded by graphite on the above-quoted ureilitic samples is presented in Table 3.

## DISCUSSION

Micro-Raman spectroscopy and XRD analyses in Y-74123 revealed the presence of diamond and graphite aggregates in the interstitial space between silicate grains, as commonly observed in other ureilites (e.g., Hanneman et al. 1967; Vdovykin 1970). Our results from the XRD analysis on Y-74123 confirm the coexistence of nano- and microdiamonds associated with nanographite. In the carbon-bearing aggregates, we also detected Fe metal and troilite, which fill the interstitial space between graphite-diamond crystals or occur at the border of the carbon aggregates (Fig. 4).

The observed local differences in the size of the newly formed diamonds, i.e., nano- to micrometric, may result from heterogeneous shock distribution within a heterogeneous sample. The heterogeneous distribution of shock effects is mainly ascribed to shock impedance contrast between contiguous phases. For greater contrast, the shock impedance is amplified (Ogilvie et al. 2011), as in the case of large, "rigid," olivine crystals, separated by interstitial, relatively "soft," carbon-bearing matrix. This implies that the shock pressure locally experienced by the carbon phases might have been higher than that recorded by the adjacent olivine crystal, thus, explaining the local occurrence of relatively coarse-grained diamonds. Conversely, for cases of low contrast between phases, the shock impedance would have been suppressed. Furthermore, we cannot exclude that Y-74123 suffered multiple impact events with different P-T conditions.

Our study provides further evidence in support of the diamond formation mechanism in ureilites proposed for NWA 7983 ureilite by Nestola et al. (2020). According to this mechanism, the formation of micrometer-sized diamond crystals from graphite observed in Y-74123 is likely due to the combined effect of highly heterogeneous P-T-conditions due to shock wave propagation and immediate penetration of Fe-Ni melt into carbon aggregates, whereas the formation of nanodiamonds resulted from direct transformation from graphite (i.e., even without the catalytic Fe-Ni melt). The occurrence of Fe compounds, as observed in Y-74123, could explain the formation of diamonds at pressures ≥15–20 GPa (Nestola et al. 2020), which is lower than the pressure of 30–60 GPa estimated for diamonds formed in impact cratering processes on Earth (see, e.g., Koeberl et al. 1997 and references therein). In Nestola et al. (2020) it is clearly reported how the catalyzed formation of diamonds by metallic melts

during a shock event can also account for the simultaneous formation of micro- and nanodiamonds in ureilites. These authors, with the aim to explain this process, reported an example of a pulsed heating experiment performed on a graphite-metal charge in a static high-pressure apparatus (Varfolomeeva 1971). This apparatus simulates natural impact processes (De Carli et al. 2002; Bundy and Kasper 1967), which produced diamonds up to 10 μm in size, found near to the catalyst, and nanodiamonds occurring in other parts of the experimental charge (Nestola et al. 2020 and references therein).

The proposed scenario is further supported by the average value of the temperatures determined for Y-74123 graphite [$T_{max}$ = 1314 °C (±120 °C)], which is similar to the values reported by Barbaro et al. (2020a, 2020b) for Almahata Sitta samples (e.g., AhS 209 b, AhS 72, and AhS A135A), even though slightly higher than the values reported by Ross et al. (2011) for the AhS #7 sample. As reported by Gillet and El Goresy (2013), the shock peak temperature determination for a sample with a different mineral composition should also account for the effect of the porosity, grain boundaries, and heterogeneous composition of the rock. In addition, it is important to consider that the shock waves do not propagate at the same speed in all different minerals of a polymineralic rock, as explained above. However, even if it is difficult to estimate the exact peak shock pressure values of the impact event(s), we can argue that the temperature recorded by graphite may correspond to the shock-induced temperature or to a subsequent post-shock thermal event, as hypothesized by Gillet and El Goresy (2013). We exclude the possibility that our estimated temperature values could be a pre-shock temperature because our estimation is determined on newly crystallized nanographite. Such nanographite cannot be the pristine graphite of the UPB, which should have been micrometer-sized, due to the long residence time spent in the UPB deep interior. Therefore, as reported by Barbaro et al. (2020b) for three AhS ureilitic fragments, the nanographite formed by shock.

## IMPLICATIONS

Our study on carbon phases in Yamato 74123 provides hints on the shock history of this specific meteorite, and generally, of the UPB. The XRD analysis carried out on Y-74123 showed that nanodiamonds coexist together with microdiamonds and nanographite, in agreement with observations by Nestola et al. (2020) on the NWA 7983 ureilite meteorite. In addition, by means of MRS analyses of graphite, we were able to show that: (1) the investigated sample exhibits homogeneous values of G-band centers (between 1579 and 1582 cm⁻¹) and D-band centers (between 1349 and 1356 cm⁻¹), and that (2) the $\Gamma_G$ of graphite for the G-band range between 11 and 16 cm⁻¹. These values were used to estimate an average $T_{max}$ of 1314 °C (±120 °C).

Our results support that micrometer-sized diamonds in Y-74123, as also suggested by Nestola et al. (2020) for

NWA 7983, formed with the assistance of the catalytic effect of metallic melts without requiring static high-pressures conditions within a large Mars-sized parent body. The formation of micro- and nanodiamonds and nanographite is likely to be the result of an impact event or multiple impact events. We assume that the temperature recorded by graphite, close to 1200–1300 °C, likely represents the shock-induced temperature excursion or corresponds to a subsequent post-shock temperature. The temperature values obtained in our sample Y-74123, together with further studies on ureilites, using the same approach as presented here, will contribute to widening our knowledge of the graphite resetting temperatures by shock.

In conclusion, the results from our combined SEM, XRD, and MRS study in Y-74123 suggest that one or multiple shock event(s), with the contribution of metallic melts catalysis, is likely responsible for the formation of diamond, both nano- and microdiamonds. Moreover, heterogeneity in the peak shock pressure that affected the UPB during the impact event(s) may also explain the coexistence of diamonds with notable different sizes.

## REFERENCES CITED

Barbaro, A., Domeneghetti, M.C., Goodrich, C.A., Meneghetti, M., Litti, L., Fioretti, A.M., Shaddad, M.H., Alvaro, M., and Nestola, F. (2020a) Shock temperature recorded by graphite in ureilites from Almahata Sitta. 51st Lunar and Planetary Science Conference, abstract 1480.

Barbaro, A., Domeneghetti, M., Goodrich, C., Meneghetti, M., Litti, L., Fioretti, A., Jenniskens, P., Shaddad, M., and Nestola, F. (2020b) Graphite based geothermometry on Almahata Sitta ureilites meteorites. Minerals, 10, 1005.

Berkley, J.L., Taylor, G.J., Keil, K., Harlow, G.E., and Prinz, M. (1980) The nature and origin of ureilites. Geochimica et Cosmochimica Acta, 44, 1579–1597.

Berkley, J.L., Brown, I.V., H.G., Keil, K., Carter, N.L., Mercier, J.-C.C., and Huss, G. (1976) The Kenna ureilite: an ultramafic rock with evidence for igneous, metamorphic, and shock origin. Geochimica et Cosmochimica Acta, 40, 1429–1437.

Bischoff, A., Goodrich, C.A., and Grund, T. (1999) Shock-induced origin of diamond in ureilites. 30th Annual Lunar and Planetary Science Conference, March 15–29, 1999, Houston, Texas, abstract 1100.

Boynton, W.V., Starzyk, P.M., and Schmitt, R.A. (1976) Chemical evidence for the genesis of the ureilites, the achondrite Chassigny and the nakhlites. Geochimica et Cosmochimica Acta, 40, 1439–1447.

Bundy, F.P., and Kasper, J.S. (1967) Hexagonal diamond—A new form of carbon. The Journal of Chemical Physics, 46, 3437–3446.

Cloutis, E.A., Hudon, P., Romanek, C.S., Bishop, J.L., Reddy, V., Gaffey, M.J., and Hardersen, P.S. (2010) Spectral reflectance properties of ureilites. Meteoritics & Planetary Science, 45, 1668–1611.

Cody, G.D., Alexander, C.M.O., Yabuta, H., Kilcoyne, A.L.D., Araki, T., Ade, H., Dera, P., Fogel, M., Militzer, B., and Mysen, B.O. (2008) Organic thermometry for chondritic parent bodies. Earth and Planetary Science Letters, 272, 446–455.

De Carli, P.S. (1995) Shock wave synthesis of diamond and other phases. Materials Research and Society Symposium Proceedings, 383, 21–31.

De Carli, P.S., Bowden, E., Jones, A.P., and Price, G.D. (2002) Laboratory impact experiments versus natural impact events. In Ch. Koeberl and K.G. MacLeod, Eds., Catastrophic Events and Mass Extinctions: Impacts and Beyond, Geological Society of America Special Paper 356, 595–605. Lunar and Planetary Institute.

Fukunaga, K., Matsuda, J., Nagao, K., Miyamoto, M., and Ito, K. (1987) Noble-gas enrichment in vapour-growth diamonds and the origin of diamond in ureilites. Nature, 328, 141–143.

Gillet, P., and El Goresy, A. (2013) Shock events in the Solar System: The message from minerals in terrestrial planets and asteroids. Annual Review of Earth and Planetary Sciences, 41, 257–285.

Goodrich, C.A. (1992) Ureilites: A critical review. Meteoritics, 27, 327–352.

Goodrich, C.A., Jones, J.H., and Berkley, J.L. (1987) Origin and evolution of the ureilite parent magmas: Multi-stage igneous activity on a large parent body. Geochimica et Cosmochimica Acta, 51, 2255–2273.

Goodrich, C.A., Hartmann, W.K., O'Brien, D.P., Weidenschilling, S.J., Wilson, L., Michel, P., and Jutzi, M. (2015) Origin and history of ureilitic material in the solar system: The view from asteroid 2008 TC$_3$ and the Almahata Sitta meteorite. Meteoritics & Planetary Science, 50, 782–809.

Goodrich, C.A., Nestola, F., Jakubek, R., Erickson, T., Fries, M., Fioretti, A.M., Ross, D.K., and Brenker, F.E. (2020) The origin of diamond in ureilites. 51st Lunar and Planetary Science Conference, abstract 1411.

Grady, M.M., Wright, I.P., Swart, P.K., and Pillinger, C.T. (1985) The carbon and nitrogen isotopic composition of ureilites: Implications for their genesis. Geochimica et Cosmochimica Acta, 49, 903–915.

Grund, T., and Bischoff, A. (1999) Cathodoluminescence properties of diamonds in ureilites: further evidences for a shock-induced origin. 62nd Annual Meteoritical Society Meeting, abstract 5074.

Hanneman, R.E., Strong, H.M., and Bundy, F.P. (1967) Hexagonal diamonds in meteorites: Implications. Science, 155, 995–997.

Hezel, D.C., Dubrovinsky, L., Nasdala, L., Cauzid, J., Simionovici, A., Gellissen, M., and Schonbeck, T. (2008) In situ micro-Raman and X-ray diffraction study of diamonds and petrology of the new ureilite UAE 001 from the United Arab Emirates. Meteoritics & Planetary Science, 43, 1127–1136.

Hintenberger, H., Jochum, K.P., Braun, O., Christ, P., and Martin, W. (1978) The Antarctic meteorite Yamato 74123—A new ureilite. Earth and Planetary Science Letters, 40, 187–193.

Hough, R.M., Gilmour, I., Pillinger, C.T., Arden, J.W., Gilkess, K.W.R., Yuan, J., and Milledge, H.J. (1995) Diamond and silicon carbide in impact melt rock from the Ries impact crater. Nature, 378, 41–44.

Koeberl, C., Masaitis, V.L., Shafranovsky, G.I., Gilmour, I., Langenhorst, F., and Schrauder, M. (1997) Diamonds from the Popigai impact structure, Russia. Geology, 25, 967–970.

Le Guillou, C., Rouzaud, J.N., Remusat, L., Jambon, A., and Bourot-Denise, M. (2010) Structures, origin and evolution of various carbon phases in the ureilite Northwest Africa 4742 compared with laboratory-shocked graphite. Geochimica et Cosmochimica Acta, 74, 4167–4185.

Lipschutz, M.E. (1964) Origin of Diamonds in the Ureilites. Science, 143, 1431–1434.

Lorenz, C.A., Shiryaev, A.A., Vlasov, I.I., and Borisovsky, S.E. (2019) Metamorphism of four desert ureilites and luminescence spectroscopy of defects in ureilitic diamonds. Meteoritics & Planetary Science, 54, 1197–1214.

Masaitis, V.L. (1998) Popigai crater: Origin and distribution of diamond-bearing impactites. Meteoritics & Planetary Science, 33, 349–359.

Meteoritical Bulletin Database (2020) Available: https://www.lpi.usra.edu/meteor/.

Miyahara, M., Ohtani, E., El Goresy, A., Lin, Y., Feng, L., Zhang, J.-C., Gillet, P., Nagase, T., Muto, J., and Nishijima, M. (2015) Unique large diamonds in a ureilite from Almahata Sitta 2008 TC 3 asteroid. Geochimica et Cosmochimica Acta, 163, 14–26.

Murri, M., Smith, R.L., McColl, K., Hart, M., Alvaro, M., Jones, A.P., Németh, P., Salzmann, C.G., Corà, F., Domeneghetti, M.C., and others (2019) Quantifying hexagonal stacking in diamond. Scientific Reports, 9, 10334.

Nabiei, F., Badro, J., Dennenwaldt, T., Oveisi, E., Cantoni, M., Hébert, C., Goresy, A., El, Barrat, J., and Gillet, P. (2018) A large planetary body inferred from diamond inclusions in a ureilite meteorite. Nature Communications, 9, 1327.

Nagata, T. (1980) Magnetic classification of Antarctic meteorites. Proceedings of the 21st Lunar and Planetary Science Conference, p. 1789–1799. Lunar and Planetary Science Institute, Houston, Texas.

Nakamuta, Y., and Aoki, Y. (2000) Mineralogical evidence for the origin of diamond in ureilites. Meteoritics & Planetary Science, 35, 487–493.

Nakamuta, Y., Kitajima, F., and Shimada, K. (2016) In situ observation, X-ray diffraction and Raman analyses of carbon minerals in ureilites: Origin and formation mechanisms of diamond in ureilites. Journal of Mineralogical and Petrological Sciences, 111, 252–269.

Németh, P., Garvie, L.A.J., Aoki, T., Dubrovinskaia, N., Dubrovinsky, L., and Buseck, P.R. (2014) Lonsdaleite is faulted and twinned cubic diamond and does not exist as a discrete material. Nature Communications, 5, 5447.

Németh, P., McColl, K., Smith, R.L., Murri, M., Garvie, L.A.J., Alvaro, M., Pécz, B., Jones, A.P., Corà, F., Salzmann, C.G., and McMillan, P.F. (2020a) Diamond-graphene composite nanostructures. Nano Letters, 20, 3611–3619.

Németh, P., McColl, K., Garvie, L.A.J., Salzmann, C.G., Murri, M., and McMillan, P.F. (2020b) Complex nanostructures in diamond. Nature Materials, 19, 1126 –1131.

Nestola, F., Goodrich, C.A., Morana, M., Barbaro, A., Jakubek, R.S., Chris, O., Brenker, F.E., Domeneghetti, M.C., Dalconi, M.C., Alvaro, M., and others (2020) Impact shock origin of diamond in ureilite meteorites. Proceedings of the National Academy of Sciences, 117, 25310–25318. https://doi.org/10.1073/

pnas.1919067117.

Ogilvie, P., Gibson, R.L., Reimold, W.U., Deutsch, A., and Hornemann, U. (2011) Experimental investigation of shock metamorphic effects in a metapelitic granulite: The importance of shock impedance contrast between components. Meteoritics & Planetary Science, 46, 1565–1586.

Ohfuji, H., Irifune, T., Litasov, K.D., Yamashita, T., Isobe, F., Afanasiev, V.P., and Pokhilenko, N.P. (2015) Natural occurrence of pure nano-polycrystalline diamond from impact crater. Scientific Reports, 5, 14702.

Ross, A.J., Steele, A., Fries, M.D., Kater, L., Downes, H., Jones, A.P., Smith, C.L., Jenniskens, P.M., Zolensky, M.E., and Shaddad, M.H. (2011) MicroRaman spectroscopy of diamond and graphite in Almahata Sitta and comparison with other ureilites. Meteoritics & Planetary Science, 46, 364–378.

Rubin, A. (2006) Shock, post-shock annealing, and post-annealing shock in ureilites. Meteoritics & Planetary Science, 41, 125–133.

Sabbah, H., Morrow, A.L., Jenniskens, P., Shaddad, M.H., and Zare, R.N. (2010) Polycyclic aromatic hydrocarbons in asteroid 2008 TC₃: Dispersion of organic compounds inside asteroids. Meteoritics & Planetary Science, 45, 1710–1717.

Salzmann, C.G., Murray, B.J., and Shephard, J.J. (2015) Extent of stacking disorder in diamond. Diamond and Related Materials, 59, 69–72.

Scherrer, P. (1918) Estimation of the size and internal structure of colloidal particles by means of röntgen. Journal of Mathematical Physics, 2, 98–100.

Scott, E.R.D., Keil, K., and Taylor, G.J. (1992) Origin of ureilites by partial melt-ing and explosive volcanism on carbon-rich asteroids. Proceedings of the 23rd Lunar and Planetary Science Conference, pp. 1253–1254.

Stöffler, D., Keil, K., and Edward, R.D.S. (1991) Shock metamorphism of ordinary chondrites. Geochimica et Cosmochimica Acta, 55, 3845–3867.

Stöffler, D., Hamann, C., and Metzler, K. (2018) Invited Review Shock meta-morphism of planetary silicate rocks and sediments: Proposal for an updated classification system. Meteoritics & Planetary Science, 49, 5–49.

Takeda, H., Mori, H., Keizo, Y., and Shiraishi, K. (1980) Mineralogical examination of the Allan Hills achondrites and their bearing on the parent bodies. Memoirs of National Institute of Polar Research. Special Issue, 17, 119–144.

Urey, H.C. (1956) Diamond, meteorites, and the origin of the solar system. The Astrophysical Journal, 124, 623–637.

Varfolomeeva, T.D. (1971) Synthesis and investigation of polycrystalline dia-mond. Ph.D. thesis, Institute for High Pressure Physics, USSR Academy of Sciences, 154.

Vdovykin, G. (1970) Ureilites. Space Science Reviews, 10, 483–510.

# Formation of fused aggregates under long-term microgravity conditions aboard the ISS with implications for early solar system particle aggregation

Tamara E. KOCH [iD]*[1], Dominik SPAHR[1], Beverley J. TKALCEC [iD][1], Oliver CHRIST[2],
Philomena-Theresa GENZEL[1], Miles LINDNER [iD][1], David MERGES[1], Fabian WILDE[3],
Björn WINKLER[1], and Frank E. BRENKER[1,4]

[1]Institute of Geosciences, Goethe University Frankfurt, Altenhoeferallee 1, 60438 Frankfurt am Main, Germany
[2]Department of Geoscience, University of Padua, Via Gradenigo 6, 35131 Padua, Italy
[3]Helmholtz-Zentrum Hereon, Max-Planck Strasse 1, 21502 Geesthacht, Germany
[4]Hawai'i Institute of Geophysics and Planetology, School of Ocean and Earth Science and Technology, University of Hawai'i
at Mānoa, 1680 East-West Road, Honolulu, Hawaii 96822, USA
*Corresponding author. E-mail: t.koch@em.uni-frankfurt.de

**Abstract**–In order to gain further insights into early solar system aggregation processes, we carried out an experiment on board the International Space Station, which allowed us to study the behavior of dust particles exposed to electric arc discharges under long-term microgravity. The experiment led to the formation of robust, elongated, fluffy aggregates, which were studied by scanning electron microscopy, electron backscatter diffraction, and synchrotron micro-computed tomography. The morphologies of these aggregates strongly resemble the typical shapes of fractal fluffy-type calcium-aluminum-rich inclusions (CAIs). We conclude that a small amount of melting could have supplied the required stability for such fractal structures to have survived transportation and aggregation to and compaction within planetesimals. Other aggregates produced in our experiment have a massy morphology and contain relict grains, likely resulting from the collision of grains with different degrees of melting, also observed in some natural CAIs. Some particles are surrounded by igneous rims, which remind in thickness and crystal orientation of Wark–Lovering rims; another aggregate shows similarities to disk-shaped CAIs. These results imply that a (flash-)heating event with subsequent aggregation could have been involved in the formation of different morphological CAI characteristics.

## INTRODUCTION

The aggregation of particles in the solar nebula is generally considered the first process leading to planet formation (Blum & Wurm, 2008; Dominik et al., 2006). Refractory inclusions such as calcium-aluminum-rich inclusions (CAIs) and amoeboid olivine aggregates (AOAs) are considered to be the oldest material of our solar system (Connelly et al., 2012; Krot et al., 2009) and likely witnesses of early aggregation processes. The chemical properties of CAIs and AOAs have been intensively studied in the past with regard to their condensation origin (e.g., Connelly et al., 2012; Han & Brearley, 2015; Krot et al., 2009; Krot, Petaev, Russell, et al., 2004; Krot, Petaev, & Yurimoto, 2004; Sugiura et al., 2009). Their structural characteristics, such as morphologies, texture, and porosity, bear further

knowledge about the processes regarding the circumstances of aggregation, reheating, annealing, recrystallization, compaction, as well as solar nebula dynamics and material transportation (Komatsu et al., 2001, 2009; Rubin, 2012; Sugiura et al., 2009).

With $^{207}$Pb-$^{206}$Pb ages of $4567.3 \pm 0.16$ Ma (Connelly et al., 2012), CAIs formed as the first solids of the solar system, close to the Sun and probably over a period of 0.3 Ma (Kita et al., 2013). The sojourn time of CAIs in their original condensation region was probably very short, about 2000 yr, until they were either drawn into the Sun or transported outward (Taillifet et al., 2014). Because several generations of CAIs have been recognized, CAI transportation to the outer regions of the disk, by a yet undefined process, must have been a frequent event (reviewed in Krot, 2019).

CAIs (especially in CV chondrites) are classified according to their mineralogy in types A, B, and C (Krot, 2019) and further characterized by morphology, texture, and microstructure. Type A CAIs occur either as spheroidal and compact CAIs (Compact Type A: CTA) that have experienced melting, or as irregularly shaped, nonmolten fluffy-type CAIs (Fluffy-type A: FTA). Type B CAIs are usually interpreted to have formed by melting and fractional crystallization (Blander & Fuchs, 1975).

Fluffy-type CAIs have very irregular, fractal structures, which resemble the structures formed from hit-and-stick collision experiments and modeling (e.g., Blum & Wurm, 2008; Blum et al., 2000). Aggregation of micrometer particles to millimeter-sized objects by surface adhesion at 1 AU was probably a fast process of 10–100 yr (Brauer et al., 2007; Charnoz & Taillifet, 2012). However, the question arises how these fragile, fractal structures could survive turbulences and transportation to the outer protoplanetary disk (PPD), chondrite aggregation, and subsequent compaction. One explanation is that FTA CAIs potentially aggregated parallel to their condensation (Russell & Howard, 2013). Another theory assumes FTA CAIs result from hit-and-stick collisions of CTA CAIs and minor melting (Rubin, 2012).

Some CAIs consist of several nodules covered in multimineral layers, the so-called Wark–Lovering rims (WLRs; e.g., Lorenz et al., 2019; MacPherson et al., 1982; Wark & Lovering, 1977). Different formation scenarios have been proposed, such as condensation (Bolser et al., 2016; MacPherson & Grossman, 1984; Wark & Lovering, 1977) or metasomatosis on the parent body (MacPherson et al., 1982). Other studies proposed that flash-heating, which melted the outer region of the PPD, could be involved in WLR formation (Han et al., 2020; Wark & Boynton, 2001). It is also unclear whether WLRs formed immediately after CAI formation or about 1 Ma after the formation of the latter, as isotopic studies give conflicting information, which, however, could also be due to later isotopic disturbances in the nebula (Han et al., 2020).

Some igneous Type B CAIs have a disk- or bowl-shaped morphology (Ivanova et al., 2008), which was interpreted to result from aerodynamical deformation and shock flattening (Lorenz et al., 2019), or more complex scenarios which include ejection from the inner solar system and remelting during reentry at hypersonic speed (Liffman et al., 2016). Further relations between the morphology of CAIs and aerodynamical effects have been proposed in the most recent study of Zhang et al. (2021) in which the studied CAIs and AOAs have an elongated or a bent fractal morphology, interpreted as resulting from movement induced by, for example, radial drift.

Experiments can help to understand early solar system processes, and different experimental approaches have been established. Microgravity experiments regarding particle aggregation in the solar nebula are well established and have already delivered valuable findings (e.g., Beitz et al., 2012; Blum, 2010; Blum et al., 2000, 2002; Steinpilz et al., 2020; Wurm & Blum, 1998). Experiments addressing the process of thermal annealing of early solar system materials, which are mostly focused on chondrule formation (Connolly & Libourel, 2005), have so far only been carried out on Earth and have mostly involved static samples.

To complement these different types of experiments, we developed a proof-of-concept experiment, which was carried out under long-term microgravity conditions aboard the International Space Station (ISS) to combine aggregation, heating, and thermal annealing of dust particles (Spahr et al., 2020). In this experiment, freely floating $Mg_2SiO_4$ dust particles were exposed to arc discharges inside a glass sample chamber with the aim to test how arc discharges influence the behavior of dust particles. A camera allowed the observation of the particles in real time and the sample material was analyzed after sample return to Earth. In the study presented here, we show the formation of aggregates using flash-heating under microgravity conditions, which can be linked to the formation of refractory inclusions with regard to their morphology and microstructure.

## METHODS AND MATERIALS

### ISS Experiments

The experimental setup is described in detail in Spahr et al. (2020). The experiment was set up inside a $10 \times 10 \times 15$ cm$^3$ sized NanoRacks NanoLab, which was connected to the ISS by USB. The sample chamber consisted of quartz glass and two tungsten electrodes with a diameter of 1 mm were fused into the glass on opposite sides. The distance between the tips of the electrodes was approximately 2 mm. The sample chamber was loaded with 30 mg of the sample material and $100 \pm 1$ mbar Ar gas.

A detailed description of the generation and calibration of the arc discharges is given in Spahr et al. (2020). In total, 81 arc discharges with energies of 5–8 J and durations between 300 and 500 μs per discharge were induced, which exceed the energy necessary for a complete melting of the dust particles (Spahr, personal communication). The generation of the arc discharges also applied an electric field between the electrodes beginning approximately 2 min before the arc discharges. The area between the electrodes was filmed during the charging process and the arc discharges with
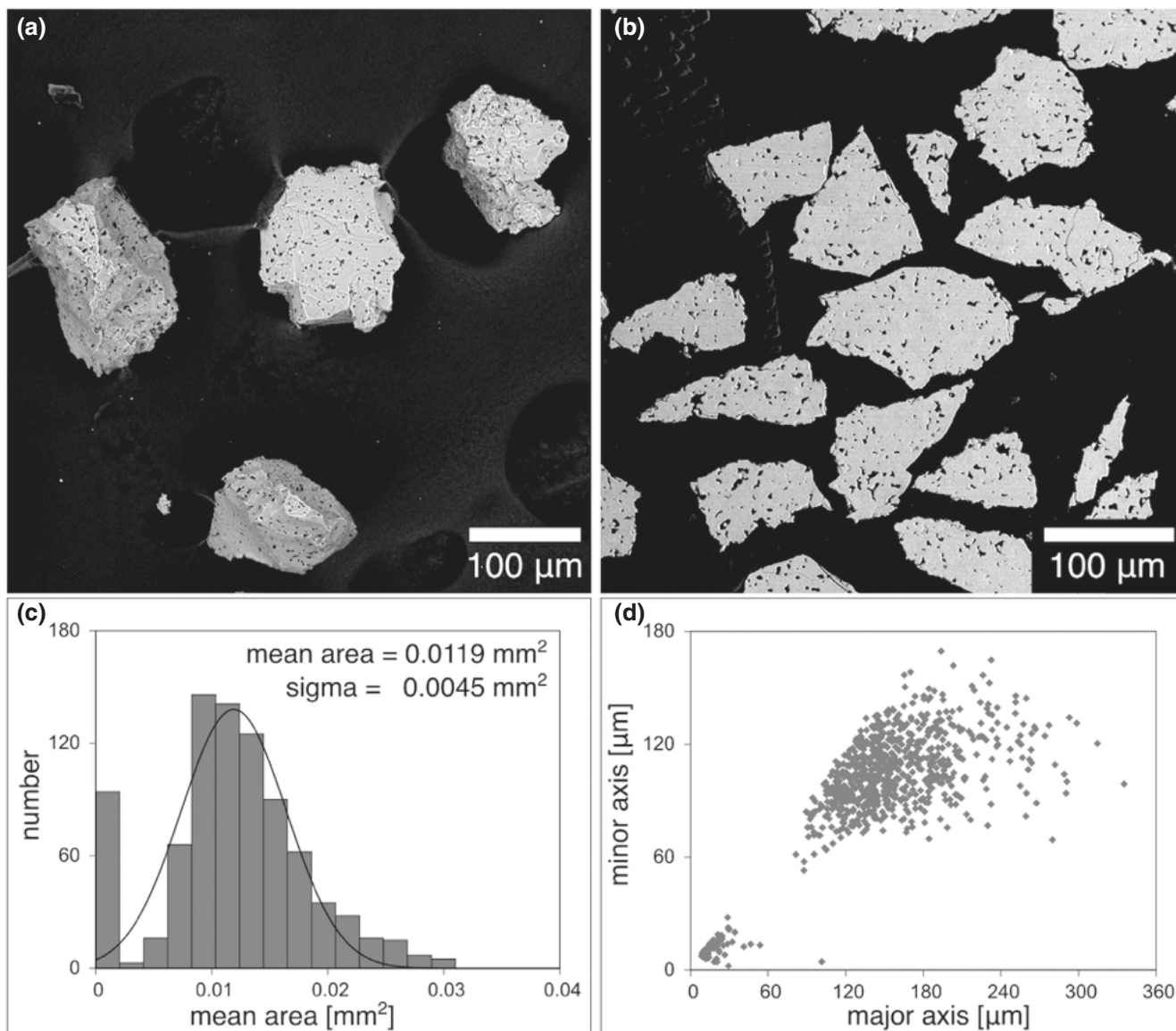
Fig. 1. Initial sample material. a) Focus-stacked representative porous initial dust particles used as starting material. b) Polished grains of the initial starting material. The particles have highly heterogeneous morphologies and a large amount of evenly distributed small pores. c) Histogram of the grain size distribution of a random sample containing 849 grains fitted with a normal distribution function. d) Correlation between the minor and major axes of best-fit ellipses of the initial material.

a Raspberry Pi V2 camera with a field of view (FOV) of 2.73 × 3.63 mm.

### Sample Material

The initial sample material consisted of well-characterized synthetic forsterite particles (Spahr et al., 2020). Figure 1a shows a focus-stacked scanning electron microscopy (SEM) backscatter electron (BSE) image of three representative initial particles. Figure 1b shows several embedded and polished initial grains. Characteristics for the polished samples are numerous

evenly distributed small pores. The grains are irregularly shaped with rough surfaces. Electron backscatter diffraction (EBSD) analysis of the initial particles showed that the particles are fine-grained, consisting of crystals with (circular equivalent) diameters of 5–10 μm, with a few exceptions where larger crystals >20 μm are present (Koch, Spahr, Tkalcec, et al., 2021). In the initial sample material, the crystals are randomly oriented within each grain.

The grain size analysis of the initial sample material was carried out using ImageJ (Rueden et al., 2017). Therefore, the grains were evenly distributed in a petri dish and photographed under an optical microscope.

The photographs were transformed into black and white images, where the particles are displayed as black areas with the shape of the particles. This type of image will be called a threshold image in the following text.

Figure 1c shows a histogram of the areas of a random sampling of 849 grains fitted with a normal distribution function. The mean area obtained from the fit is 0.012 mm$^2$ and, due to the heterogeneity of the particle shapes, the distribution is rather broad ($\sigma = 0.0045$ mm$^2$). Figure 1d shows the correlation of the major to the minor ellipse axes, likewise indicating the variability of the particle morphologies. The grain size analysis of the transformed samples was undertaken with the same method.

The sample chamber was loaded with 30 mg of the sample material. Approximating the average volume of a single grain by a spherule with a diameter of 126 μm and a porosity of 10 vol%; the total number of particles is in the range of 10$^4$ particles, which represents a particle density of approximately $1.6 \times 10^{-3}$ g cm$^{-3}$.

## Analytical Procedure and Sample Preparation

Scanning electron microscopy imaging was performed using a Phenom World ProX desktop SEM equipped with an electron backscatter detector at the Geoscience Institute at Goethe University. Energy-dispersive X-ray spectroscopy (EDX) was carried out with an integrated silicon drift detector (SDD) for a semi-quantitative characterization of the chemical composition. The noncoated samples were measured under low vacuum conditions; the polished and carbon-coated samples were measured under high vacuum conditions. For imaging, we used an acceleration voltage of 10 kV while for EDX analysis, a voltage of 15 kV was employed. Multiple BSE images were acquired with different focal planes and combined afterward with the Helicon Focus 7 Pro (Kozub et al., 2018) software from Helicon. EDX data were analyzed using the Phenom Pro Suite software.

EBSD fabric analysis is especially suited to identify structural and textural properties of materials and is increasingly employed as an analytic tool to investigate the remnants of solar nebular processes in planetary materials (Bland et al., 2011; Tkalcec et al., 2013). EBSD was performed at the Geoscience Institute at Goethe University Frankfurt with a JEOL scanning electron microscope JSM 6490. The SEM is equipped with a Nordlys II phosphor screen EBSD detector with Channel 5 software from Oxford Instruments and HKL Technology. EBSD was performed with an acceleration voltage of 15 kV, a working distance of 20 mm, and a Si-wafer as calibrant. EBSD data were acquired by automated mapping performed at step sizes of 0.8–1 μm

with low gain, $2 \times 2$ pixel binning, and a mean angular deviation limit of <1.3°. The pre-experiment, initial sample material, as well as the postexperiment resulting material were embedded in Araldite epoxy resin, polished with Syton polish and thinly coated with carbon. Following data acquisition, no noise reduction was performed on the acquired EBSD data. Contoured pole figures are displayed as multiples of uniform distribution (m.u.d.), with a half width of 10°.

Synchrotron-based micro-computer tomography (micro-CT) was performed at PETRA III (DESY) in Hamburg, Germany. All data were collected on the micro tomography beamline P05 (Moosmann et al., 2014; Ogurreck et al., 2013; Wilde et al., 2016), operated by Helmholtz–Zentrum Hereon, using a 15 keV beam monochromatized by a double crystal monochromator. The images were acquired with a 24× magnification using a CMOS camera resulting in an approximately $1.8 \times 1.8$ mm$^2$ FOV with a spatial resolution down to 1 μm. Scans were performed with an acquisition time of 350 ms. A binning factor of $2 \times 2$ pixel resulted in a binned pixel size of approximately $0.61$ μm $\times 0.61$ μm. The samples were completely embedded in Araldite epoxy resin.

## RESULTS

### Analysis of the Video Recording

The experiments were filmed and the videos could be analyzed in order to observe the behavior of particles in response to arc discharges. Figure 2a shows the FOV prior to the arc discharge experiments. The tips of the electrodes are visible on opposite sides of the image. Some initial grains stick to the electrodes and sample chamber walls and appear out of focus in the center of the FOV. The space between the electrodes was empty. The first two arc discharges were induced while no particles were levitating between the electrodes. The arc discharges agitated the particles inside the sample chamber. Subsequently, the moving particles were attracted by the electric field between the electrodes and formed chains parallel to the electric field lines. The distance between the single chains of particles decreased with increasing charge buildup and the particles formed a dense aggregate levitating between the electrodes, which is shown in Fig. 2b. Some particles appear darker than others, which is due to the illumination conditions. The loose aggregate was destroyed by the arc discharges and the particles were agitated to a random particle motion. The particles were then attracted by the electric field between the electrodes, which was applied between two arc discharges and formed again chains of particles. However, the number of particle chains which formed
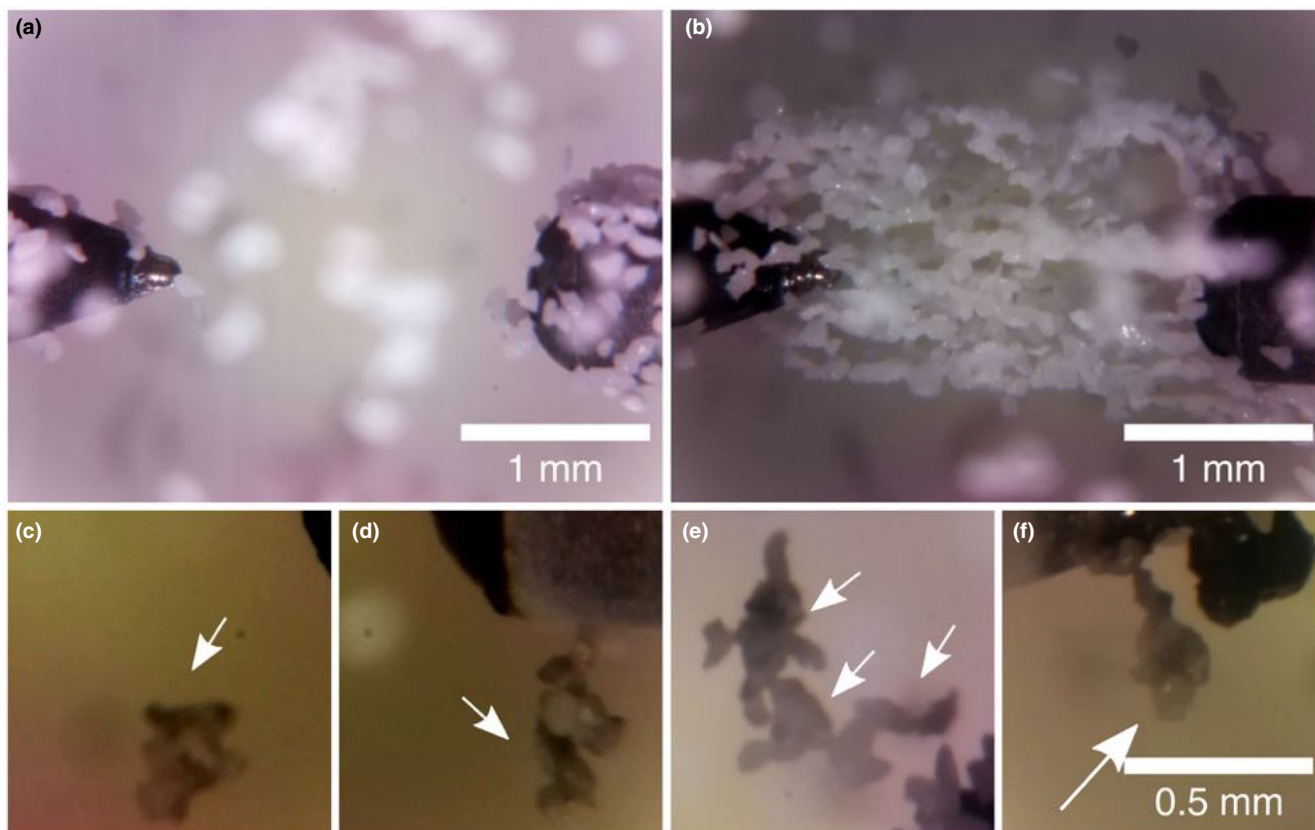
Fig. 2. Selected frames from the video material and particle aggregation during the experiment. a) The field of view prior to the arc discharge experiments. The tips of the electrodes are shown on opposite sides of the image. Some initial particles stick to the electrodes and the sample chamber walls. b) The particles formed chains along the field lines between the two electrodes prior to the third arc discharge. c) A massy aggregate (white arrows) appeared after the 16th arc discharge (contrast enhanced). d) An elongated aggregate (white arrows) appeared after the 34th arc discharge (contrast enhanced). e) Three fused aggregates after the 75th arc discharge (white arrows). f) An elongated, bulbous aggregate (white arrow) detected after the 81st arc discharge (contrast enhanced). Scale bar for (c)–(g) is displayed in (f). The aggregates appear darker because of different automatic settings of the camera and tungsten contaminations on the particles and sample chamber walls, which sputtered from the electrodes during the arc discharges. (Color figure can be viewed at wileyonlinelibrary.com.)

between the electrodes decreased with the number of arc discharges to approximately two to three chains of particles. In total, particle chains were present prior to 27 arc discharges.

The first small fused aggregate (two to three fused particles) was observed after the fourth arc discharge and the number of observed aggregates increased with increasing arc discharges. The aggregates were observed either when they crossed the FOV agitated by the discharges or when they were attracted by the electrodes when the capacitors were charged. Selected frames from the video material showing some representative aggregates are shown in Figs. 2c–g. These aggregates appear darker than the initial grains due to different automatic lighting adjustments of the camera and because of tungsten contamination on the particles and sample chamber walls, which sputtered from the electrodes during the arc discharges.

The massy, approximately 300 µm sized aggregate in Fig. 2c crossed the FOV after the 16th arc discharge. Figure 2d shows an elongated aggregate attracted to the electrode after the 34th arc discharge. Figure 2e is a frame shot from the video after the 75th arc discharge, where three different aggregates levitated parallel to the electric field lines between the electrodes similar to the particles in Fig. 2b. One of these aggregates is elongated (top), while the other two aggregates are curved. The elongated, bulbous aggregate in Fig. 2f appeared after the last arc discharge.

It was not possible to assign a specific aggregate to a specific discharge event or to distinguish whether the particles melted inside the plasma channel or by thermal radiation due to the frame rate. The focus plane of the camera objective was very small and many aggregates crossing the FOV were not in focus to allow subsequent
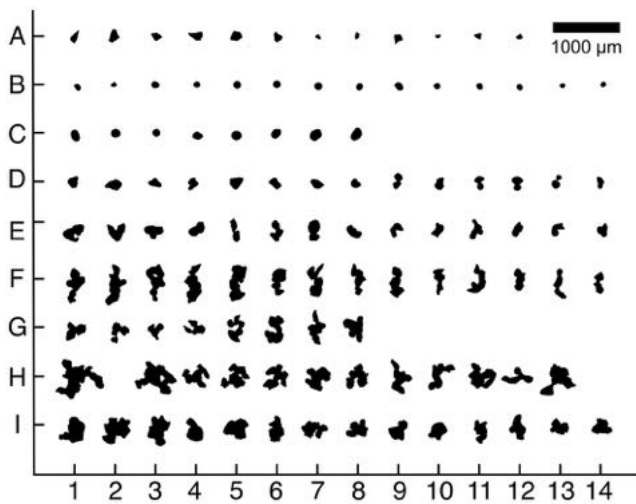
Fig. 3. Threshold image of the initial grains and formed objects. Different types of experimental outcomes were detected. A: Representative initial sample grains. B and C: Melt spherules. D and E: Small aggregates. F: Elongated aggregates. G: Small fluffy or three-winged aggregates. H: Fluffy aggregates with a three-winged boomerang-shaped morphology. I: Aggregates that are completely massy or have a massy center. The object numbers in this diagram serve for identification of the specific objects referred to in the following analysis.

identification (and discharge allocation) at the end of the experiment.

**Morphology Analysis of Fused Aggregates**

After sample return, the transformed objects were picked from the total sample material inside a petri dish. The aggregates were photographed and selected images were transformed into threshold images using ImageJ. More than 100 newly formed objects including single spherules and fused aggregates could be detected. Due to the large amount of sample material in the recovered sample chamber, it seems likely that this number is underestimated for melt spherules and small aggregates that could be hidden in the remaining dust.

The formed objects can be divided into different groups according to their morphological characteristics. Figure 3 shows the threshold images of the initial grains (A) and the experimentally transformed objects (B–I). The coordinate numbers in this diagram are used as reference frame for identification of the specific aggregates described in the following text. It is important to mention that these threshold images are only two-dimensional representations of three-dimensional objects, therefore the subdivision of the objects into different morphological groups is rather a rough estimation than an exact classification scheme.

Table 1. Ratio of the longest ($b$) versus shortest ($c$) dimensions of the elongated aggregates (Fig. 3 row F).

| No. | F1 | F2 | F3 | F4 | F5 | F6 | F7 |
|---|---|---|---|---|---|---|---|
| $b/c$ | 1.9 | 1.9 | 1.9 | 2.2 | 2.1 | 1.9 | 2.1 |
| No. | F8 | F9 | F10 | F11 | F12 | F13 | F14 |
| $b/c$ | 2.3 | 2.0 | 2.2 | 1.7 | 1.8 | 2.3 | 2.3 |

However, some important and systemic characteristics of the formed objects could be observed.

The most abundant sample type group consists of 21 single melt spherules (rows B and C) in addition to five melt spherules that are fused to other single particles (rows C and D). This number is probably underestimated, because not all melt spherules could be detected among the high amount of initial particles. Another large group represents small aggregates consisting of two to four grains, which are shown in rows D and E. The aggregates displayed in row F represent aggregates with an elongated morphology. Table 1 summarizes the ratios between the longest ($b$) and shortest ($c$) dimension of the 14 elongated aggregates shown in row F. The mean $b/c$ ratio is 2.1 ± 2.

The most conspicuous morphology is displayed by the aggregates in rows G and H. Their morphology is characterized from curved fused chains of particles (e.g., #G5, G6); very irregular fractal structures (e.g., #H5, H6); up to clear, three-winged, "boomerang-shaped" morphologies (#H1, #H4). However, due to the limitation of this classification scheme, some aggregates shown in row G could be also grouped to row H and vice versa. Furthermore, some aggregates shown in row F could also be assigned to G or H.

Row I includes aggregates, which consist of several fused grains merged to one massy object, where the different initial grains could no longer be distinguished. Some single grains were fused to the surface. To simplify, these aggregates will be called massy aggregates in the following text.

The area sizes of the different aggregates are plotted in the histogram in Fig. 4a, the correlation of the major to the minor ellipse axes of the newly formed objects in comparison to the initial sample material in Fig. 4b. There is a strong decrease in frequency toward larger sizes, especially considering the number of single melt spherules is probably underestimated. The total area of all aggregates divided by a mean aggregate diameter of 126 μm results in approximately 300–400 reacted initial grains, which is 3–4% of the initially loaded sample amount.

**Micro-CT Analysis**

Some aggregates were analyzed with synchrotron micro-CT to study their morphology and internal
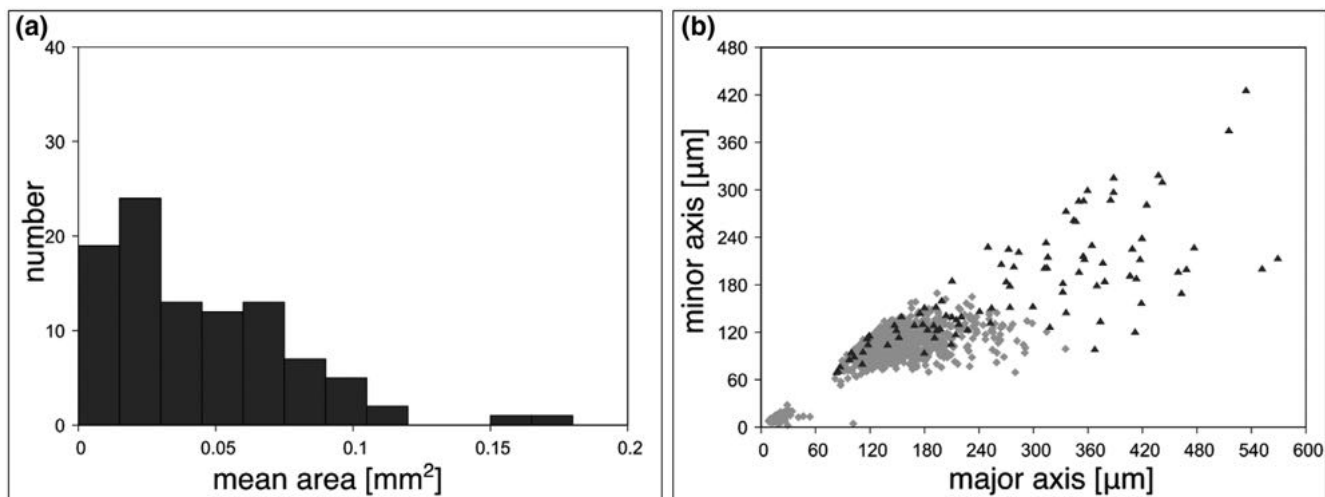
Fig. 4. Size analysis of the newly formed objects. a) Histogram of the area size distribution. b) Major axis versus the minor axis of the approximated ellipsoids of the resulting material (dark gray) in comparison to the sizes of the initial material (light gray).
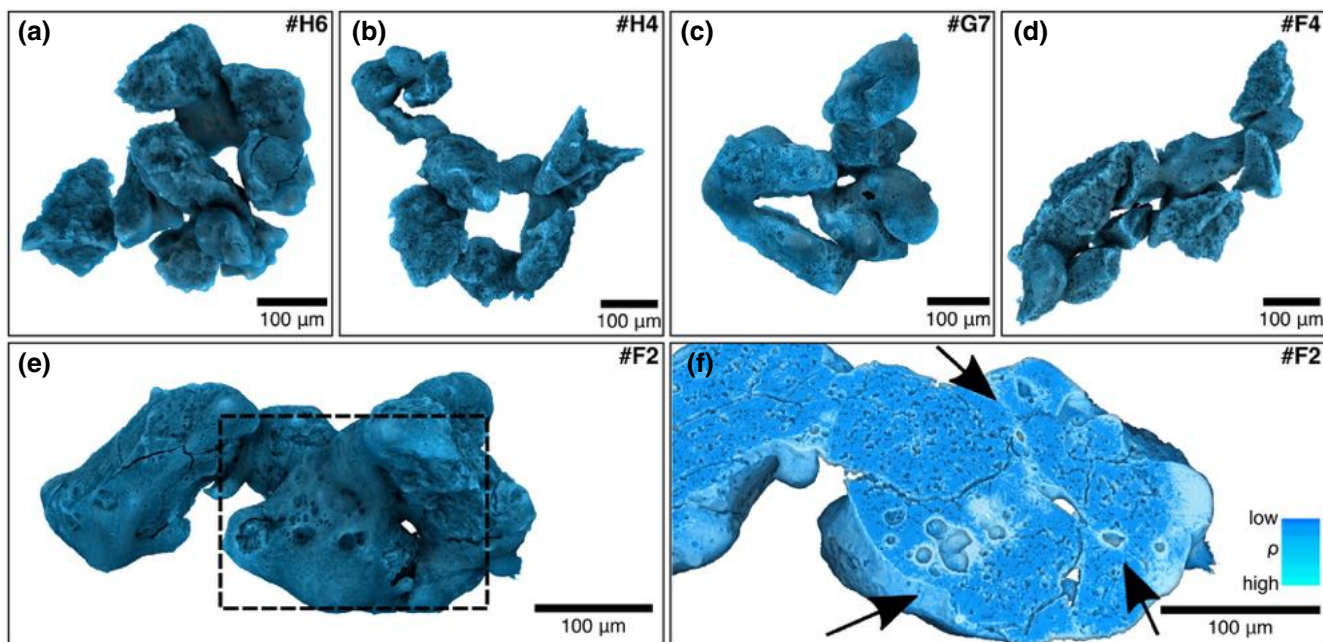


Fig. 5. CT projection of some generated fused aggregates. a–c) Aggregates with a boomerang-shaped morphology. d, e) Elongated aggregates. The aggregate in (d) consists mostly of grains with the initial angular and porous surface. The surface of the aggregate in (e) is mostly smooth with a few porous areas. f) A virtual slice through the aggregate in (e) (black dash square) reveals a generally more porous interior. The triple junction in the middle of the right part of the aggregate suggests that at least three grains were fused and form a triple junction. While the centers of the fused grains appear unprocessed, the interstitial areas (marked by arrows) have lost their original pore structure and instead, larger, spheroidal voids are present. Furthermore, these areas appear brighter, which is indicative of a higher density and is probably due to tungsten precipitation. The outlines of the pores and cracks appear bright because of edge enhancement due to coherence. (Color figure can be viewed at wileyonlinelibrary. com.)

structure. Figures 5a–c show aggregates from rows G and H with fractal morphologies, whereas Figs. 5d and 5e show elongated aggregates (from row F). The aggregates shown in Fig. 5 consist of approximately 7–10 initial

particles. The aggregate in Fig. 5d consists mostly of angular grains with porous surfaces similar to the initial starting material. The surface of the aggregate in Fig. 5e is mostly smooth. Figure 5f shows a virtual slice through
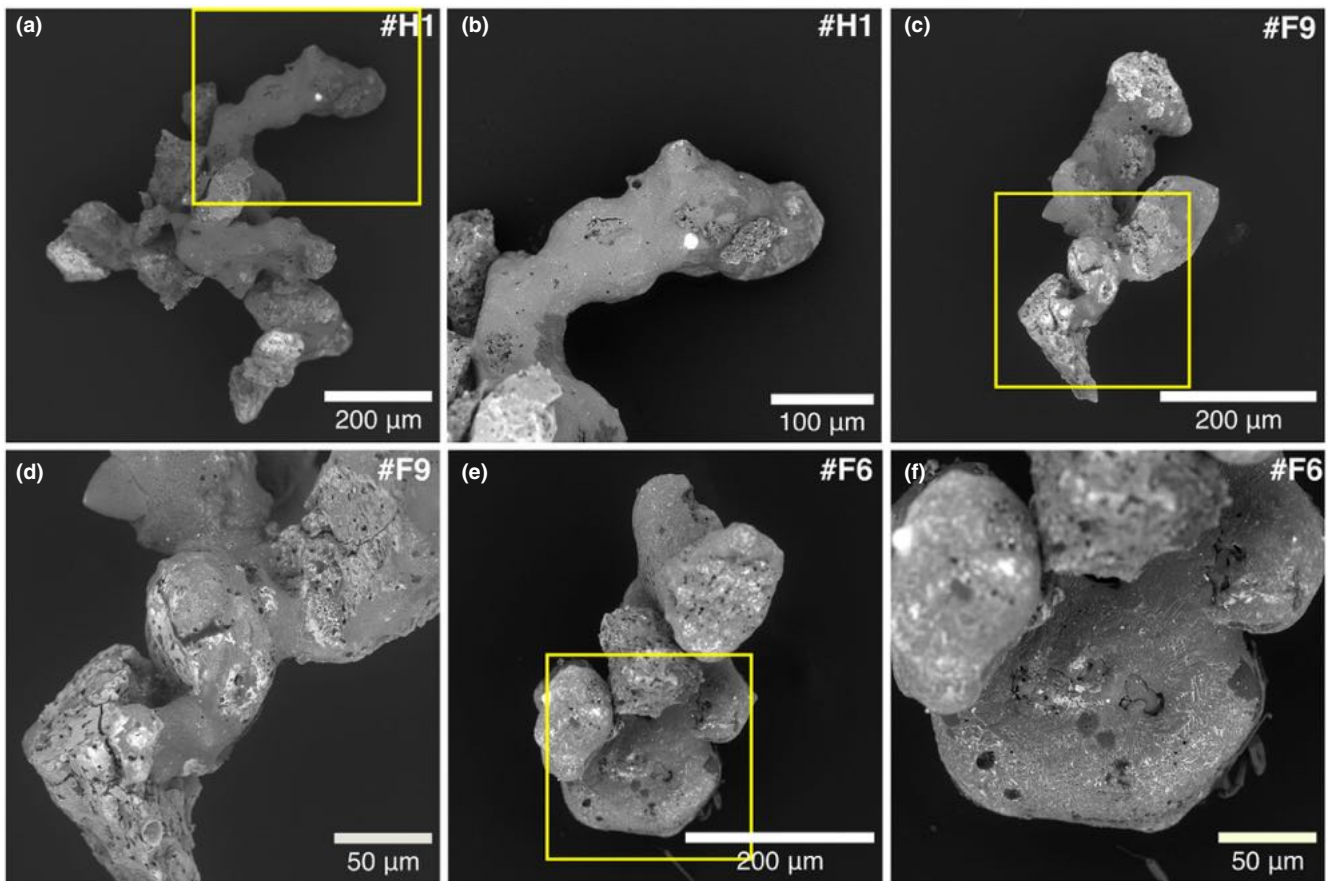
Fig. 6. Focus-stacked SEM BSE images of representative fused aggregates. a) Aggregate with a nearly perfectly three-winged, boomerang-shaped morphology. b) Close-up of the largest wing showing a molten surface with tungsten precipitation lines. Opening in the surface reveals a more porous interior. c) Elongated aggregate. d) Close-up of the aggregate in (c) showing completely molten inner region between particles. e) Elongated aggregate with a flat, molten disk. f) Close-up of the disk with tungsten precipitation. Yellow boxes in (a), (c), and (e) denote the positions of the close-up images in (b), (d), and (f), respectively. (Color figure can be viewed at wileyonlinelibrary.com.)

the aggregate in Fig. 5e (black dash square), revealing that at least three initial grains were fused. The grain boundaries (white arrows) are molten, displaying larger, spherical pores and a slightly higher density (brighter in the image) than in the unmolten areas. The three boundaries meet in the center in a triple junction (Fig. 5f, center).

**SEM Analysis**

SEM analysis was also used to study the morphology and composition of the aggregates. The analysis of the single melt spherules was part of an earlier study (Koch, Spahr, Tkalcec, et al., 2021). Figure 6 shows focus-stacked BSE images of some representative elongated fractal-shaped aggregates. All aggregates consist of dust grains with various degrees of melting. Figure 6a shows the largest formed object, which has formed from approximately 20 initial grains.

The object has an almost perfectly symmetric, three-winged morphology with a diameter of approximately 720 µm. Figure 6b shows a close-up of the longest arm, which consists of a bent chain of fused grains. A high percentage of the surface is molten material; however, the internal structure is visible through some cavities in the surface.

Figure 6c shows one of the elongated aggregates with a length of 425 µm. The surface of the grains in the middle area of the aggregate was completely molten (Fig. 6d), the outer grains show the initial surface structure. The object in Fig. 6e has a length of approximately 500 µm. One part of the aggregate consists of a 170 µm sized flat disk (Fig. 6f) displaying a very strong tungsten pattern on its surface.

In general, the molten surfaces of the different aggregates show fine lines of tungsten precipitation similar to Fig. 6f, which appear bright in the BSE images. This precipitation arises from evaporation of
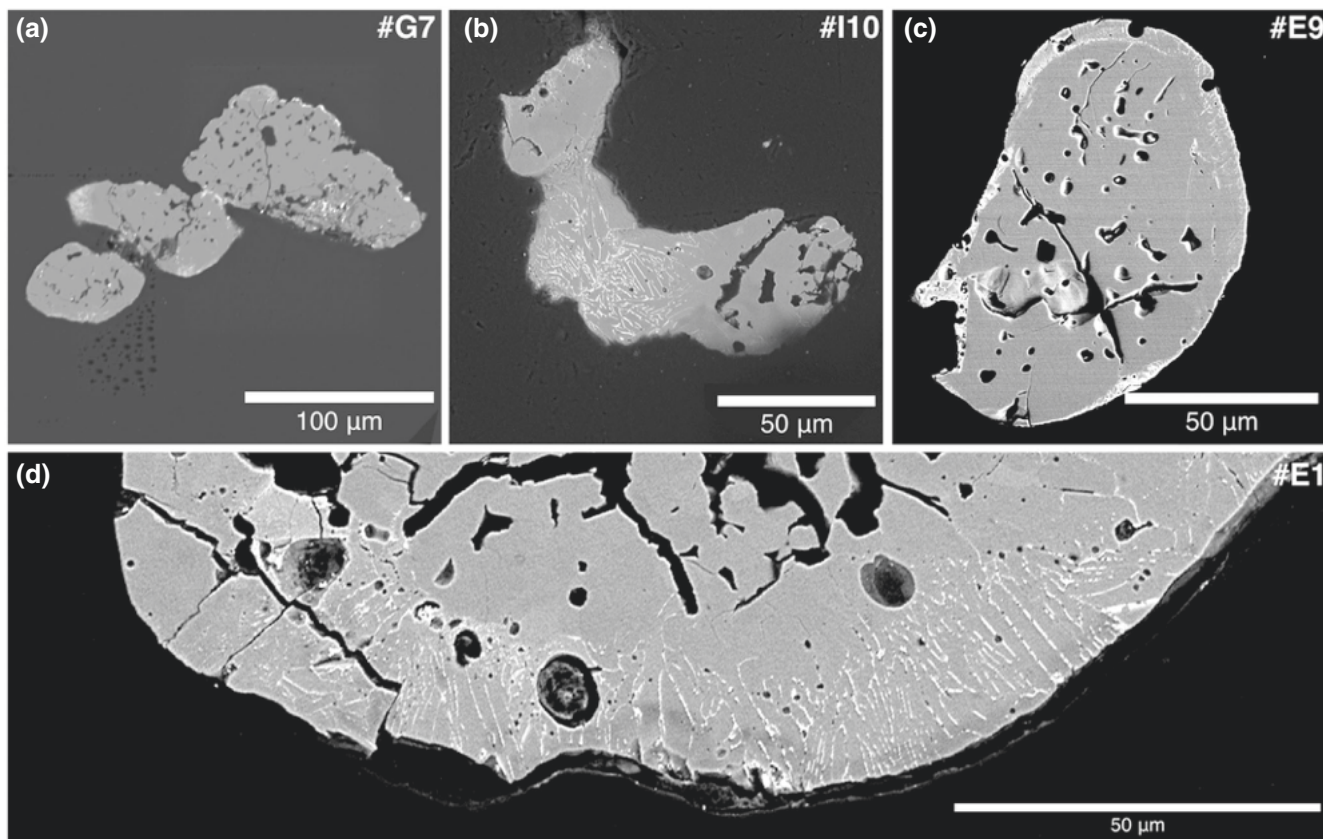
Fig. 7. SEM analysis of polished aggregates. The melted areas and grains of the aggregates can be identified by the absence of the initial pore structure, by some sort of fusion crust on the surface, and by tungsten inclusions. The molten areas of the particles show tungsten inclusions in round inclusions and precipitations along the grain boundaries. The tungsten, which was evaporated from the electrodes during the arc discharges, interacted with the melt and precipitated along the grain boundaries during crystallization. a) Three grains which still reveal the original pore structure and were only fused on the surface. b) Three fused aggregates with three different thermal histories. The center grain displays abundant tungsten precipitation lines and was probably completely molten. The upper grain has lost its initial pore structure but includes less tungsten. The third grain shows molten outer regions, but the initial pore structure the interior regions. c) Particle of aggregate #E9, which is completely surrounded by a tungsten-bearing igneous rim. The inner part of the grain is nearly unprocessed; however, the pores have slightly changed and appear more round than in the initial material. d) Close-up of one of the fused grains of the fused aggregate #E1. The grain shows an igneous rim with a thickness of approximately 17–22 μm displaying the typical tungsten precipitation lines and spherical pores indicative of melting.

the tungsten electrodes. However, as the aggregates were not carbon-coated prior to SEM analysis, surface charging may also be responsible for some bright artifacts.

Some aggregates were polished before SEM analysis (Fig. 7). The polishing reveals different thermal histories of particles in more detail and even grains that are directly fused to each other have experienced very different degrees of melting. The melted areas and grains can be identified by the absence of the initial pore structure, by spherical pores, by some sort of fusion crust on the surface, and by tungsten inclusions. The molten areas of the particles show tungsten inclusions in round inclusions and precipitation along the grain boundaries. The tungsten, which was

evaporated from the electrodes during the arc discharges, interacted with the melt and precipitated along the grain boundaries during crystallization.

Figure 7a shows a grain which is only molten on the surface next to two nearly unprocessed initial particles. Figure 7b shows three or four fused grains. One grain was probably completely molten with very few tungsten inclusions on one side and some round pores. The elongated grain in the middle is interspersed by tungsten precipitation next to a nearly unprocessed particle. Figure 7c shows a grain from aggregate #E9, which underwent melting on the surface, while the inner structure of the grains underwent only light thermal annealing. Figure 7d shows a close-up of one of the fused grains of the fused aggregate #E1. The grain
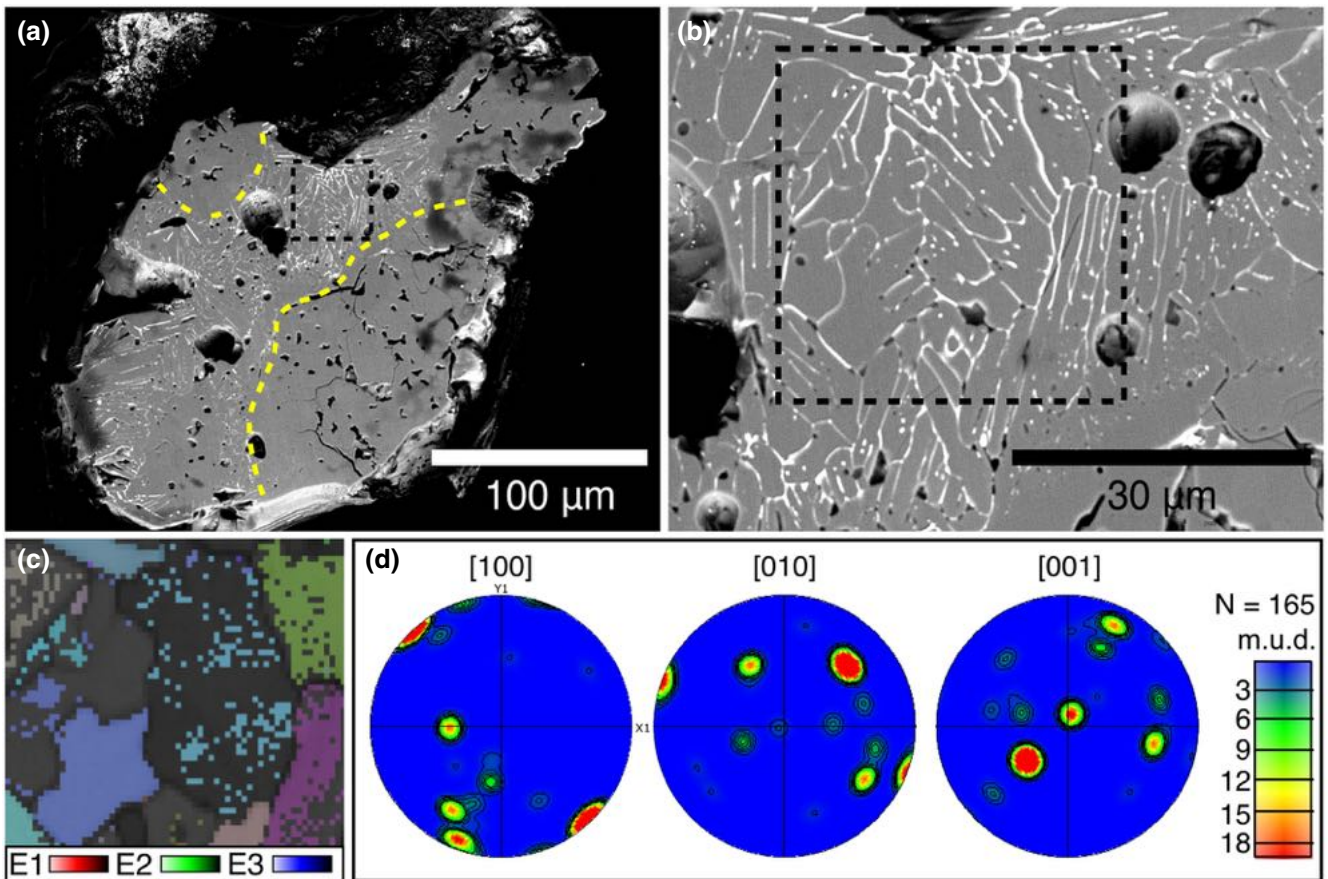
Fig. 8. SEM and EBSD analyses of a polished massy aggregate #I12. a) SEM BSE overview of the polished aggregate. The yellow dashed lines indicate the boundaries between molten and original sample material. b) A close-up of the molten area (black dashed square). The bright lines and inclusions represent tungsten precipitation. c) EBSD band contrast image with overlying all-Euler angle map of forsterite of the area marked by the dashed square in (a) and (b). E1, E2, and E3 represent the Euler angles. d) Stereographic projections of EBSD data of the area shown in (c). (Color figure can be viewed at wileyonlinelibrary.com.)

shows an igneous rim with a thickness of approximately 17–22 μm displaying the typical tungsten precipitation lines and spherical pores indicative of melting.

Figure 8 shows the SEM and EBSD analysis of the polished aggregate #I12. The aggregate has a massy core and is droplet-shaped. Its size suggests that it fused from four to six initial grains. Figure 8a shows an overview of the polished aggregate. Several areas with the original pore structures could be identified (yellow dashed lines). Figure 8b shows a close-up of the molten area between the initial areas. The molten area shows the typical tungsten precipitation pattern with parallel lamellae. This area was studied with EBSD in more detail and all indexed patterns were indexed as forsterite. Figure 8c shows the band contrast image superimposed with an all-Euler angle map. The grain sizes identified in the band contrast image, displayed by black boundaries from the overlapping of two adjacent signals and defined by a misorientation threshold of 10°,

are larger than those originally inferred from the tungsten precipitation patterns. This indicates that misorientation angles between the intragrain tungsten lamella are less than 10°. The all-Euler map confirms the presence of some large grains, several of which display well-indexed interiors with negligible intragrain misorientation, whereas others, for example the large center grain, reveal several nonindexed areas. In the latter case, however, all indexed points show the same uniform all-Euler orientation confirming the single-grain identification shown by the grain boundaries of the subimposed band contrast map. The crystallographic orientations of these large forsterite grains are revealed by pole figures (Fig. 8d) contoured by m.u.d. set at maximum 12. Because the original data was not subjected to any noise reduction, the few tight point maxima (red) likely reflect duplication (nonadjacent points measured from the same large grain but identified as individual grains) in grains where indexing
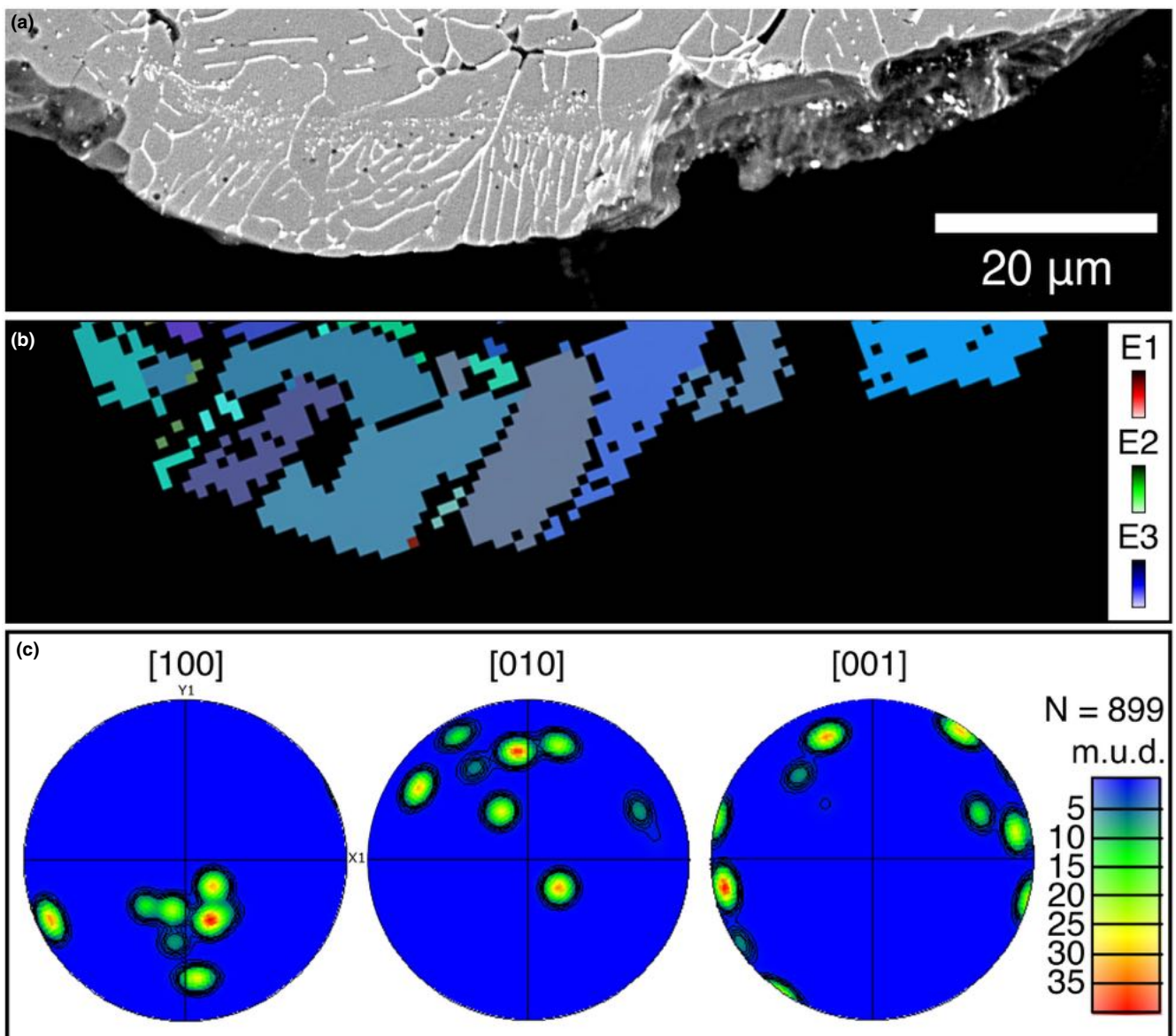
Fig. 9. EBSD analysis of the igneous rim of an aggregate. a) BSE image of the rim of one particle of aggregate #E1. The lines that appear white in the BSE image represent tungsten precipitation. Grains show a tungsten-lamellae (TL) and tungsten-free (TF) zone. b) EBSD all-Euler map displaying the grain boundaries reveals that the observed sets of mostly parallel tungsten lamellae are intracrystal. c) Stereographic projections of EBSD data of the rim. The grains show preferred orientation in all three crystallographic axes. (Color figure can be viewed at wileyonlinelibrary.com.)

was not continuous. Thus, each large red m.u.d. maximum contour is interpreted as a single grain. The crystallographic [100] axes plot as broad N-S point maxima of several grains and the [010] axes possibly as a broad E-W girdle, although the latter should be seen with caution due to the small number of grains involved.

One of the igneous rims (particle #E1) was also studied with EBSD. The BSE image in Fig. 9a reveals that the rim of particle #E1 is clearly different

compared to the initial material. Tungsten precipitation is strongly present in grain boundaries (Fig. 9a) and often forms parallel lamellae perpendicular to the particle surface. In addition, a multitude of tiny tungsten spots appear to be arranged in a linear layer parallel to (and about 14 µm inside) the particle rim. This tungsten layer runs perpendicular to the tungsten lamellae, which it appears to truncate, thus dividing each grain into the tungsten-lamellae-bearing (TL) and tungsten-free (TF) zones.
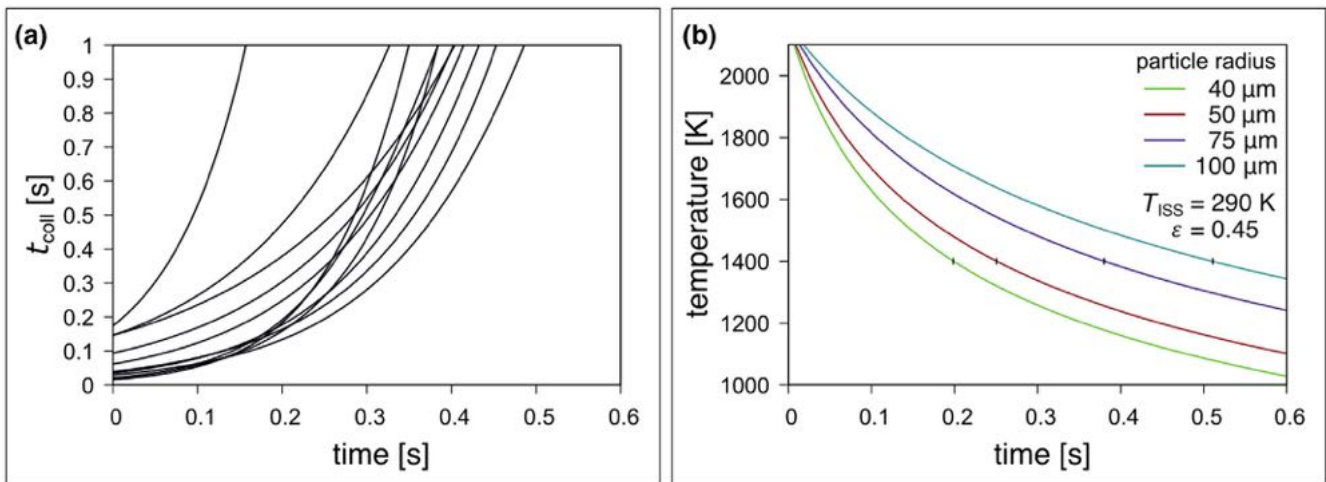
Fig. 10. Collision times $t_{coll}$ of particles inside the sample chamber and cooling rates of the particles after arc discharges. a) $t_{coll}$ versus the time after arc discharges is plotted for several grains after different arc discharges. b) Calculated temperatures of particles with different radii versus time after arc discharges inside the sample chamber. (Color figure can be viewed at wileyonlinelibrary.com.)

The corresponding EBSD all-Euler phase map reveals a number of large grains all aligned with their longest dimension perpendicular to the surface. The crystal directions of the grains plotted in the pole figures in Fig. 9c confirm a strong crystallographic preferred orientation of all grains. The tungsten lamellae are oriented perpendicular to the particle surface and parallel to the longest dimension of the grain in each case, dividing the part of the grain closest to the rim into parallel zones with negligible misorientation to one another.

## Time Scales of Aggregation

The duration of aggregate formation in the experiments depended on the collision time scale and the cooling rates of the particles. The collision time $t_{coll}$ describes the mean time of a grain between two collisions (Marrocchi et al., 2019; Nakagawa et al., 1981) and can be expressed as Equation 1:

$$t_{coll} = \frac{1}{n_p 4\pi a^2 \Delta v_{coll}} \tag{1}$$

where $\Delta v_{coll}$ is the particle–particle velocity, which is assumed to be similar to the collision velocity; $a$ is the mean particle radius; and $n_p$ is the particle density (5500 particles cm$^{-3}$). The particle velocities $v_{coll}$ after arc discharges were determined for different particles from the videos (see Koch, Spahr, Merges, et al., 2021). The measured particle velocities are in the range of >25 mm s$^{-1}$ with a subsequent exponential deceleration due to gas drag. We calculated $t_{coll}$ for different velocity profiles using the fitting parameters from Koch, Spahr, Merges, et al. (2021). Figure 10a shows some representative collision times of particles after arc discharges dependent on the time after the discharge events. Immediately after the arc discharge, the mean time between two collisions of a particle is in the range of 0.01 and 0.2 s. Consequently, aggregates which consist of approximately 20 particles could have formed in 0.2–4.0 s. However, the particle size $a$ will increase with aggregate formation, which also decreases the number of particles in the sample chamber. However, these effects are neglected in the calculations.

Another limitation for the duration of aggregate formation is the cooling rate of particles, because the particles have to be plastic to fuse in collisions. The lower temperature limit for the formation of compound chondrules was defined to be 1400 K, which represents the lowest temperature where silicate melts were present in chondrule melt (Bischoff et al., 2017; Ciesla et al., 2004). We used this temperature as a lower limit for the calculation of the time scale of aggregate formation in the experiment, because the initial sample material consists of Mg$_2$SiO$_4$.

The cooling rates of chondrules melted by lightning are usually modeled by radiative cooling of a gray body (Equation 2) (Morris & Desch, 2010). The temperature of the chondrule analogue after the arc discharge is given by the liquidus temperature of forsterite of 2163 K (Bowen & Schairer, 1925) and the temperature aboard the ISS is estimated to be 290 K. Equation 2 gives the change of the internal energy $U$ of a radiating spherical gray body with time:

$$\frac{\partial U}{\partial t} = \epsilon \cdot \sigma \cdot A \cdot (T_{\text{sample0}}^4 - T_{\text{ISS}}^4) \qquad (2)$$

where $U$ is the internal energy, $t$ is the time after the heating pulse in s, $\epsilon$ is the emissivity (for reference, a black body has an emissivity of 1), $\sigma$ is the Stefan–Boltzmann constant, $A$ is the surface area of the spherule, and $T_{\text{sample0}}$ is the temperature of the heated spherule at time 0 and $T_{\text{ISS}}$ is the temperature of the surrounding, both in K. $\Delta U$ for a short d$t$ can be obtained using Equation 3.

$$\Delta U = \epsilon \cdot \sigma \cdot A \cdot (T_{\text{sample}}^4 - T_{\text{ISS}}^4) \cdot \mathrm{d}t \qquad (3)$$

The change in $U$ can also be described by means of the temperature-dependent specific heat capacity $c_{\text{p}}(T)$ in J mol$^{-1}$ K$^{-1}$, the change in temperature of the spherule $\Delta T$ in K, and the amount of substance in mol (Equation 4). The amount of substance $n$ is calculated for different spherule sizes using the volume of the spherule, the density of forsterite (3.275 g cm$^{-3}$), and the molar mass of forsterite (140.693 g mol$^{-1}$) (Anthony et al., 2018).

$$U = c_{\text{p}}(T) \cdot n \cdot (\Delta T) \qquad (4)$$

Combining Equations 3 and 4 gives an expression for the change in temperature of the spherule during a short time of radiation (Equation 4).

$$\Delta T = \frac{\epsilon \cdot \sigma \cdot A (T_{\text{sample0}}^4 - T_{\text{ISS}}^4) \cdot \mathrm{d}t}{c_{\text{p}}(T) \cdot n} \qquad (5)$$

The resulting $\Delta T$ is subtracted from $T_{\text{sample0}}$ to derive the new temperature of the spherule $T_{\text{sample1}}$. Using this new temperature, the calculations are iterated $N$ times until $T_{\text{sample}N}$ is sufficiently close to $T_{\text{ISS}}$ (291 K in this case). The specific heat capacity $c_{\text{p}}(T)$ in Equation 4 is calculated for each iteration step with the data from the NIST Standard Reference Database (see NIST, 2020).

The cooling rates of the particles were determined to be $10^7$–$10^4$ K h$^{-1}$ shortly after the arc discharges (Koch, Spahr, Tkalcec, et al., 2021). Figure 10b shows the temperature of the particles with different sizes after the discharge events. The particles were cooled to 1400 K in between 0.2 and 0.5 s. It is important to mention that the model was calculated for solid droplets. However, forsterite melt drops should have high temperatures (<2163 K) and similar high cooling rates at these temperature. Therefore, this model also provides an appropriate estimation for the aggregation times. Thus, it is likely that aggregate formation in the experiment was a very fast process of <0.5 s after the

discharge events, which is in accordance with the results from the collision time determination.

However, these calculations only work for fully molten, spherical particles and partially molten grains could cool much faster. Therefore, partially molten grains had to collide with other particles much faster than fully molten particles and therefore it is likely that aggregates formed from particles which were very close to each other during the discharge event, perhaps the particles which were aggregated in the electric field prior to the arc discharges. However, it was not possible to observe the collisions of particles due to the frame rate.

## Morphology Analysis of Natural CAIs

To compare the morphology of the aggregates formed in the experiment with natural CAIs, a random sample of representative CAIs in the CV3 chondrite NWA 13656 were analyzed regarding their morphology. Figure 11 shows optical microscopic images of different types of fractal inclusions. Figure 11a shows an inclusion with three to four wings. Figures 11b and 11c show inclusions which have a massy center and several attached nodules. Figure 11d shows a very elongated inclusion.

Threshold images of the different inclusions in NWA 13656 were used for the morphology analysis. Figure 12 shows the threshold images of the NWA 13656 inclusions sorted according to their morphology: small inclusions consisting of only a few single nodules (J), elongated inclusions (K), bent fractal inclusions (L), fractal aggregates with four- and three-winged morphology (M), and inclusions with a massy center (N). However, it should be noted that they represent two-dimensional cross sections of CAIs and the three-dimensional morphology could show another morphology-type.

Figure 13 shows the size analysis of the natural inclusions. It is important to mention that we used a random sample of CAIs, which resemble the three different aggregate types produced in the experiment. NWA 13656 includes also a wide range of spherical or completely molten CAIs in each size. The histogram in Fig. 13a shows a heterogeneous distribution of the natural CAI sizes. However, this size distribution is biased due to the sample preparation, which only displays a two-dimensional image of the CAIs. Figure 12b shows the plotted minor versus major ellipsoid axis of the best-fit ellipsoids of the natural CAIs in comparison with the initial starting material of our experiment and the experimentally formed aggregates. The natural CAIs plot in the same range relative to the experimentally formed aggregates standardized by a factor of 5.
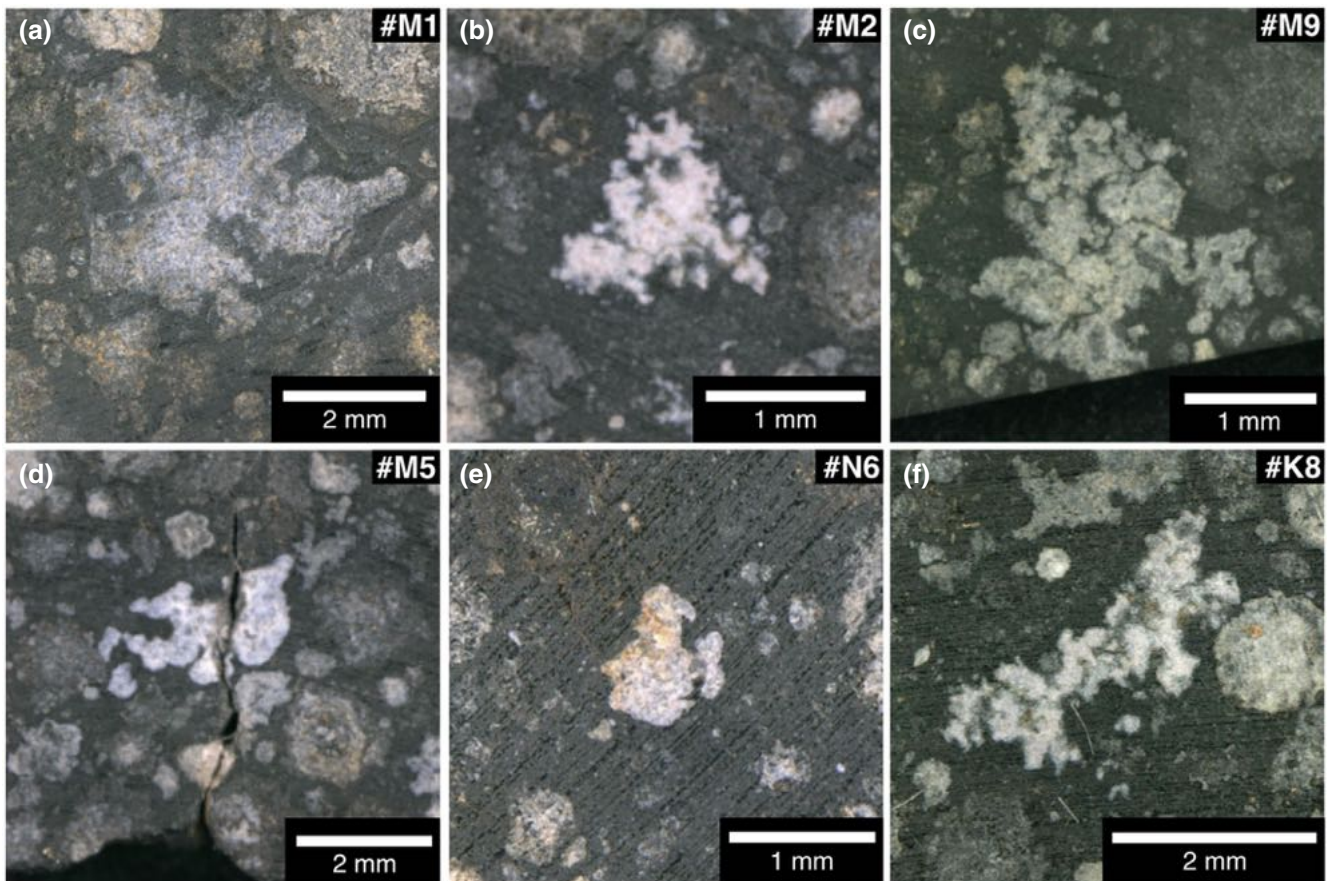
Fig. 11. Photographs of irregular inclusions on slices of NWA 13656. a) Inclusion with four wings. b) Tringle-shaped inclusion. c) Three-winged inclusion. d) Inclusion with a massy center and two attached nodular wings. e) Inclusion with a massy center and several attached nodules. f) Elongated inclusion. (Color figure can be viewed at wileyonlinelibrary.com.)

Table 2 shows the ratios between the longest (*b*) versus the shortest (*c*) direction of the natural CAIs. The values are generally in the same size range as those of the experimentally formed aggregates (Table 1) with some outliers of higher ratios >3, which could be a cutting effect. The mean value of the ratios excluding the outliers is 2.1 ± 0.3.

## DISCUSSION

In the experiment aboard the ISS, two types of experimental outcomes were produced, single melt droplets and fused aggregates. While the melt spherules have been discussed in their role as chondrule analogs in a previous study (Koch, Spahr, Tkalcec, et al., 2021), we concentrate here on the fused aggregates.

### Aggregate Formation in the Experiment

The early appearance of aggregates also argues for a formation of these aggregates beginning during the first arc discharges. Most aggregates produced in the experiments show some typical morphologies, which can be broadly divided into elongated aggregates, fluffy aggregates with curved and boomerang-shaped morphologies, and massy aggregates. These aggregates were formed from collisions between particles which had experienced different degrees of melting from pristine unmolten and/or melted particles. Still ductile, these aggregates moved with high velocities in various directions and some aggregates transformed into the typical fractal or boomerang-shaped morphologies. The calculated cooling rates and collision times indicate an aggregate formation in ≪0.5 s, which also implies that the aggregates solidified while still in motion.

Another question which arises is whether a single aggregate was formed after a single flash-heating event or by collisions of small aggregates with newly melted particles. The systematics of the aggregate morphologies supports the idea that the aggregates were formed in a single process. The alignment of
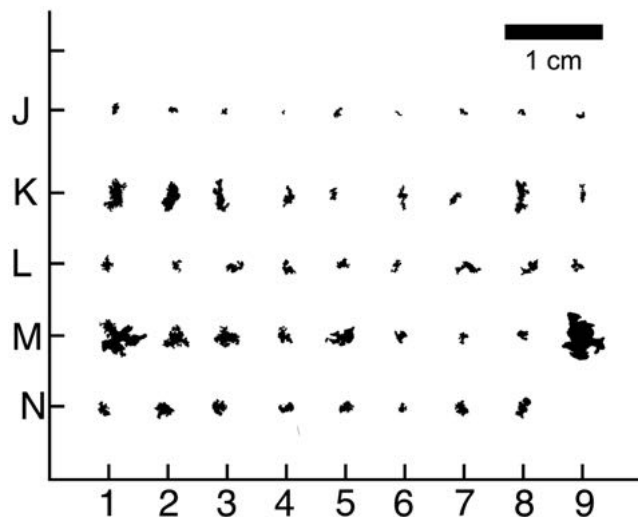
Fig. 12. Threshold image of different natural fractal inclusions in NWA 13656. Different types of inclusions are observed. J: Small inclusions consisting of only a few singles nodules. K: Elongated inclusions. L: Bent fractal inclusions. M: Fractal aggregates with four- and three-winged boomerang-shaped morphology. N: Inclusions with a massy center.

particles in the electric field between the electrodes prior to the arc discharges could have also influenced the formation of aggregates. The particle density between the electrodes (>80 vol%) was much higher than in the total sample chamber when the flash-heating event was triggered, and the particles could have immediately collided with their neighboring particles. This could have influenced the duration of aggregate formation which could have been much faster than our calculation of $\ll 0.5$ s.

Aggregates with a massy center could have formed from collisions of several molten droplets. The analysis of single melt droplets showed that the experiment was able to completely melt single particles (Koch, Spahr, Tkalcec, et al., 2021). Some of these melt droplets could have collided with other completely molten grains, grains in the ductile state, or initial particles and formed massy aggregates. However, it is also possible that a fractal aggregate was partially melted by another heating event and formed a massy aggregate.

Furthermore, we could not find evidence for fragmentation of the aggregates. This could be due to several reasons. First, the aggregates were not directly hit by the ignition sparks. Further, aggregates could have been remelted to massy aggregates. Last, the collision energy between the moving particles and the aggregates could have been too low for fragmentation and collisions between two particles or aggregates which experienced melting resulted in sticking.

## Relation to Early Solar System Processes

There are several similarities between the aggregates formed in our experiments and early solar system aggregates. In general, many of the aggregates formed in our experiment aboard the ISS resemble fluffy-type CAIs (MacPherson & Grossman, 1984), both in size and in their irregular-shaped morphologies. All different morphology types, for example, elongated aggregates, fractal and boomerang/bent aggregates, and massy aggregates can be found as morphologies of CAIs in a natural CV3 chondrite.

Furthermore, Zhang et al. (2021) performed CT analysis of refractory inclusions of five CV3 meteorites to study their three-dimensional morphology and found that among the six intact inclusions, three showed an elongated morphology with $b/c$ ratios of 1.5–2.1 and two had a fractal and "swan-like" morphology. The mean $b/c$ ratio of $2.1 \pm 2$ of the elongated aggregates formed in our experiment is similar to that observed for the natural refractory inclusions in the study of Zhang et al. (2021). Furthermore, the natural "swan-like" and bent inclusions shown in their study resemble aggregates formed in our experiment. The $b/c$ ratio of the elongated, natural CAIs observed in NWA 13656 is also in accordance with the $b/c$ ratio determined by Zhang et al. (2021) and the experimental outcomes of this study. For unknown reasons, aggregates and CAIs prefer a ratio of their longest to their shortest dimension in the range of 2. It is also notable that the largest aggregates formed in the experiment (Fig. 3h) and most of the largest fluffy-type CAIs in NWA 13656 (Figs. 11a–c) have the three-winged morphology.

The fluffy morphology of the formed aggregates resembles that of those formed from low velocity hit-and-stick collisions (Blum & Wurm, 2008) but were formed by a flash-heating event in the sample chamber. Earlier studies have already shown that CAI aggregation induced by turbulence produces CAIs with the same size distribution as CAIs in chondrites (Charnoz et al., 2015; Taillifet et al., 2014). The combination of the different analytical and theoretical studies discussed above together with our experiment implies that collisions of (flash-)heated particles can reproduce the typical fluffy-type CAIs. The aggregates formed in this experiment, even those that fused only superficially, remained stable over the whole duration of this experiment and during subsequent return transportation to Earth under gravity conditions, which should lead to friction and collisions with other particles, aggregates, and the sample chamber walls. In this regard we may note that CAIs observed in chondrites, even very fractal fluffy CAIs, have survived transport from their formation region to the chondrite
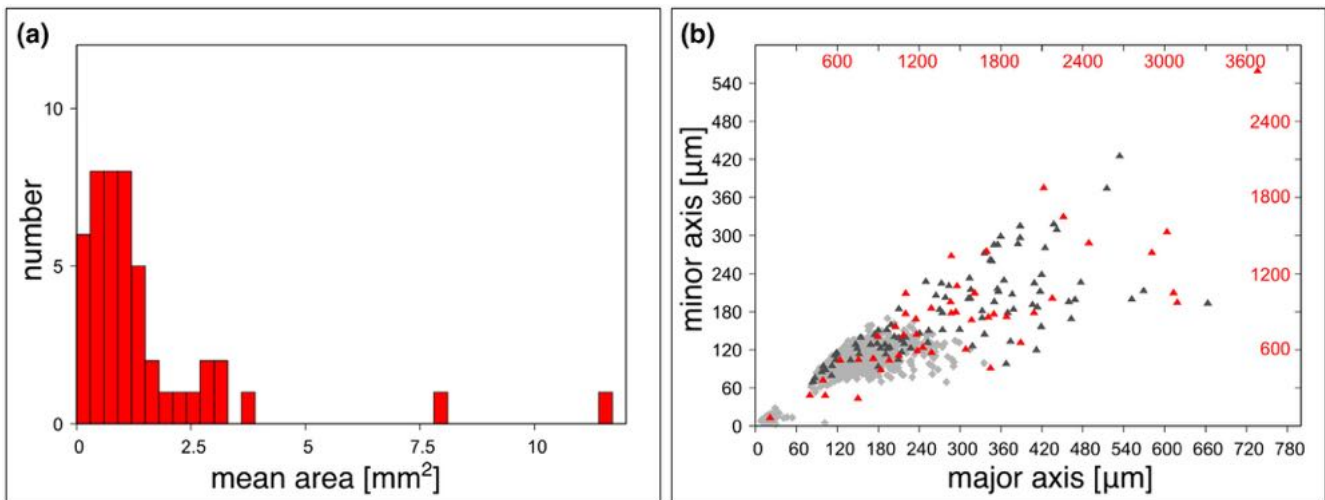
Fig. 13. Size analysis of irregular natural inclusions in NWA 13656. a) Histogram of the area size distribution. b) Major axis versus minor axis of the approximated ellipsoids (red) in comparison to the sizes of the experimental initial starting material (light gray) and the experimentally formed aggregates (dark gray). The sizes of the irregular natural inclusions in NWA 13656 are denoted by the red scale numbers since the natural CAIs have sizes of about a factor 5 larger than the experimentally formed aggregates (black-scale numbers). (Color figure can be viewed at wileyonlinelibrary.com.)

Table 2. Ratio of the longest ($b$) versus shortest ($c$) dimensions of different natural CAIs in NWA 13656.

| No. | J1 | J2 | K1 | K2 | K3 | K5 | K7 |
|-----|-----|-----|-----|-----|-----|-----|-----|
| $b/c$ | 1.9 | 1.8 | 2.6 | 2.1 | 3.5 | 2.0 | 2.7 |
| No. | K8 | K9 | N4 | N8 | | | |
| $b/c$ | 3.4 | 3.2 | 2.1 | 1.8 | | | |

aggregation area by jets, turbulent diffusion, gravitational instabilities, or advection due to disk expansion (e.g., Cuzzi et al., 2003, 2005; Cuzzi & Hogan, 2003; Gounelle et al., 2001; Shu et al., 2001; Weidenschilling, 2003), which requires a certain amount of structural stability. Melting has already been proposed to influence the formation and stability of fluffy CAIs (Rubin, 2012). However, it has also been argued that the contact points of CAI nodules do not show evidence for melting or sintering (Russell & Howard, 2013). Yet we have shown that the interlocks between grains in the experiments have sometimes no visible melting zone. Furthermore, fluffy-type CAIs show evidence for melting next to unprocessed material (Russell & Howard, 2013), similar to the adjacency of molten and unprocessed material produced in the presented experiment. Consequently, a small amount of melting could have supplied the required stability for such fractal structures to have survived transportation and aggregation to and compaction within planetesimals.

Some particles of the experimentally formed aggregates are surrounded by igneous rims with a

thickness of approximately 20 µm. The thickness of the rims formed in our experiments is in the same size range as WLRs in natural CAIs (Bolser et al., 2016; Krot et al., 2017). The experimentally formed rims show a strong preferred orientation, which is similar to the orientation of the natural WLRs studied by Bolser et al. (2016) who explained the formation of WLRs by condensation from the nebula. However, Wark and Boynton (2001) suggested that flash-heating was involved in WLR formation and the recent study of Han et al. (2020) proposed that WLR formed by flash-heating followed by fast crystallization and gas solid reactions in a turbulent environment. Our results support the proposal that flash-heating could have induced or influenced WLR formation. However, the typically observed mineral sequence in WLRs could not be reproduced in our experiment due to the single phase used as starting material. Future experiments involving multiphase starting material could address whether flash-heating could also lead to multilayered multimineral WLR analogues.

Disk- or bowl-shaped aggregates have also been observed in chondrites and interpreted as the results of shock flattening (Lorenz et al., 2019). Although we could only detect one aggregate that consists of a flat, molten disk (#F6), it indicates that aerodynamical forces, which occurred by the fast acceleration of the particles after the induced arc discharges, can also lead to a flattening of the molten droplet.

The studied massy aggregates formed experimentally resemble natural igneous CAIs; however,

they include many areas that did not experience melting. Aléon et al. (2013) reported an igneous CAI which shows evidence for partial melting, concluding that this CAI was the result of collisions of proto-CAIs which were partially molten. This interpretation is similar to our idea for the formation of massy aggregates in the experiment. It is also in agreement with the formation scenario for compound CAIs proposed by Ivanova et al. (2015). This aggregate type may represent a good example for CAI recycling during repeated events. Rubin (2012) suggested that type B CAIs formed from collisions of molten type A CAIs and that the difference during the formation of fluffy-type CAIs and this specific CAI is that the grains had different degrees of melting. This idea is in accordance with our interpretation of the formation of the fractal aggregates and massy aggregates formed during the experiment aboard the ISS.

In the experiment aboard the ISS, the different aggregates formed over a very short period of probably $\ll 0.5$ s with a very high cooling rate. The total particle density in our sample chamber is approximately $10^5$–$10^8$ higher than that assumed for the natural CAI-forming region of the PPD (Zsom et al., 2010). In addition, the electric field prior to the flash-heating events caused an even higher particle density. However, it was proposed that the PPD had local enrichments of particles (Bischoff et al., 2017). These local higher particle densities in the PPD could be, for instance, the result of electrostatic or magnetic influences, which have been produced in this or some previous experiments (Love et al., 2014; Marshall et al., 2005; Nuth et al., 1994). The cooling rates of type B CAIs is another limiting factor in the formation of CAIs which are formed by flash-heating aggregates. They are generally thought to be much slower (approximately 50 K h$^{-1}$, e.g., MacPherson, Grossman, et al., 1984; MacPherson, Paque, et al., 1984) than the cooling rates determined for the particles in the experiments; however, a slower cooling rate would be required to form aggregates in a less dust-rich environment.

## CONCLUSION

We carried out an experiment at long-term microgravity conditions aboard the ISS where freely floating particles were exposed to arc discharges. The experiment produced fused aggregates which resemble many specific morphological CAI characteristics reported in the literature, such as the fluffy-type CAI morphologies, igneous CAI textures with relict grains, disk-like CAIs, and WLRs. The fractal structures formed in the experiment are very stable which could explain why the fractal structures of fluffy-type CAIs

survived transportation to the chondrite accretion region and chondrite parent body formation. The high acceleration of particles would lead to disk- and bowl-shaped CAIs. Collisions of CAI nodules with different degrees of melting can form igneous and compound CAIs. In summary, these results imply that periodically repeated local (flash-)heating events with subsequent aggregation of particles could have been involved in CAI formation after their condensation.

*Editorial Handling*—Dr. Michael Zolensky

## REFERENCES

Aléon, J., Marin-Carbonne, J., Taillifet, E., Mckeegan, K., Charnoz, S., and Baillie, K. 2013. Igneous CAI Growth by Coagulation and Partial Melting of Smaller Proto-CAIs: Insights from a Compact Type A CAI and from Modeling (Abstract #2530). 44th Lunar and Planetary Science Conference. CD-ROM.

Anthony, J. W., Bideaux, R. A., Bladh, K. W., and Nichols, M. C. (Eds.). 2018. *Handbook of Mineralogy*. Chantilly: Mineralogical Society of America.

Beitz, E., Guettler, C., Weidling, R., and Blum, J. 2012. Free Collisions in a Microgravity Many-Particle Experiment-II: The Collision Dynamics of Dust-Coated Chondrules. *Icarus* 218: 701–6.

Bischoff, A., Wurm, G., Chaussidon, M., Horstmann, M., Metzler, K., Weyrauch, M., and Weinauer, J. 2017. The Allende Multicompound Chondrule (ACC)—Chondrule Formation in a Local Super-Dense Region of the Early Solar System. *Meteoritics & Planetary Science* 52: 906–24.

Bland, P. A., Howard, L. E., Prior, D. J., Wheeler, J., Hough, R. M., and Dyl, K. A. 2011. Earliest Rock Fabric Formed in the Solar System Preserved in a Chondrule Rim. *Nature Geoscience* 4: 244–7.

Blander, M., and Fuchs, L. H. 1975. Calcium-Aluminum-Rich Inclusions in the Allende Meteorite: Evidence for a Liquid Origin. *Geochimica et Cosmochimica Acta* 39: 1605–19.

Blum, J. 2010. Astrophysical Microgravity Experiments with Dust Particles. *Microgravity Science and Technology* 22: 517–27.

Blum, J., and Wurm, G. 2008. The Growth Mechanisms of Macroscopic Bodies in Protoplanetary Disks. *Annual Review of Astronomy and Astrophysics* 46: 21–56.

Blum, J., Wurm, G., Kempf, S., Poppe, T., Klahr, H., Kozasa, T., Rott, M. et al. 2000. Growth and Form of Planetary Seedlings: Results from a Microgravity Aggregation Experiment. *Physical Review Letters* 85: 2426–9.

Blum, J., Wurm, G., Poppe, T., Kempf, S., and Kozasa, T. 2002. First Results from the Cosmic Dust Aggregation Experiment CODAG. *Advances in Space Research* 29: 497–503.

Bolser, D., Zega, T. J., Asaduzzaman, A., Bringuier, S., Simon, S. B., Grossman, L., Thompson, M. S., and Domanik, K. J. 2016. Microstructural analysis of Wark-Lovering Rims in the Allende and Axtell CV3 Chondrites: Implications for High-Temperature Nebular Processes. *Meteoritics & Planetary Science* 51: 743–56.

Bowen, N. L., and Schairer, J. F. 1925. The System MgO-FeO-SiO$_2$. *American Journal of Science* 29: 151–217.

Brauer, F., Dullemond, C. P., and Henning, T. 2007. Coagulation, Fragmentation and Radial Motion of Solid Particles in Protoplanetary Disks. *Astronomy & Astrophysics* 480: 859–77.

Charnoz, S., Aléon, J., Chaumard, N., Baillie, K., and Taillifet, E. 2015. Growth of Calcium–Aluminum-Rich Inclusions by Coagulation and Fragmentation in a Turbulent Protoplanetary Disk: Observations and Simulations. *Icarus* 252: 440–53.

Charnoz, S., and Taillifet, E. 2012. A Method for Coupling Dynamical and Collisional Evolution of Dust in Circumstellar Disks: The Effect of a Dead Zone. *The Astrophysical Journal* 753: 119.

Ciesla, F. J., Lauretta, D. S., and Hood, L. L. 2004. The Frequency of Compound Chondrules and Implications for Chondrule Formation. *Meteoritics & Planetary Science* 39: 531–44.

Connelly, J. N., Bizzarro, M., Krot, A. N., Nordlund, A., Wielandt, D., and Ivanova, M. A. 2012. The Absolute Chronology and Thermal Processing of Solids in the Solar Protoplanetary Disk. *Science* 338: 651–5.

Connolly Jr., H. C., and Libourel, G. E. 2005. *Experimental Constraints on Chondrule Formation*. Chondrites and the Protoplanetary Disk, ASP Conference Series, 341, 286. San Francisco: Astronomical Society of the Pacific.

Cuzzi, J., Ciesla, F., Petaev, M., Krot, A., Scott, E., and Weidenschilling, S. 2005. Nebula Evolution of Thermally Processed Solids: Reconciling Models and Meteorites. ASP

Conference Series 341, 732–73. San Francisco: Astronomical Society of the Pacific.

Cuzzi, J. N., Davis, S. S., and Dobrovolskis, A. R. 2003. Blowing in the Wind. II. Creation and Redistribution of Refractory Inclusions in a Turbulent Protoplanetary Nebula. *Icarus* 166: 385–402.

Cuzzi, J. N., and Hogan, R. C. 2003. Blowing in the Wind: I. Velocities of Chondrule-Sized Particles in a Turbulent Protoplanetary Nebula. *Icarus* 164: 127–38.

Dominik, C., Blum, J., Cuzzi, J., and Wurm, G. 2006. Growth of Dust as the Initial Step Toward Planet Formation. In *Protostars and Planets V*. Tucson: University of Arizona Press.

Gounelle, M., Shu, F. H., Shang, H., Glassgold, A. E., Rehm, K. E., and Lee, T. 2001. Extinct Radioactivities and Protosolar Cosmic Rays: Self-Shielding and Light Elements. *The Astrophysical Journal* 548: 1051–70.

Han, J., and Brearley, A. J. 2015. Microstructural Evidence for Complex Formation Histories of Amoeboid Olivine Aggregates from the ALHA77307 CO3.0 Chondrite. *Meteoritics & Planetary Science* 50: 904–25.

Han, J., Keller, L. P., Liu, M.-C., Needham, A. W., Hertwig, A. T., Messenger, S., and Simon, J. I. 2020. A Coordinated Microstructural and Isotopic Study of a Wark-Lovering Rim on a Vigarano CAI. *Geochimica et Cosmochimica Acta* 269: 639–60.

Ivanova, M. A., Kononkova, N. N., Krot, A. N., Greenwood, R. C., Franchi, I. A., Verchovsky, A. B., Trieloff, M., Korochantseva, E. V., and Brandstätter F. 2008. The Isheyevo Meteorite: Mineralogy, Petrology, Bulk Chemistry, Oxygen, Nitrogen, Carbon Isotopic Compositions, and 40Ar-39Ar ages. *Meteoritics & Planetary Science* 43: 915–40.

Ivanova, M. A., Lorenz, C. A., Krot, A. N., and MacPherson, G. J. 2015. A Compound Ca-, Al-Rich Inclusion from CV3 Chondrite Northwest Africa 3118: Implications for Understanding Processes During CAI Formation. *Meteoritics & Planetary Science* 50: 1512–28.

Kita, N. T., Yin, Q.-Z., MacPherson, G. J., Ushikubo, T., Jacobsen, B., Nagashima, K., Kurahashi, E., Krot, A. N., and Jacobsen, S. B. 2013. $^{26}$Al-$^{26}$Mg Isotope Systematics of the First Solids in the Early Solar System. *Meteoritics & Planetary Science* 48: 1383–400.

Koch, T. E., Spahr, D., Merges, D., Winkler, B., and Brenker, F. E. 2021. Mg$_2$SiO$_4$ Particle Aggregation Aboard the ISS—Influence of Electric Fields on Aggregation Behavior, Particle Velocity and Shape-Preferred Orientation. *Astronomy & Astrophysics* 653: A1.

Koch, T. E., Spahr, D., Tkalcec, B. J., Lindne, M., Merges, D., Wilde, F., Winkler, B., and Brenker, F. E. 2021. Formation of Chondrule Analogues Aboard the International Space Station. *Meteoritics & Planetary Science* 56: 1669–84.

Komatsu, M., Krot, A. N., Petaev, M. I., Ulyanov, A. A., Keil, K., and Miyamoto, M. 2001. Mineralogy and Petrography of Amoeboid Olivine Aggregates from the Reduced CV3 Chondrites Efremovka, Leoville and Vigarano: Products of Nebular Condensation, Accretion and Annealing. *Meteoritics & Planetary Science* 36: 629–41.

Komatsu, M., Mikouchi, T., and Miyamoto, M. 2009. High-Temperature Annealing of Amoeboid Olivine Aggregates: Heating Experiments on Olivine-Anorthite Mixtures. *Polar Science* 3: 31–55.

Kozub, D., Khmelik, V., Shapoval, J., Chentsov, V., Yatsenko, S., Litovchenko, B., and Starikh, V. 2018.

Helicon Focus 7.0.2 Pro. https://www.heliconsoft.com/heliconsoft-products/helicon-focus/.

Krot, A. N. 2019. Refractory Inclusions in Carbonaceous Chondrites: Records of Early Solar System Processes. *Meteoritics & Planetary Science* 54: 1647–91.

Krot, A. N., Amelin, Y., Bland, P., Ciesla, F. J., Connelly, J., Davis, A. M., Huss, G. R. et al. 2009. Origin and Chronology of Chondritic Components: A Review. *Geochimica et Cosmochimica Acta* 73: 4963–97.

Krot, A. N., Nagashima, K., van Kooten, E. M. M., and Bizzarro, M. 2017. High-Temperature Rims Around Calcium–Aluminum-Rich Inclusions from the CR, CB and CH Carbonaceous Chondrites. *Geochimica et Cosmochimica Acta* 201: 155–84.

Krot, A. N., Petaev, M. I., Russell, S. S., Itoh, S., Fagan, T. J., Yurimoto, H., Chizmadia, L. et al. 2004. Amoeboid Olivine Aggregates and Related Objects in Carbonaceous Chondrites: Records of Nebular and Asteroid Processes. *Chemie der Erde—Geochemistry* 64: 185–239.

Krot, A. N., Petaev, M. I., and Yurimoto, H. 2004. Amoeboid Olivine Aggregates with Low-Ca Pyroxenes: A Genetic Link Between Refractory Inclusions and Chondrules? *Geochimica et Cosmochimica Acta* 68: 1923–41.

Liffman, K., Cuello, N., and Paterson, D. A. 2016. A Unified Framework for Producing CAI Melting, Wark–Lovering Rims and Bowl-Shaped CAIs. *Monthly Notices of the Royal Astronomical Society* 462: 1137–63. https://doi.org/10.1093/mnras/stw1563

Lorenz, C., Ivanova, M., Krot, A., and Shuvalov, V. 2019. Formation of Disk- and Bowl-Shaped Igneous Ca, Al-Rich Inclusions: Constraints from their Morphology, Textures, Mineralogy and Modelling. *Geochemistry* 79: 125523.

Love, S. G., Pettit, D. R., and Messenger, S. R. 2014. Particle Aggregation in Microgravity: Informal Experiments on the International Space Station. *Meteoritics & Planetary Science* 49: 732–9.

MacPherson, G. J., and Grossman L. 1984. "Fluffy" Type A Ca-, Al-Rich Inclusions in the Allende Meteorite. *Geochimica et Cosmochimica Acta* 48: 29–46.

MacPherson, G. J., Grossman, L., Allen, J. M., and Beckett, J. R. 1982. Origin of Rims on Coarse-Grained Inclusions in the Allende Meteorite. 12th Lunar and Planetary Science Conference. pp. 1079–91.

MacPherson, G. J., Grossman, L., Hashimoto, A., Bar-Matthews, M., and Tanaka, T. 1984. Petrographic Studies of Refractory Inclusions from the Murchison Meteorite. *Journal of Geophysical Research: Solid Earth* 89: C299–312.

MacPherson, G. J., Paque, J. M., Stolper, E., and Grossman, L. 1984. The Origin and Significance of Reverse Zoning in Melilite from Allende Type B Inclusions. *The Journal of Geology* 92: 289–305.

Marrocchi, Y., Villeneuve, J., Jacquet, E., Piralla, M., and Chaussidon, M. 2019. Rapid Condensation of the First Solar System Solids. *Proceedings of the National Academy of Sciences* 116: 23461–6.

Marshall, J. R., Sauke, T. B., and Cuzzi, J. N. 2005. Microgravity Studies of Aggregation in Particulate Clouds. *Geophysical Research Letters* 32: L11202.

Moosmann, J., Ershov, A., Weinhardt, V., Baumbach, T., Prasad, M. S., LaBonne, C., Xiao, X., Kashef, J., and Hofmann, R. 2014. Time-Lapse X-Ray Phase-Contrast Microtomography for In Vivo Imaging and Analysis of Morphogenesis. *Nature Protocols* 9: 294–304.

Morris, M. A., and Desch, S. J. 2010. Thermal Histories of Chondrules in Solar Nebula Shocks. *The Astrophysical Journal* 722: 1474–94.

Nakagawa, Y., Nakazawa, K., and Hayashi, C. 1981. Growth and Sedimentation of Dust Grains in the Primordial Solar Nebula. *Icarus* 45: 517–28.

NIST. 2020. NIST: National Institute of Standards and Technology. Solid Phase Heat Capacity. https://webbook.nist.gov/cgi/cbook.cgi?ID=C10034943&amp;Units=SI&Mask=2&Type=JANAFS&Plot=on#JANAFS (6 June 2020).

Nuth, J. N., Berg, O., Faris, J., and Wasiliewski, P. 1994. Magnetically Enhanced Coagulation of Very Small Iron Grains. *Icarus* 107: 155–63.

Ogurreck, M., Wilde, F., Herzen, J., Beckmann, F., Nazmov, V., Mohr, J., Haibel, A., Müller, M., and Schreyer, A. 2013. The Nanotomography Endstation at the PETRA III Imaging Beamline. *Journal of Physics: Conference Series* 425: 182002.

Rubin, A. 2012. A New Model for the Origin of Type-B and Fluffy Type-A CAIs: Analogies to Remelted Compound Chondrules. *Meteoritics & Planetary Science* 47: 1062–74.

Rueden, C. T., Schindelin, J., Hiner, M. C., DeZonia, B. E., Walter, A. E., Arena, E. T., and Eliceiri, K. W. 2017. Image J2: ImageJ for the Next Generation of Scientific Image Data. *BMC Bioinformatics* 18: 529.

Russell, S. S., and Howard, L. 2013. The Texture of a Fine-Grained Calcium–Aluminium-Rich Inclusion (CAI) in Three Dimensions and Implications for Early Solar System Condensation. *Geochimica et Cosmochimica Acta* 116: 52–62.

Shu, F. H., Shang, H., Gounelle, M., Glassgold, A. E., and Lee, T. 2001. The Origin of Chondrules and Refractory Inclusions in Chondritic Meteorites. *The Astrophysical Journal* 548: 1029–50.

Spahr, D., Koch, T. E., Merges, D., Beck, A. A., Bohlender, B., Carlsson, J. M., Christ, O. et al. 2020. A Chondrule Formation Experiment Aboard the ISS: Experimental Set-Up and Test Experiments. *Icarus* 350: 113898.

Steinpilz, T., Joeris, K., Jungmann, F., Wolf, D., Brendel, L., Teiser, J., Shinbrot, T., and Wurm, G. 2020. Electrical Charging Overcomes the Bouncing Barrier in Planet Formation. *Nature Physics* 16: 225–9.

Sugiura, N., Petaev, M. I., Kimura, M., Miyazaki, A., and Hiyagon, H. 2009. Nebular History of Amoeboid Olivine Aggregates. *Meteoritics & Planetary Science* 44: 559–72.

Taillifet, E., Baillié, K., Charnoz, S., and Aléon, J. 2014. Origin of Refractory Inclusion Diversity by Turbulent Transport in the Inner Solar Nebula (Abstract #2086). 45th Lunar and Planetary Science Conference. CD-ROM.

Tkalcec, B. J., Golabek, G. J., and Brenker, F. E. 2013. Solid-State Plastic Deformation in the Dynamic Interior of a Differentiated Asteroid. *Nature Geoscience* 6: 93–7.

Wark, D., and Boynton, W. V. 2001. The Formation of Rims on Calcium-Aluminum-Rich Inclusions: Step I—Flash Heating. *Meteoritics & Planetary Science* 36: 1135–66.

Wark, D. A., and Lovering, J. F. 1977. Marker Events in the Early Evolution of the Solar System: Evidence from Rims on Ca-Al-Rich Inclusions in Carbonaceous Chondrites. Proceedings, 8th Lunar Science Conference. pp. 95–112.

Weidenschilling, S. J. 2003. Radial Drift of Particles in the Solar Nebula: Implications for Planetesimal Formation. *Icarus* 165: 438–42.

Wilde, F., Ogurreck, M., Greving, I., Hammel, J. U., Beckmann, F., Hipp, A., Lottermoser, L. et al. 2016. Micro-CT at the Imaging Beamline P05 at PETRA III. *AIP Conference Proceedings* 1741: 30035.

Wurm, G., and Blum, J. 1998. Experiments on Preplanetary Dust Aggregation. *Icarus* 132: 125–36.

Zhang, M., Clark, B., King, A. J., Russell, S. S., and Lin, Y. 2021. Shape and Porosity of Refractory Inclusions in CV3 Chondrites: A Micro-Computed Tomography (µCT) Study. *Meteoritics & Planetary Science* 56: 500–14.

Zsom, A., Ormel, C. W., Güttler, C., Blum, J., and Dullemond, C. P. 2010. The Outcome of Protoplanetary Dust Growth: Pebbles, Boulders, or Planetesimals? II. Introducing the Bouncing Barrier. *Astronomy & Astrophysics* 513: A57.

# 10 Appendix C - Conference Abstracts

**CHONDRULE-LIKE OBJECTS FORMED BY LIGHTNINGS ABOARD THE INTERNATIONAL SPACE STATION ISS.** T. E. Koch[1*], D. Spahr[1], D. Merges[1], A. A. Beck[1], O. Christ[1], S. Fujita[1], P.-T. Genzel[1], J. Kerscher[1], M. Lindner[1], D. Mederos Leber[2], B. Winkler[1], F. E. Brenker[1]. [1]Goethe University Frankfurt, Institute of Geoscience, Altenhoeferallee 1, 60438 Frankfurt am Main, Germany, *t.koch@em.uni-frankfurt.de, [2]Goethe University Frankfurt, Department of Physics, Max-von-Laue-Strasse 1, 60438 Frankfurt am Main, Germany.

**Introduction:** Chondrule formation theories are still controversially debated and remain among the most discussed issues in studies concerned with planet formation. The formation of chondrules by nebular lightning belongs to one of the most plausible scenarios. This theory was introduced more than 50 years ago [1] and revised by several studies [2-5]. For a time, it appeared that the nebular lightning theory was superseded by the shock wave model [e. g. 6] or a model postulating the formation of chondrules during planet formation [7]. However, a recently published study [4] proposed a new mechanism which could produce the required amount of lightnings in the solar nebular, thus addressing one of the weaknesses of the theory. In addition, a new study on the cooling rate of different chondrules types concludes that lightnings could indeed explain several chondrule properties [8].

Several chondrule formation experiments have been carried out in order to gain more information about the cooling rates and the formation of the different chondrule types [e. g. 5, 9–13]. These experiments include studies using electric discharges or plasma arcs to melt precursor material [e. g., 5, 13].

The influence of gravity is always an important aspect which effects the outcome of planetary science experiments. For these reasons, we developed an experiment named EXCISS (Experimental Chondrule Formation aboard the International Space Station ISS) which was carried out at long-term micro gravity conditions aboard the ISS. In this experiment, synthetic forsterite ($Mg_2SiO_4$) dust particles levitating in a glass sample chamber, were exposed to electrical discharges. The aim of these experiments was to explore if dust particles melt, fuse and/or form chondrule-like objects with the help of arc discharges [14,15]. Another decisive difference to previous experiments (e.g. [5]) is the use of relatively low energy discharges to avoid the fragmentation of the samples.

**Experimental Details:** The experiment was carried out inside a 1.5 U NanoRacks NanoLab aboard the ISS from Nov 2018 to Jan 2019. The sample material consists of well characterized, porous synthetic forsterite dust particles with grain sizes between 80–120 μm. The sample chamber was manufactured of optically transparent glass filled with Ar at 100 mbar pressure. W-electrodes were fused into the glass. The experiments were filmed with a Raspberry Pi Camera V2 using a frame rate of 40 fps.

In total, 81 arc discharges with energies between 1 and 8 J were induced. After sample return in August 2019, we commenced with the analysis of the products by scanning electron microscopy (SEM). Samples were hand-picked, embedded in epoxy, polished and carbon-coated for the SEM analysis.

**Results:** An analysis of the videos showed the accumulation of particles between the electrodes. The first change of the particles was discernible after the 4th arc discharge, and further discharges led to the formation of aggregates from several particles and spherules.

After sample return we identified about 80 objects which are clearly distinct from the initial sample material. These objects vary from small droplet shaped entities to aggregates of more than 10 particles.

The back-scattered electron (BSE) image in Figure 1 shows a close-up of a typical aggregate consisting of parts which were completely molten and are now fused to unaltered grains with a smooth interface. Tungsten from the plasma was incorporated during melting, and as tungsten is incompatible with forsterite, it precipitated along the grain boundaries on crystallization during cooling. The grains are often arranged as bundles of parallel lamellae. Melting also caused the disappearance of the small, evenly distributed pores in the starting material and the formation of larger voids.

The individual melt droplets have a diameter of approx. 100 μm which is similar to the grain size of the starting material, while the agglomerates formed by the fusion of molten and unmolten material have diameters of up to 600 μm. Figure 2 shows a back scattered electron image of a single molten spherule, highlighting the disappearance of the small pores, the formation of larger voids, of a curved smooth surface without the ridges of the initial grains and the precipitation of tungsten along grain boundaries.

**Discussion and Conclusion:** The results clearly show that in our experiment aboard the ISS we were able to completely melt 100 μm sized particles, i.e., melting was not only restricted to grain surfaces. Currently, we cannot discriminate whether melting occurred in the plasma arc or nearby due to thermal radiation. The coexistence of molten and unmolten grains resembles the presence of precursor coarse olivine grains found in natural chondrules [11]. The experiment clearly showed that using low energy discharges lead to the formation of aggregates and chondrule-like objects.

**CHONDRULE-LIKE OBJECTS FORMED BY LIGHTNINGS ABOARD THE INTERNATIONAL SPACE STATION ISS.**

T. E. Koch[1*], D. Spahr[1], D. Merges[1], A. A. Beck[1], O. Christ[1], S. Fujita[1], P.-T. Genzel[1], J. Kerscher[1], M. Lindner[1], D. Mederos Leber[2], B. Winkler[1], F. E. Brenker[1]. [1]Goethe University Frankfurt, Institute of Geoscience, Altenhoeferallee 1, 60438 Frankfurt am Main, Germany, *t.koch@em.uni-frankfurt.de, [2]Goethe University Frankfurt, Department of Physics, Max-von-Laue-Strasse 1, 60438 Frankfurt am Main, Germany.

**Introduction:** Chondrule formation theories are still controversially debated and remain among the most discussed issues in studies concerned with planet formation. The formation of chondrules by nebular lightning belongs to one of the most plausible scenarios. This theory was introduced more than 50 years ago [1] and revised by several studies [2-5]. For a time, it appeared that the nebular lightning theory was superseded by the shock wave model [e. g. 6] or a model postulating the formation of chondrules during planet formation [7]. However, a recently published study [4] proposed a new mechanism which could produce the required amount of lightnings in the solar nebular, thus addressing one of the weaknesses of the theory. In addition, a new study on the cooling rate of different chondrules types concludes that lightnings could indeed explain several chondrule properties [8].

Several chondrule formation experiments have been carried out in order to gain more information about the cooling rates and the formation of the different chondrule types [e. g. 5, 9–13]. These experiments include studies using electric discharges or plasma arcs to melt precursor material [e. g., 5, 13].

The influence of gravity is always an important aspect which effects the outcome of planetary science experiments. For these reasons, we developed an experiment named EXCISS (Experimental Chondrule Formation aboard the International Space Station ISS) which was carried out at long-term micro gravity conditions aboard the ISS. In this experiment, synthetic forsterite ($Mg_2SiO_4$) dust particles levitating in a glass sample chamber, were exposed to electrical discharges. The aim of these experiments was to explore if dust particles melt, fuse and/or form chondrule-like objects with the help of arc discharges [14,15]. Another decisive difference to previous experiments (e.g. [5]) is the use of relatively low energy discharges to avoid the fragmentation of the samples.

**Experimental Details:** The experiment was carried out inside a 1.5 U NanoRacks NanoLab aboard the ISS from Nov 2018 to Jan 2019. The sample material consists of well characterized, porous synthetic forsterite dust particles with grain sizes between 80–120 μm. The sample chamber was manufactured of optically transparent glass filled with Ar at 100 mbar pressure. W-electrodes were fused into the glass. The experiments were filmed with a Raspberry Pi Camera V2 using a frame rate of 40 fps.

In total, 81 arc discharges with energies between 1 and 8 J were induced. After sample return in August 2019, we commenced with the analysis of the products by scanning electron microscopy (SEM). Samples were hand-picked, embedded in epoxy, polished and carbon-coated for the SEM analysis.

**Results:** An analysis of the videos showed the accumulation of particles between the electrodes. The first change of the particles was discernible after the 4th arc discharge, and further discharges led to the formation of aggregates from several particles and spherules.

After sample return we identified about 80 objects which are clearly distinct from the initial sample material. These objects vary from small droplet shaped entities to aggregates of more than 10 particles.

The back-scattered electron (BSE) image in Figure 1 shows a close-up of a typical aggregate consisting of parts which were completely molten and are now fused to unaltered grains with a smooth interface. Tungsten from the plasma was incorporated during melting, and as tungsten is incompatible with forsterite, it precipitated along the grain boundaries on crystallization during cooling. The grains are often arranged as bundles of parallel lamellae. Melting also caused the disappearance of the small, evenly distributed pores in the starting material and the formation of larger voids.

The individual melt droplets have a diameter of approx. 100 μm which is similar to the grain size of the starting material, while the agglomerates formed by the fusion of molten and unmolten material have diameters of up to 600 μm. Figure 2 shows a back scattered electron image of a single molten spherule, highlighting the disappearance of the small pores, the formation of larger voids, of a curved smooth surface without the ridges of the initial grains and the precipitation of tungsten along grain boundaries.

**Discussion and Conclusion:** The results clearly show that in our experiment aboard the ISS we were able to completely melt 100 μm sized particles, i.e., melting was not only restricted to grain surfaces. Currently, we cannot discriminate whether melting occurred in the plasma arc or nearby due to thermal radiation. The coexistence of molten and unmolten grains resembles the presence of precursor coarse olivine grains found in natural chondrules [11]. The experiment clearly showed that using low energy discharges lead to the formation of aggregates and chondrule-like objects.

The cooling rate is sufficiently slow to allow the formation of crystals with edge lengths of more than 15 μm.

**References:**
[1] Whipple F. L. (1966) *Science* 153, 54–56. [2] Horányi, M. et al. (1995) *Icarus* 114, 174–185. [3] Desch S. J. and Cuzzi, J. N. (2000) *Icarus* 143, 87–105. [4] Johansen A. and Okuzumi A. (2018) *Astron. & Astrophys.* A31, 1–22. [5] Güttler C. et al. (2008) *Icarus*, 195, 504–510. [6] Desch S. J. and Conolly H. C. Jr (2002) *Meteoritics & Planetary Science* 37, 183–207. [7] Johnson B. J. et al. (2015) *Nature* 517, 339–341. [8] Libourel G. and Portail M. (2018) *Sciences Advances* 4, 1–12. [9] Conolly H. C. Jr and Hewins R. H. (1995) *Geochim. Cosmochim. Ac.* 59, 3231–3246. [10] Hewins R. H. and Fox G. E. (2004) *Geochim. Cosmochim. Ac.* 68, 917–926. [11] Hewins R. H. et al. (2005) *Chondrites and the Protoplanetary Disk* 341, 287–316. [13] Morlok A. et al. (2012) *Meteoritics & Planet. Sci.* 47, 2269–2280. [14] Koch T. E. et al. (2018) *Ann. Meet. Met. Soc.* 82, Abstract #6139. [15] Koch T. E. et al. (2019) *LPSC L*, Abstract#1560.
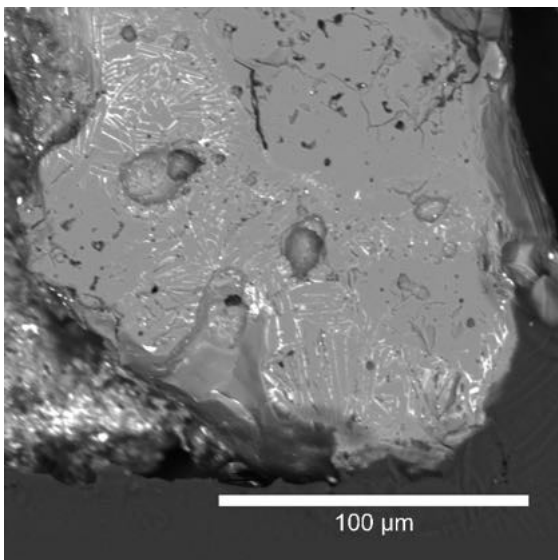
Fig. 1: SEM BSE image of an aggregate of approx. 5 grains with olivine (grey) and tungsten (white). The image reveals a completely molten area with precipitated tungsten at the grain boundaries (left) joined to unaltered grains with characteristic small pores.
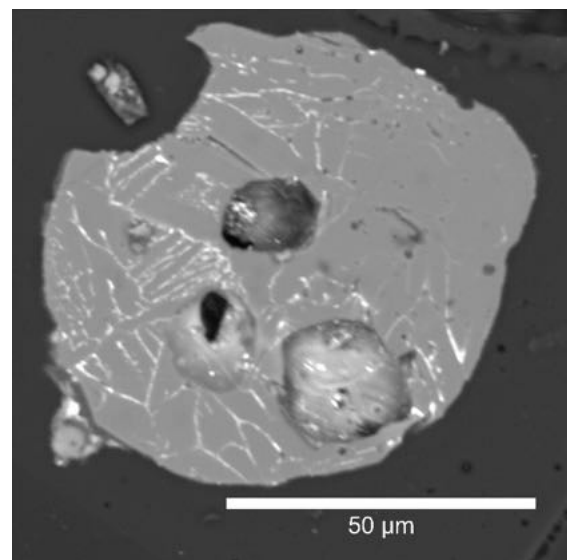


Fig. 2: SEM BSE image of a melt spherule. Tungsten (white lines) has precipitated along the grain boundaries of forsterite crystals (grey). Instead of the evenly distributed small pores in the starting material significantly larger voids are now present.

# SHOCK TEMPERATURE RECORDED BY GRAPHITE IN UREILITES FROM ALMAHATA SITTA.

Anna Barbaro[1], M. Chiara Domeneghetti[1] Moreno Meneghetti[2], Lucio Litti[2], Anna Maria Fioretti[3], Cyrena Goodrich[4], Oliver Christ[5], Frank E. Brenker[6], Muawia H. Shaddad[7], Matteo Alvaro[1], Fabrizio Nestola[5,6]; [1]Department of Earth and Environmental Sciences, University of Pavia, Pavia, Italy (anna.barbaro01@universitadipavia.it; chiara.domeneghetti@unipv.it); [2]Department of Chemical Sciences, University of Padova, Padova, Italy; [3]CNR Institute of Geoscience and Earth Resources, Padova, Italy; [4]Lunar and Planetary Institute, USRA, Houston TX USA (goodrich@lpi.usra.edu); [5]Department of Geosciences, University of Padova, Padova, Italy (fabrizio.nestola@unipd.it); [6]Geoscience Institute, Goethe-University Frankfurt, Frankfurt, Germany; [7]Department of Physics and Astronomy, University of Khartoum, Khartoum, Sudan;

**Introduction:** Ureilites are a major group of achondrites that have very high (up to ~8.5 wt.%) carbon contents [1,2]. The origin and history of their carbon phases (mainly graphite and minor diamond) are important for understanding their petrogenesis, and the distribution of carbon in the early solar system. We have been studying the origin of diamonds in ureilites from Almahata Sitta [3,4]. The Almahata Sitta meteorite fell in 2008 from the impact of asteroid 2008 $TC_3$, and is a polymict breccia with approximately 70% ureilitic clasts [5,6]. These ureilite samples have the lowest degree of terrestrial weathering of any ureilites, which makes them ideal for studying the origin of the carbon phases in ureilites.

In Almahata Sitta (AhS) ureilites 72 and 209b [4], diamonds with crystallite sizes at the nanometric scale (diamond particles < 100 nm) were found associated with nanographite. This same association was found in main group ureilite NWA 7983, and also included micrometric sized diamonds [3,4]. The diamonds in these samples were interpreted to be a product of impact shock from original graphite.

**Aim:** In order to obtain reliable information on the temperature evolution recorded by the graphite phases in ureilites, we applied a graphite-based geothermometer (applied to chondrites by [7], and to other AhS ureilites by [8]) on non-polished fragments of AhS 209b, AhS 72 and AhS A135A.

In addition, using calibrations by [9,10] based on the ratio of Raman D-bands and G-bands intensities, we were able to determine the crystallite size of graphite. These results could provide crucial information on the thermal history and origin of the graphite and associated diamonds.

**Experimental:** The Raman spectra of graphite from three ureilitic stones (AhS 209b, AhS 72 and AhS A135A) were collected by Micro-Raman Spectroscopy (MRS). **Fig.1** shows the characteristic peaks positions of the G, D and D' bands of graphite present in the investigated AhS samples. These analyses were performed in order to retrieve the temperature recorded by graphite, hereafter $T_{max}$, using the approach adopted by [8]. This approach is based on the measurement of the Full Width at Half Maximum (FWHM) of the graphite G band which, by comparison to previous geothermometric approaches, can provide temperatures of high temperature environments (i.e.>900-1000 °C). In addition, the peak position of the graphite Raman spectra and the I(D)/I(G) ratio (I=integrated intensity; D=D band; G=G band) obtained by MRS allowed us to assess the crystallite size of the investigated graphite [8].
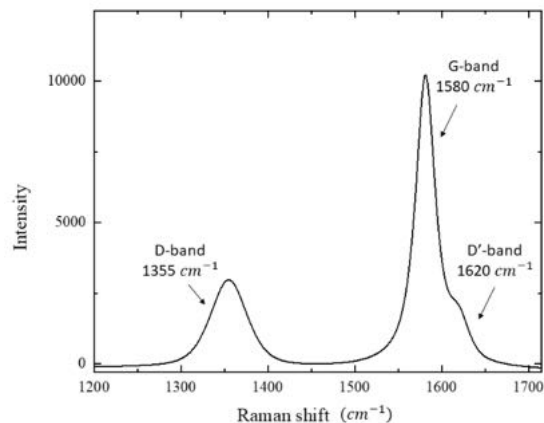


**Fig.1** Raman spectrum of graphite in AhS 209B.

**Results:** The calculated temperatures are close to 1200-1300 °C (±120 °C) slightly higher than 990 (±120) °C reported by [8] on the ureilitic fragment AhS 7. However, if we account for the temperature uncertainties of this approach (i.e. ±120 °C), our data agree with those by [8]. This range of temperatures also agrees with peak equilibration temperatures of ureilites determined by pyroxene thermometry [11,12]. Graphite in our samples is disordered and shows a crystallite size ranging between about 60 and 150 nm in agreement with that observed in [4] by X-ray diffraction.

**Conclusion:** Combining our results with those of [4,5] we suggest that the mineral association of nanodiamonds, microdiamonds and nanographite in ureilites was produced in an impact event at peak pressures not higher than ~15 GPa (based on olivine mosaicism, see [4]). The temperature obtained from graphite would represent the temperature related to the shock event. Although the obtained temperature is similar to igneous equilibration temperatures of ureilites, the observation that the graphite is

nanometric, rather than in the form of large single crystals as in non-shocked ureilites [1,13], argues that it- records shock conditions. This impact shock event could have occurred during the catastrophic disruption of the ureilite parent body.

**References:**
[1]     C. A. Goodrich et al. (2015), Meteorit. Planet. Sci. **50**, 782-809.
[2]     G. . Vdovykin, *Space Sci. Rev.* **10**, 483–510 (1970).
[3]     C. A. Goodrich et al. (2019), this conference.
[4]     F. Nestola, et al. (2020), submitted (PNAS).
[5]     M. H. Shaddad et al. (2010), , Meteorit. Planet. Sci. **1589**, 1557–1589.
[6]     P. Jenniskens (2009), et al., Nature **458**, 485–488.
[7]     G. D. Cody, et al. (2008), Earth Planet. Sci. Lett. **272**, 446–455.
[8]     A. J. Ross, et al. (2011), Meteorit. Planet. Sci. **46**, 364–378.
[9]     F. Tuinstra, J. L. Koenig, J. (1970), Chem. Phys. **53**, 1126–1130.
[10]    A. C. Ferrari, J. Robertson (2000), Phys. Rev. B **61**, 95–107.
[11]    J. S. Herrin, et al. (2010), Meteorit. Planet. Sci. **45**, 1789–1803.
[12]    P. H. Warren, A. E. Rubin (2010), Geochim. Cosmochim. Acta **74**, 5109–5133.
[13]    A. H. Treiman, L. Berkley, (1994), *Meteorit. Planet. Sci.* **848**, 843–848.

# CARLETONMOOREITE (Ni₃Si) IN SHOCKED DIAMOND-BEARING KENNA UREILITE.

A. Barbaro[1]*, M. C. Domeneghetti[1], K. D. Litasov[2, 3], L. Ferrière[4], L. Pittarello[4], O. Christ[5], S. Lorenzon[5], M. Alvaro[1] and F. Nestola[5,6]; [1]Department of Earth and Environmental Sciences, University of Pavia, Pavia, Italy (*anna.barbaro01@universitadipavia.it; chiara.domeneghetti@unipv.it), [2]Vereshchagin Institute for High Pressure Physics RAS, Troitsk, Moscow, 108840, Russia, [3] Fersman Mineralogical Museum RAS, Moscow, 115162, Russia, [4]Natural History Museum, Department of Mineralogy and Petrography, Burgring 7, 1010 Vienna, Austria, [5] Department of Geosciences, University of Padova, Padova, Italy (fabrizio.nestola@unipd.it), [6]Geoscience Institute, Goethe-University Frankfurt, Altenhöferalee 1, 60348 Frankfurt, Germany.

**Introduction:** The origin and history of carbon phases (up to ~8.5 wt.%) in ureilites are important for understanding their petrogenesis and the distribution of carbon in the early solar system. Ureilites are a major group of achondrites [1, 2], which consist of ultramafic rocks, mainly composed of olivine and pigeonite, and minor carbon (mostly graphite and diamond) [3]. Recent studies on ureilites [4, 5, 6] stated that the coexistence of large monocrystalline diamonds, nanodiamonds together with nanographite in ureilites could be explained by the transformation from graphite enhanced by the catalysis of Fe-Ni-C liquid during impact shock events.

**Sample and methodology:** This study was performed on the Kenna meteorite, which is an ureilite recovered in February 1972 near the town of Kenna, Roosvelt County, New Mexico (USA). In order to obtain reliable information on the carbon-bearing aggregates (diamond, graphite, and minor phases) contained in the Kenna ureilite, we adopted the same experimental approach by [4, 5, 6]. In particular, we performed scanning electron microscopy [equipped with energy dispersive spectroscopy (SEM-EDS)], micro-X-ray diffraction (XRD), and micro-Raman spectroscopy (MRS) to characterize the carbon phases and to estimate the pressure (by textural features of silicates) and temperature (by graphite geothermometry [7, 8]) conditions undergone by this meteorite.

**Results and Discussion:** In addition to olivine and pigeonite, within the carbon-bearing areas we identified microdiamonds (up to about 10 μm in size), nanographite and magnetite. During our investigation, for the first time in ureilites, and as a second finding in a natural sample, the Ni₃Si phase, called carletonmooreite (IMA 2018-068), was found. It was originally discovered in 2018 within the Norton County aubrite meteorite [9,10].

The shock features observed in the silicate minerals as well as the presence of microdiamonds and nanographite indicate that Kenna underwent a shock event with a peak pressure of at least 15 GPa. Temperatures estimated using a graphite geothermometer are close to 1180 °C. Thus, Kenna is a medium-shocked ureilite, yet it contains microdiamonds, which are typically found in highly shocked carbon-bearing meteorites, instead of the more common nanodiamonds. This can be explained by a relatively long shock event duration (in the order of few seconds) and/or by the catalytic effect of Fe-Ni phases (e.g., carletonmooreite) known to favor the diamond crystallization.

**Conclusions:** Combining our results, with those in [4, 5, 6], we confirm that the mineral association constituted by nanodiamonds, microdiamonds, and nanographite found in ureilites was produced by impact(s) at peak pressures no lower than ~15 GPa [4]. The nanometric size of graphite and carletonmooreite indicates that they record shock conditions which occurred during impact events involving the ureilite parent body. Then, the temperature obtained from graphite would represent the temperature related to the shock event. The presence of carletonmooreite (Ni₃Si) in the Kenna sample also highlights the important role that Fe-Ni phases can play in diamond growth.

**References:** [1] Berkley J. L. and Jones J. H. (1982) *J. Geophys. Res.* 87:A353–A364. [2] G. P. Vdovykin (1970) *Space Sci. Rev.* 10:483–510. [3] Goodrich C. A. (1992) *MAPS* 27:327–352. [4] Nestola F. et al. (2020) *PNAS* 41:25310–25318. [5] Barbaro A. et al. (2020) *Minerals* 10:1005. [6] Barbaro et al. (2021a) *Am. Min.* (accepted; https://doi.org/10.2138/am-2021-7856). [7] Cody G. D. et al. (2008) *Earth Planet. Sci. Lett.* 272:446–455. [8] Ross A. J. et al. (2011) *MAPS* 46:364–378. [9] Ma C. et al. (2018) *Eur. J. Mineral.* 30:1037–1043. [10] Garvie L. A. J. et al. (2021) *Am. Min.* (in press; https://doi.org/10.2138/am-2021-7645).

**FORMATION OF FUSED AGGREGATES ABOARD THE ISS WITH IMPLICATIONS FOR EARLY SOLAR SYSTEM PARTICLE AGGREGATION.** T. E. Koch[1], D. Spahr[1], B. J. Tkalcec[1], O. Christ[2], P.T. Genzel[1], D. Merges[1], F. Wilde[3], B. Winkler and F. E. Brenker[1,4]

[1]Insitute of Geosciences, Goethe University Frankfurt, 60438 Frankfurt am Main, Germany, [2] Department of Geoscience, University of Padua, Via Gradenigo 6, 35131 Padua, Italy, [3]Helmholtz-Zentrum Hereon, Max-Planck Strasse 1, 21502 Geesthacht, Germany [4]Hawaiʻi Institute of Geophysics and Planetology, School of Ocean and Earth Science and Technology, University of Hawaiʻi at Mānoa, 1680 East-West Road, Honolulu, HI 96822, USA

**Introduction:** Calcium-aluminum-rich inclusions (CAIs) are the oldest material of our Solar System [e. g. 1] and likely witnesses of early aggregation processes [e. g. 2–4]. Fluffy-type CAIs have very irregular, fractal structures and the question arises how they could survive transportation to the outer protoplanetary disk (PPD), chondrite aggregation and compaction. Melting events were considered to be involved in the formation of different CAI characterstics such as igneous type B CAIs, Wark-Lovering-rims and compound CAIs [3–6].

We developed an experiment which was carried out under long-term microgravity conditions aboard the International Space Station (ISS) to combine aggregation and thermal annealing of dust particles [9]. In the study presented here, we show the formation of aggregates using flash heating under microgravity conditions, which can be linked to the formation of refractory inclusions with regard to their morphology and microstructure.

**Experimental Set-up:**  The experimental set-up was mounted inside a $10 \times 10 \times 15$ cm$^3$ sized container [9]. The sample chamber was manufactured from glass with  a size of $\approx 2 \times 2 \times 2$ cm$^3$.  Arc discharges with energies of 5–8 J and durations between 300 and 500 μs per discharge were induced and the experiments were filmed [9]. The initial sample material consisted of well-characterized synthetic forsterite particles in the size range of 80–130 μm [9].

**Methods:** The resulting aggregates were analyzed using synchrotron micro-CT, scanning electron microscopy (SEM) and electron back-scattered diffraction (EBSD) and morphologies were compared with those of natural CAIs in Northwest Africa (NWA) 13656, a CAI-rich CV3 chondrite.

**Results:** The fused aggregates can be divided into three groups regarding their morphology: (1) elongated aggregates consisting of $\approx$ 3 to 15 initial grains with a ratio of longest to shortest dimension of $\approx$ 2; (2) three winged boomerang-shaped fractal aggregates formed from $\approx$ 5–20 particles: and (3) aggregates with a bulk center of $\approx$ 5–20 fused particles. These three morphologies are similar to the natural fluffy-type CAIs observed in NWA 13656. The analysis of polished fractal aggregates showed that the particles have various degree of melting. Some aggregates show no melt intersection between the particles. Some particles in the aggregates are surrounded by igneous rims while the center of the grain remained unprocessed. EBSD revealed that the rims have a crystallographic preferred orientation with the [001] axis perpendicular to the surface. The bulk aggregates consist of fused particles with various degrees of melting. The high cooling rates and particle velocities determined for the single particles imply that the particles aggregated and fused in a very short time < 0.5 s.

**Discussion & Conclusion:** The morphologies of many aggregates strongly resemble the typical shapes of fractal fluffy-type CAIs. The particles probably collided still molten on the surface and solidified fast still in motion. The elongated aggregates show similar dimension ratios to natural CAIs [9]. Since these fractal structures have survived the long and turbulent transportation from the ISS to the Goethe University in Frankfurt, it is plausible that a small amount of melting may have supplied the required stability for natural fractal CAIs to have survived transportation to chondrule formation regions and aggregation to planetesimals.

The formation of the bulk aggregates by grain collision with different degrees of melting resembles observations in natural CAIs  [4]. Igneous rims surrounding some of the resulting particles remind in thickness and crystal orientation of natural Wark-Lovering rims [10], however this requires further investigation since our experiment was limited to pure forsterite.. These results imply that localized (flash)-heating events with subsequent aggregation can form aggregates which show many different CAI characteristics.

**References:** [1] Connelly J. N. et al. (2012) S*cience* 338, 651–655. [2] Dominik C. et al. (2006) *Protostars Planets V Rev.* 783–800.  [3] Rubin A. (2012) *Meteoritics & Planetary Science* 47, 1062–1074. [4] Ivanova et al. (2015) *Meteorit. Planet. Sci.* 50, 1512–1528. [5] Aléon J. et al. (2013) *LPS XLIV,* Abstract #2530. [6] Wark D. and Boynton W. V. (2001) *Meteoritics & Planetary Science* 36, 1135–1166. [7] Spahr D. et al. (2020) *Icarus.* 350, 113898. [8] Koch T. E. et al. (2021) *LPS LII*, Abstract #1950. [9] Zhang M et al. (2021) *Meteorit. Planet. Sci.* 56, 500–514. [10] Bolser D. et al. (2016) *Meteoritics & Planetary Science* 51, 743–756.

# SHOCK TEMPERATURE RECORDS IN GRAPHITE FROM THE NORTHWEST AFRICA 6871 UREILITE

O. Christ[1*], A. Barbaro[2], F.E. Brenker[3], M.C. Domeneghetti[2], F. Nestola[1,3], [1]Department of Geosciences, University of Padova, Via Gradenigo 6, 35131 Padova, Italy (*oliver.christ@phd.unipd.it), [2]Department of Earth and Environmental Sciences, University of Pavia, Via Ferrata 1, 27100 Pavia, Italy, [3]Geoscience Institute, Goethe-University Frankfurt, Altenhöferallee 1, 60348 Frankfurt, Germany

**Introduction:** Ureilites are coarse-grained ultramafic achondrites consisting mainly of olivine and pyroxene [1]. In addition, some contain carbon in concentrations of up to 8 wt.% [2], which occurs mainly in form of graphite and diamond. Although the presence of diamond in ureilites is know for more than a century [3], the formation process of these diamonds remains a higly debated topic. Recent publications regarding this topic proposed that ureilitic diamonds formed either in a large planetary body [4] or during impact events with destroyed the ureilite parent body catalyzed by the presence of (Fe,Ni,Co)-C melts [5,6,7,8]. Based on this, we investigated the ureilite Northwest Africa 6871 with the same methological approach as [6] in combination with a graphite-geothermometer, to understand if microdiamond is a common feature of shocked ureilites and to further characterize the shock event which destroyed the ureilite parent body.

**Sample and Methods:** Northwest Africa 6871 is a find from 2011 which was classified as a highly shocked (S6) ureilite [9]. We used scanning electron microscopy (SEM) with energy dispersive spectroscopy (EDS) to identify carbon bearing aggregates throughout the sample. After identifying aggregates based on their chemistry, they were cut out of the sample for phase identification by micro-Raman spectroscopy (MRS) and micro-X-ray diffraction (XRD). In addition to the phase identification, we applied a graphite-geothermometer based on micro-Raman spectroscopy [10,11].

**Results and Discussion:** XRD revealed that the carbon bearing aggregates consist of nanographite, nanodiamond and microdiamond, but also metallic iron and sulfides. Detailed observations of the diffractograms reveal that graphite is partly compressed and that diamond shows stacking-disorder. Both, compressed graphite and the diamond stacking faults can be used as shock indicators [12,13]. On the basis of MRS data, the graphite based geothermeter delivered a mean temperature of about 1412°C. The occurrence of "compressed" nanographite [12], nanodiamond (with stacking-disorder) and microdiamond aggregates, which are intergrown with metallic iron and sulfides, supports the theory that diamond in ureilites were formed by one or more shock events.

**Conclusions:** Our results are similar to those of [6,7,8] and show that microdiamond is a general constituent of carbon bearing aggregates in shocked ureilites. The formation of microdiamond took place during an impact event which effected the ureilite parent body and triggered the transformation of graphite to diamond, catalyzed by (Fe,Ni,Co)-C melts at pressures as low as 15 GPa [6]. Compared to available literature data, the temperature of 1412°C measured by MRS on graphite represents the highest temperature recorded for a ureilite so far [7,8,11]. Further, it exceeds the magmatic temperature for ureilites obtained by two-pyroxene thermometer which is 1190–1250 °C [14]. Hence, we ascribe the temperature recorded by graphite to the shock event which destroyed the ureilite parent body, reduced the size of graphite to nanometric and formed the diamonds [15].

**References:** [1] Goodrich (1992) *Meteoritics* **27**. [2] Goodrich et al. (2020), *Lunar and Planetary Science Conference*. [3] Kunz (1888), *Science*. [4] Nabiei et al. (2018), *Nature Communications* **9**. [5] Litasov et al. (2019) *Minerals* **9**. [6] Nestola et al. (2020), *Proceedings of the National Academy of Sciences* **117**. [7] Barbaro et al. (2020), *Minerals* **10**. [8] Barbaro et al. (2021), accepted in *American Mineralogist* (https://doi.org/10.2138/am-2021-7856). [9] Ruzicka et al. (2014) The Meteoritical Bulletin, No. 100. [10] Cody et al. (2008), *Earth and Planetary Science Letters.* **272**. [11] Ross et al. (2011), *Meteoritics & Planetary Science* **46**. [12] Nakamuta and Aoki (2000) *Meteoritics & Planetary Science* **35**. [13] Németh et al. (2014) *Nature Communications* **5**. [14] Herrin et al. (2010), *Meteoritics & Planetary Science* **45**. [15] Christ et al. (under review).

**FORSTERITE DUST AGGREGATION ABOARD THE INTERNATIONAL SPACE STATION (ISS).** T. E. Koch[1*], D. Spahr[1], D. Merges[1], O. Christ[1,2], P.-T. Genzel[1], M. Lindner[1], B. Winkler[1] and F. E. Brenker[1]. [1]Goethe University Frankfurt, Institute of Geoscience, 60438 Frankfurt am Main, Germany, [2]University of Padua: Padova, Veneto, Italy. *t.koch@em.uni-frankfurt.de

**Introduction:** Particle aggregation plays a major role in different stages of planet formation. The formation of particle cluster aggregates is considered to be among the first processes leading to planet formation in the Solar Nebula [1,2] and amoeboid olivine aggregates and fluffy-type Calcium-Aluminum-rich inclusions, are thought to be formed by particle aggregation at an early stage [3,4]. Many chondrules have accreted a layer of dust, the so called fine grained rim [5]. However, there are many open questions regarding the size range, morphology, and sticking probability to understand these complex solar nebular processes in detail [1]. Electrostatic forces were proposed to affect the aggregation of dust particles and chondrules. First experiments have already shown the influence of electrostatic forces on the sticking behavior of particles [6, 7].

We carried out an experiment aboard the International Space Station ISS, which was primarily developed to examine chondrule formation [8]. As a positive side effect, we could study the aggregation behavior of dust particles in an electric field and their response to electric discharges. The observation of aggregation processes and the behavior of the particles after an electric discharge can potentially offer important constraints on of how particles behave after a shock wave or lightning propagated through the solar nebular.

**Experiments:** The experiment was carried out inside a 1.5 U NanoRacks NanoLab aboard the ISS from Nov 2018 to Jan 2019 [8]. The sample material consisted of well-characterized, polycrystalline, synthetic $Mg_2SiO_4$ forsterite dust particles with grain sizes between 80–130 µm [8]. The particles are angular with irregular shapes. The sample chamber was manufactured of optically transparent glass filled with Ar at 100 mbar pressure. W-electrodes were fused into the glass. The experiments were filmed with a Raspberry Pi Camera V2 using a frame rate of 40 fps. The trajectories and the resulting velocities of the different particles after ignitions were analyzed frame by frame. Due to the low frame rate, the particle velocities in the approx. first 10 frames were determined by the length of particle traces during an exposure.

**Results:** The first images recorded after the experiment commenced showed that the space between the electrodes was completely empty. Charging of the capacitor led to the appearance of a $2 \times 2 \times 4$ mm sized aggregate. This aggregate must have formed prior to the start of the experiment. This aggregate probably contained all dust particles in the sample chamber. Low energetic electric discharges disintegrated some parts of the aggregate; however, the particles reunited within seconds. When the capacitors were charged to higher voltages, the stronger electric field caused an alignment of the particles along the field lines. The longest particle axis was thereby oriented parallel to the field lines. High energetic arc discharges accelerated the particles to velocities up to $60\,mm\,s^{-1}$ with a subsequent exponential velocity decrease to $< 5\,mm\,s^{-1}$ within 0.5 s. The particles slowly returned to the space between the electrodes and the number of aligned particles decreased with ongoing discharges.

**Discussion:** Our experiment demonstrated that dust particles can form large, closely packed aggregates under microgravity conditions. The observed aggregate was relatively stable regarding low energetic discharges and sputtered particles returned immediately to the aggregate, which shows strong effect of attraction between the particles. The electric field between the electrodes led to the strong deceleration of fast particles. Furthermore, the strong electric field led to longitudinally alignment of the particles, which can decrease the packing density of aggregates compared to random oriented, heterogeneous-shaped grains. Preferred orientation of elongated crystals was e. g. observed in dust rims and matrix which was interpreted as an effect of low energetic shock waves [5,9], however we have shown that electric fields can also lead to orientation effects.

**References:** [1] Wurm G. and Blum J. (1998) *Icarus 132*, 125–136. [2] Blum J. and Wurm G. (2000) *Icarus 143*, 138–146. [3] Krot, A. N et al. (2004) *Geochim. Cosmochim. Acta* 68, 1923–1941 [4] MacPherson, G. J. et al. (2005) *Chondrites and the Protoplanetary Disk 341*, 225–250. [5] Bland P. A. et al. (2011) *Nat. Geosci., 4* 244–247. [6] S. G. Love G. G. et al. (2014) *Meteorit. Planet. Sci.* 49, 732–739. [7] T. Steinpilz et al. (2020) *Nat. Phys.* 16, 225–229. [8] D. Spahr et al. (2020) *Icarus* 350. [9] Watt, L. (2006) *Meteorit. Planet. Sci.* 41, 989–1001.

**IMPACT SHOCK ORIGIN OF CARBON PHASES IN YAMATO 74123 UREILITE.** A. Barbaro[1], F. Nestola[2,3], L. Pittarello[4], L. Ferrière[4], M. Murri[5], K. D. Litasov[6,7], O. Christ[2], M. Alvaro[1], and M. C. Domeneghetti[1]; [1]Department of Earth and Environmental Sciences, University of Pavia, Pavia, Italy (anna.barbaro01@universitadipavia.it; chiara.domeneghetti@unipv.it); [2]Department of Geosciences, University of Padova, Padova, Italy (fabrizio.nestola@unipd.it); [3]Geoscience Institute, Goethe-University Frankfurt, Altenhöferalee 1, 60323 Frankfurt, Germany; [4]Natural History Museum Vienna, Department of Mineralogy and Petrography, Burgring 7, 1010 Vienna, Austria; [5]Department of Earth and Environmental Sciences, University of Milano-Bicocca, I-20126 Milano, Italy; [6]Vereshchagin Institute for High Pressure Physics RAS, Troitsk, Moscow, 108840, Russia; [7]Fersman Mineralogical Museum RAS, Moscow, 115162, Russia.

**Introduction:** The origin and history of carbon phases (up to ~8.5% wt.%) in ureilite meteorites are controversial and important for understanding their petrogenesis and the distribution of carbon in the early solar system. Ureilites are a major group of achondrites [1, 2], and consist of ultramafic rocks, mainly composed of olivine and pigeonite and minor interstitial carbon (mostly graphite and diamond) [3]. Recent studies on ureilites [4, 5] proposed that the coexistence of large monocrystalline diamonds and nanodiamonds together with nanographite in these meteorites could be explained by the transformation from graphite through the catalysis of Fe-Ni-C melts triggered by an impact event. Yamato 74123 (Y-74123) is an Antarctic ureilite found in February 1974 by the Japanese expedition on the Yamato mountains. This is the first work focusing in detail on the investigation of carbon phases in Y-74123 [6].

**Aim:** Our study aims at providing further evidence of shock origin for diamond in ureilites and, at the same time, at shedding light on the importance of the heterogeneous propagation and local scattering of the shock wave and the role of Ni-Fe bearing alloys in diamond crystal growth during impact event(s).

In order to obtain reliable data on the carbon-bearing aggregates (i.e., diamond, graphite, and other minor phases) from the Y-74123 ureilite, we used here the same experimental techniques previously adopted by [4, 5].

**Methods:** Our investigations were performed using a scanning electron microscope equipped with energy dispersive X-ray spectroscopy (SEM-EDS) in low vacuum mode, micro-X-ray diffraction (XRD), and micro-Raman spectroscopy (MRS). These techniques allow the characterization of the carbon phases and the estimation of the pressure (by textural features of silicates) and temperature (by graphite geothermometry [7, 8]) conditions experienced by Y-74123. In detail, the Full Width Half Maximum values of the G-band of graphite were used to apply the geothermometer by [7, 8] with the aim to calculate the temperature range recorded by graphite ($T_{max}$) in this meteorite.
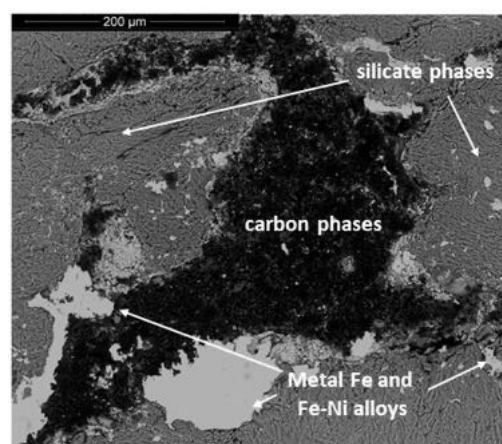


**Figure 1.** BSE image of a carbon aggregate from which the investigated carbon bearing subsample was removed. Also note the presence of silicate phases and metal Fe and Fe-Ni alloys (metal + troilite + oxide).

**Results:** Petrographic observations on silicate phases (such as undulate extinction, planar fractures, and locally, mosaicism in olivine) suggest that Y-74123 was shocked at pressure in the range of 15-20 GPa, corresponding to a shock level S4 [9, 10, 11]. Our SEM analysis of a non-carbon coated Y-74123 fragment confirmed the presence of silicate phases and interstitial carbon phases intergrown with Fe-Ni metals (Fig. 1).

XRD analysis revealed, in addition to olivine and pigeonite, the coexistence of nanodiamond and microdiamonds (up to about 10 μm in size) together with nanographite and troilite within the carbon-bearing areas. The average size of nanodiamonds and nanographite was estimated to 11-15 and 8 nm, respectively, using Scherrer equation [12].

MRS analysis, performed on the same subsample, showed that graphite in Y-74123 is disordered. Our calculations indicate a $T_{max}$ between 1265 and 1365 °C.

**Discussion:** The coexistence of microdiamond nanodiamonds, and nanographite together with Fe-

phases, as revealed by XRD, is similar to observatio[...] reported by [4]. The apparent local differences in size [...] the newly formed diamonds, i.e., nano- to micro-met[...] in size, may result from a heterogeneous propagation a[...] local scattering of the shock wave within a heterogene[...] sample [13]. The temperature range obtained using t[...] geothermometer by [7, 8] is slightly higher than t[...] temperature reported by [8] on the ureilitic fragment [...] Almahata Sitta (AhS) #7 (990 °C). However, if [...] account for the temperature uncertainties of this approa[...] (i.e., ±120 °C [9]), our data agree with those obtain[...] using the same approach on AhS fragments [5].

**Conclusions:** Combining our SEM, XRD, and MRS [...] results together with the shock-deformation features [...] observed in olivine, such as planar fractures and mosaicism, we suggest that diamond grains in Y-74123 were formed by a shock event ($\geq$ 15 GPa) on the Ureilitic Parent Body. These results on Y-74123 are consistent with those obtained on the NWA 7983 ureilite [4] and further support the hypothesis that the simultaneous formation of nano- and microdiamonds is likely related to the catalytic effect of Fe-Ni melts and the heterogeneous propagation and local scattering of the shock wave, as already reported for Almahata Sitta ureilite fragments by [4]. The heterogeneous distribution of shock effects in ureilites can be mainly attributed to shock impedance contrast between contiguous phases [13].

In addition, since the XRD observation shows that graphite is nanometric in size, this supports the assumption that graphite was formed by shock. Thus, the temperature estimated here, between 1265 and 1365 °C, as obtained from graphite, represents the peak temperature experienced by the sample during the impact event.

**References:**
[1]     Berkley J. L. and Jones J. H. 1982. *JGR,* 87, A353–364.
[2]     Vdovykin G. 1970. *Space Sci. Rev.* **10**, 483–510.
[3]     Goodrich C. A. et al. 1992. *MAPS.* **27**, 327–352.
[4]     Nestola F. et al. 2020. *PNAS* **41**, 25310–25318.
[5]     Barbaro A. et al. 2020. *Minerals* **10**, 1005 https://doi.org/10.3390/min10111005.
[6]     Barbaro A. et al. 2021. *Am. Min.* Under review.
[7]     Cody G. D. et al. 2008. *Earth and Plan. Sci. Lett.* **272**, 446–455.
[8]     Ross A. J. et al. 2011. *MAPS* **46**, 364–378.
[9]     Stöeffler D. et al. 1991. *Geochim. et Cosmochim. Acta* **55**, 3845–3867.
[10]     Stöeffler D. et al. 2018.*MAPS* **49**, 5-49.
[11]      Nakamuta Y. et al. 2016. *J. Mineral. Petrol. Sci.* **111,** 252–269.
[12]      Scherrer P. 1918. *J. Math. Phys.* **2**, 98–100.
[13]     Ogilvie P. et al. 2011. *MAPS* **46**, 1565–1586.

# TEMPERATURE RECORDS FROM GRAPHITE IN THE TWO DIFFERENTLY SHOCKED UREILITES NORTHWEST AFRICA 6871 AND NORTHWEST AFRICA 3140 – IS THERE A CORRELATION TO THE SHOCK DEGREE?

O. Christ[1], A. Barbaro[2], M. C. Domeneghetti[2], F. E. Brenker[3], and F. Nestola[1], [1]Department of Geosciences, University of Padova, Via G. Gradenigo 6, 35131 Padova, Italy, (oliver.christ@phd.unipd.it), [2]Department of Earth and Environmental Sciences, University of Pavia, Via Ferrata 1, 27100 Pavia, Italy, [3]Geoscience Institute, Goethe-University Frankfurt, Altenhöferallee 1, 60323 Frankfurt, Germany.

**Introduction:** Ureilites are the second largest group of achondrites and known to contain significant amounts of diamond [1]. The formation of this diamond was debated strongly in the scientific community [2 and references therein]. Recently, it was shown that large diamonds can be formed during shock events, most likely the shock event which destroyed either the ureilite parent body or a ureilite daughter body [2]. To obtain more insight into the shock event which produced diamond, we analyzed carbon aggregates from two differently shocked ureilites (U–S3 and U–S6 [3]) by Scanning Electron Microscopy (SEM), X-ray diffraction (XRD) and micro-Raman spectroscopy (MRS).

**Samples:** Northwest Africa (NWA) 6871 and Northwest Africa (NWA) 3140 are funds from Morocco. NWA 6871 consists mainly of olivine, while NWA 3140 consists of olivine and pyroxene. However, both samples contain abundant carbon aggregates which occur interstitial between the silicate grains and were extracted from the samples.

**Methods:** Carbon aggregates were identified by scanning electron microscopy (SEM) using a FEI Quanta 200 instrument operating at low vacuum which enables analyses without carbon coating. XRD was carried out using a Rigaku Oxford Diffraction SuperNova single-crystal diffractometer equipped with a 200K Dectris detector operating with a micro-source MoK$\alpha$ X-ray radiation. Carbon aggregates were mounted on top of borosilicate glass fibers and analyzed in 1° steps in a range of 1–360°. MRS measurements were conducted using a WITec alpha300 R spectrometer (wavelength = 532 nm). Further, the graphite-based geothermometer by [4] was applied, which uses the full width at half maximum of the graphite G-band.

**Results:** From optical microscopy observations, NWA 6871 is a highly shocked ureilite with a shock degree of U–S6, while NWA 3140 is medium shocked with a shock degree of U–S3. SEM and XRD showed that both samples contain carbon aggregates consisting of microdiamond, nanodiamond and nanographite closely intergrown with metal alloys and iron sulfides (e.g., FeNi, FeS). In NWA 6871, stacking order faults in diamond and compressed graphite can be observed, which are usually considered as shock indicators [5,6]. The MRS analyses allowed us to obtain the full width at half maximum of G-band ($\Gamma_G$) from which we estimated the temperature recorded by graphite to be 1411±32 °C for NWA 6871 and 1419±23 °C for NWA 3140.

**Discussion:** Two differently shocked ureilites contain carbon aggregates, however in NWA 6871 these aggregates are often elongated and blade-shaped as those reported by [e.g., 2] while aggregates in NWA 3140 are amoeboid. Of these carbon aggregates, graphite records a temperature of ~1400 °C, a temperature which exceeds magmatic temperatures for ureilites obtained by other geothermometers based on cation distribution in silicates [7 and references therein]. The graphite-based geothermometer by [4] has recently been adopted for graphite in ureilites, first by [8] and later by [9–11]. These authors proposed, assuming that micro-graphite was reduced in size during the impact event, that the temperatures recorded by graphite in ureilites could be related to the shock event which destroyed the ureilite parent body or the ureilite daughter body. Surprisingly, the temperature is the same for two samples with different shock degrees. However, the temperature falls into the temperature field for the catalytic transformation of graphite to diamond [12]. Further, the pressures of U–S3 (~10-15 GPa) and U–S6 (~55-70 GPa) are more than sufficient to produce diamond with the help of catalyzing metals, which are present in the form of FeNi and FeS.

**Conclusions:** The direct formation from graphite to diamond in ureilites with the help of catalysts upon shock was further proved. The graphite-based geothermometer records the highest temperature recorded by graphite so far. Graphite is nanometric in size and was most likely reduced in size from micrographite during the shock event. The temperature recorded by graphite was most likely reached during the shock event. It is noteworthy, that there is no apparent correlation between the temperature graphite has experienced and the degree of shock.

**References:** [1] Goodrich C.A. (1992) *Meteoritics, 27,* 327–352. [2] Nestola F. et al. (2020) *Proceedings of the National Academy of Science, 117,* 25310–25318. [3] Stöffler D. et al. (2018) *Meteoritics & Planetary Science, 53, 5–49.* [4] Cody G. D. et al. (2008) *Earth and Planetary Science Letters, 272,* 446–455. [5] Németh P. et al. (2014) *Nature Communications, 5,* 1–5. [6] Nakamuta Y. and Aoki Y. (2002) *Meteoritics*

*& Planetary Science*, *35*, 487–493. [7] Collinet M. and Grove T.L. (2020) *Meteoritics & Planetary Science*, *55*, 832–856. [8] Ross A.J. et al. (2011) *Meteoritics & Planetary Science*, *46*, 364–378 [9] Barbaro A. et al. (2020) *Minerals*, *10*. [10] Barbaro A. et al. (2021) *Geochimica et Cosmochimica Acta*, *309*, 286–298. [11] Barbaro A. et al. (2021) *American Mineralogist*, in press. [12] Dobrzhinetskaya L. F. (2012) *Gondwana Research*, *21*, 207–223.